Reactor Designs for Safe and Intensified Hydrogenations and Oxidations: From Micro- to Membrane Reactors

Baldassarre Venezia

Department of Chemical Engineering

University College London

November 2021

A thesis submitted for the degree of Doctor of Philosophy

I, Baldassarre Venezia, confirm that the work presented in this thesis is my own. Where information has been derived from other sources, I confirm that this has been indicated in the thesis.

_____

Signature

_____

Date

Abstract

The current and pressing environmental challenges are leading towards an important paradigm shift within the chemical industry. Green chemistry can be performed by using selective catalysts, and renewable and environment-friendly feedstock. For this reason, it is essential to provide scientists with platform tools that can allow safe and reliable catalyst testing, screening and studies. At the same time, as the use of green feedstock, such as oxygen and hydrogen, can pose new hazards, the design of intensified reactors can represent an unmissable opportunity to drive this green shift within the safe and scalable production of valuable molecules.

This thesis reports reactor design solutions of different scale that have been devised to guarantee safe and intensified catalytic hydrogenations and oxidations for catalyst testing and continuous production purposes. Starting with the aim of studying a catalyst under realistic operating conditions, a silicon microfabricated reactor was designed and tested for the gas phase combustion of methane and carbon monoxide over palladium and platinum catalysts. Owing to its small volume and to its isothermal temperature profile, this microreactor proved to be a safe and effective tool for performing information-rich experiments, while exhibiting a plug-flow behaviour with negligible external and internal mass transfer resistances. Reactions were performed in combination with X-ray absorption and IR spectroscopy, allowed by the detailed microfabrication reactor design, to investigate the catalyst structure-activity relationships in steady-state and transient experiments.

Boosting the catalyst activity can be achieved using catalytic nanoparticles, which offer an increased surface area compared to their bulk equivalents and hence an improved reaction rate. However, accessibility of the reactants to supported nanoparticles can be limited by the diffusion phenomena occurring around and inside a catalyst support. A recent trend of supporting nanoparticles onto surfaces modified using polyelectrolyte assemblies has attracted attention owing to the low temperature, ease and environmentally friendly preparation process.

Finely tuned *ex situ* synthesised palladium nanoparticles were adsorbed on the inner surface of a tubular Teflon AF-2400 membrane, which was modified

with polyelectrolytes in a layer-by-layer configuration. The membrane was used as a tubular reactor inside an outer tube with pressurised hydrogen, and nanoparticles of different size and shape were tested in the continuous hydrogenation of nitrobenzene to aniline. The observed reactivity depended on the different nanoparticle size and on the palladium oxidation state. The use of a tube-in-tube membrane reactor ensured process safety owing to the small volume of gas stored in the tube annular section and to the continuous processing. Alcohol oxidations using molecular oxygen can be dangerous due to the risk of creating explosive mixtures with the organic substrate. Two slurry loop reactors were developed using the same Teflon AF-2400 membrane in different configurations: a tube-in-tube and a flat membrane configuration for scalable reactions. These were designed and tested to carry out safe aerobic oxidation of alcohols. The membrane separated the oxygen from the organic phase and allowed a controlled dosing of the gaseous reactant. In order to boost the turnover frequency, the catalyst was used in the form of a slurry which was recirculated in a loop where it contacted the membrane saturator and a crossflow filter. This allowed the withdrawal of the liquid products from the loop. The reactors could be operated continuously, and provided improved process safety and comparable catalyst turnover frequency to conventional batch processes. When scaling up reactors, inadequate mixing can occur impacting on process safety and product quality. A Taylor-vortex membrane reactor is presented for the first time, combining the benefits of a flexible baffle structure inside a Taylor-vortex system that can hinder axial dispersion, and a supported tubular membrane for safe gas-liquid reactions. Stable conversion and product selectivity were achieved in the homogeneously catalysed continuous aerobic oxidation of benzyl alcohol. No pervaporation of organics through the membrane was detected during reaction, making this reactor a safe and a scalable tool for continuous gas-liquid reactions.

Impact statement

Today, a chemical company must adapt to an increasingly competitive market and respond to stringent and mounting ecological requirements [1]. This is leading to a need for developing efficient and less energy-intensive processes where catalysis is receiving ever-growing attention. The reactor is at the heart of a chemical process, and its design and operation are pivotal to the catalyst performance.

This thesis presents reactor design solutions that can be employed for studying catalysts and for the continuous scalable production of chemicals, which can be of great benefit to chemists and engineers, and lead to positive economic and environmental impacts. The reactors developed in this work are designed to conduct safe catalyst tests, studies of catalyst structure-activity relationships under realistic industrial conditions, and to offer a basis for plug-and-play scaled-up reactor designs used in the continuous production of valuable molecules. The results from this thesis are highlighted in publications and presentations and are available to the scientific community. The reactors demonstrated in this thesis are presented in order of increasing volume capacity and inlet flowrate, with the first reactor being a microreactor used for *operando* studies of gas-phase catalytic reactions. This is a versatile and unique tool for rapidly generating information on catalyst performance that can benefit researchers, owing to the high space velocities that can be employed, the absence of dead volumes, and the integration with X-ray and IR spectroscopies. These techniques can be used to investigate the catalyst state and the species involved during reaction, which is useful information in the catalyst development phase. This work received the attention of the associate editor Bin Liu, who selected it among three outstanding recent research papers published in *Catalysis Science & Technology*. It also features on the inside front cover of the journal and on the Diamond Light Source website among the Science highlights of 2020.

The last reactor demonstrated in the thesis is a litre-scale membrane reactor designed for continuous gas-liquid reactions. This was built in collaboration with Autichem Ltd, a company that develops flow reactors for pilot scale and multi-tonne production applications. It is a Taylor-vortex reactor that, for the

first time, integrates a tubular membrane for safe gas-liquid continuous reactions, and allows enhanced mixing thanks to a novel baffle design. With this membrane reactor, molecular oxygen can be pressurised inside the membrane and be safely employed to oxidise alcohols in flow, avoiding the use of toxic inorganic oxidants. This work is expected to have a positive impact on process safety and intensification, as well as being beneficial to sustainability, allowing the use of greener reagents. It will also be useful for the development of newer multipurpose reactors, helping to shift the chemical industry paradigm away from the conventional use of batch reactors towards the increasingly popular intensified flow reactors.

Acknowledgements

First of all, I would like to express my gratitude to my supervisor, Prof Asterios Gavriilidis, for his mentorship, his support throughout my PhD and for giving me the opportunity to present my work at international conferences and collaborate in interdisciplinary projects.

I offer my appreciation to Prof Sankar Gopinathan and Dr Santhosh Matam for their academic consulting in the silicon microreactor project, shining a light in the dark meanderings of X-ray and IR spectroscopy.

Thanks to Dr Enhong Cao, for guiding me through the challenges, tips and nuances of microreactors and to David Morris whose industrial experience, skills and knowledge were of paramount importance in the development of the Taylor-vortex membrane reactor. For the realisation of most of the other continuous reactors presented in this thesis, particular thanks go to the departmental workshop and especially to Simon Dawes whose skills and experience were key in the successful materialisation of these ideas.

A big thanks to Dr Simon Barrass for his generous help in building safe experimental rigs and to Albert Corredera for making bespoke electrical equipment and to both for providing me with good insights for hazard studies. Thanks to Nick Snead for helping me automate the setups with LabVIEW, and for spending his time checking on me during those day-long reactions. I would also like to thank the Chemical Engineering Research Society (CheERS) at UCL for organising such nice events, bringing together researchers and enriching PhD life with memorable pub games. Thanks to my student Daniel, whose excellent work and generosity I will not forget and to my special friends and colleagues with whom I shared the office during my PhD, especially Anand and Spyros for being supportive companions in our never-ending evening chats. A big thanks also goes to my friends in London, Conor, Giannis, Ilaria, Kostas, Marco, with whom I share really good memories.

Finally, I want to thank my parents, Angela e Giovanni, for always being my steady reference point, and a special person whose love and support were my driving force throughout the last part of this journey: Thank you Sally.

Contents

List of figures

List of tables

Nomenclature

Latin symbols

a	specific volumetric surface area, m^{-1}
a_m	specific membrane surface area, cm^2/g
a_p	the external surface area of the catalyst per unit mass, m^2/kg
A	area, m^2
A_L	light absorbance, a.u.
cd	atomic covalent diameter, m
$\hat{c}_p$	molar heat capacity, $J/(mol \cdot K)$
C	concentration, mol/m^3
CCT	catalyst contact time, $g \cdot s/g$
C_{WP}	Weisz-Prater number, -
$\hat{C}$	normalised concentration, -
d_h	hydraulic diameter, m
d_p	particle diameter, m
D_{ax}	axial dispersion coefficient, m^2/s
D_e	effective diffusivity, m^2/s
D_m	molecular diffusivity, m^2/s
E	residence time distribution function, -
E_a	activation energy, J/mol
E_{exp}	energy of explosion, J
F	molar flowrate, mol/s
g	gravitational acceleration vector, m/s^2
h_{rib}	baffle/rib thickness, m
H	height or head, m
H_E	Henry constant, Pa/M
I	beam intensity, a.u.
I_s	intensity of segregation, -
J_V	volumetric flux, $m^3/(m^2 \cdot s)$
k'	pseudo-first order reaction rate constant, $m^3/(s \cdot kg)$

k_{GL}	gas-liquid mass transfer coefficient from the gas film side, m/s
k_{GS}	gas-solid mass transfer coefficient, m/s
k_L	gas-liquid mass transfer coefficient from the liquid film side, m/s
k_{LS}	liquid-solid mass transfer coefficient, m/s
L	length, m
LEL	lower explosion limit, -
m	mass, kg
$\dot{m}$	mass flowrate, kg/s
MM	molar mass, kg/mol
MR	Mears number, -
n	order of reaction, -
N	number, -
n_m	molar amount of metal catalyst, mol
OCR	oxygen consumption rate, mL/min
p	pressure, Pa
P	power, W
Pe	Péclet number, -
P_m	membrane permeability coefficient, $m^3 \cdot m/(s \cdot Pa \cdot m^2)$
Q	heat flow, W
r	reaction rate, $mol/(s \cdot m^3)$
r'	reaction rate per unit of catalyst mass, $mol/(s \cdot kg)$
r_i	rotor radius, m
r_o	inner vessel radius, m
R	recycle ratio, -
Re	Reynolds number, -
R_G	ideal gas constant, $J/(mol \cdot K)$
RSS	normalised residual sum of squares, -
R^2	coefficient of determination, -
s	solubility, Pa^{-1}
S	product selectivity, -
Sc	Schmidt number, -
Sh	Sherwood number, -
t	time, s

T	temperature, K
Ta	Taylor number, -
ΔT_{ad}	adiabatic temperature rise, K
TOF	turnover frequency, mol/(mol·h)
u	velocity , m/s
U	heat transfer coefficient, W/(m^2·K)
v	volumetric flowrate, mL/min
$\tilde{V}$	molar volume, mol/m^3
V_R	reactor volume, m^3
x	molar fraction in the liquid phase, -
X	conversion, -
y	molar fraction in the vapour/gas phase, -
z_{rib}	inter-baffle distance, m

Greek symbols

α_p	fraction of atoms below the surface layer in a nanoparticle, -
δ_m	membrane thickness, m
ε	specific power input, kW/m^3
η	effectiveness factor, -
θ	dimensionless time, -
λ_f	fluid thermal diffusivity, m^2/s
μ	dynamic viscosity, Pa·s
v	kinematic viscosity, m^2/s
v_i	stoichiometric coefficient of species i, -
ρ	density, kg/m^3
ρ_{cat}	catalyst slurry concentration, g/L
σ	standard deviation, -
σ_c	constriction factor, -
σ^2	variance, -
τ	mean residence time, s
τ_b	catalyst bed tortuosity, -

τ_p	particle tortuosity, -
φ	porosity, -
ψ	extinction coefficient, -
ω	frequency, rad/s
Ω	rotational speed, rpm

Subscripts

A	reactant A
Ace	acetophenone
AN	aniline
b	catalyst bed or bulk
Bz	benzene
BzAc	benzoic acid
BzAl	benzaldehyde
BzBz	benzyl benzoate
c	critical
cat	catalyst
CHO	aldehyde/ketone
CH_4	methane
CnAl	cinnamaldehyde
D	disproportionation
G	gas
GrAl	geranial
H_2	hydrogen
i	species i or interface
in	inlet/initial
m	membrane or catalyst metal
NB	nitrobenzene
NS	nitrosobenzene
N_2	nitrogen
o	initial
O	direct oxidation

out	outlet/final
O_2	oxygen
p	particle
P	permeation
PipAl	piperonal
r	reactant or radial
rec	recycle
ref	reference
R	reactor
s	solid surface
Sty	styrene
t	time dependent or transmitted
Tol	toluene
TV	Taylor vortex
vap	vapour
z	axial
0	initial or incident
3PP	3-phenyl-1-propanol

Chapter I. Introduction

The mounting pressure to achieve sustainable chemical processes is driving the modernisation of chemical industry through the study of more selective and cleaner catalytic reactions. Reactors are at the heart of a chemical process and their design and operation are key for ensuring safe, effective and reproducible catalytic studies and continuous production of chemicals.

This chapter discusses the motivation and the objectives of this thesis as well as presenting its outline.

1.1. Motivation and objectives

Since the early 90's there has been a progressive realisation in the chemical engineering world about the need for developing more sustainable and efficient technologies, owing to the ever stringent ecological standards and to the growing competition within the chemical industry [2]. In this context, process intensification has gradually risen as a solution to bringing cleaner, safer and more energy efficient technologies. As part of the early stages of designing sustainable and efficient chemical plants, catalysts, which are used to accelerate reactions, need to be developed and studied to better understand their selectivity and reactivity under operating conditions, and screened to select the most suitable for the process. In this context, the chemical reactor plays an important role in hosting the catalyst and affecting its performance, providing useful information to the chemical engineer about structure-activity relationships, product selectivity and kinetics. The chemical reactor is at the heart of a chemical process, where raw materials are converted into useful and valuable products. Its performance, alongside its capital and operating costs, dictates the downstream processing steps and the costs of the final product.

It is common to find reactors that involve multiple reacting phases in their operation, in the presence of homogeneous or heterogeneous catalysts [3-5]. Close contact between different reactants and the catalyst is pivotal to overcome mass transfer resistances, maximise the catalyst performance and achieve an intrinsic reaction rate. In this way a more efficient use of the catalyst can be attained, requiring smaller amounts of catalyst operating with a higher efficiency. However, when using solid catalysts the diffusion of reactants inside and to the catalyst particles can become a bottle-neck to the overall reaction rate. In more detail, the mass transfer steps encountered in a heterogeneously catalysed gas-solid or liquid-solid reaction are:

1. External mass transfer: diffusion of the reactants from the liquid/gas bulk phase through the liquid/gas film around the catalyst particle.
2. Internal mass transfer: diffusion of the reactants within the pores of the catalyst.

These represent a common problem in chemical reactor design that can affect reactors employed for both catalyst testing, by generating biased information, and in the continuous production of valuable chemicals, by lowering catalyst efficiency and productivity. An integral part of the process intensification philosophy is to maximise the reaction efficiency, minimise the environmental impact and guarantee a safe process operation [6, 7].

Safety considerations are of paramount importance when designing a chemical process that involves the presence of hazardous chemicals, pressurised gases or reactions that are potentially prone to run-away. Some of the reactor design features that can mitigate the risks associated with the reaction are: efficient heat dissipation, controlled dosage of the reactants, and reduction of the reactor size and/or compressed gas volumes.

In this context, reactor designs that bridge the process intensification features of quality and safety are highly desired. The aim of this thesis is to develop flow chemistry technology and tools that provide advancements towards sustainable chemical productions by catalytic processes. The underlying rationale behind this work is that key features of process intensification can be applied to the design of efficient and safe chemical reactors for the study of catalysts and for carrying out multi-gram lab-scale continuous production of valuable molecules. This will be achieved through the following three objectives:

1. Development of reactors with enhanced mass and heat transfer, efficient catalyst use, flexible plug-and-play configuration and improved process safety.
2. Development of reactors for the comparative, performance, and *operando* structural studies of catalysts.
3. Development of reactors for multi-gram lab-scale production of chemicals.

Five different reactors at increasing scales are presented, from micro- to membrane reactors which provide unique advantages from enhancing catalytic activity to improving process safety.

1.1.1. Micro- and millireactors for catalyst studies

The development of microreactor technology started in the 90's and is one of the results of process intensification which expanded with the advances of continuous flow and microfabrication techniques [8]. The popularity of microreactors has been driven by the excellent heat and mass transfer enhancements that they can provide to reactions in flow, along with an easy operation at a small scale and the use of inexpensive materials [9]. Owing to these characteristics, microreactors have been employed in a variety of reactions at both small and large scales [8]. In particular, microreactor technology has progressed focussing on providing chemists and engineers with tools to extract information on reaction kinetics and mechanisms. This owing to the ever-advancing analytical tools for online process monitoring and to the miniaturised reactor volumes which enable achieving high throughput information and a narrow residence time distribution of the reactants. However, studying catalysts under well-defined realistic conditions in reactors that can be coupled with analytical and spectroscopic techniques is challenging. Furthermore, these reactors should be safe, have no dead volumes and offer enhanced heat and mass transfer. Therefore, in the third chapter of this thesis the design of a silicon microreactor is presented, which demonstrates a successful integration of X-ray and IR spectroscopies for studying methane and carbon monoxide oxidation over heterogeneous catalysts with in-line gas outlet composition analysis. This chapter offers insights on the microfabricated design that allowed high energy X-ray beams and IR radiation to be shone on the catalyst, along with results from time-resolved experiments, useful to understand the catalyst reactivity under dynamic conditions.

1.1.2. Membrane reactors for catalyst testing and continuous production

While microreactors enable a safe operation at a small scale, at increasing reactor volumes the process safety features resulting from a reduced reactor size start to decline [10, 11]. Continuous flow can still provide a safe operation in milli- and litre-scale reactors, such as an enhanced control over the reaction

parameters, improved mixing and better heat management compared to batch reactors [12]. Hazardous chemistries can be accessed in different ways using continuous flow. An example comes from liquid phase oxidations using molecular oxygen, which could be performed by either mixing the liquid substrate with oxygen diluted in nitrogen, or by separating the reacting phases using a gas-permeable membrane [13]. The latter allows a more controlled dosing of the gaseous reactants, without compromising the concentration of oxygen employed. Furthermore, membranes can be versatile and used for any other gas-liquid reactions such as liquid phase hydrogenations. For these reasons, process intensification can be achieved using membrane reactors, also owing to their ability to offer support for catalysts and enhance gas-liquid mass transfer [14].

In this thesis, four membrane reactors for catalyst testing and continuous production are presented in ascending order of size from milli- to litre-scale. These reactors host different catalyst configurations including adsorbed palladium nanoparticles on a gas-permeable membrane used to study their performance, or a catalyst slurry in flow for enhancing mass transfer and maximising catalyst usage.

1.2. Thesis outline

The thesis is structured into eight chapters, with the first one being the Introduction and the second one the Literature review, reporting successful examples of process intensified reactor designs and catalyst configurations applied to continuous hydrogenation and oxidation reactions. The use of microreactors and membrane reactors are then discussed in detail as tools to achieve process intensification and guarantee process safety at different scales. A schematic of the thesis outline is shown in Figure 1.1.
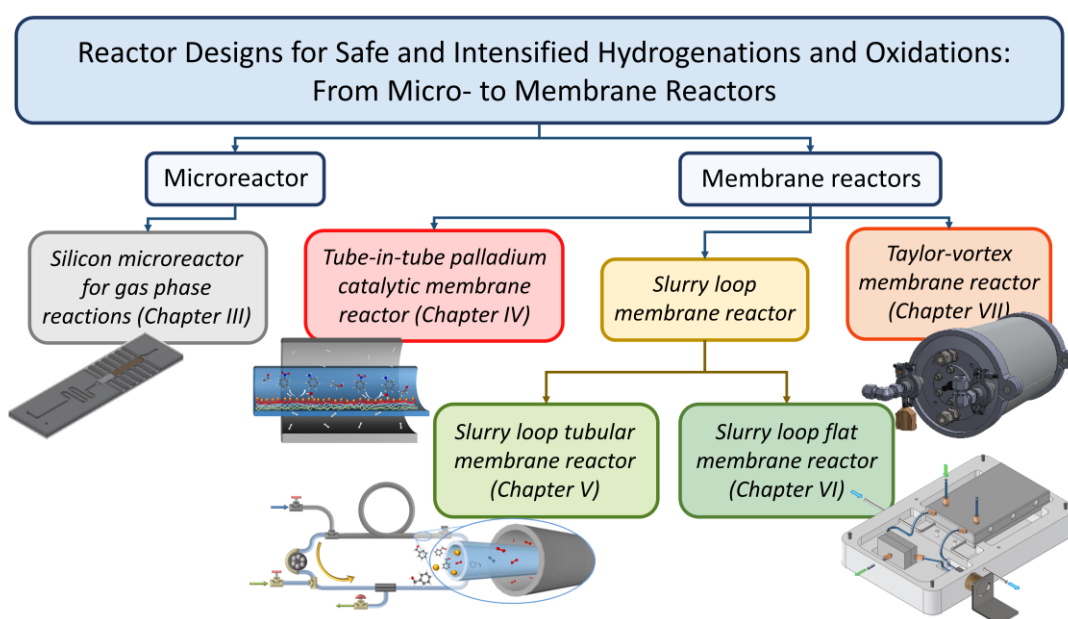
Figure 1.1. Schematic of the thesis outline.

The list of reactor solutions presented in this thesis starts from the smallest, a silicon microreactor, which is presented in **Chapter III**. Owing to its small size and to its plug-flow behaviour, the reactor was used as a safe and effective tool to conduct *operando* studies of palladium and platinum catalysts packed in a microchannel, where methane and carbon monoxide catalytic combustions were performed. The contents of this chapter have been published in "Silicon microfabricated reactor for *operando* XAS/DRIFTS studies of heterogeneous catalytic reactions", Catalysis Science & Technology, 2020, 10, 7842-7856.

Chapter IV presents a Teflon AF-2400 tubular membrane reactor in a tube-in-tube configuration with a modified inner surface that hosts adsorbed *ex situ*

synthesised and finely tuned catalytic palladium nanoparticles of different size and shape. Nitrobenzene hydrogenation was carried out in flow, with molecular hydrogen being pressurised outside the tubular membrane, and different catalyst nanoparticles were compared in their performance. The contents of this chapter can be found in "Catalytic Teflon AF-2400 membrane reactor with adsorbed *ex situ* synthesized Pd-based nanoparticles for nitrobenzene hydrogenation", Catalysis Today, 2021, 362, 104-112.

In **Chapter V** the same tubular membrane is presented as an oxygen saturator in a slurry loop reactor for the continuous aerobic oxidation of benzyl alcohol. The reactor used an industrial catalyst mixed with the organic substrate in a slurry form that circulated in a loop to which the oxygen saturator and a filter were connected. A comparative study was conducted employing the same catalyst in a conventional autoclave and in a packed-bed reactor operated in a trickle-flow operation mode. The information presented in this chapter can also be found in "Slurry loop tubular membrane reactor for the catalysed aerobic oxidation of benzyl alcohol", Chemical Engineering Journal, 2019, 378, 122250.

Chapter VI describes a second slurry loop membrane reactor with a plug-and-play configuration where scalability was attempted by increasing its loop volume and the substrate inlet flowrate. A flat Teflon AF-2400 membrane was used as a gas saturator in the loop and was sealed on wide slurry channels that allowed operations at increased catalyst slurry loadings. The use of electrical heaters and of an insulated box in which the whole reactor was placed guaranteed a plug-and-play operation. This reactor was demonstrated in the continuous and batch lab-scale aerobic oxidation of various primary and secondary alcohols, while the hydrogenation of styrene was carried out as part of a characterisation study to determine the volumetric gas-liquid mass transfer coefficient.

Chapter VII is dedicated to the Taylor-vortex membrane reactor, a novel flow reactor for continuous gas-liquid reactions. The design consists of a cylindrical rotor inside a concentric cylindrical vessel. In the annulus created by the rotor and the vessel, a tubular membrane was supported by means of horizontal baffles that divided the liquid volume in segregated axial compartments. Macromixing was characterised at different rotor agitation speeds and inlet

flowrates and the reactor was demonstrated in the oxidation of benzyl alcohol using a homogeneous palladium catalyst and pressurised molecular oxygen in the tubular membrane. Furthermore, pervaporation was monitored during reaction to ensure process safety.

The conclusions with a future outlook are highlighted in the final chapter, **Chapter VIII**.

Chapter II. Literature review

Reactors with enhanced mass and heat transfer, along with high performance catalysts and a safe operation are keys to the development of sustainable processes. Micro- and membrane reactors have found widespread application in organic synthesis and in performing safe and enhanced exothermic and hazardous reactions in flow. In this chapter, a review on some recent advances on green catalytic processes is presented along with their challenges that can be addressed with the use of process intensification.

2.1. Challenges in the modern fine chemical industry

In the last three decades, the bulk and fine chemical industry have been facing serious environmental problems [15-18]. Several synthetic practices are responsible for the generation of large amounts of waste and a growing pressure is prompting chemists to find solutions to minimise it [15].

Compared to the bulk chemical industry, the fine chemical and pharma industries suffer the most from this environmental issue. The Environmental factor, also known as E-factor, is an indicator of the environmental footprint of a chemical process, and represents the total mass of waste generated per mass of main product of a reaction. The E-factor in the fine chemicals and pharma industry is one or two orders of magnitude higher than that in the bulk chemical industry. Among the main reasons are the multiple synthetic steps necessary to produce the complex fine chemical molecules, and the amount of by-products that each step involves. Furthermore, the common use of inorganic stoichiometric reagents in place of catalysts is also partially responsible. Some examples include the use of metals (*e.g.* Na, Mg) and metal hydrides (*e.g.* $LiAlH_4$ and $NaBH_4$) as reducing agents, and permanganate, manganese dioxide and Cr(VI) used in oxidation reactions.

Oxidations are among the oldest and most economically significant commercial reactions. More than 50% of all chemicals produced in catalytic processes undergo at least one oxidation step [19]. Oxidation reactions play a pivotal role in the chemical industry by being employed in the synthesis of various key functional groups, such as alcohols, aldehydes, ketones, carboxylic acids and epoxides [20-24]. In particular, alcohol oxidations are used to produce aldehydes and ketones, which are useful in the manufacture of fragrances and represent valuable molecular platforms in organic syntheses [24-29].

Because of its evident availability and negligible environmental impact, molecular oxygen has been considered for the development of environmentally benign selective oxidation of alcohols [13, 16, 24, 30-40]. In combination with selective catalysts, oxygen can improve the atom economy by reducing the formation of by-products [34].

Similarly to the aerobic oxidation of alcohols, the use of molecular hydrogen as a reactant in hydrogenations, follows the green chemistry principles of improved atom economy and, depending on the source, use of renewable feedstock [41, 42]. Green hydrogenations can find applications in the fine chemical and pharma industry such as in the hydrogenation of unsaturated carbon-carbon bonds, aldehydes/ketones and nitro to amino groups [2, 21, 22].

2.2. Catalysis for hydrogenation and oxidation reactions

As stated in the twelve guiding principles of green chemistry, catalysis is a fundamental tool to achieve sustainable syntheses and a way to prevent formation of waste and improve the reaction atom economy [41, 43].

Industrial catalysts can be divided into two classes: heterogeneous and homogeneous catalysts [19].

2.2.1. Heterogeneous catalysts and applications to hydrogenations and aerobic oxidation of alcohols

In industry, catalysts are generally incorporated in supports, such as carbon, alumina, silica/mesoporous silica or zeolites. These provide mechanical stability, expose the active catalyst metal to a larger surface area for reaction and minimise the required catalyst loading [19]. This is a common practice in industrial applications except for Raney-type catalysts, which are used in bulky amounts in hydrogenation reactions [19]. There are various physical and chemical methods that can be employed to incorporate an active metal on a support. Among these methods, impregnation, precipitation, adsorption and ion-exchange of the active metal precursor on a ceramic support are the most common [19].

Examples of heterogeneous catalysts employed for the green solvent-free oxidation of alcohols can be found in the works published by the group of Hutchings. The researchers from Cardiff University investigated the role of gold and palladium in the selective oxidation of alcohols to the corresponding aldehydes. Palladium is among the most popular precious metals used in the aerobic oxidation of alcohols, owing to its high catalytic activity [34]. Scheme 2.1 shows the classical dehydrogenation mechanism of the oxidation of an alcohol over palladium. The first step is the insertion of the metal atom between the O-H bond of the alcohol to produce a metal alkoxide and a metal hydride species. Subsequently, the alkoxide is dehydrogenated by β-hydride elimination yielding the corresponding aldehyde which desorbs from the surface. Finally, the palladium site is regenerated *via* reaction of molecular oxygen with the adsorbed hydrogen atoms to produce water [34].
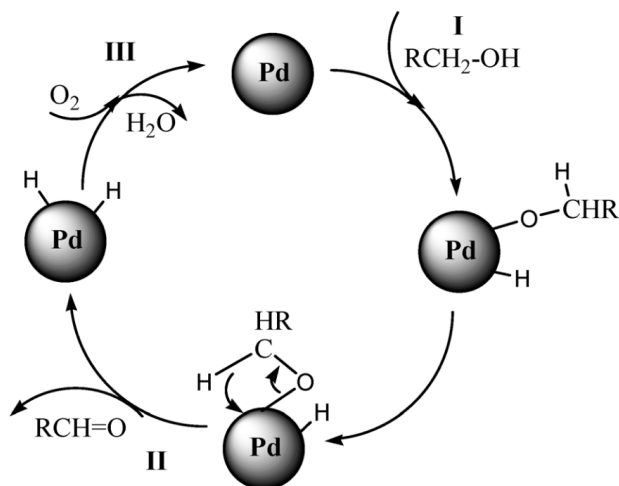
Scheme 2.1. Schematic of the heterogeneously catalysed aerobic oxidation of a primary alcohol to the corresponding aldehyde over palladium. Reprinted from Guo *et al.*, Recent advances in heterogeneous selective oxidation catalysis for sustainable chemistry, Chemical Society Reviews, 2014, 43, 3480-3524, with permissions from the Royal Society of Chemistry.

The alloying with Au has proven to have beneficial catalytic effects in the oxidation of alcohols [44]. Studies on the benzyl alcohol oxidation, generally taken as a model reaction for this family of reactions, have shown that the Au-Pd combination considerably enhances conversion and selectivity to benzaldehyde [45, 46]. Compared to the monometallic Au or Pd, Au-Pd nanocrystals improve activity by a factor of 25 [46]. Enache *et al.* investigated the effect of gold addition to palladium and more specifically the influence of their crystal morphology on the catalytic activity [46]. One interesting finding was that in the case of 2.5 wt% Au - 2.5 wt% Pd/TiO$_2$, the crystallites were made of a bulk Au core and an outer Pd shell. This phase segregation, produced after calcination, created a bimetallic surface in which gold acted as an electron promoter to palladium, hence explaining the high turnover frequencies for the benzyl alcohol oxidation [46].

In heterogeneous catalysis, impregnation of the metal precursor over a support is widely applied. This is performed by thermally treating the support impregnated with the metal precursor solution. However, despite its facile application, this method does not provide a high degree of control over the resulting crystallite morphology, composition and size distribution [47]. To

overcome these issues, a new technique has been developed by Hutchings and co-workers at Cardiff University [47]. This method is an improvement of the conventional impregnation technique, and it is known as "excess-anion" modification. An excess of Cl^- ions is introduced in the impregnation medium by adding HCl [47, 48]. The increase in the concentration of ions favours the formation of a homogeneous solution of $AuCl_4^-$ and $PdCl_4^-$ ions which are then reduced to the corresponding metals. The formed dried material is then heated up to 400 °C and treated under flow of 5% H_2 in Ar in order to reduce the nanoparticle precursors and abate the residual chloride ions [48]. An important finding was that, compared to the catalysts prepared *via* the conventional impregnation technique, the Au-Pd/TiO_2 catalysts prepared by the "modified impregnation method" revealed no significant deactivation over several days of reaction, as well as a high activity in the solvent-free aerobic oxidation of benzyl alcohol, allowing also to have a better control over the catalyst particle composition [47].

2.2.1.1. Nanoparticle science in heterogeneous catalysis

The studies conducted by the group of Hutchings highlighted the importance of the preparation method and the resulting catalyst particle size in achieving highly active and durable catalysts. In this context, the recent advances in nanoparticle science have raised considerable attention over the last few years [49-53]. Compared to their bulk equivalents, nanoparticles offer a larger surface-to-volume ratio, a higher catalytic activity, and the different reactivity resulting from their various shapes and compositions can be beneficial in hydrogenation and oxidation reactions [52, 54-58]. Figure 2.1 shows an example of decreasing surface-to-total atoms ratio for cuboctahedral nanoparticles of increasing diameter [59].
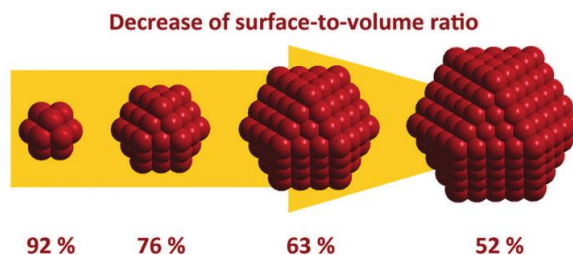
Figure 2.1. Decrease of the surface-to-volume ratio for cuboctahedral nanoparticles. Reprinted from Sonström *et al.*, Supported colloidal nanoparticles in heterogeneous gas phase catalysis: on the way to tailored catalysts, Physical Chemistry Chemical Physics, 2011, 13, 19270-19284, with permissions from the Royal Society of Chemistry.

Among the different synthetic methods, the synthesis of colloidal nanoparticles represents a facile method of preparation [59], producing nanoparticles that can be either adsorbed onto a support [52], or being used unsupported in the reaction media [54, 60]. In the study reported by Roldan Cuenya, platinum nanoparticles were synthesised by dissolving diblock copolymers (PS-P2VP) in toluene, which act as ligands, and upon loading of the H_2PtCl_6 metal precursor [52]. The resulting nanoparticles were then coated onto a γ-Al_2O_3 powder support and the ligand was removed after a thermal treatment under O_2 at 375 °C. The four similarly sized nanoparticles (0.8 - 1 nm) of different shapes were then tested for the 2-propanol partial oxidation and it was observed that bilayer Pt NPs displayed the lowest reaction onset temperature and the best performance among the other nanoparticles, due to both an effect of the support and to the high number of low-coordinated atoms, arising from their peculiar geometry.

Nanoparticle size control can be pivotal in order to maximise catalyst turnover frequency, and thus optimise catalyst economy. This was demonstrated in a work by Sun *et al.* in which ultrafine Pt nanoparticles in the range of 1.9 - 3.5 nm were uniformly deposited on multi-walled carbon nanotubes (MWNT), achieving a narrow particle size distribution, even at loadings up to 50 wt% [61]. The catalysts were prepared by dispersing the nanotubes in an ethanol solution of $H_2PtCl_6 \cdot 6H_2O$ which was mixed with $NaBH_4$ in ethanol to reduce the precursor to platinum metal. After washing and thermal treatment at 60 °C

for 6 h, the resulting catalysts with different platinum loadings were tested in the solvent-free nitrobenzene hydrogenation to aniline under different operating conditions. Between 0.01 and 0.1 mol of nitrobenzene dissolved in the product aniline were hydrogenated using 1.4 - 5 mg of Pt/MWNT catalyst in a high pressure stainless steel reactor operating at 6 - 40 bar hydrogen pressure and at temperatures up to 60 °C. An unprecedently high catalyst activity was observed when 0.01 mol of nitrobenzene were hydrogenated to aniline with a 100 % yield in 7 min, corresponding to a turnover frequency of 66900 h^{-1} using 5 wt% Pt/MWNT at 60 °C and 40 bar H_2. Moreover, the scientists observed a structure-sensitivity of the reaction for nanoparticles ranging between 2 and 2.4 nm. In particular, the product of the average total turnover frequency multiplied by the nanoparticle diameter, was higher for nanoparticles of 2 nm, than for those larger than 2.4 nm.

2.2.2. Homogeneous catalysts and applications to the aerobic oxidation of alcohols

The presence of multiple phases and a solid catalyst support, characterised by a certain shape and porosity, represents an obstacle to the reactant diffusion from the liquid bulk to the active sites on the catalyst surface. This is particularly true for those reactions generally catalysed by noble metals and with a fast intrinsic kinetics, including hydrogenations [62]. In this context, the use of homogeneous catalysts can overcome this limitation. Homogeneous catalysts are usually metal complexes soluble in the solvent and the liquid substrates, resulting in the absence of external solid-liquid and internal solid resistances [63]. Owing to corrosion and metal fouling on the reactor walls, and to the difficult separation and reuse of the catalyst, homogeneous catalysts are not widely used in industry [30]. However, due to their nature, homogeneous catalysts are only limited by the extent of micromixing, allowing them to achieve high yields and turnover frequencies.

An example of a homogeneous catalyst system is the $Pd(OAc)_2$ with $NaHCO_3$ in DMSO, reported for the first time in 1998 by Peterson and Larock, and used in the aerobic oxidation of primary and secondary alcohols to the corresponding aldehydes and ketones [64]. The catalytic system was fine-

tuned in later years to replace DMSO with more environment-friendly solvents [65], and with different bases, including pyridine, to achieve improved activity [66]. The reaction mechanism of the catalytic Pd^{II}/Pd^{0} system in the aerobic oxidation of alcohols is somehow similar to what is presented in Scheme 2.1 [63]. This involves the coordination of the alcohol to the Pd^{II} atom and the deprotonation of the alcohol by the base to form the Pd^{II}-alkoxide intermediate. Similarly to the heterogeneous process, the carbonyl group is freed in the β-hydride elimination and the Pd^{II}-hydride intermediate is formed. This undergoes reductive elimination to form the reduced Pd^{0} species which is metastable and can aggregate forming black bulk palladium metal. To prevent this from happening, molecular oxygen should oxidise the Pd^{0} back to the initial Pd^{II} species, before this starts to form clusters.

2.3. Process challenges in green catalysis

As previously mentioned, the use of molecular oxygen and hydrogen in oxidation and hydrogenation reactions follows the green chemistry metrics of improved atom economy and use of renewable feedstock. However, this can be challenging from a practical and sustainable industrial perspective [27, 67, 68]. A genuine safety concern arises when mixing oxygen with flammable organics and alternative approaches including the dilution of oxygen with inert gases have been considered to overcome this hazard [35, 69]. Nevertheless, this does not always represent an ideal solution as higher pressures would be required to reach the desired product selectivity and rate [70].

On the other side, hydrogenations generally necessitate high pressures to achieve the desired conversion and selectivity, for which conventional batch reactors are generally not recommended, and dedicated pressure-resistant autoclaves are used with exceptional safety precautions [68].

Furthermore, both hydrogenations and oxidations are usually characterised by high enthalpies of reaction [21, 68]. For example, the oxidation of benzyl alcohol to benzaldehyde has a net reaction enthalpy of -187 kJ/mol at 25 °C and 1 atm [71], and the hydrogenation of nitrobenzene to aniline is characterised by a reaction enthalpy of -544 kJ/mol at 200 °C [72]. This poses the problem of effectively dissipating the heat generated during reaction, which can lead to hotspots that are detrimental to the catalyst, or worse, cause solvent boil-off or a runaway reaction.

In addition to the hazards mentioned above, and in agreement with the green chemistry principles, reactions should be conducted under minimal mass transfer resistances in order to maximise catalyst efficiency and minimise catalyst loading [68]. Design of safe and intensified continuous reactors for catalyst testing and production can represent a solution to the abovementioned problems. The sections below report a literature review on the recent advances of process intensification in reactor design.

2.4. Reactor design solutions for safe and intensified hydrogenation and oxidation reactions

The chemical industry has been historically dominated by the use of multi-purpose and flexible batch stirred vessels [73]. However, their widespread use and ease of operation come at a cost. Stirred tank reactors often suffer from high pressure limitations and inhomogeneous temperature distribution and mixing of the reactants within the different phases involved in the reaction [73]. These issues are generally amplified at large scales, leading to a decrease in productivity and catalyst usage.

2.4.1. Process intensification

In the last decades, a new approach to the design of unit operations has emerged, aiming at developing efficient and cost effective chemical processes [6]. This is known as process intensification (PI) and can be achieved through the design of novel equipment and the modification of existing process techniques, leading to novel and substantial positive changes with respect to previous technologies [6, 74]. In detail, PI can be defined using the following simplified metrics elaborated in previous works [6, 14, 75]:

1. Improved reaction atom efficiency
2. Reduced process ecological footprint
3. Decreased reactor/equipment capital cost
4. Enhanced process energy efficiency
5. Decreased use of supplementary reagents and catalysts
6. Lower operating temperatures and pressures
7. Safe operation

Many are the examples in the chemical industry of intensified reactors that have had a clear and positive effect on process efficiency, reaction time, equipment volume, and product purity [6, 76, 77]. Among them is the spinning disk reactor investigated in one of the SmithKline processes that led to dramatic reduction in reaction time and accessorial equipment [6, 78]. Process intensification can also be achieved by the integration of unit operations which can dramatically reduce the number of processing steps [6, 79]. A remarkable

example reported in many textbooks, is the development of a methyl acetate process from the Eastman Chemical Company that was capable of integrating reaction and distillation, reducing the number of equipment parts from 28 to 3 [6]. Another exemplary result of process intensification at industrial scale is the Venturi loop reactor, capable of operating with a catalyst slurry in either continuous or batch mode and providing intense mixing between the multiple reacting phases. The Venturi Loop reactor as shown in Figure 2.2 consists of a Venturi ejector through which the catalyst and the substrate are pumped and circulated in a loop, withdrawing and mixing the reacting gas into the flowing slurry. Such configuration is found in the industrially established Buss reactor (Buss ChemTech AG) [80], which has applications in both fine chemistry and pharma industry [3, 4, 81, 82].
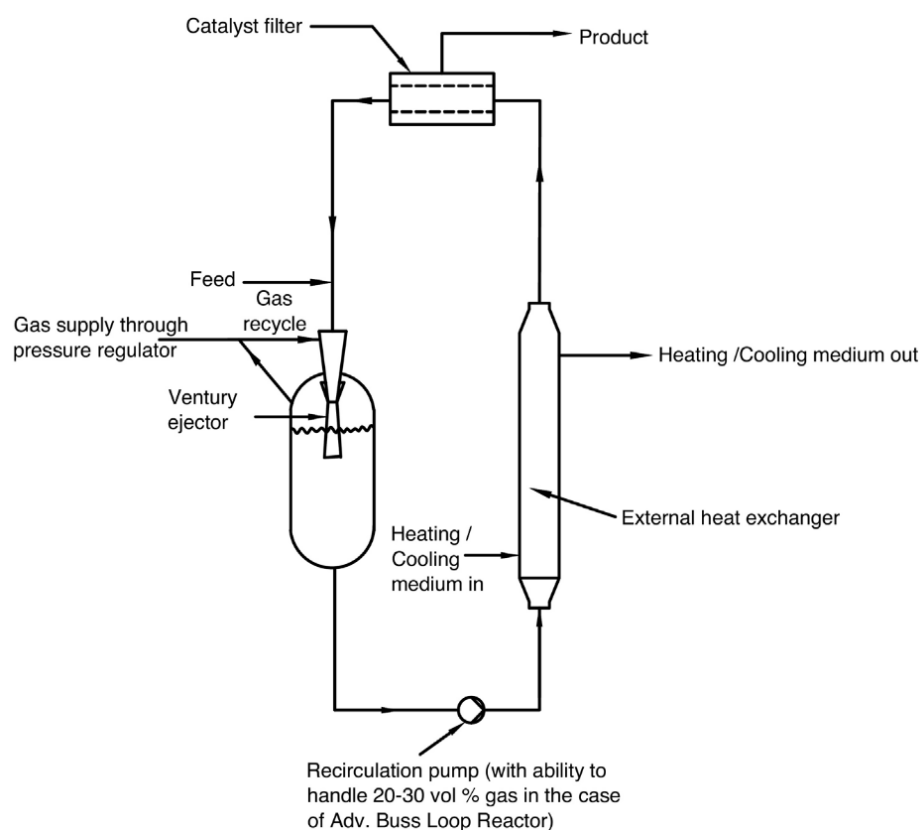
Figure 2.2. Schematic of the continuous Venturi loop reactor. Reprinted from Pangarkar *et al.*, Process intensification in multiphase reactors: from concept to reality, Chemical Engineering & Processing: Process Intensification, 2017, 120, 1-8, with permissions from Elsevier.

Table 2.1 shows the results from a comparative study on aniline hydrogenation to cyclohexylamine performed in a conventional batch stirred tank reactor (STR) and in a Venturi loop reactor (VLR) [2]. Both the volumetric gas-liquid mass transfer, k_La, and the external liquid-solid mass transfer coefficient, k_{LS}, are orders of magnitude higher in the VLR than those achieved in the STR. This results in the kinetics being the only controlling step and in a lower volume required for reaction, along with a reduction of the equipment capital cost. Furthermore, only a smaller concentration of catalyst is needed in the VLR, reducing the catalyst cost, which can be significant especially if noble metals are employed. Finally, the energy consumed, and thus the amount of CO_2 emitted, is lower (23 kJ/kg) compared to that of the STR (34 kJ/kg), meeting the sustainability target of PI.

Table 2.1. Comparative study between a conventional stirred reactor and a Venturi loop reactor in the hydrogenation of aniline to 25000 tonne/annum of cyclohexylamine. Temperature: 130 °C, pressure: 1 MPa. Adapted from Pangarkar [2].

	Stirred tank reactor	Venturi Loop Reactor
Catalyst loading, kg/m^3	20	10
k_La, s^{-1}	$4 \cdot 10^{-3}$	> 10
k_{LS}, m/s	$8.2 \cdot 10^{-5}$	> 10
Main process resistance	Gas-liquid	Kinetics
Reactor volume, m^3	1626	4.2
Power input, kW/m^3	0.02	5.32
Energy needed per mass of product, kJ/kg	34	23

2.4.2. Continuous flow reactors

The referenced Venturi loop reactor proved to be a feasible and green alternative to the well-established stirred tank reactor, given its enhanced heat management and capability of handling high pressures [80]. In a more general perspective, continuous flow chemistry has also been envisioned as a valuable and a sustainable alternative to multi-purpose pressurised batch systems, which dominate the fine and pharma industry [83]. The recent emergence and increase in popularity of flow chemistry has provided researchers with different tools to perform hazardous reactions in a controlled fashion [12, 35, 70, 73, 84-89]. This is because continuous processing offers improved heat management compared to conventional batch reactors, provides control over the residence time of the reagents and reduces process times [12, 31, 68, 84]. For these reasons, hydrogenations and aerobic oxidations can be ideal candidates for continuous processing, as they are highly exothermic, limited by mass transfer resistances, be prone to thermal runaway and involve the use of hazardous gaseous reactants [11, 16, 35, 68, 89, 90]. Furthermore, as all safety specialists know, the minimisation of hazards handling is the best way to prevent accidents, and these are some of the principles required by the EU legislation in terms of process safety (*e.g.* EC Framework Directive, 1990) [7]. In this context, process-intensified continuous flow reactors can reduce the volume/time required for reaction and thus the chemical inventory [7, 85].

2.4.2.1. Continuous reactors for catalyst testing

As stated already in Chapter I, the rising pressure from the current ecological standards in chemical processes is driving chemists towards the study of more selective catalysts to improve the chemical process green credits.
Continuous reactors can be used as a platform to study catalyst performance in flow, decoupled from mass transfer resistances. Catalyst testing generally aims at providing information on the activity, selectivity and stability of a catalyst, and can be divided into: preliminary screening, kinetics study and pilot plant tests, where industrial conditions are mimicked as much as possible [91]. In this context, continuous reactors are preferred over batch reactors, owing

to the possibility of indipendently controlling residence time in a catalytic system, and efficiently dissipate the high enthalpy of reaction produced in hydrogenation and oxidation reactions. Furthermore, reactor design is pivotal to avoid concentration and temperature gradients, and mass transfer resistances within the catalyst, which would lead to unbiased conclusions on the catalyst intrinsic kinetics.

An example of a continuous reactor for catalyst testing that is now commercially available is the XCube^{TM} reactor (see Figure 2.3). In this reactor, one or two metal cartridges measuring 4 mm x 70 mm can be loaded with packed catalyst, heated and used for continuous flow hydrogenations and oxidations [71]. One of its applications can be found in the continuous hydrogenation of olefins and nitrobenzenes, using platinum nanoparticles dispersed in an amphiphilic polymer [92]. In 31 s of residence time, 99% yield of the hydrogenated product could be achieved. To demonstrate its use in continuous production, a 63 - 70 h long test was carried out to produce ten grams of ethylbenzene and aniline from the styrene and nitrobenzene hydrogenations [92].

Figure 2.3. Picture of the XCube^{TM} flow reactor (left) and the catalyst cartridge (right). Reprinted from Osako *et al.*, Continuous-flow hydrogenation of olefins and nitrobenzenes catalyzed by platinum nanoparticles dispersed in an amphiphilic polymer, RSC Advances, 2015, 5, 45760-45766, with permissions from the Royal Society of Chemistry.

Aerobic oxidations of alcohols were also performed in the XCube^{TM} reactor and presented in the work of Zotova *et al.* [71]. In this study, different primary and secondary alcohols at an inlet concentration of 0.1 M in toluene were oxidised using 5 bar O_2 pressure and 90 °C. However, 0.29 g of 5 wt% Ru/Al_2O_3 catalyst were employed in the reaction and the reactor was used in a batch mode, with the outlet being recirculated back to the inlet. Nevertheless, the XCube^{TM} reactor's excellent plug-and-play configuration is the reason of its undisputed success in laboratory research.

In general, high-pressure packed-bed reactors are quite common in heterogeneously catalysed flow syntheses [12, 71, 93-96]. This is because it is possible to easily recover and reuse the catalyst after reaction, and the reactor generally allows to be operated under a wide range of temperatures and pressures [94]. Yet, the need for large catalyst particles in order to reduce pressure drops inevitably leads to a reduction of the catalyst efficiency. Moreover, when scaling out packed-bed reactors, non-uniform temperature distributions can cause degradation of sensitive functional groups in molecular intermediates [97]. For this reason, reactor size reduction and the use of fine catalyst particles can be feasible solutions [91].

2.4.2.2. Continuous reactors for lab-scale production

The scale-up of continuous reactors is a fundamental step for chemical engineers in process development and optimisation. In most industrial cases it represents the synthesis of the know-how generated from previous reactor developments [98]. However, in a more systematic approach, the scale-up of lab-scale mini- and mesoflow reactors can be achieved by [99]:

1. Reactor parallelisation (numbering-up)

2. Increase of reactor length or size (scale-out)

While the first may seem the easiest option, the synchronisation of pumps, thermal regulation and product collection can lead to an increase in process complexity, making numbering up mostly applicable to microreactors [8]. Scale-out or increase in reactor volume can be easier when using tubular reactors, although it may require a reconfiguration of the setup and a re-

assessment of the risks associated with the resulting changes in mixing and heat management.

An example of a multi-gram lab-scale production can be found in the work from the group of Stahl conducted in collaboration with Ely Lilly. In this study, the authors used the homogeneous $Pd(OAc)_2$/pyridine system to catalyse the aerobic oxidation of various alcohols in flow [100]. Continuous oxidations were carried out in a stainless-steel tubular reactor (400 mL, 0.5'' OD, 316 stainless steel) which could have an external jacket or be placed in a convection oven for temperature control. The substrate and the homogeneous catalyst solutions were pumped using high-pressure stainless steel syringes and the product was collected in a vessel for the separation of the liquid and the vapour phases (see Figure 2.4). The group of Stahl tried to address the flammability hazard using diluted oxygen and operating outside the flammability window [100, 101]. The catalyst solution containing 0.03 M $Pd(OAc)_2$ was pre-mixed with diluted O_2 (8% O_2/N_2) and then mixed with the substrate solution containing 0.6 M alcohol and 0.12 M pyridine. Alcohols were oxidised at 100 °C, 34.5 bar and under a residence time of 2.5 h with a scale of production of few tens of grams of isolated aldehydes/ketones.

A kilogram-scale application was demonstrated by substituting the 400 mL coiled-tube with a 7 L stainless steel tube (0.375'' OD), which increased the liquid residence time to 4.5 h and was used to oxidise 1 kg of 1-phenylethanol to acetophenone with a 99.5% yield.
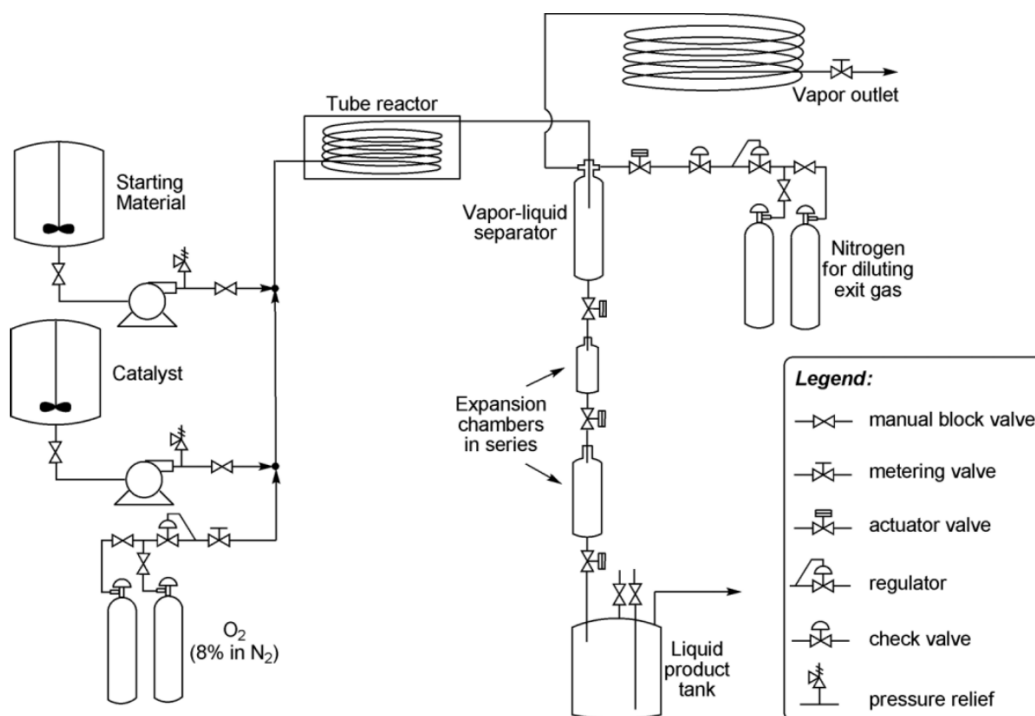
Figure 2.4. Setup schematic of a continuous flow tubular reactor for the homogeneously Pd catalysed aerobic oxidation of alcohols. Reprinted from Ye *et al.*, Development of safe and scalable continuous-flow methods for palladium-catalyzed aerobic oxidation reactions, Green Chemistry, 2010, 2, 1180-1186, with permissions from the Royal Society of Chemistry.

In this work, the use of high pressure was needed to overcome the limiting oxygen concentration in the gas phase, in order to reach the desired selectivity and product yield. In this perspective, membrane reactors can represent a safe and suitable solution when using higher oxygen concentrations at lower pressures. Owing to their ability to separate, distribute and allow a controlled reaction, membrane reactors offer solid and cost-effective configurations that can allow safe operation without compromising the gaseous reactant concentration [13].

In the next paragraphs, a review on micro- and membrane reactors, as continuous reactors for intensified catalyst studies and safe continuous reactions, is presented.

2.4.3. Microreactors for continuous reactions

The use of miniaturised equipment fits perfectly within the PI philosophy [102], so much so that Stankiewicz suggested in his paper to replace "*big is best*" by "*small is beautiful*", when defining process intensification [6]. The reduction in the cost, ease of operation and the low operating power consumption have made microreactors immensely popular in the last twenty years in both research and industry [103]. Their advantage mostly relies on their characteristic dimension. Microreactor channel diameters are in the range of 10 - 500 µm and lengths of 1 - 10 cm [104], with inherently large specific surface areas up to 10^4 m^2/m^3, compared to 10^2 m^2/m^3 of conventional industrial reactors [88, 105]. The small channel dimension lowers diffusion lengths and enhances mass transfer within the flowing reaction mixture, leading to a better usage of the catalyst and the reactor volume [103]. Moreover, owing to their large specific surface area, heat transfer is improved, leading to a better control of the reaction temperature [106].

2.4.3.1. Microreactors for production of fine chemicals

The U.S.A. Food and Drug Administration (FDA) which regulates pharmaceuticals and their quality, approved the use of continuous manufacturing for delivering safe and enhanced synthesis of drugs at an industrial scale [107]. In 2015, the FDA approved the drugs against cystic fibrosis (Orkambi and Sydemko), breast cancer (Verzenio) and HIV (Prezista) produced using continuous methods [108]. In more recent times, the rapid worldwide spread of the SARS-CoV-2 virus (COVID-19) has pushed pharmaceutical companies to quickly produce and deliver drugs and vaccines against the virus [109]. Using a microreactor, researchers from the group of Kappe have synthesised a precursor of remdesivir, an antiviral used to fight COVID-19, in less than 1 min residence time [109].

Microreactors have been employed in pharmaceutical [110-114] and nanomaterial production [8], where process intensification is achieved due to the enhanced mass and heat transfer, improved safety and better control over reaction conditions. An example of a safe and controlled synthesis using microreactors is that of nitroglycerine. Nitroglycerine is known to be a powerful

explosive, but also a pharmaceutical to treat angina. A safe and successful approach to its synthesis has been implemented using microreactors [115]. Researchers at the Fraunhofer Institute for Chemical Technology in Pfinztal managed to synthesise nitroglycerine at a productivity that could be scaled up to tons per week by numbering up microreactors [116].

In research and development, microreactors have helped chemists discover and access new synthetic routes that would be difficult otherwise using conventional reactors. This is mainly due to their broader safe operating window, along with the possibility of using high pressures and temperatures under safe conditions [117], and fast mixing that can enable handling unstable compounds [118]. This can be achieved thanks to the modularity that results from using microreactors [119]. As shown in Figure 2.5, different microreactor units can be connected in series to allow multiple reactant injections at specific points, control their mixing and residence time and allow to operate at different temperatures [119].
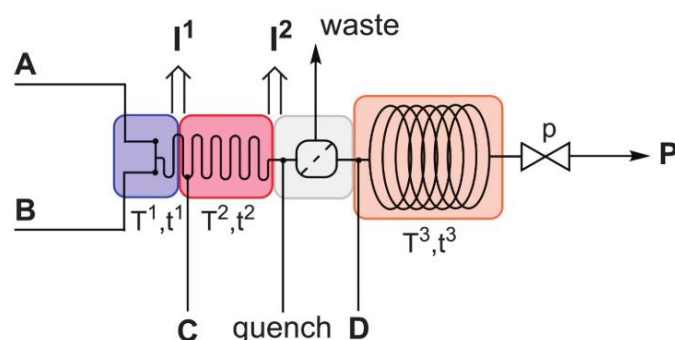
Figure 2.5. A schematic of a continuous flow microreactor which allows four reactants, A, B, C and D, to be pumped at specific points and through sections with different residence times, t, and temperatures, T, in order to produce intermediates, I and a final product, P. A back pressure regulator guarantees constant pressure, p. Reprinted from Gutmann *et al.*, Forbidden Chemistries - Paths to a Sustainable Future Engaging Continuous Processing, Journal of Flow Chemistry, 2017, 7, 65-71, with permissions from Springer.

2.4.3.2. Microreactors for *operando* spectroscopic studies

Microreactors are useful tools to study *in situ* catalyst performance, structure and reaction kinetics, owing to their compatibility with different types of online analytical instrumentations that can provide information on real-time conversion, selectivity, as well as catalyst structure and performance. This is particularly useful in the field of *operando* spectroscopy, a technique that combines the spectroscopic characterisation of a catalyst during reaction, while measuring its activity and selectivity [120-123]. The popularity of *operando* spectroscopy surged in the last two decades, owing to its ability to offer a view over catalyst structure-performance relationships under realistic operating conditions. The field of *operando* spectroscopy can be explored using a plethora of spectroscopic and microscopic tools, and a combination of these. Among these, X-ray absorption spectroscopy (XAS) and infrared spectroscopy (IR) are the most popular techniques [121, 124-128]. XAS is an element-specific technique that provides information on the structural, electronic and chemical state of an atom in the catalyst [120, 129, 130]. On the other hand, to understand the vibrational state of the catalyst surface species, including adsorbed molecules, IR can be employed [131, 132].

Operando studies rely on the use of reactor cells where the catalyst is generally hosted in the form of pellets and where reactions are carried out. Modified Harrick cells are among the most widespread types of spectroscopic cells and they have been employed in combined XAS and IR studies [133-135]. However, these generally suffer from various issues including a broad residence time distribution of the reactants and the presence of temperature and concentration gradients within the cell [136-138]. Furthermore, the presence of mass transfer resistances within the catalyst bed often leads to biased conclusions regarding the catalyst activity, and high space velocities are commonly required to derive more reliable kinetic data [139].

Microreactors have proven to be successful *operando* spectroscopic cells, due to the previously mentioned characteristics, including a narrow residence time distribution of the reactants [9, 140-146]. Different spectroscopic studies have been conducted using microreactors, including Raman [140, 147, 148], IR [149-151], X-ray diffraction (XRD) [143, 152, 153] and XAS [143, 144, 152,

154]. The benefits that microreactors can provide to *operando* spectroscopic studies also include the complex geometries that can be achieved with micromachining. Microfabrication enables researchers to machine accurate and flexible microchannel configurations that can be used as spectroscopic windows. In their *operando* microscopic and spectroscopic study of ethylene hydrogenation and CO oxidation, Zhao *et al.* showed how a microreactor cell can be used to provide structural and electronic information regarding the catalyst, as well as identify catalyst surface and gas bulk species involved in the reaction [145]. This was done by shining electron, X-ray, laser and infrared beams while analysing the gas composition using gas chromatography (see Figure 2.6).
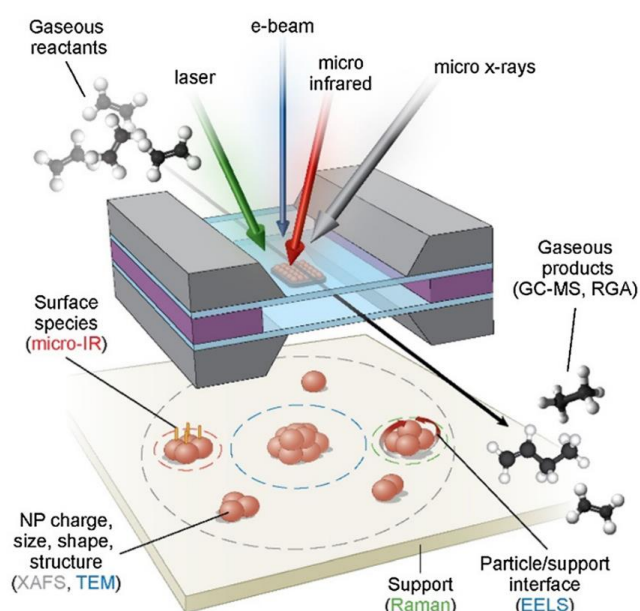
Figure 2.6. *Operando* spectroscopic study conducted in a microreactor with silicon nitride windows using X-ray, infrared, electron and laser beams. Reprinted from Zhao *et al.*, *Operando* Characterization of Catalysts through use of a Portable Microreactor, ChemCatChem, 2015, 7, 3683-3691, with permissions from John Wiley and Sons.

2.4.3.3. Safety aspects of microreactors

Miniaturisation has its safety benefits. Along with improved performance, microreactors can be safe tools for conducting reactions in flow. Due to their dimensions, microreactors only require a small amount of reagents and catalyst material, thus minimising the risks associated with the loss of containment of possible hazardous compounds. Concerning the risk of explosions during operation, the energy released in an explosion is proportional to the total amount of exploding material raised to the power of 1/3, as shown in Equation (2.1) [11]. This implies that the smaller the volume of a reactor, the lower the severity of an explosion.

$$E_{exp} \propto m_R^{1/3}$$ (2.1)

However, microreactors are not inherently safe under any circumstances [11, 155]. This is due to the fact that the explosion front can propagate through the inlet lines to the reactant vessels where it can become more disastrous. For this reason, the use of non-return valves or the careful design of the microchannel width can be used to overcome this hazard [11, 155, 156]. Nevertheless, it is unquestionable that microreactors are able to broaden the safe operating window. This is exemplified in Figure 2.7 [11], in which it is possible to see that the upper flammability limit of an ethene/oxygen mixture can be decreased by using microreactors instead of conventional reactors. The underlying cause is in the continuous operation which decreases the chances of forming hotspots that can trigger an explosion [11].
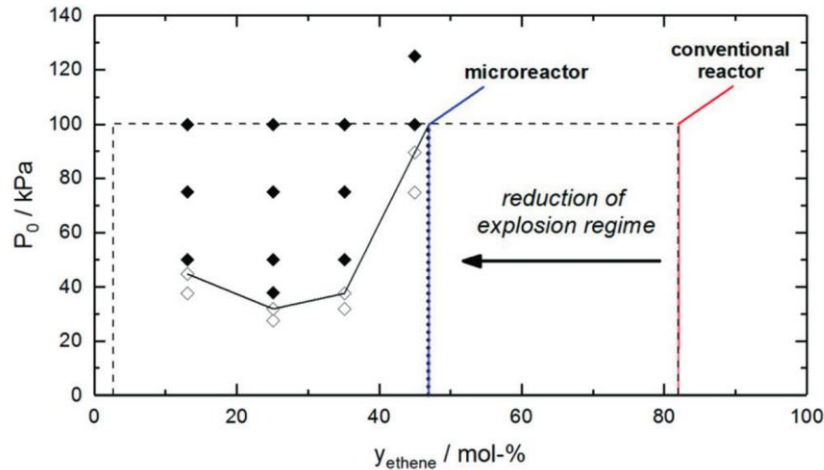
Figure 2.7. Explosive behaviour of ethene/oxygen reaction mixtures at different pressures. The use of continuous flow microreactors allows reduction of the explosion regime. Reprinted from Kockmann *et al.*, Safety assessment in development and operation of modular continuous-flow processes, Reaction Chemistry & Engineering, 2017, 2, 258-280, with permissions from the Royal Society of Chemistry.

Process safety usually deals with managing the heat generated or subtracted during a reaction. Hot spots can generally form in micropacked-bed reactors [157], however they can be inhibited by the use of large flowrates, low temperatures and pressures [11]. In the case of an inlet pump failure in which liquid reactant flowrates suddenly stop and the liquid is still reacting inside the reactor, heat transfer will occur only by diffusive mechanisms. The solution of the dimensionless differential equation of the heat balance can allow us to determine the critical channel diameter below which, given a certain reaction enthalpy, no runaway reaction occurs. This is presented in Equation (2.2) and it applies to infinitely long channels that are metallic, so that heat transfer mainly occurs within the liquid by diffusive mechanisms, with λ_f being the fluid thermal diffusivity [10, 158].

$$d_h = \left(\frac{8\, \lambda_f\, R_G\, T_w^2}{E_a\, \Delta T_{ad}}\, t_R \right)^{1/2} \tag{2.2}$$

The equation shows that the higher the adiabatic temperature rise of a reaction, ΔT_{ad}, the smaller the hydraulic diameter of the channel, d_h, needs to

be to avoid a runaway reaction. In this equation, T_w is the temperature at the wall, E_a the reaction activation energy and t_R the characteristic reaction time.

2.4.4. Membrane reactors for continuous reactions

Microreactors are well suited to extract information on catalyst performance and reaction kinetics. However, given the restricted flow capacity resulting from the microchannel size, their throughput is generally limited to 0.1 - 10 g/h and scale-up can be challenging owing to the tendency of microchannels to block during operation [99]. Continuous reactors from 500 µm to a few mm internal diameter, also called mini- or millireactors, can have improved flow capacities, lower pressure drops and be able to handle multikilogram quantities of material [99]. Among continuous flow reactors, membrane reactors have emerged in popularity for their improved process safety at a larger scale due to their ability to distribute and control the dosing of gaseous reactants in gas-liquid exothermic reactions [13, 31, 159, 160]. Membrane contactors represent a promising technology for applications in catalysis, as they can combine phase separation and reaction, along with providing the possibility of heat integration [161-164]. Such advantages start becoming relevant for process scale-up as processing costs can be significantly decreased [163].

2.4.4.1. Ceramic membrane reactors

Ceramic and polymeric membranes are among the most common types of membranes that can be found in the chemical industry. Ceramic ones usually consist of a support layer, generally made of α-alumina with large pores and a thin layer made of a different material (*e.g.* titania, zirconia, silica, etc.) which controls the diffusive flux [165]. The macroporous support guarantees mechanical strength while sometimes a mesoporous intermediate layer is also used in order to decrease the surface roughness [166]. The resulting membrane structure affects how the different species diffuse. In fact, some nanoporous membranes can be permselective to certain molecules with respect to others, depending on their size.

Ceramic membrane geometries can vary from tubes to flat discs, or monolithic multi-channel elements and the shape is significantly important as it affects the specific surface area of the reactor unit [162]. An example of a ceramic membrane reactor was published by Prof Gavriilidis' group. A 250 mm long ceramic tubular membrane (OD: 10 mm, ID: 7 mm, Pall) consisting of support layers of alumina and a top 8 µm zirconia layer (50 nm pore size) was filled with a packed Au-Pd/TiO$_2$ catalyst and used in the aerobic oxidation of benzyl alcohol [167]. Benzyl alcohol flowed inside the tubular membrane while oxygen was pressurised outside the membrane and permeated through it during reaction. Results showed that dilution of benzyl alcohol in o-xylene and a high catalyst contact time led to an increase in benzyl alcohol conversion and benzaldehyde selectivity [167]. High residence times allowed more time for oxygen to penetrate in the catalytic layer, while less oxygen was required in the reaction at high benzyl alcohol dilutions [167]. However, to avoid breakthrough of oxygen into the organic liquid, the gas pressure was held at less than 0.1 bar lower than the liquid pressure, allowing only a small operating window for liquid and gas pressure fluctuations [167]. This higher liquid pressure also inevitably leads to a permeation and pervaporation of the organic liquid in the gas phase after hours of operation, which can be accelerated by the presence of internal cracks or defects in the membrane.

2.4.4.2. Polymeric membrane reactors

Dense polymeric membranes can be used to overcome these issues. Since the discovery of polytetrafluoroethylene (PTFE) in 1938 by DuPont, the interest in using fluoropolymers spread rather quickly [168]. Despite their lower resistance at high temperatures compared to ceramic membranes, these polymers show exceptional properties, such as chemical inertness and gas permeability. In the 1980s the Teflon amorphous fluoropolymer (AF) family was discovered. Teflon AF is a material with remarkable properties, including high permeability to light gases and a high liquid pressure breakthrough [168, 169]. These properties are ascribed to its peculiar chemical structure (see Figure 2.8). In fact, the presence of perfluorodioxolane units prevents the polymer from forming a semicrystalline microstructure typical of PTFE [170].

This amorphous structure enables them with a fractional free volume of about 0.327 (Teflon AF-2400) and with an incredible gas permeability [168, 169].
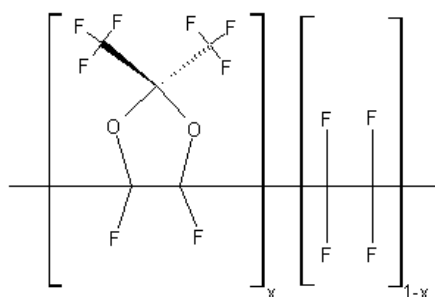
Figure 2.8. Chemical structure of Teflon AF, where x = 0.87 for the Teflon AF-2400 and x = 0.65 for the Teflon AF-1600 [168].

Despite these remarkable properties, the cost of Teflon AF is more than three orders of magnitude higher than that of other fluoropolymers, such as ethylene tetrafluoroethylene (ETFE), polytetrafluoroethylene (PTFE) or its copolymer perfluoroalkoxy (PFA) [171]. Moreover, the glassy amorphous structure makes Teflon AF membranes easy to break during assembly. Therefore, in some applications, other common perfluoropolymers are used in place of Teflon AF. Table 2.2 reports the pure gas permeability for some fluoropolymers, including melt-pressed Teflon AF-2400 [168].

Table 2.2. Pure gas permeabilities through different types of fluoropolymers.

Material	T, °C	Permeability of pure gas, barrer			
		H_2	CO_2	O_2	N_2
Teflon AF-2400 [168]	35	2090	2200	960	480
Tefzel^{TM} EFTE [172]	25	n.a.	3.0	1.2	0.4
PTFE [173]	25	9.8	11.7	4.2	1.4
PFA [171, 174]	25	n.a.	10.7	5.3	1.5

The transport of gas molecules through isotropic non-porous polymeric membranes can be described by the relationship expressed in Equation (2.3). At a given pressure difference between upstream, p_2, and downstream, p_1, the permeability coefficient, P_m, of a membrane is directly proportional to the

steady-state gas flux, J_V, of gas that permeates the membrane, and the thickness of the membrane, δ_m [169, 175].

$$P_m = \frac{J_V}{(p_2 - p_1)} \delta_m \qquad (2.3)$$

Permeability is a complex function of the sorbed penetrants, the polymer, the temperature, and in the case of condensable gases, of the gas feed and the operating pressure [169, 175]. Its SI unit is $(m^3 \cdot m)/(s \cdot Pa \cdot m^2)$, but it is very common to find the "barrer", equivalent to 10^{-10} $(cm^3(STP) \cdot cm)/(s \cdot cmHg \cdot cm^2)$. For non-porous polymer films the transport is governed by a solution-diffusion mechanism, and the permeability described in Equation (2.3) can also be expressed as a function of an average diffusion coefficient, D_m, and solubility of the permeating species, s, as shown in Equation (2.4).

$$P_m = D_m \cdot s \qquad (2.4)$$

The effect of temperature on the permeability is described in Equation (2.5). This is an Arrhenius formula, where $P_{m,\infty}$ is a pre-exponential factor and $E_{a,P}$ is the activation energy of permeation.

$$P_m = P_{m,\infty} \, \exp\left(-\frac{E_{a,P}}{R_G T}\right) \qquad (2.5)$$

Values of the permeation activation energy for some gas molecules through Teflon AF-2400 are shown in Table 2.3.

Table 2.3. Activation energy of permeation, $E_{a,P}$, for Teflon AF-2400. Feed pressure: 50 psig, permeate pressure: atmospheric [169].

Gas molecule	N_2	O_2	He	CO_2
$E_{a,P}$, J/mol	-400	-2500	+1600	-6700

2.4.4.3. Continuous reactions using the Teflon AF-2400 membrane

The group of Prof Ley at the University of Cambridge first succeeded in developing a tube-in-tube membrane reactor consisting of a tubular Teflon AF-2400 inside a larger PTFE tube. The outer tube contained pressurised gas that

permeated through the membrane and reacted with the flowing organic liquid [176]. The resulting configuration of the tube-in-tube reactor can be seen in Figure 2.9, where the sealing was done using Swagelok fittings [177].
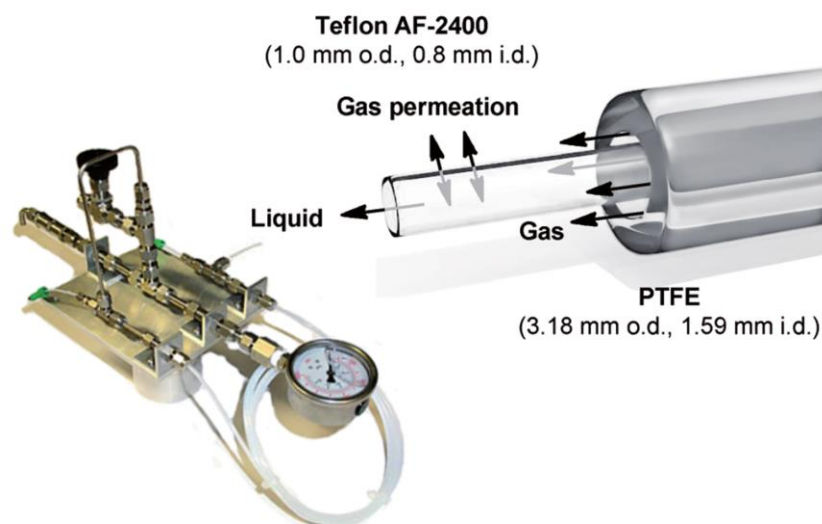
Figure 2.9. Teflon AF-2400 tube-in-tube membrane reactor configuration, with Swagelok fittings. Reprinted from Bourne *et al.*, Flow Chemistry Syntheses of Styrenes, Unsymmetrical Stilbenes and Branched Aldehydes, ChemCatChem, 2013, 3, 159-172, with permissions from John Wiley and Sons.

Gas-liquid reactions such as ozonolysis of alkenes [170], carboxylation of Grignard reagents [176, 178], methoxycarbonylation of aryl, heteroaromatic and vinyl iodides [179], hydrogenations in flow [180, 181], Heck reactions with ethylene and hydroformylation reactions [177], and generation of hazardous compounds [182, 183] have been performed using a Teflon AF-2400 membrane. As good candidates for continuous flow processing, also aerobic oxidations have been conducted in Teflon AF-2400 membrane reactors [13, 31, 40]. In the work of Chaudhuri *et al.*, a tube-in-tube Teflon AF-2400 membrane saturator was used as O_2/air pre-saturator at 7-8 bar gas pressure and connected to a packed-bed of Au-doped Fe_3O_4/SiO_2 magnetic particles placed inside an induction oven, which provided thermal activation to the nanoparticles during reaction [184]. The reactor was used to oxidise diluted benzylic and allylic alcohols to aldehydes and ketones in flow. However, the

reaction was limited by the solubility of oxygen in the solvent at the operating pressure, and high conversions (> 90%) were reached at 150 °C, and at inlet flowrates of less than 0.2 mL/min, with 6 mg of Au inside the packed bed.

A work conducted in Prof Gavriilidis' group demonstrates a Teflon AF-2400 tubular membrane employed in a tube-in-tube membrane reactor for the aerobic oxidation of benzyl alcohol [185]. The substrate was oxidised at 120 °C with 1 wt% Au-Pd/TiO$_2$ catalyst packed inside the tubular membrane (ID: 0.8 mm, OD: 1 mm), and oxygen was pressurised in the annulus outside the membrane [185]. Figure 2.10 is a schematic of the membrane reactor configuration. The increase in the external oxygen pressure and in the catalyst contact time led to a rise in benzyl alcohol conversion and benzaldehyde selectivity, which could be ascribed to an increased oxygen permeation through the membrane at high pressures and thus to a higher oxygen availability inside the liquid [185].
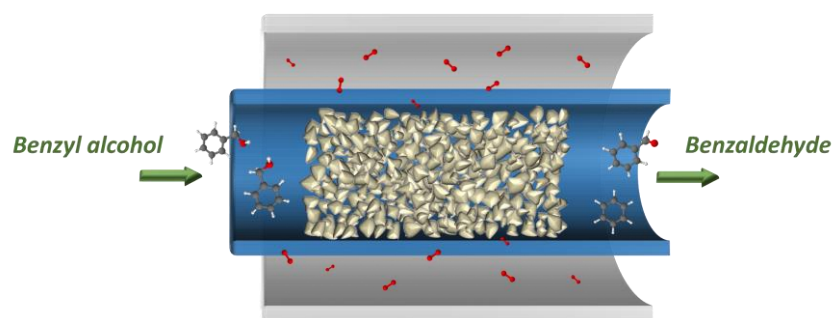
Figure 2.10. Tube-in-tube Teflon AF-2400 membrane packed-bed reactor for the continuous aerobic oxidation of benzyl alcohol [185].

However, as the authors noted, potential drawbacks of this system are represented by the ineffective heat transport through the annular gap filled with gas, especially when carrying out exothermic reactions [186]. In an attempt to scale-up the reaction and avoiding the use of a larger tubular diameter, the authors developed a Teflon AF-2400 flat membrane packed-bed reactor for the continuous aerobic oxidation of benzyl alcohol, consisting of a rectangular stainless-steel microchannel hosting the same catalyst packed bed with a 0.07 mm thick flat membrane on one side of the channel [186]. The channel was 75 mm long, 3 mm wide and 1 mm deep, while a scaled-up version had an

enlarged width of 32 mm. This operated at 120 °C and up to 8.2 bar oxygen pressure, achieving a 58% conversion with a 69% benzaldehyde selectivity at a benzyl alcohol flowrate of 50 μL/min and 1 g of catalyst. However, results indicated that the reactor operated in a transverse O_2 mass transfer controlled regime and thus under limiting supply of oxygen to the very active catalyst utilised.

2.4.4.4. Safety aspects of polymeric membrane reactors

As mentioned before, membranes are great tools for improving process safety by physically separating the reacting phases and avoiding any potential risk of uncontrolled reactions. However, if during an aerobic oxidation, the vapour concentration of the organic material in the oxidant gaseous phase lies within the flammability window at the operating temperature and pressure, it can ignite leading to fire or explosion in the presence of an ignition source (*e.g.* electric spark, friction or heat) [187]. In fact, molecules in the liquid phase can diffuse through a membrane, owing to their solubility in the material, and reach the gaseous phase. This is known as pervaporation and it must be controlled in order to avoid the formation of explosive mixtures during reaction.

If the concentration of the organic vapour is below the lower explosion limit (*LEL*), or above the upper explosion limit (*UEL*) of that component, then the mixture is not flammable. These values are usually referred to air, and sometimes "explosion" is replaced with "flammability" (*LFL*, *UFL*) depending on the speed of ignition [187, 188]. In the case of a mixture of components, the flammability window can be calculated using Le Chatelier's mixing rule, shown in Equation (2.6), where *n* is the number of components with a specific vapour fraction, y_i, and a lower explosion limit, LEL_i [189]. This equation also holds for the upper flammability limit.

$$LEL_{mix} = \left(\sum_{i=1}^{n} \frac{y_i}{LEL_i} \right)^{-1} \tag{2.6}$$

The effect of the operating parameters is of fundamental importance. As an example, for each 100 °C increase in temperature the *LELs* decrease by 8% of their original value, while the *UELs* increase by the same amount. An increase in pressure would result in an increased flash point of the flammable

mixture and in the broadening of the flammability window [187]. When oxygen concentration is increased up to its purity, the *LEL* is generally not much affected but the *UEL* increases considerably and the ignition temperature decreases. Moreover, using pure oxygen or oxygen-enriched air decreases the minimum ignition energy required to ignite a flammable vapour and raises its burning velocity [187].

2.5. Concluding remarks

The literature review shows how the application of green chemistry principles to flow chemistry can be challenging. Mass and heat transfer resistances can undermine the catalyst efficiency, and exothermic reactions can pose a risk to operators and affect the catalyst performance.

The following chapters address some of the outstanding research questions regarding the development of micro- and membrane flow reactors. Microreactors are suitable tools that improve process safety due to their reduced size. However, designs that can combine catalyst studies with an intensified operation are still highly desirable. As already highlighted in the literature review, for gas-liquid catalytic reactions and lab-scale multi-gram production of valuable molecules, membrane reactors are a viable option. However, membrane reactor designs need to be coupled with catalyst configurations that can boost the reaction and optimise the catalyst use.

In the next chapters, a microreactor and four membrane reactors are presented as tools to achieve process intensification at different scales. The reactors are tested in gas and gas-liquid oxidations and hydrogenations, as these are suitable candidates for demonstration in continuous flow, owing to their high enthalpies of reaction and the hazards associated with flammability and pressurised gas.

Chapter III. Silicon-glass microreactor for heterogeneous catalyst studies: Case study of *operando* XAS/IR CH$_4$ and CO catalytic oxidations
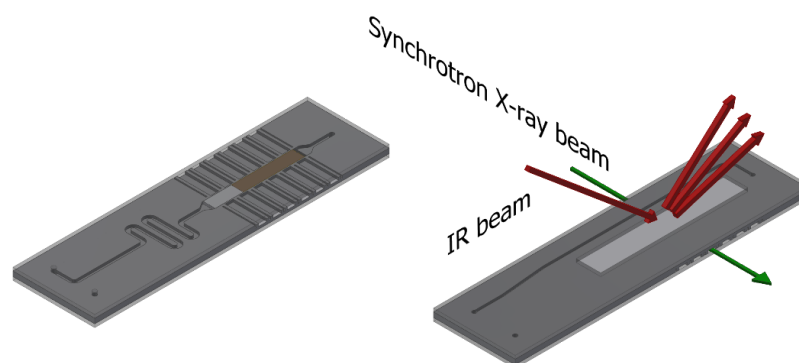
The microfabricated reactor developed and demonstrated in this work was used to perform safe and intensified heterogeneously catalysed methane combustion and carbon monoxide oxidation. The reactor was demonstrated in the *operando* XAS combustion of methane and temperature-resolved reduction of the catalyst using 2 wt% Pd/Al$_2$O$_3$ catalyst, and in the *operando* DRIFTS CO oxidation over 1 wt% Pt/Al$_2$O$_3$. The combustion of methane was performed at different temperatures: 250, 300, 350 and 400 °C and the microreactor showed an isothermal temperature profile and the absence of external and internal mass transfer resistances. The safety arising from the use of a microreactor along with a plug-flow behaviour and the absence of internal and external mass transfer resistances make this reactor a unique tool for performing *operando* catalytic studies using high space velocities and transient response experiments.

3.1. Introduction

As stated in Chapter II, among the reactors used for studying catalysts in combination with spectroscopic analyses are the Harrick cells, which offer a robust design that can be employed under broad operating conditions. However, one of their main drawbacks is usually the presence of a large dead volume which can cause a by-pass of reactants and inhomogeneous reaction conditions. Different attempts have been made to optimise the reactor cell and offer alternative designs to common commercial spectroscopic reactor cells [190-192]. In their work, Agostini *et al.* proposed a modification of the common spectroscopic cell with a body-dome configuration that was optimised for time-resolved XAS/DRIFTS/MS studies [193]. This reactor cell consisted of a main body that hosted the catalyst powder in a sample holder and the heater, while the dome had windows for X-ray and IR beams. Two carbon-glass windows allowed the X-ray beam to be shone on the catalyst while a CaF_2 window was used for the IR radiation. The reactor could be operated at 600 °C and 6 bar and the dead volume was about 0.5 cm^3, which, with the addition of a dome for high pressure experiments, was incremented to 1 cm^3.

The reactor proposed by Chiarello *et al.* reported a different configuration for *in situ* XAS and DRIFTS studies [191]. Their design had a reduced dead volume compared to a modified Harrick [134] or SpectraTech cell [194], with a mean residence time of the gas of 5 s. However, since the X-ray and IR beams were focussed on the same optical window, the authors had to drill a hole in the IR CaF_2 window and plug it with a carbon-based glue to allow transmission of X-rays.

A spectroscopic packed-bed reactor was demonstrated by Dann *et al.* in the study of CO oxidation kinetic oscillations over a Pd/Al_2O_3 using energy dispersive EXAFS (EDE) and DRIFTS [192]. The reactor was made of aluminium and had a 5 mm x 5 mm cross-sectional channel that hosted the catalyst particles (250 - 335 µm). Thin walls on the side allowed X-ray spectroscopy to be conducted in transmission mode, while a CaF_2 top window enabled the investigation of the catalytic reaction using IR spectroscopy. A heating plate was placed under the reactor, with a thermocouple located near

the outlet region. The reactor was tested up to 140 °C and 8 different axial positions could be probed in the simultaneous *operando* EDE/DRIFTS studies. Silicon microreactors can be used for performing *operando* structure-activity studies of catalysts, owing to their remarkably high thermal conductivity, chemical compatibility with most reagents, as well as good mechanical strength and transparency to high-energy X-ray and IR beams [152].

In a previous work from UCL, a silicon-glass reactor was demonstrated for the continuous dehydrogenation of methanol to formaldehyde, in which the microchannel was sputter-coated with silver and probed using Raman spectroscopy [140]. The *operando* study was conducted analysing the catalyst structure and activity, and the effect of temperature and reaction feed composition. An *in situ* XAS study in fluorescence mode at the silver K-edge was also performed using the same reactor, demonstrating its applicability to two spectroscopic techniques [144]. However, deposition by sputtering is limited to unsupported metal catalysts, and the catalyst loading depends on the available surface area.

This chapter reports a novel silicon-glass microreactor hosting a packed-bed of supported for the *operando* XAS and DRIFTS studies of heterogeneously catalysed methane combustion and carbon monoxide oxidation. X-ray absorption spectroscopy was demonstrated in the methane combustion catalysed by 2 wt% Pd/Al_2O_3, while DRIFTS was applied over the surface of 1 wt% Pt/Al_2O_3 catalyst during the carbon monoxide oxidation.

3.2. Materials and methods

3.2.1. Microreactor cell design[1]

The structure of the silicon microreactor comprises of a silicon layer sandwiched between two glass layers. A central microchannel in the silicon layer is used for hosting the catalyst and flowing the gaseous reactants, while other channels were designed for taking XAS measurements. The technical drawing of the reactor is presented in Figure 3.1. The back side shows a serpentine channel that is used as the gas inlet with a width and depth of 1000 µm and 600 µm, respectively, and that leads to the main channel where the reaction takes place. This is 3000 µm wide and 600 µm deep and hosts the packed-bed of catalyst. In order to retain the catalyst, a set of pillars was designed at the outlet end of the reaction channel. Each pillar is 500 µm long and 40 µm wide and is placed in a row in 20 µm intervals. Six X-ray slits were designed perpendicularly and on each side of the reaction channel with a width and depth of 2000 µm and 600 µm, respectively. These allow the catalyst bed to be probed at different positions along its axis, in transmission mode. During operation, the X-ray beams have to cross a 250 µm thick wall on each side of the reaction channel before and after illuminating the catalyst. Close and parallel to the six X-ray slits, seven thermocouple channels were designed in order to measure the axial temperature profile using a 0.25 mm diameter thermocouple (Omega Engineering). This can be visualised in Figure 3.2, where the schematic of the reactor is presented. The square channels for temperature measurements have a width and depth of 600 µm. The back side and the front side of the microreactor share a common hole which allow the gas exiting the reaction channel to join the front side channel (see Figure 3.1). This is 600 µm wide and 200 µm deep.

---

[1] The microreactor was designed and developed by Dr Enhong Cao.
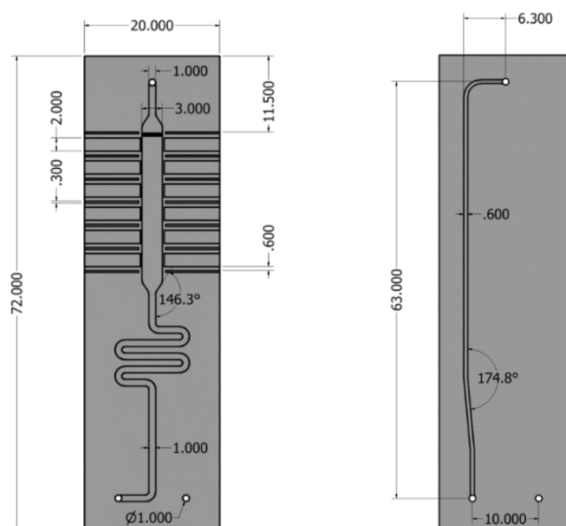
Figure 3.1. Back side (left) and front side (right) of the microreactor silicon layer. Dimensions are reported in millimetres.

The silicon layer was sealed on its front and back side together with two 0.8 mm thick glass layers (Corning 7740). The glass layers have the same dimensions, but the front side glass layer has a hollow window (36 mm x 6 mm; length x depth) to allow the IR beam to be shone on the silicon layer and on the catalyst underneath. In order to allow for the inlet and outlet to be connected to the gas lines, two holes were drilled on the back-side of the glass wafer.

Figure 3.2 shows a 15 mm long packed-bed catalyst with silica beads used to distribute the flow, gas inlet and outlet, X-ray slits, thermocouple wells and IR window. Overall, the reactor is 72 mm long, 20 mm wide and 2.6 mm thick. Pictures of the reactor are presented in Appendix A.

Back side   **Front side**
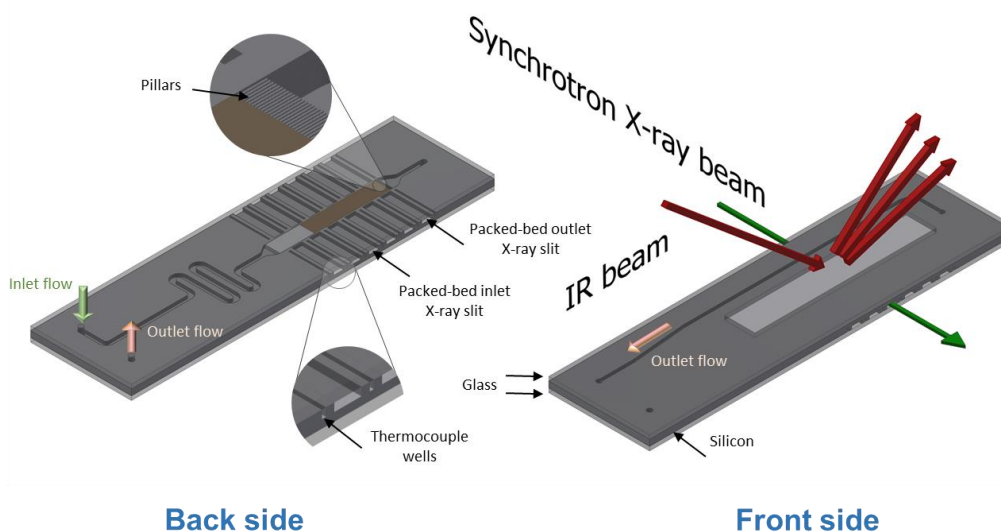
Figure 3.2. Back and front side of the silicon-glass microreactor used in *operando* XAS/MS and DRIFTS/MS studies. The catalyst is shown on the back side in brown with glass beads in light grey colour. Small features including the pillars used for retaining the catalyst particles and the thermocouple wells are magnified.

3.2.2. Microfabrication process[2]

Double-sided photolithography (Q4000-6, Quintel) was used in the fabrication of the reactor, followed by deep reactive-ion etching (DRIE, STS ASE) performed on a double-sided 1 mm thick and 100 mm wide circular silicon wafer (undoped float zone grown, CRYSTRAN UK). The microfabrication process of the wafer was carried out in three steps. First, the front side was patterned and etched to 200 µm, and was then covered with a photoresist (SPR-220-7, Rohm and Haas). The wafer was then heated up to 90 °C for 10 min. Afterwards, the processed wafer was cleaned with a Piranha solution (H_2SO_4: H_2O_2 = 3:1) at 100 °C for 15 min and another lithographic step was performed. DRIE was performed to etch the reactor channel at a depth of 600 µm, and the holes that were etched through to create the connections with the gas inlet and outlet lines. Three silicon chips were cut out of one wafer and

---

[2] The fabrication process was performed by Dr Enhong Cao at the Department of Chemical Engineering at UCL and at the London Centre for Nanotechnology.

were bonded on each side with the glass layers *via* double-sided anodic bonding. This was done at 420 °C on a hot plate (Stuart SD162) and under a DC voltage of 500 V by attaching the cathode to the silicon and the anode to the glass. In the second step, the silicon-glass chip was cooled down, cleaned with a Piranha solution and placed on the hot plate. This time, the silicon layer was facing up and the glass layer to be bonded was placed on top. The second anodic bonding occurred at a temperature of 420 °C and under a DC voltage of 500 - 700 V.

3.2.3. Heating unit

Figure 3.3 shows the reactor assembled inside an in-house heating unit which consisted of a ceramic heater (25 mm x 50 mm x 2.5 mm, ULTRAMIC® ceramic heaters, Watlow) inside a stainless steel holder. The inlet and outlet ports were sealed using high temperatures O-rings (Perlast G80A, O Rings Ltd) and tightening two clamps. The maximum operating temperature of 400 °C was limited by the electrical connections material of the thermocouple inside the heater, which could be changed to reach higher temperatures.
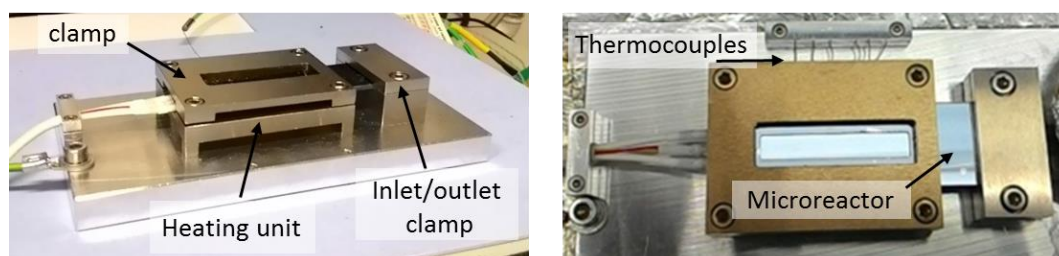
Figure 3.3. Ceramic heating assembly with the clamped silicon-glass microreactor and with thermocouples to measure the temperature profile.

3.2.4. Catalytic combustion of methane[3]

The microreactor was tested at UCL in the catalytic combustion of methane over a 2 wt% Pd/Al_2O_3 catalyst before performing the *operando* spectroscopic studies. The catalyst was prepared by impregnation and the synthesis and its characterisation are reported by Richards *et al.* [195]. An amount of 28.5 mg

---

[3] The laboratory tests on the silicon microreactor were conducted by Dr Enhong Cao at UCL.

in the 53-63 µm sieve fraction was loaded in the microreactor by applying vacuum at the outlet port. The catalyst formed a 15 mm long bed followed by 75 µm large glass beads at the inlet, to distribute the flow before entering the packed-bed. Calcination was conducted in the microreactor at 400 °C (ramp of 10 °C/min) under 10% O_2/He for 30 min. Afterwards, the reactor was cooled down to 200 °C and a gas mixture of 1% CH_4 and 4% of O_2 in He was flowed at a flowrate of 40 NmL/min. The oxidation of methane was carried out at five different temperatures: 200, 250, 300, 350 and 400 °C (10 °C/min ramping rate) each with a dwell time of 45 min and the temperature was measured along the catalyst bed.

The reaction formula is shown in Equation (3.1). Online gas chromatography (GC, Agilent 7196) was used to analyse the gas effluents using a thermal conductivity detector and two columns (HP-PLOT Molesieve and GS-CarbonPLOT). Only carbon dioxide was detected, showing that the methane was completely oxidised.

$$CH_4 + 2\ O_2 \rightarrow CO_2 + 2\ H_2O \tag{3.1}$$
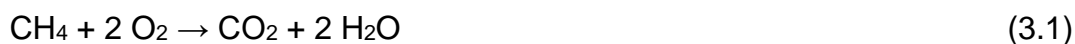
In order to assess the catalyst performance, the average turnover frequency, *TOF*, was used. This is a number that averages out the contributions from all the surface and bulk metal atoms of the catalyst, from the inlet to the outlet of the reactor. It is calculated using Equation (3.2), where the reactant inlet molar flowrate, $F_{r,in}$, is multiplied by the conversion, *X*, defined in Equation (3.3), and divided by the molar amount of metal catalyst, n_m. Conversion in continuous and batch reactors is calculated from the inlet/initial, $C_{r,in}$, and the outlet/final concentration of the reactant, $C_{r,out}$.

$$TOF = \frac{F_{r,in}\ X}{n_m} \tag{3.2}$$

$$X = \frac{C_{r,in} - C_{r,out}}{C_{r,in}} \tag{3.3}$$

In those experiments where temperature was varied, the apparent activation energy, E_a could be estimated using the Arrhenius equation shown in Equation (3.4), where TOF_∞ is a pre-exponential factor. The natural logarithm of the turnover frequency was plotted against the absolute temperature reciprocal

and the activation energy was determined by the slope of the linear correlation. This could be done assuming a constant concentration of the reactants on the metal catalyst.

$$\ln(TOF) = \ln(TOF_\infty) - \frac{E_a}{R_G T} \tag{3.4}$$

3.2.5. *Operando* XAS/MS and DRIFTS/MS

3.2.5.1.   XAS during methane combustion

The setup for the *operando* XAS and DRIFTS experiments is shown in Figure 3.4. *Operando* XAS/MS experiments were performed during the catalytic combustion of methane over 2 wt% Pd/Al_2O_3 at the B18 beamline of the Diamond Light Source (DLS), Didcot, UK.

XAS studies were done at the Pd K-edge in transmission using a quick EXAFS (QEXAFS) setup comprising of a fast-scanning Si(311) double crystal monochromator [196]. The size of the X-ray beam was adjusted to 200 µm x 200 µm and the reactor was placed onto a platform which could be moved in order to align the X-ray beam inside the X-ray slits. Figure 3.5 shows the schematic of the experimental rig used for the XAS/MS and DRIFTS/MS *operando* studies. For the XAS measurements, there were three detectors: one measuring the incident intensity of the beam, I_0, the second one for the transmitted beam through the sample, I_t, and the third one measuring the reference intensity, I_{ref}. The standard palladium foil was positioned between the I_t and I_{ref} detectors, and each scan was taken using an exposure of 180 s. XAS was performed at the inlet and outlet ends of the packed-bed catalyst and an online mass spectrometer (MS) was used to monitor the effluent gases from the reactor.
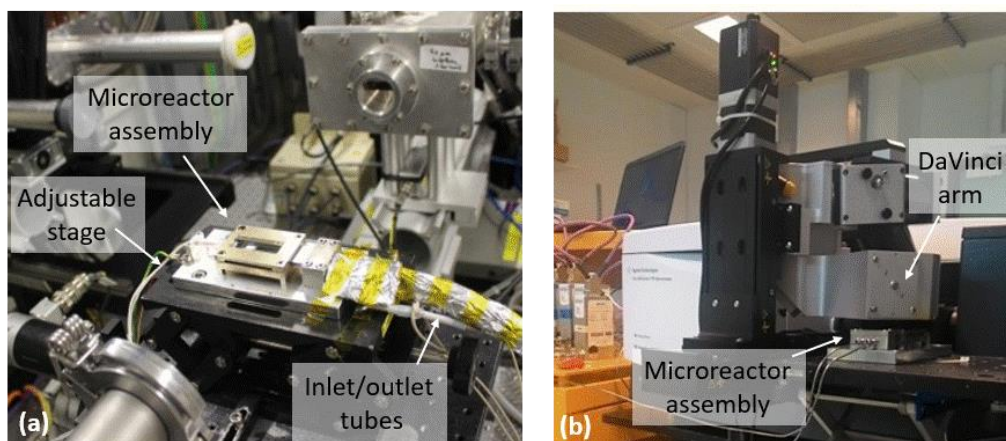
Figure 3.4. Experimental setup using the silicon-glass microreactor for (a) *operando* XAS/MS at the B18 beamline at the Diamond Light Source and for (b) *operando* DRIFTS/MS at the Research Complex at Harwell.
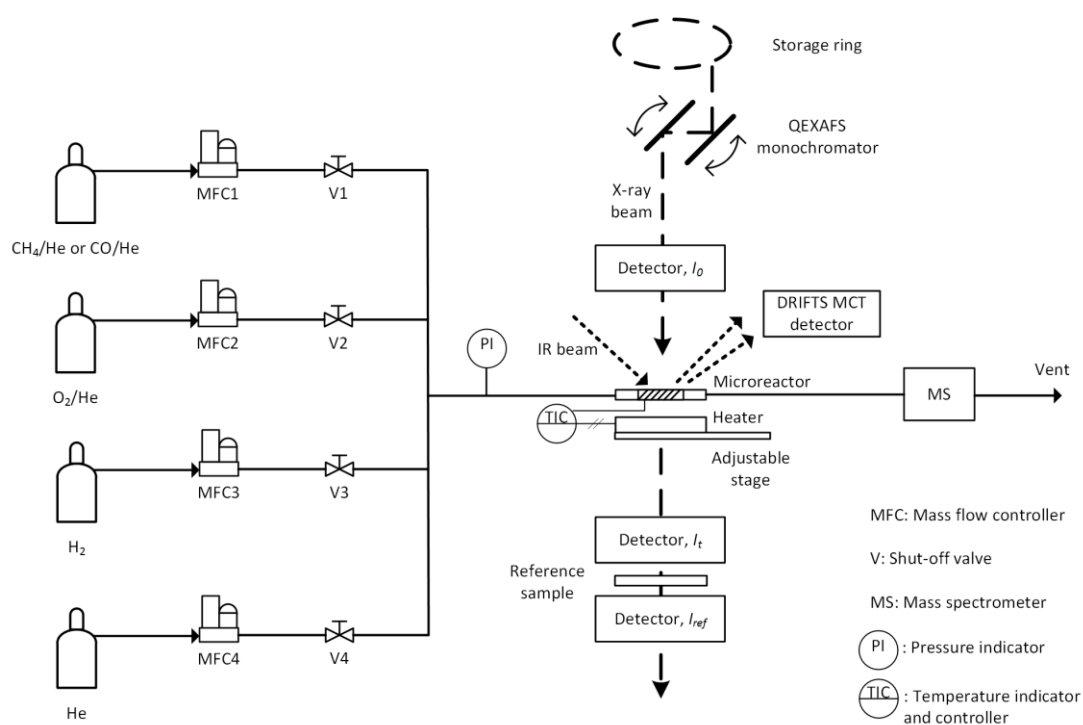
Figure 3.5. Schematic of the experimental setup for the *operando* XAS/MS and DRIFTS/MS studies using the silicon-glass microreactor.

Methane was oxidised using the 2 wt% Pd/Al_2O_3 catalyst (27.7 mg of 53 - 63 µm sieve fraction) as in the laboratory reaction test. Calcination occurred at 400 °C (10 °C/min) for 30 min under 10% O_2/He flow. The reactor was then cooled down to 250 °C and the reactant mixture made of 1% CH_4, 4% O_2 and

5% Ar in He was flowed at a total flow rate of 40 NmL/min. Reaction started at 250 °C and the temperature was increased stepwise (every 50 °C) up to 400 °C at a rate of 10 °C/min with a dwell time of 45 min for each temperature. During reaction the catalyst was probed at the inlet position in transmission mode.

3.2.5.2. XAS/MS during palladium reduction under methane flow

To demonstrate the applicability of the microreactor to transient experiments, reduction of the oxidised catalyst was performed at a ramping temperature under methane flow. After calcination at 400 °C, the reactor was cooled down to 225 °C under a flowrate of 10% O_2/He. The reduction started when the flowrate was switched to 1% CH_4/He at 40 NmL/min and the temperature was increased at 1 °C/min till 298 °C, while probing the catalyst at the inlet position. Once the reduction was complete, 10% O_2/He was flowed again and the temperature was increased up to 400 °C for a further calcination. In the meanwhile, the reactor was moved from its original position in order to align the X-ray beam to the outlet port. The reduction of the catalyst was repeated using 1% CH_4/He at 40 NmL/min from 225 to 305 °C (1 °C/min). In the two experiments, XAS scans were taken every 3.46 min, generating 21 and 24 spectra, respectively. The XAS data were post-processed using the Athena software and the details are reported in Appendix A.

3.2.5.3. DRIFTS/MS during methane[4] and CO oxidation

For the DRIFTS experiment, an Agilent Cary 680 series spectrometer with a Harrick DaVinci arm (Figure 3.4b) was used. The DaVinci arm was coupled with Praying Mantis optics that allowed the IR beam to be focussed onto the catalyst bed. *Operando* experiments were conducted using a MS (Hiden QGA) enabling the analysis of the reaction products. Similarly to the *operando* XAS experiments, the microreactor was located onto an adjustable platform, placed 4.7 mm below the DaVinci arm. Spectra were acquired by taking 64 scans with a resolution of 4 cm^{-1} using a mercury cadmium telluride (MCT) detector which

---

[4] *Operando* DRIFTS during methane combustion in the microreactor and the Harrick cell was conducted by Dr Enhong Cao and Dr Santhosh Matam at the Research Complex at Harwell.

was cooled down using liquid nitrogen. The spectra were taken in the middle of the catalyst bed, between the inlet and the outlet ends.

DRIFTS was performed during the catalytic combustion of methane over the 2 wt% Pd/Al_2O_3 catalyst and over a commercial 1 wt% Pt/Al_2O_3 in the CO oxidation. The combustion of methane during DRIFTS was conducted between 250 and 400 °C under the same conditions as in the *operando* XAS study. In this experiment, 28 mg of catalyst were used in a sieve fraction of 53 - 63 μm and for comparison, the same reaction was performed in a Harrick DRIFTS cell.

Carbon monoxide was oxidised in the microreactor using 29.6 mg of a commercial 1 wt% Pt/Al_2O_3 catalyst (Sigma-Aldrich) in a sieve fraction of 38 - 53 μm. Equation (3.5) shows the reaction formula.

$$2\ CO + O_2 \rightarrow 2\ CO_2 \tag{3.5}$$

Prior to this reaction, the catalyst was calcined at 400 °C (10 °C/min ramping rate) for 60 min under 10% O_2/He flow. Reduction was then carried out after flushing He and switching to 10% H_2/He. This was done at 400 °C for 30 min, after which the gas mixture was switched to He and the temperature decreased to 30 °C. The applicability of the microreactor to temperature-resolved oxidations was demonstrated by ramping the temperature from 30 to 400 °C (at 5 °C/min) while flowing 10% O_2/He at 30 NmL/min, and 10% CO/He at 10 NmL/min. DRIFTS scans were taken every 30 s and the reaction products were analysed online using a MS. After reaction, the gas mixture was switched to 10% O_2/He and the catalyst was calcined for 30 min at 400 °C. Temperature was decreased to 30 °C (10 °C/min) under a O_2/He atmosphere. The same oxidation of CO was re-performed, but this time on a pre-oxidised catalyst. The same temperature ramping and reaction mixture of the CO oxidation over a pre-reduced catalyst were employed for the second reaction. After the two oxidation reactions, the reactor was cooled down to 310 °C and a stoichiometric mixture of oxygen (10% O_2/He at 5 NmL/min) and carbon monoxide (10% CO/He at 10 NmL/min), balanced with He (25 NmL/min) was flowed into the reactor. In order to demonstrate the spatially resolved *operando* DRIFTS, the IR beam was shone along the catalyst bed from the inlet to the outlet end at 2 mm steps.

3.3. Results and discussion

3.3.1. Catalytic combustion of methane

Results from the reaction tests conducted at UCL on the combustion of methane over 2 wt% Pd/Al_2O_3 are shown in Figure 3.6. Reaction started at 250 °C with an outlet concentration of 0.99% which decreased to 0.48% at 400 °C. At the highest temperature, the average turnover frequency of methane was 107 h^{-1}. It is possible to find in previous studies similar *TOF* for methane over Pd/Al_2O_3 catalysts at 400 °C and 1 atm (Table 3.1) [197-201] .
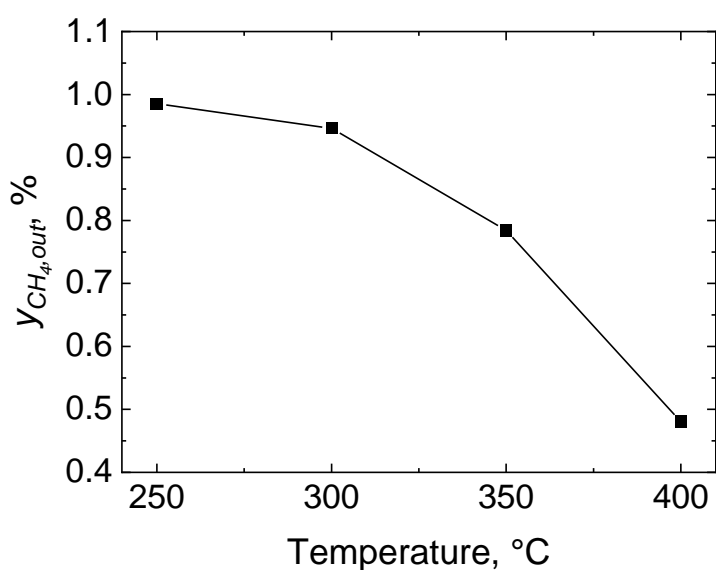
Figure 3.6. Methane combustion over 2 wt% Pd/Al_2O_3 catalyst at 250, 300, 350 and 400 °C. The outlet methane molar fraction, $y_{CH4,out}$ is plotted against the reaction temperature.

Table 3.1. Methane turnover frequency over Pd/Al$_2$O$_3$ catalysts at 400 °C and 1 atm from the literature.

Reference	Pd, wt%	Catalyst pretreatment	$y_{CH4,in}$, %	O$_2$/CH$_4$, -	TOF, h^{-1}
Burch *et al.* [197]	4	Calcination	0.8	20	91
Briot *et al.* [198]	1.95	Reduction	1	4	10
Briot *et al.* [198]	1.95	Ageing	1	4	65
Burch *et al.* [199]	4	Calcination	0.3	5	35
Mouaddib *et al.* [200]	1.93	Reduction	1	4	5
Mouaddib *et al.* [200]	1.93	Ageing	1	4	70
This work	2	Reduction	1	4	107

The temperature profile was evaluated along the catalyst bed during the catalytic combustion of methane and Figure 3.7 shows the results. No large temperature gradients were detected in the catalyst bed, especially below 400 °C. At this temperature, the highest variation in temperature along the bed was ± 1 °C from the set temperature.
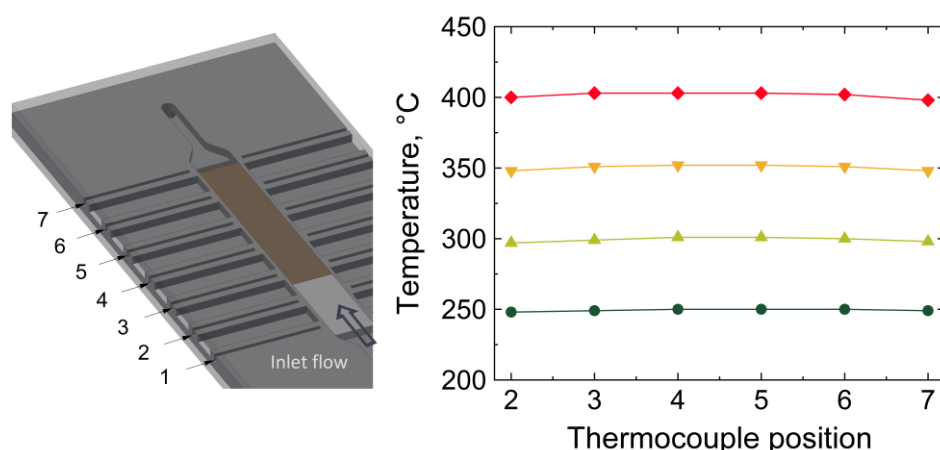
Figure 3.7. Temperature profiles along the reactor bed during methane combustion over 2 wt% Pd/Al$_2$O$_3$ catalyst at different reactor set temperatures: 250, 300, 350 and 400 °C. The thermocouple positions are six of the seven thermowells shown in the figure on the left.

3.3.1.1. Axial dispersion in the micropacked-bed reactor

The residence time distribution in the microreactor was assessed by estimating the axial dispersion coefficient, using the fluid properties under the reaction conditions. Dispersion in a packed-bed reactor can be determined knowing the flow regime and the fluid physical properties [202]. The former can be described by the particle Reynolds number, Re_p, while the physical properties are captured by the Schmidt number, Sc, defined in Equation (3.6) and Equation (3.7), respectively.

$$Re_p = \frac{u \, \rho \, d_p}{\mu} \tag{3.6}$$

$$Sc = \frac{\mu}{\rho \, D_m} \tag{3.7}$$

In these definitions, d_p is the catalyst particle diameter, u the free-stream superficial velocity, ρ the fluid density, D_m the reactant molecular diffusivity, and μ the dynamic viscosity. The density can be calculated using the ideal gas law assuming the gas made entirely of helium and the molecular diffusivity of methane in helium is reported by Cussler at 298 K and atmospheric pressure, being equal to 0.675 cm^2/s [203]. However, diffusivity is a function of temperature and to determine D_m at 673.15 K, Equation (3.8) can be used [204].

$$D_m(T_2) = D_m(T_1)\left(\frac{T_2}{T_1}\right)^{1.75} \tag{3.8}$$

For the helium viscosity, this can be calculated at 400 °C (673.15 K) using Equation (3.9), as reported by Kestin and Leidenfrost [205].

$$\mu_{He}(\mu P) = 5.023\, T(K)^{0.647} \tag{3.9}$$

Table 3.2 reports the reactor dimensions while Table 3.3 shows the fluid and physical properties of the reacting 1% CH_4/He and 4% O_2/He gases at 40 NmL/min and 400 °C, including Re_p and Sc.

Table 3.2. Characteristic dimensions of the catalyst bed in the silicon-glass microreactor.

Property	Value
Width, m	$3\cdot10^{-3}$
Depth, m	$600\cdot10^{-6}$
Length, m	$15\cdot10^{-3}$
Empty cross sectional area, m^2	$1.8\cdot10^{-6}$
Empty volume (V_R) m^3	$0.027\cdot10^{-6}$

Table 3.3. Catalyst and gas fluid dynamic properties of 1% CH_4/He and 4% O_2/He at 400 °C in the silicon-glass microreactor.

Property	Value
d_p, µm	60
v, NmL/min	40
u, m/s	0.37
ρ, kg/m³	0.072
D_m, m²/s	2.81·10⁻⁴
μ, mPa·s	0.034
Re_p	0.047
Sc	1.71

The axial dispersion coefficient, D_{ax}, is related to the dimensionless Péclet number, Pe, which can be calculated from the particle Péclet number, Pe_p, and the catalyst bed length, L_b, in the case of packed-bed reactors as shown in Equation (3.10) [206]. Pe_p can be calculated knowing Re_p and Sc according to Equation (3.11) and using a correction factor that accounts for the catalyst bed porosity, φ_b (0.4) [204], and the catalyst bed tortuosity, τ_b (1.4) [207]. Equation (3.11) holds for a ratio between the channel diameter and the particle size, d_p, higher than 15, and a ratio between the catalyst bed length, L_b, and the reactor diameter, larger than 20 [207]. In this work, the latter was 25 (with respect to the channel depth). However, given the rectangular cross section of the channel, there are two ratios related to the cross sectional area: the ratio between the channel depth and the catalyst particle (10), and that between the channel width and the particle diameter (50).

$$Pe = \frac{u\,L_b}{D_{ax}} = Pe_p \frac{L_b}{d_p} \tag{3.10}$$

$$\frac{1}{Pe_p} = \frac{\varphi_b}{\tau_b} \frac{1}{Re_p\,Sc} + \frac{1}{2} \tag{3.11}$$

According to Gierman, the reactor can be treated as a plug-flow if the Péclet number is larger than a certain value, which is a function of the conversion, X, and the order of reaction, n, as shown in Equation (3.12) [206, 208]. At 400 °C,

methane conversion was 0.52, hence the value on the right-hand side of Equation (3.12) is approximately 6 (assuming first-order reaction).

$$Pe > 8\,n\,\ln\left(\frac{1}{1-X}\right) \qquad (3.12)$$

In Table 3.4 the calculated values for Pe_p and Pe are reported and it is possible to see that Pe is about ten times higher than 6, suggesting that the reactor is operating under plug-flow regime.

Table 3.4. Particle Péclet, Pe_p, and Péclet number, Pe, for the catalyst bed inside the silicon-glass microreactor operating at 400 °C under 40 NmL/min of 1% CH_4/He and 4% O_2/He.

Pe_p	Pe
0.24	61 (> 6)

3.3.1.2. External and internal mass transfer

The performance of the microreactor not only depends on the narrow residence time distribution within the catalyst bed, but also and especially on the efficiency of the catalyst. This can be evaluated by assessing the mass transfer resistances that may occur outside (external) or inside (internal) the catalyst particles.

Mears proposed a method to determine whether it is possible to neglect external mass transfer resistances of the reacting species moving from the gas bulk phase to the surface of the catalyst particle [204, 209]. This is shown in Equation (3.13), where r' is the observed reaction rate per unit of catalyst mass (mol/s/kg), ρ_b is the catalyst bulk density and k_{GS} the external gas-solid mass transfer coefficient. C_{Ab} is the reactant concentration in the bulk phase that can be calculated from the ideal gas law considering a partial methane pressure of 0.01 atm (1% in 1 atm). In his derivation, Mears proposed that when the group (MR) in Equation (3.13) is smaller than 0.15, the external mass transfer can be neglected. This method gives an average value across the reactor, as the apparent reaction rate averages out the catalyst contributions from the inlet to the outlet.

$$MR = \frac{r' \, \rho_b \, d_p \, n}{2 \, k_{GS} C_{Ab}} < 0.15 \tag{3.13}$$

In order to determine the Mears group, MR, it is essential to estimate the external gas-solid mass transfer coefficient, k_{GS}, which can be derived from the Sherwood number, Sh, defined in Equation (3.14), that for very low Re_p, can be approximated using Equation (3.15) [206].

$$Sh = \frac{k_{GS} \, d_p}{D_m} \tag{3.14}$$

$$Sh \approx 0.07 \, Re_p \qquad 0.1 < Re_p < 10 \tag{3.15}$$

Table 3.5 reports the calculated external mass transfer (0.014 m/s) and the Mears number (0.07) which is clearly below 0.15, indicating that the silicon-glass microreactor was operating under no external mass transfer limitations.

Table 3.5. External gas-solid mass transfer coefficient, k_{GS}, and Mears number, MR, in the catalyst bed inside the silicon-glass reactor operating at 400 °C under 40 NmL/min of 1% CH_4/He and 4% O_2/He.

k_{GS}, m/s	MR
0.014	0.07 (< 0.15)

Concerning the internal mass transfer resistances, it is possible to adopt the Weisz-Prater criterion. This states that for a first order reaction kinetics occurring in a spherical catalyst particle, the internal mass transfer resistance can be neglected if the dimensionless group, C_{WP}, defined in Equation (3.16) is much smaller than 1 [204]. In this definition, ρ_p is the catalyst particle density, d_p its diameter, C_{As} the concentration of methane at the particle surface and D_e the effective diffusivity. This can be estimated from Equation (3.17), where τ_p is the tortuosity (3.0), φ_p the porosity (0.4) within the catalyst particle and σ_c the constriction factor (0.8) [204]. As the external mass transfer resistance can be neglected, C_{As} is equal to C_{Ab}.

$$C_{WP} = \frac{r' \, \rho_p \, d_p^2}{4 \, C_{As} \, D_e} << 1 \tag{3.16}$$

$$D_e = \frac{\varphi_p \, \sigma_c}{\tau_p} D_m \qquad (3.17)$$

The group $r' \, \rho_p$ can be determined using Equation (3.18) where $r' \, \rho_b$ is the reaction rate per reactor volume and φ_b is the catalyst bed porosity (assumed to be 0.4) [204].

$$r' \, \rho_p = r' \rho_b \frac{1}{(1 - \varphi_b)} \qquad (3.18)$$

Table 3.6 shows effective diffusivity and the Weisz-Prater number being much smaller than 1, indicating that the methane combustion was carried out in the silicon-glass microreactor under no internal mass transfer limitations.

Table 3.6. Effective diffusivity and Weisz-Prater number in the catalyst bed of the silicon-glass microreactor operating at 400 °C with 40 NmL/min of 1% CH_4/He and 4% O_2/He.

D_e, m^2/s	C_{WP}
$1.8 \cdot 10^{-5}$	0.003 (<< 1)

3.3.2. *Operando* XAS/MS

3.3.2.1. Combustion of methane on Pd/Al$_2$O$_3$

Operando X-ray Absorption Near Edge Structure (XANES) spectra along with the outlet methane concentration are presented in Figure 3.8. As reported in the laboratory test results (*vide supra*), methane combustion started at 250 °C and reached a conversion of approx. 50% at 400 °C. An Arrhenius plot is presented in Figure 3.8b where a linear fitting is performed for the ln(*TOF*) plotted against the inverse of temperature. The apparent activation energy resulting from the slope of the linear fitting is approx. 80.7 kJ/mol, which is similar to other values reported in the literature for methane oxidation over a Pd/Al$_2$O$_3$ catalyst. Van Giezen *et al.* reported a 86 kJ/mol using a pre-calcined 7.3 wt% Pd/Al$_2$O$_3$ in a reacting mixture of 1% CH_4 and 4% O_2 in helium [210]. Values of 76 kJ/mol and 75 kJ/mol were also found by Ribeiro *et al.* for a pre-calcined 8.5 wt% Pd/Al$_2$O$_3$, and by Mouaddib *et al.* for a 1.93 wt% Pd/Al$_2$O$_3$ aged under reaction conditions at 600 °C [200, 211].

Figure 3.8c shows the XANES spectra overlay and it is possible to notice that the point at 24368 eV is the same at all studied reaction temperatures. To estimate the palladium speciation, linear combination fitting (LCF) of the XANES spectra was performed (see Figure 3.8d). Results show that palladium was largely in its oxidised state at all reaction temperatures. These results are further corroborated with the Fourier Transform of the corresponding Extended X-ray Absorption Fine Structure (EXAFS) (see Appendix A).
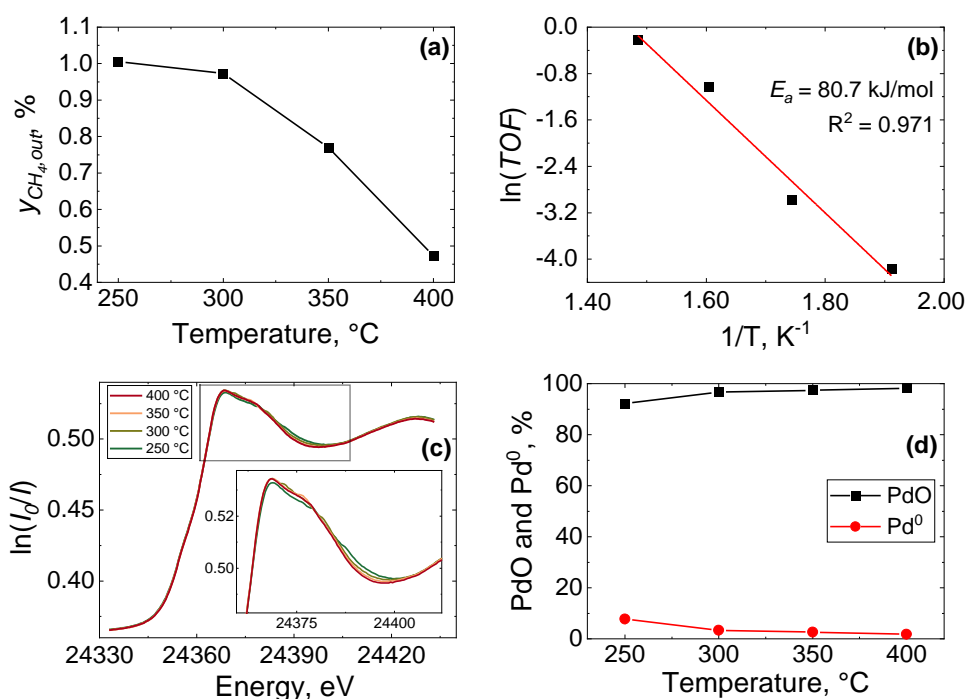
Figure 3.8. (a) Methane outlet concentration, $y_{CH4,in}$ during combustion over 2 wt% Pd/Al$_2$O$_3$ in the silicon-glass microreactor, (b) Arrhenius plot of the turnover frequency, (c) normalised *operando* XANES spectra at the Pd K-edge of the inlet of the catalyst bed and (d) palladium speciation obtained by LCF of the XANES spectra.

3.3.2.2.   Temperature-resolved reduction of Pd/Al$_2$O$_3$

The microreactor was tested in a temperature-resolved experiment in which palladium was reduced with methane while temperature was increased by approx. 3.5 °C between two consecutive scans (3.46 min). In this dynamic condition, the microreactor could immediately adapt and provide time-

dependent data, owing to its excellent heat transfer and short residence time of 0.04 s, given a gas flowrate of 40 NmL/min in a catalyst channel of 27 µL (when empty).

Figure 3.9 shows the results relative to the reactor inlet, including stacked XANES, PdO and Pd metal component percentages and the FT of the EXAFS data, all as a function of the ramping temperature. Reduction of the palladium catalyst at the inlet of the packed bed occurred gradually as highlighted by the XANES spectra. The palladium metal speciation could be quantified from the LCF performed on the XANES spectra. This shows the isosbestic point occurring at 246 °C (*i.e.*, point at which Pd and PdO compositions are equal).

(a)

(b)

(c)
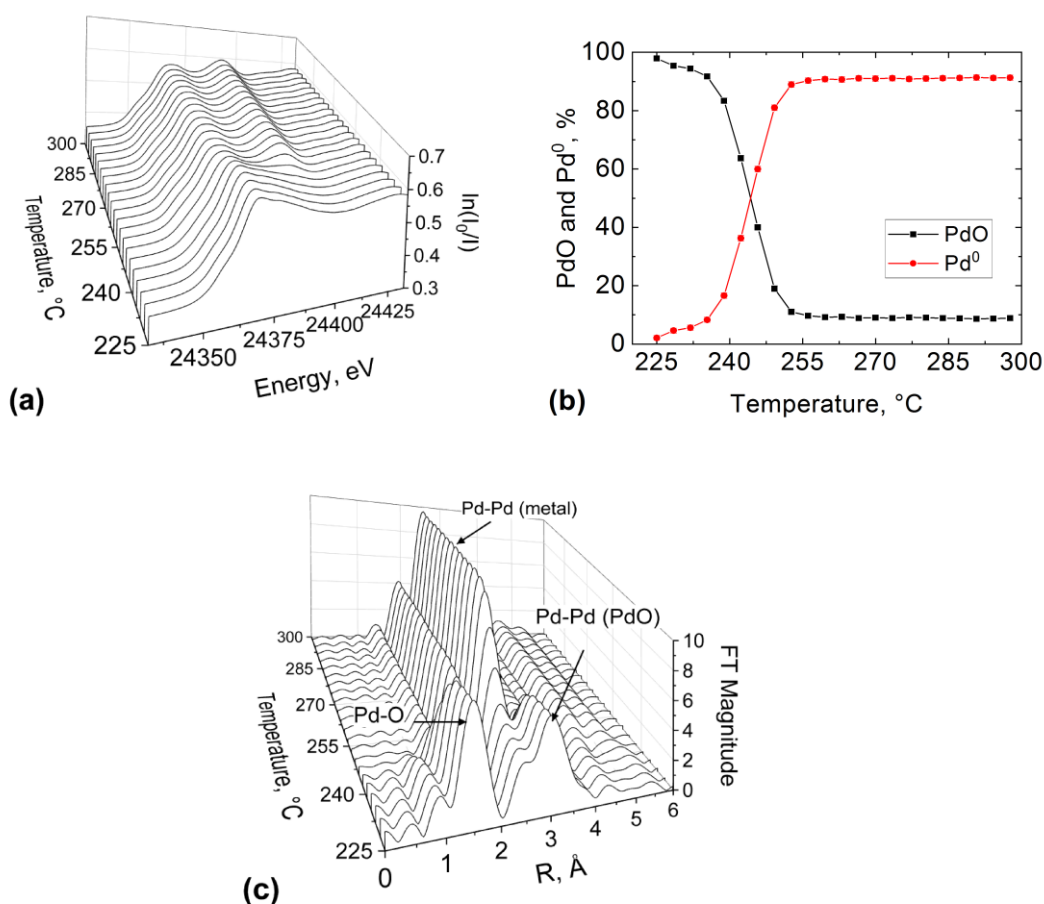
Figure 3.9. XAS study at the Pd K-edge of the 2 wt% Pd/Al$_2$O$_3$ catalyst at the bed inlet position of the silicon-glass microreactor during the temperature-resolved reduction with methane: (a) normalised XANES spectra, (b) palladium speciation obtained by LCF of the XANES spectra and (c) phase shift uncorrected Fourier transform of EXAFS.

The FT graph of the EXAFS shown in Figure 3.9c further corroborates the results. At 225 °C the graph presents two peaks at approx. 1.5 Å (phase shift uncorrected) and 3 Å corresponding to the first and second coordination shells, respectively. This can be attributed to Pd-O and Pd-Pd bonds of PdO species, indicating that the catalyst was mainly in its oxidised state. When the temperature was increased the characteristic peak of the Pd-Pd in the first coordination shell of metallic Pd emerged at approx. 2.4 Å (phase shift uncorrected), with a simultaneous gradual decrease of the PdO peaks in the first coordination shell at about 1.5 Å (phase shift uncorrected), suggesting a reduction of the palladium oxide to palladium metal.

The outlet end of the catalyst bed was probed by X-rays during the second temperature-resolved reduction and the results are reported in Figure 3.10. From the XANES spectra it is possible to see a delay in the palladium reduction, which occurred at 280 °C. Similarly, the LCF result shows an isosbestic point occurring at 285 °C. This could be due to the effects of the further calcination that the catalyst underwent before the second temperature-resolved reduction, which might have sintered the catalyst. The LCF result also shows the presence of a metallic Pd at lower temperature, suggesting that the first calcination was more effective than the second one.
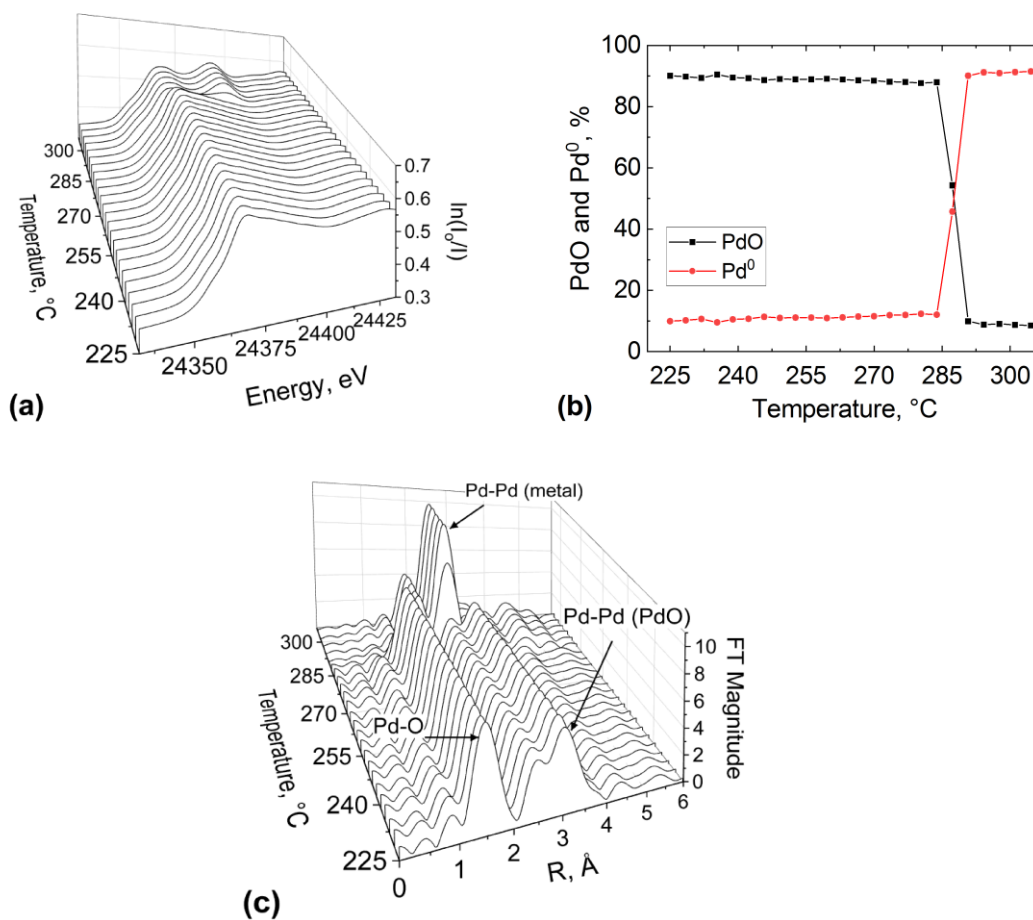
Figure 3.10. XAS study at the Pd K-edge of the 2 wt% Pd/Al$_2$O$_3$ catalyst at the bed outlet position of the silicon-glass microreactor during the temperature-resolved reduction with methane: (a) normalised XANES spectra, (b) palladium speciation obtained by LCF of the XANES spectra and (c) phase shift uncorrected Fourier transform of EXAFS.

The FT of the EXAFS (Figure 3.10c) shows the characteristic first coordination shell peak of the Pd-Pd at 2.4 Å emerging at approx. 290 °C, while at 300 °C palladium metal dominated the phase composition.

These results also show how spatial and time-dependent information can be obtained using this microreactor, with the advantage of avoiding averaging out the information along the catalyst bed, which is the case in conventional XAS spectroscopic cells.

3.3.3. *Operando* DRIFTS/MS studies

3.3.3.1. Combustion of methane on Pd/Al$_2$O$_3$

Operando DRIFTS results during methane combustion over 2 wt% Pd/Al$_2$O$_3$ are shown in Figure 3.11. In line with the laboratory test and the *operando* XAS, methane combustion started at 250 °C, and at 400 °C the outlet concentration was close to 46%.

DRIFTS spectra were collected at the centre of the catalyst bed in the microreactor (Figure 3.11b) and these show small peaks at 3000 cm^{-1} and 2360 - 2300 cm^{-1}, relative to gaseous methane (*v* C-H), and gaseous CO$_2$, respectively [212-215]. For comparison, DRIFTS spectra were also collected using a Harrick DRIFTS cell (Figure 3.11c). These show the typical methane and CO$_2$ gas phase bands at 3016 cm^{-1} and 2360-2300 cm^{-1}, respectively. In previous studies it has been shown that methane and carbon dioxide are generally detected in their gaseous forms [212-214]. Given the small volume of the microreactor, these could not been detected in a large extent.
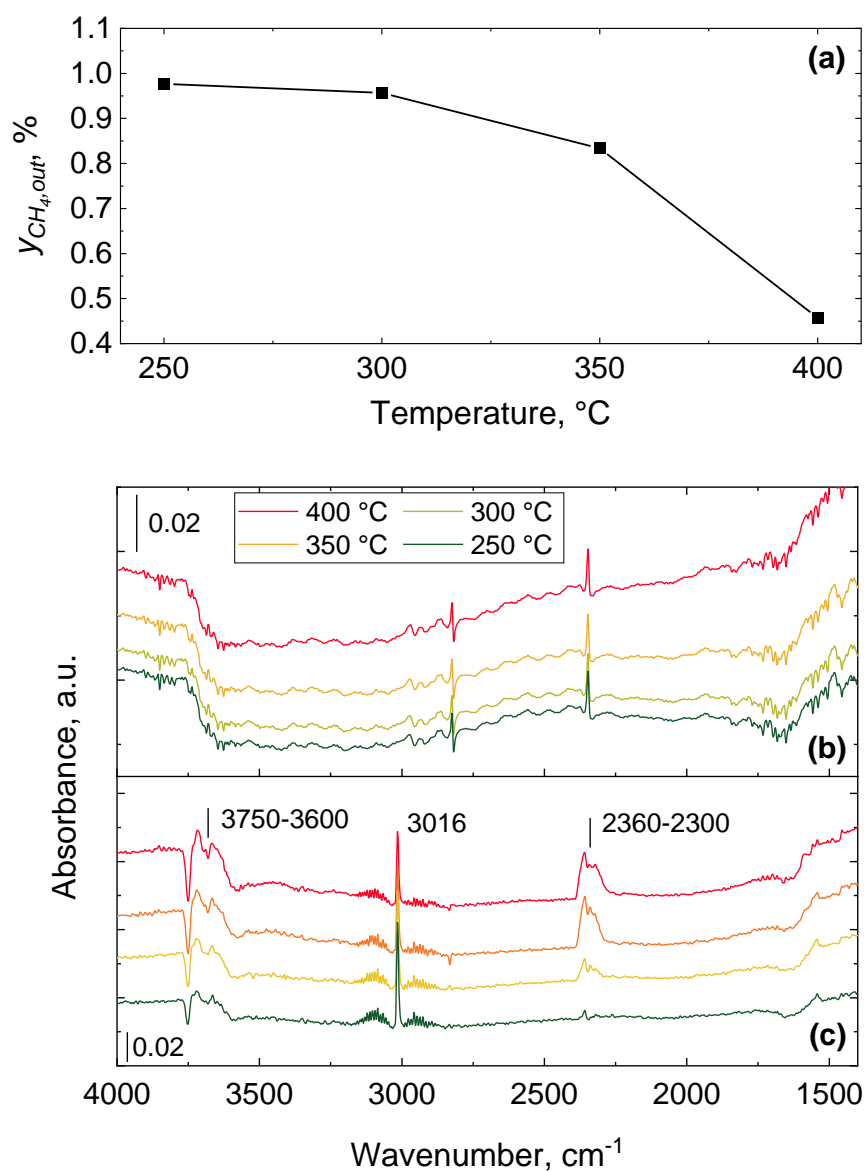
Figure 3.11. *Operando* DRIFTS during methane combustion over 2 wt% Pd/Al$_2$O$_3$ catalyst in the silicon-glass microreactor: (a) Methane outlet molar fraction, $y_{CH4,out}$, (b) difference infrared spectra recorded using the microreactor and (c) spectra obtained using a commercial Harrick cell.

3.3.3.2. Temperature-resolved CO oxidation on Pt/Al₂O₃

Operando DRIFTS in the silicon-glass microreactor was demonstrated in the temperature-resolved CO oxidation over a pre-reduced and pre-oxidised 1 wt% Pt/Al_2O_3 catalyst. Figure 3.12 shows the results relative to the CO oxidation performed over a pre-reduced platinum catalyst. The temperature was increased from 30 to 300 °C and DRIFTS spectra were taken at the centre of the catalyst bed. From the MS data it is clear that CO_2 starts appearing at about 180 °C, with a concomitant drop in CO and O_2 concentration suggesting the start of CO oxidation. At approx. 240 °C, CO is continuously converted to CO_2. DRIFTS spectra reveal two bands at 2060 and 2072 cm⁻¹, relative to linearly adsorbed CO onto two different platinum sites [216, 217]. The peak intensity increases at increasing temperature from 30 to 240 °C when they disappear abruptly due to the complete oxidation of CO, in line with the MS data.
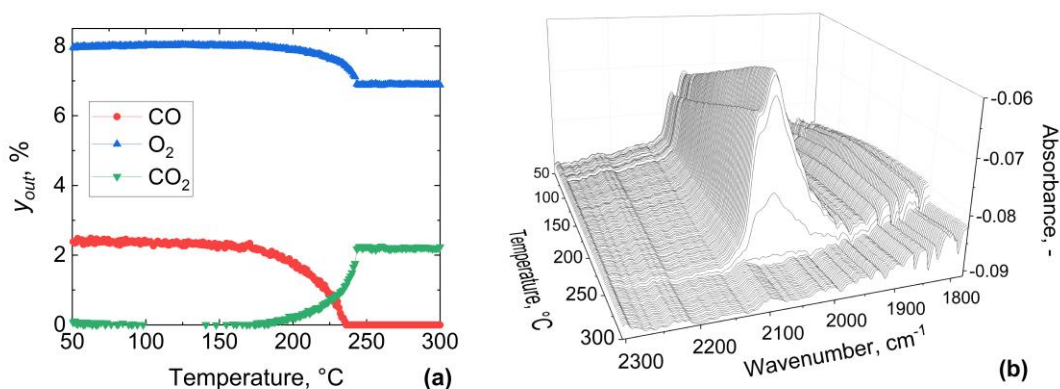
Figure 3.12. *Operando* DRIFTS during the temperature-resolved CO oxidation over a pre-reduced 1 wt% Pt/Al_2O_3 catalyst in the silicon-glass microreactor: (a) Concentration of the outlet gas phase species, y_{out}, and (b) difference infrared spectra in the middle of the catalyst bed.

Bowker studied the so-called CO "light-off", using X-ray photoelectron spectroscopy on Pd during CO oxidation [218]. The catalyst surface is covered by adsorbed CO at low temperatures, but as soon as the temperature is increased, molecular oxygen starts adsorbing, dissociating and reacting with adsorbed CO to form CO_2. As the process frees four sites for further oxygen adsorption, CO oxidation self-accelerates. Hence, the sudden disappearance

of the CO band in the DRIFTS spectra can be due to the fast and complete reaction of adsorbed CO with oxygen at high temperatures.

The results from the temperature-resolved CO oxidation over a pre-calcined 1 wt% Pt/Al_2O_3 are reported in Figure 3.13. DRIFTS spectra were taken while the temperature was ramped from 50 to 300 °C and MS was analysing the gas outlet composition. CO_2 started appearing at a temperature of 200 °C, with the simultaneous drop in CO and O_2 concentration in the gas phase. At approx. 260 °C, carbon monoxide concentration disappeared from the outlet while oxygen and carbon dioxide stabilised. The DRIFTS spectra show no band between 30 and 50 °C and a band appearing at 2086 cm^{-1} between 50 and 120 °C. At higher temperatures, the peak redshifted to 2078 cm^{-1} and a new band appeared at 2060 cm^{-1}. These grow in intensity up to 260 °C, after which they suddenly disappear, as observed for the case of CO oxidation over the pre-reduced catalyst (*vide supra*).
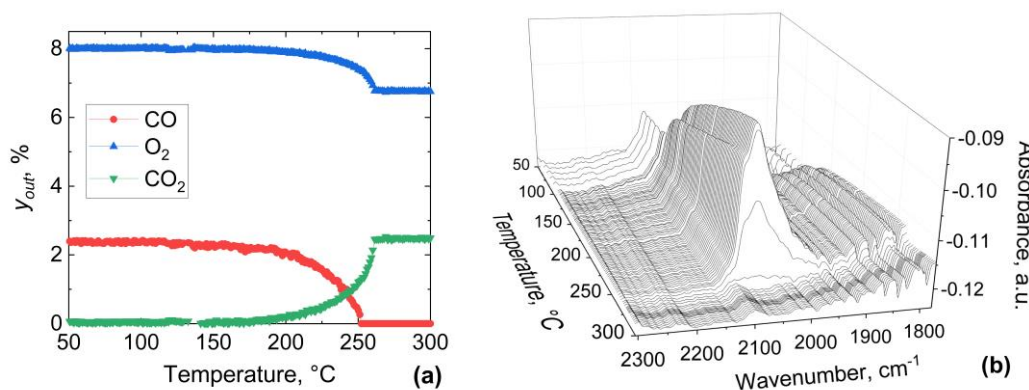
Figure 3.13. *Operando* DRIFTS during the temperature-resolved CO oxidation over a pre-oxidised 1 wt% Pt/Al_2O_3 catalyst in the silicon-glass microreactor: (a) Concentration of the outlet gas phase species, y_{out}, and (b) difference infrared spectra performed in the middle of the catalyst bed.

An Arrhenius plot of the turnover frequency for the pre-reduced and pre-oxidised catalyst is presented in Figure 3.14. From the fitting of the experimental data it is clear that the activation energies are of similar magnitude for both the pre-reduced and pre-oxidised Pt/Al_2O_3 catalysts. However, for the pre-reduced catalyst, this is equal to *ca.* 46.6 kJ/mol, which is slightly lower than that of the pre-oxidised catalyst (48.4 kJ/mol).
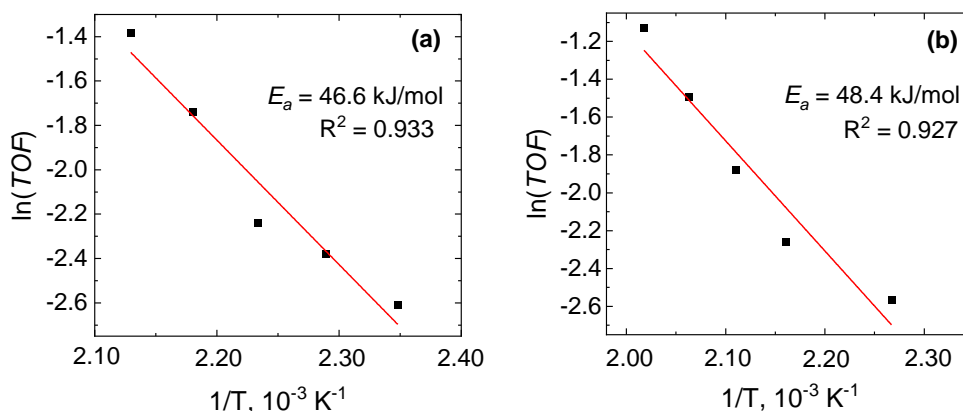
Figure 3.14. CO turnover frequency, *TOF*, over the (a) pre-reduced and (b) pre-oxidised 1 wt% Pt/Al$_2$O$_3$ catalyst during the temperature-resolved CO oxidation in a silicon-glass microreactor.

Similar values for the apparent activation energy of CO oxidising over a Pt catalyst have been reported in previous studies [219-222], ranging from 56 kJ/mol for a pre-reduced 5 wt% Pt/SiO$_2$ [222], to 84 kJ/mol for a calcined 1 - 2 wt% Pt/Al$_2$O$_3$ catalyst [219].

3.3.3.3. Spatially-resolved DRIFTS of adsorbed CO on Pt/Al$_2$O$_3$

During CO oxidation over the 1 wt% Pt/Al$_2$O$_3$ the CO adsorption over the catalyst surface was investigated using DRIFTS along the catalyst bed. Results are presented in Figure 3.15. The spectra are characterised by a broad prominent peak at 2060 cm^{-1} with a shoulder at 2075 cm^{-1}, and the intensity ratio between the two remains constant along the bed. Some studies conducted using spatially-resolved DRIFTS in a fixed-bed *operando* reactor, also reported no change in the adsorbed CO species during CO oxidation over a Pt/CeO$_2$-Al$_2$O$_3$ catalyst [149, 223].
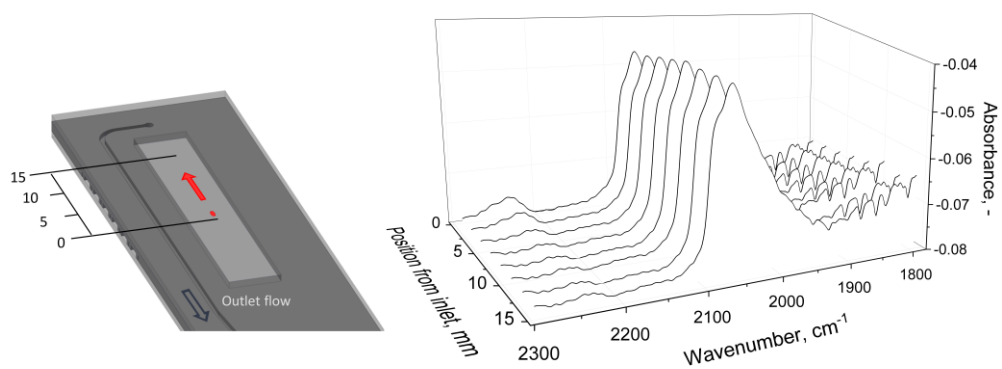
Figure 3.15. Difference infrared spectra of CO adsorbed over the pre-oxidised 1 wt% Pt/Al$_2$O$_3$ catalyst during CO oxidation at 310 °C. The picture on the left represents the silicon microreactor and the red dot indicates the DRIFTS beam with the arrow pointing at the scanning direction along the catalyst bed.

3.4. Summary and Conclusions

A novel silicon microreactor with a plug-flow behaviour has been developed with negligible external and internal mass transfer resistances, suitable for XAS and DRIFTS *operando* spectroscopy studies. Its design and materials helped achieve an isothermal temperature profile along the bed, and its reduced volume allowed to perform safe exothermic reactions. Moreover, the short gas residence time proved to be particularly suited for transient response experiments.

Operando XAS at the Pd K-edge was performed on a 2 wt% Pd/Al_2O_3 catalyst in transmission mode and results showed that during methane combustion palladium at the inlet of the catalyst bed was oxidised at all temperatures. However, DRIFTS only showed weak peaks attributable to gaseous methane and CO_2 species, owing to the reduced reactor volume. To demonstrate the applicability in temperature-resolved *operando* spectroscopy, the oxidised catalyst reacted with flowing methane under a ramping temperature. Results from *operando* XAS showed that the inlet and the outlet regions of the catalyst bed exhibited a different reduction temperature, owing to catalyst ageing at the outlet resulting from an intermediate re-calcination step. Temperature-resolved *operando* DRIFTS was conducted during CO oxidation over 1 wt% Pt/Al_2O_3 and results showed the presence of linearly adsorbed CO molecules on the pre-reduced and pre-oxidised platinum surface. Owing to its easily accessible catalyst bed from both X-ray and IR beams, spatially-resolved DRIFTS was performed during the CO oxidation at 310 °C and at 9 different axial positions along the catalyst bed.

Chapter IV. Membrane reactor with adsorbed catalytic nanoparticles for the hydrogenation of nitrobenzene
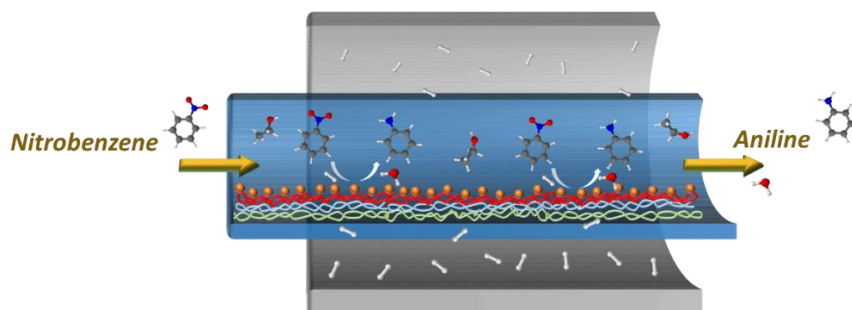
Tubular Teflon AF-2400 membranes were modified on their inner surface by adsorbing polydopamine, poly(acrylic acid) and poly(allylamine hydrochloride) to provide a functional surface for catalytic nanoparticle adsorption. Spherical, cubical, truncated octahedral palladium and dendritic platinum-palladium nanoparticles were synthesised *ex situ* and deposited in modified tubular membranes. The resulting membrane reactors were tested in the continuous nitrobenzene hydrogenation into aniline using molecular hydrogen pressurised outside the membrane. Results showed a stable conversion for 6 h of continuous reaction for the truncated octahedral and dendritic nanoparticles, while deactivation was observed in the case of the other catalytic systems. The 3.7 nm spherical nanoparticles showed the highest average turnover frequency equal to 629 h^{-1}, while the cubical displayed the highest turnover frequency based on surface atoms, *ca.* 3000 h^{-1}. The membrane reactor described in this chapter offers improved process safety compared to batch operation, due to the small volume of pressurised gas, and control over the gas permeation during reaction using a Teflon AF-2400 membrane.

4.1. Introduction

Packed-bed reactors dominate the continuous reactor portfolio due to their user-friendliness and flexibility of operation. However, different catalyst supporting techniques can be used to improve catalyst efficiency and minimise catalyst loading. Catalyst coating of reactor channel walls may be applied to reduce pressure drops, but on the other side it may be catalyst-specific and introduce further mass transfer resistances within the catalyst layer [224]. Among recent unconventional ways, nanoparticles supported on channel walls of continuous reactors can be used to increase the catalyst surface area and boost mass transfer of reactants. In this context, the layer-by-layer (LbL) assembly of polyelectrolytes represents a versatile and easy method to modify surfaces onto which nanoparticle structures can be adsorbed [225]. This method consists of alternating polyelectrolyte layers that adhere to one another *via* electrostatic interactions owing to their functional building blocks [226]. The LbL method has found applications in different fields, including the adsorption of nanoparticles [20]. An example can be found in the work of Dotzauer *et al.*, in which a solution of the negatively charged poly(acrylic acid) (PAA) was impregnated on the surface of a ceramic membrane, followed by the deposition of poly(allylamine hydrochloride) (PAH) which is a cationic polymer. The negatively charged citrate-reduced catalyst nanoparticles were prepared *ex situ* and deposited on the outer layer of the PAH [227]. Dotzauer *et al.* have demonstrated the feasibility of this technique in a wet air oxidation reaction [227]. An aqueous solution of formic acid, acetic acid and phenol was flowed in the modified tubular membrane contactor while air was pressurised outside the ceramic contactor and the oxidation occurred on the catalytic surface. Results showed a higher catalyst activity in the modified membrane compared to the traditional catalyst impregnation technique.

The LbL technique was also applied to polymeric substrates including a tubular PTFE on top of a surface functionalised with polydopamine (PDA) [228]. A solution of the polyanion poly(sodium styrene sulfonate) (PSS) was adsorbed on the PDA-functionalised surface, thermally treated and then, similarly to the work of Dotzauer *et al.* [227], a PAH solution was deposited as the outer layer [228]. Palladium nanocatalysts were prepared *in situ* by reducing the $PdCl_4^{2-}$

ions that were flowed on the PAH surface and that were bound to its amino groups [228]. The resulting coated wall was used as a reactor for the hydrogenation of nitrobenzene, which was flowed together with the gas in the modified PTFE tube. Conversion was found to be stable at about 99% for more than 8 h of continuous operation [228].

In this chapter, the work on the LbL-modification of a tubular Teflon AF-2400 membrane inner surface is presented, onto which size- and shape-tuned *ex situ* synthesised palladium-based nanoparticle were adsorbed. The modified membranes were inserted inside a second tube, in a tube-in-tube configuration, and the resulting reactors were tested in the hydrogenation of nitrobenzene in flow with pressurised molecular hydrogen outside the membrane.

4.2. Materials and methods

4.2.1. Nanoparticle synthesis[5]

Nanoparticle solutions were synthesised in batch using sodium tetrachloropalladate(II) (Na_2PdCl_4, 99.99% trace metal basis) as metal precursor for the palladium nanoparticles, potassium tetrachloroplatinate(II) (K_2PtCl_4, 99.99% trace metal basis) as platinum precursor, polyvinylpyrrolidone (PVP, average Mn: ~55,000), potassium bromide (FT-IR grade, ≥99% trace metals basis), L-ascorbic acid (reagent grade), citric acid monohydrate (ACS reagent, ≥99.0%) and PEG-PPG-PEG (average Mn: 5,800), all purchased from Sigma-Aldrich.

- Pd spheres: The synthesis follows that of Piao *et al.* [229]. An amount of 29.4 mg of Na_2PdCl_4 was dissolved in 1 mL of DI water. In parallel, 200 mg of PEG-PPG-PEG were dissolved in 10 mL of DI water. Once the polymer was fully dissolved, 0.1 mL of the solution containing the Pd precursor were injected in the polymer solution and stirred for 24 h at room temperature.

- Pd truncated octahedra: The synthesis follows that of Lim *et al.* [230]. An amount of 68.4 mg of Na_2PdCl_4 was dissolved in 3.6 mL of DI water. In parallel, 105 mg of PVP, 60 mg of L-ascorbic acid and 60 mg of citric acid were dissolved in 8 mL of DI water and heated up to 100 °C under reflux in a stirred three-neck flask placed in an oil bath. A volume of 3 mL of the solution of the palladium precursor was injected in the heated flask and after 3 h, the solution was removed and cooled down to room temperature in open air.

- Pd cubes: The recipe follows that reported by Lim *et al.* [231]. An amount of 67.1 mg of Na_2PdCl_4 was dissolved in a 3.6 mL DI water solution containing 1.68 M KBr the day before the synthesis. Amounts of 105 mg of PVP, 60 mg of L-ascorbic acid and 60 mg of citric acid were dissolved in 8 mL of DI water and heated up to 80 °C in a stirred three-neck flask placed inside an oil bath. A volume of 3 mL of the palladium precursor

---

[5] The nanoparticle syntheses were performed by Dr Luca Panariello and Daniel Biri.

solution was injected in the heated solution and stirred for 3 h, after which the solution was removed and cooled at room temperature in open air.

- Pd-Pt dendrites: The recipe followed is that reported by Lim *et al.* [230]. Pd octahedra were prepared as described in the section above. An amount of 1 mL of this solution was added to 6 mL of DI water, in which 35 mg of PVP and 60 mg of L-ascorbic acid were dissolved. This solution was injected in a three-neck flask placed in an oil bath and heated up to 90 °C while stirring. In parallel, 27 mg of K_2PtCl_4 were dissolved in 3 mL of DI water and injected in the heated solution containing the palladium octahedric nanoparticles, PVP and ascorbic acid. After 3 h, the solution was removed and cooled at room temperature in open air.

After each synthesis, the colloidal solutions were individually poured into a dialysis membrane (MW cut-off: 12-14 kDa, Medicell Membranes Ltd) and dipped in a DI water bath for 24 h, in order to remove unreacted precursors and excess of reducing agent.

4.2.2. Membrane modification and nanoparticle adsorption

The inner surface of the tubular Teflon AF-2400 membrane (ID: 0.8 mm, OD: 1.0 mm, length: 30 cm, Biogeneral US) was modified by flowing polymeric solutions using plastic syringes (20 mL, HSW) driven by a syringe pump (Harvard Apparatus, Ph.D. Ultra). The first modification was performed with PDA, following the procedure of the group of Messersmith [232, 233]. An amount of 16 mg of dopamine hydrochloride (Sigma-Aldrich) was dissolved in 8 mL Tris-HCl buffer solution at a pH of 8.5 (0.010 M, 2BScientific). The resulting solution was pumped inside 30 cm of the tubular membrane under a constant flowrate of 17 µL/min for 8 h so to allow gradual adsorption of the PDA on the membrane surface. Once the solution was pumped, the buffer solution was flowed for 1 hour at 20 µL/min, to provide further functionality. The membrane was then dried in an oven (Lenton) at 60 °C overnight. For the adsorption of the two other polyelectrolytic solutions, the recipe adopted by Dotzauer *et al.* and Liu *et al.* was followed [228, 234]. The anionic solution of poly(acrylic acid) (PAA, Sigma-Aldrich) was prepared by mixing 0.67 mL of polymer with 3.33 mL of DI water and 117 mg of NaCl. The pH was increased

to 3 by adding 2 M NaOH in DI water droplets. The resulting solution was pumped at a flowrate of 20 µL/min for 2 h through the PDA-modified membrane, and subsequently with DI water at 40 µL/min for 1 hour. Before the third modification, the membrane was placed in the oven at 60 °C for 2 h. The cationic solution of poly(allylamine hydrochloride) (PAH, Sigma-Aldrich) was prepared by dissolving 700 mg of the polymer in 2 mL DI water and 58 mg NaCl. Stirring of the solution was performed to achieve a clear solution and the pH was adjusted to 6.5 by addition of 2 M NaOH aqueous solution droplets. The resulting solution was pumped at 20 µL/min for 2 h inside the modified membrane, after which DI water was flowed at 40 µL/min for 2 h, followed by drying in the oven at 60 °C for 2 h.

Nanoparticle solutions were pumped through the LbL-modified Teflon AF-2400 membrane at 10 µL/min for 12 h to achieve a catalytic layer of adsorbed nanoparticles. Figure 4.1 summarises the steps followed in the preparation of the catalytic membrane reactor.

1. Polydopamine coating 2. Polyanion adsorption 3.Polycation adsorption 4. Nanoparticle adsorption
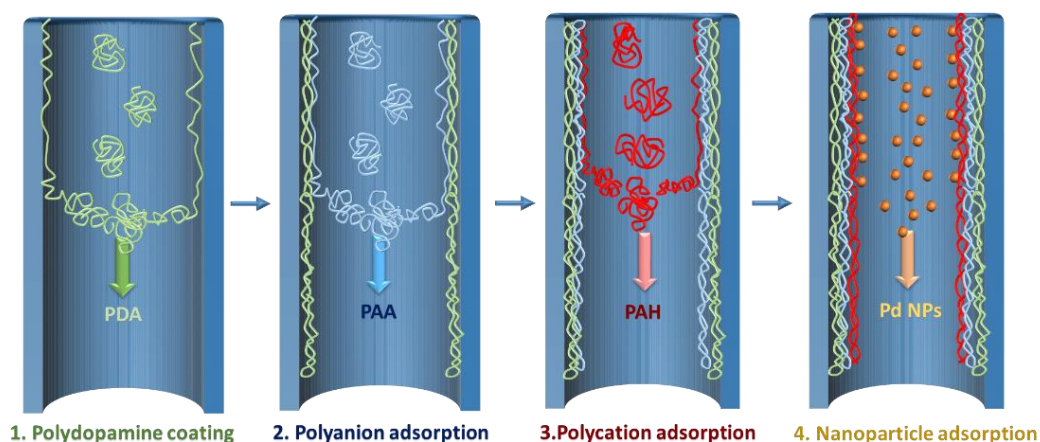
Figure 4.1. Schematics of the PDA/PAA/PAH layer-by-layer modification steps on the internal surface of a Teflon AF-2400 tubular membrane followed by nanoparticle adsorption.

4.2.3. Materials characterisation

After their synthesis, the nanoparticles were characterised using transmission electron microscopy (TEM, JEOL 2100 EXii, 120 kV acceleration voltage) to investigate their morphology and average particle size. The inner surface of the membranes before and after the LbL modification and before reaction was

examined using atomic force microscopy (AFM, Bruker Dimension Icon). This was used in Peak Force Tapping Mode at 2 kHz Peak Force Frequency and 0.5 - 1 Hz line rate at 256 scans per line resolution. Post-processing of the microscopy pictures was performed by a second degree polynomial flattening. A surface elemental composition of the membrane was conducted using X-ray photoelectron spectroscopy (XPS, Al source 1486.6 eV, Thermo Scientific K-alpha), with data calibrated to 285 eV of C 1s spectra. The metal loading of the catalytic membranes was quantified before and after reaction using inductively coupled plasma mass spectroscopy (ICP-MS, Varian 820). To perform this characterisation, the catalytic membranes were cut into pieces and treated with aqua regia (3 volumes HCl, 1 volume HNO_3). The leachate was then used for analysis.

4.2.4. Nitrobenzene hydrogenation

Scheme 4.1 shows the generally accepted Haber's reaction mechanism [235, 236]. There are two relevant reaction pathways: The first is the direct three-step reduction of the nitro group into the nitroso, hydroxylamine and amine group. The second pathway involves a condensation reaction of nitrosobenzene and N-phenylhydroxylamine to produce azoxybenzene, which can be further reduced into aniline in a two-step hydrogenation involving the consecutive production of azobenzene and hydrazobenzene. However, the mechanism for nitrobenzene hydrogenation still represents a topic of research and a clear reaction mechanism has not been established yet [235, 237].
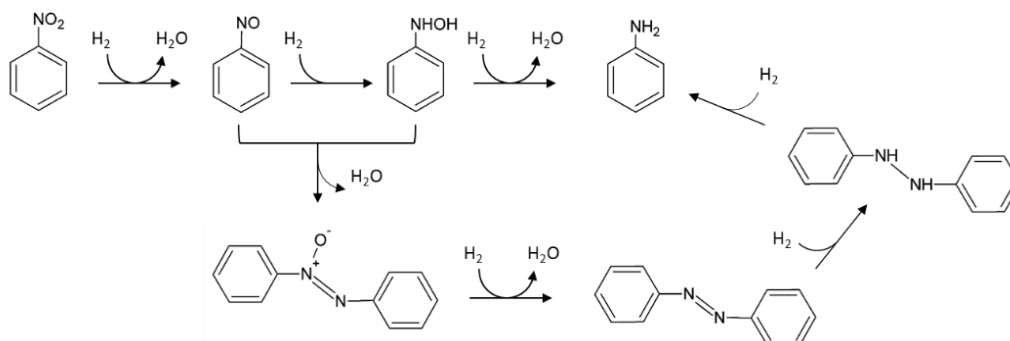
Scheme 4.1. Reaction pathways for the reduction of nitrobenzene into aniline.

4.2.5. Reactor design and operation

The catalytic membranes were cut to 20 cm corresponding to a membrane inner surface area of 5 cm^2 and were inserted inside a 15 cm long polytetrafluoroethylene (PTFE) tube (ID: 0.063'', OD: 1/8'', Thames Restek UK). The tube-in-tube system was sealed with two T-junctions (Upchurch) connected at the two ends of the tubular membrane using two polyether ether ketone (PEEK) nuts (1/4-28 UNF, Upchurch). Hydrogen from the generator (PH200, Peak Scientific) was pressurised and kept stagnant outside the membrane and inside the outer PTFE tube, with the gas outlet sealed at the second T-junction.

Nitrobenzene at a concentration ranging between 30 and 100 mM in ethanol (both purchased from Sigma-Aldrich) was pumped inside the tube-in-tube catalytic membrane at a constant flowrate of 15 µL/min (*ca.* 5 min average liquid residence time) using an 8 mL stainless-steel syringe driven by a syringe pump (Harvard Apparatus, Ph.D. Ultra). The liquid pressure was measured at the outlet of the tube-in-tube membrane reactor using a pressure sensor (Omega). Connected to the outlet, a back-pressure regulator (Zaiput, BPR-01) ensured the desired pressure upstream, which was held at 1 bar higher than the gas one to prevent the formation of gas bubbles. In this way, during reaction, pressurised hydrogen could diffuse through the membrane and through the liquid to reach the catalytic nanoparticles adsorbed on the inner surface and react with nitrobenzene.

Figure 4.2 is a schematic of the experimental setup. To ensure a constant temperature, the tube-in-tube membrane reactor was kept inside a temperature bath filled with water at 30 °C and placed on a hotplate (Stuart US152).
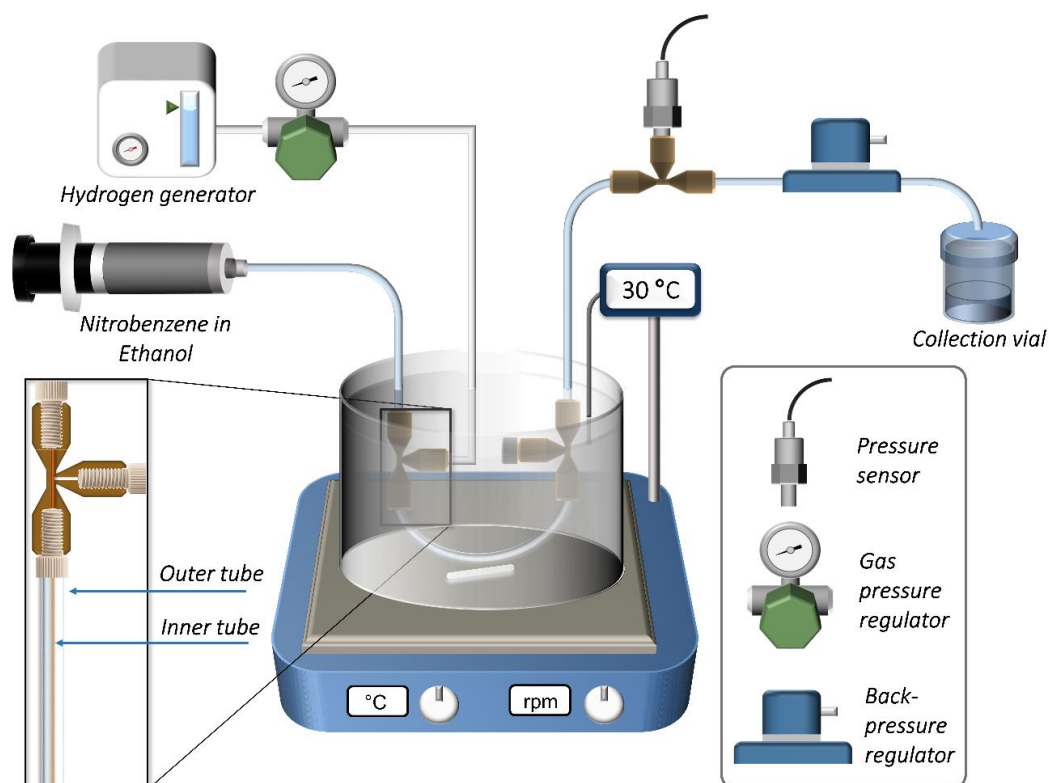
Figure 4.2. Setup schematic of the tube-in-tube LbL-modified Teflon AF-2400 membrane reactor with adsorbed Pd-based nanoparticles for the nitrobenzene hydrogenation in flow.

The liquid outlet from the membrane reactor was analysed using a gas chromatograph (7820A, Agilent Technologies), a flame ionisation detector with a HP-INNOWAX (19091-133) capillary column and a liquid auto-sampler. Two main products were detected, aniline and nitrosobenzene, and the nitrogen balance was calculated from the inlet and outlet compositions, ranging between 98% and 102% for all the reactions.

Product selectivity, S_i, is calculated using Equation (4.1), where $C_{i,out}$ is the final/outlet concentration of the reaction product i and v_i is the number of moles of substrate needed to produce one mole of product i.

$$S_i = \frac{v_i \, C_{i,out}}{X \, C_{r,in}} \tag{4.1}$$

The performance of the catalyst was quantified using the average turnover frequency, defined in Equation (3.2), in which the molar amount of metal was the amount of palladium, while in the case of Pd-Pt nanoparticles, this was the

overall amount of palladium and platinum moles. The turnover frequency relative to the surface atoms, TOF_p, was calculated using Equation (4.2), where α_p is the ratio between the number of bulk atoms below the first external layer of metal atoms and the total number of atoms in the nanoparticles (see Appendix B).

$$TOF_p = \frac{TOF}{1 - \alpha_p} \tag{4.2}$$

4.3. Results and discussion

4.3.1. TEM characterisation of nanoparticles[6]

Figure 4.3 shows the TEM micrographs with the corresponding particle size distribution histograms of the palladium-based nanoparticles. Table 4.1 reports the average nanoparticle sizes with their standard deviations, obtained by analysing at least 120 particles per sample using Pebbles [238].
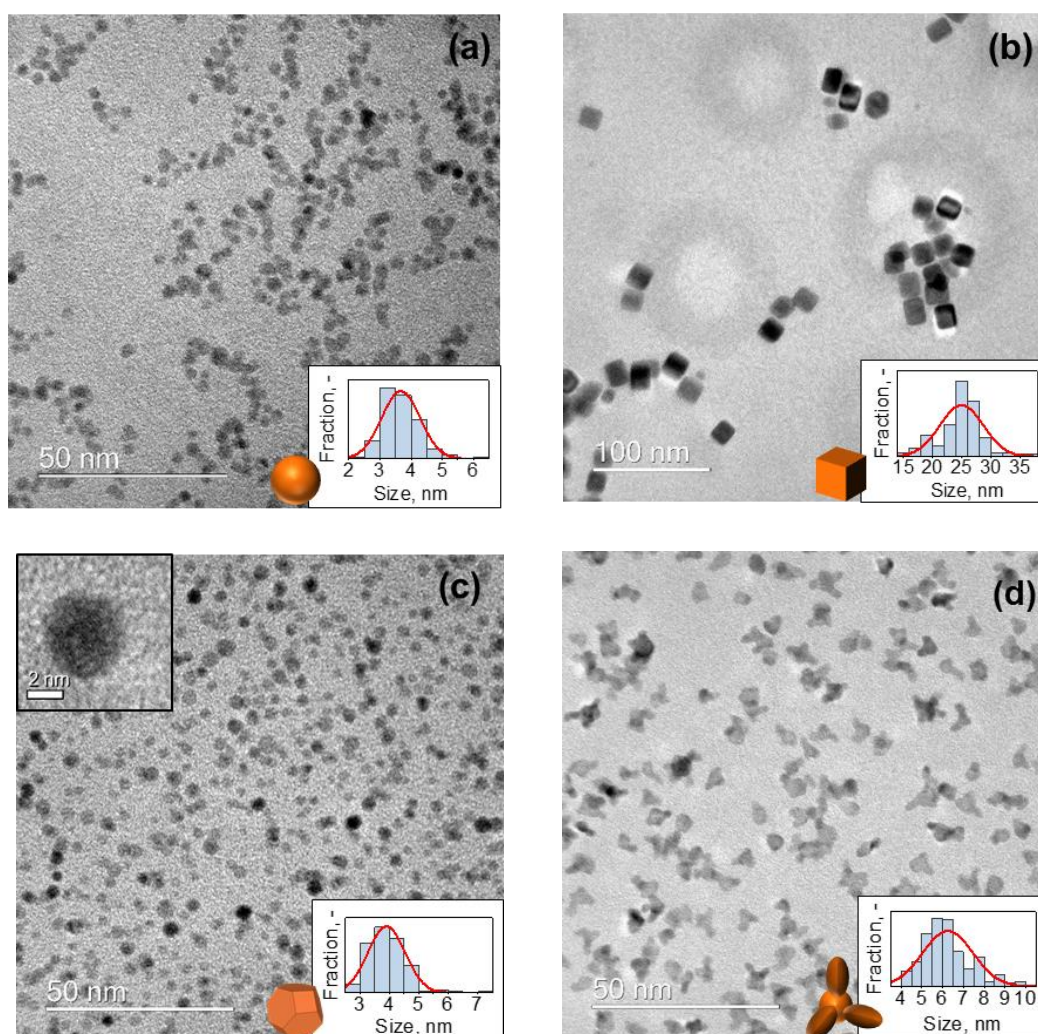
Figure 4.3. TEM micrographs of the (a) Pd spherical, (b) Pd cubical, (c) Pd truncated octahedral and (d) Pt-Pd dendritic nanoparticles.

---

[6] TEM analyses were performed by Dr Spyridon Damilos at the Department of Chemistry at UCL.

Table 4.1. Average particle size, d_p, and standard deviation, σ_p, of the palladium-based nanoparticles.

Nanoparticles	d_p, nm	σ_p, nm
Pd spheres	3.7	0.6
Pd truncated octahedra	3.9	0.6
Pd cubes	24.9	3.7
Pt-Pd dendrites	6.2	1.2

4.3.2. Atomic force microscopy analysis of membranes[7]

Figure 4.4 shows the atomic force micrographs of the unmodified and LbL-modified membrane. The bare Teflon AF-2400 membrane inner surface presents a smooth surface with a maximum surface elevation of 10 nm. As it is possible to observe for the LbL-modified surface sample, the modification produced a rougher surface with bulges of 100 nm diameter and approx. 25 nm elevation, which increased the available surface area for nanoparticle adsorption. Figure 4.5 shows the atomic force micrographs relative to the LbL-modified surfaces with adsorbed nanoparticles. Singularly resolved nanoparticles and features in the range of 10 nm were visible in the sample containing spherical nanoparticles. This is also characterised by scattered bulges, possibly deriving from the polyelectrolyte assembly. The sample containing the truncated octahedral nanoparticles presented homogeneously adsorbed nanoparticles and it is possible to observe that some bulges created by the LbL modification enabled the enlargement of the available surface area for nanoparticle adsorption. In the case of the Pd-Pt nanoparticles, it is possible to observe clusters of nanoparticles in the 40 nm size, while Pd cubes (*ca.* 25 nm) were singularly resolved by AFM and some were found incorporated in the polymeric support.

---

[7] AFM analyses were performed by Dr Richard Thorogate at the London Centre for Nanotechnology.
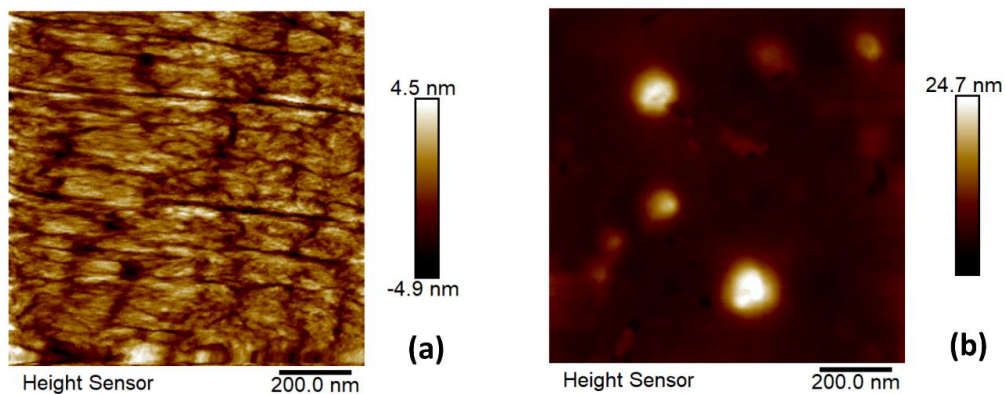
Figure 4.4. Atomic force micrographs of the (a) bare Teflon AF-2400 membrane and the (b) LbL-modified PDA/PAA/PAH membrane surface.
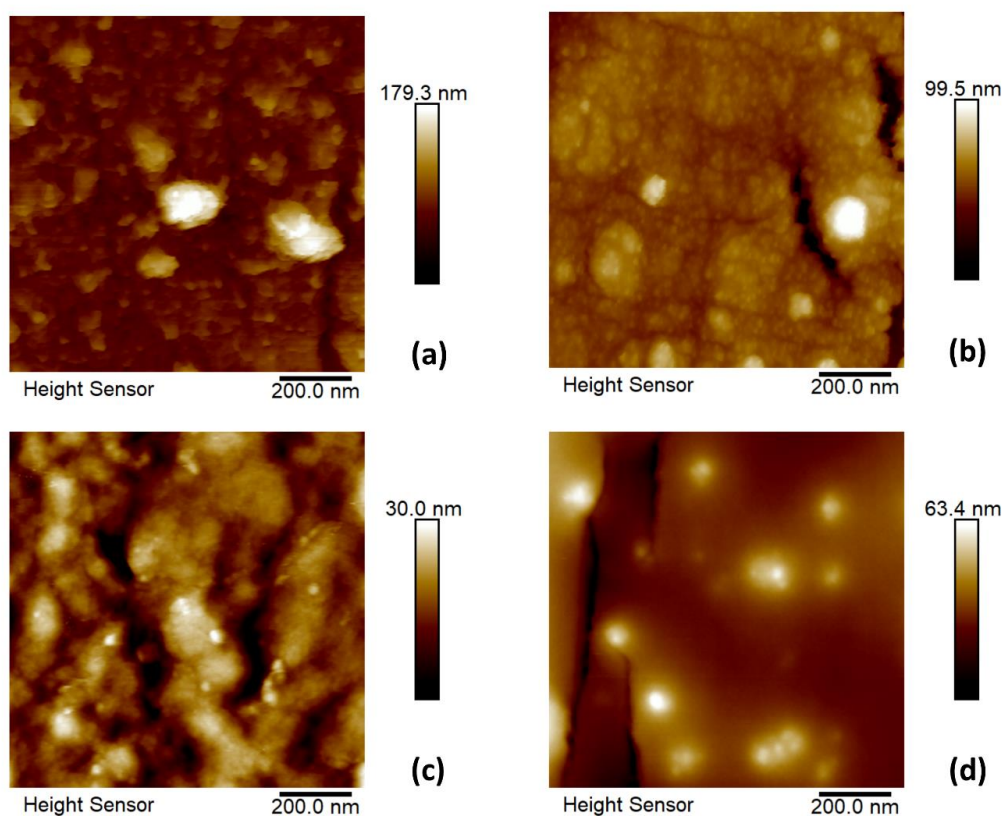
Figure 4.5. Atomic force micrographs of the LbL-modified PDA/PAA/PAH tubular Teflon AF-2400 membrane internal surface after the adsorption of (a) Pd spherical, (b) Pd truncated octahedral, (c) Pd cubical and (d) Pd-Pt dendritic nanoparticles.

4.3.3. X-ray photoelectron spectroscopy analysis[8]

Figure 4.6 shows the survey scans performed using XPS. At binding energies below 835 eV, it is possible to recognise the peaks relative to all the constituent elements of the membrane (C, F) and atomic oxygen from the layer-by-layer modification. Pd 3p and 3d were detected for all the samples and Pt 4d and 4f on the surface of the sample containing Pt-Pd nanodendrites. Figure 4.7 shows the high resolution overlay spectra around the Pd 3d region. The peaks relative to the spheres, truncated octahedra and dendrites are shifted to *ca.* 0.3 eV higher energy with respect to the cubes. These exhibited a main peak at 335.0 eV in the Pd $3d_{5/2}$ region relative to palladium metal, suggesting that the cubical nanoparticles displayed a lower degree of oxidation compared to the other Pd-based nanoparticles.
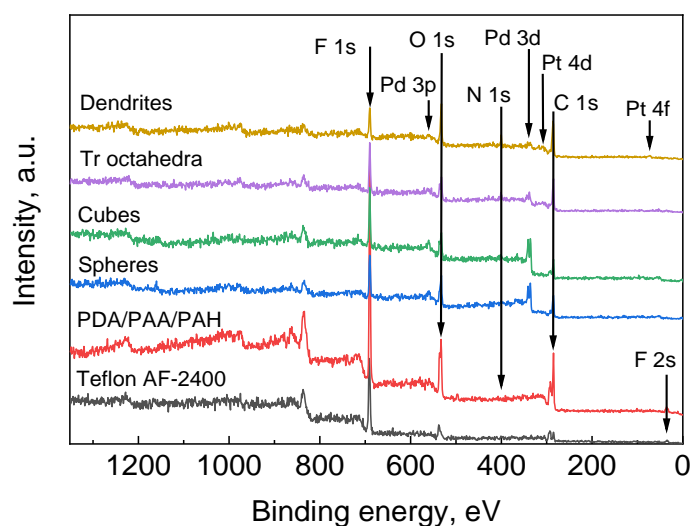
Figure 4.6. X-ray photoelectron spectra for the pristine Teflon AF-2400 membrane, the PDA/PAA/PAH LbL-modified surface and the surface with adsorbed Pd spherical, Pd cubical, Pd truncated octahedral and Pt-Pd dendritic nanoparticles.

---

[8] The XPS analysis was performed with the help of Juhun Shin at the Department of Chemistry at UCL.
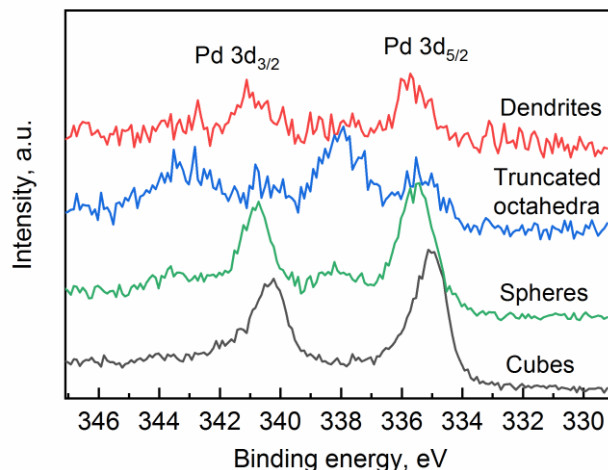
Figure 4.7. X-ray photoelectron spectra of the Pd 3d region for the spherical, truncated octahedral, cubical and dendritic Pd-based nanoparticles.

4.3.4. Hydrogenation of nitrobenzene in flow

4.3.4.1. Effect of the substrate concentration

Figure 4.8 reports conversion and product selectivity for two nitrobenzene inlet concentrations: 30 mM and 100 mM, in the reactor with adsorbed Pd spheres.
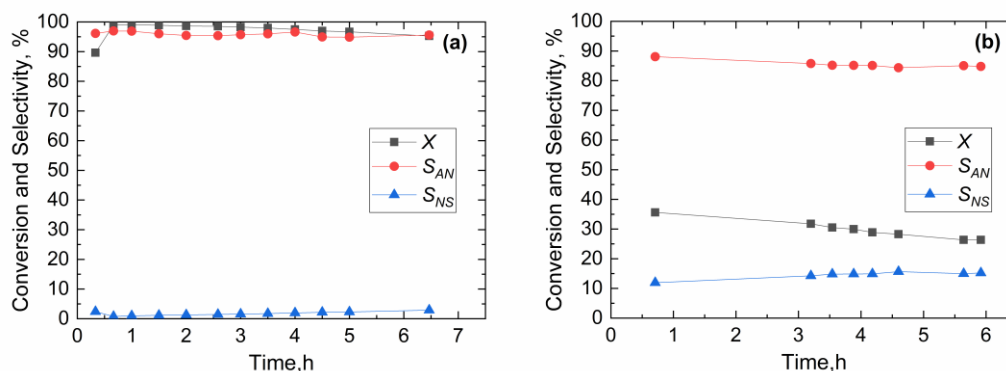
Figure 4.8. Nitrobenzene conversion, X, aniline selectivity, S_{AN} and nitrosobenzene selectivity, S_{NS}, in the hydrogenation of nitrobenzene on Pd spheres as a function of the nitrobenzene inlet concentration. Nitrobenzene inlet concentration: (a) 30 mM and (b) 100 mM. Liquid flowrate: 15 µL/min, liquid pressure: 6 bar, hydrogen pressure: 5 bar, temperature: 30 °C.

Using the lower inlet concentration, conversion of nitrobenzene and selectivity to aniline were between 95% and 100%. However, when using almost 3-fold

115

higher inlet concentration (100 mM), conversion dropped to 36%, which decreased to 26% after 5 h of continuous reaction. The selectivity to aniline ranged between 85% and 88% and that to nitrosobenzene gradually increased up to 15% in the last hours of reaction. This can be explained by the fact that at a higher inlet concentration, the nitrosobenzene produced in the first reaction step could not be hydrogenated into aniline under a lower catalyst contact time. However, when using a lower nitrobenzene concentration, nitrosobenzene could be further reduced to aniline. The hydrogen flowrate necessary to achieve 100% nitrobenzene conversion to aniline under a flowrate of 15 µL/min and an inlet concentration of 100 mM, would be 0.1 mL/min. This is *ca.* twenty times lower than the 1.9 mL/min hydrogen supply rate that the membrane can deliver at 5 bar pressure (see Appendix B), suggesting that there was no limitation of hydrogen supply during reaction.

4.3.4.2. Catalytic performance comparison

Figure 4.9 shows the results of conversion and product selectivity for the four nanoparticle types adsorbed in the LbL-modified reactors, using 100 mM inlet concentration, 30 °C reaction temperature and 5 bar hydrogen pressure.

The Pd cubes achieved a 96% conversion in the first hour, which gradually dropped to 54% in 6.5 h of reaction, with nitrosobenzene selectivity increasing from 5% to 12% and aniline selectivity decreasing from 95% to 88%. A lower (7 - 8%) but steady conversion was achieved by the Pd truncated octahedra, with an aniline selectivity of 75% and a selectivity to nitrosobenzene of *ca.* 25%. A much lower aniline (60%) and higher nitrosobenzene selectivity (40%), with a higher conversion (19-36%), was obtained by the Pd-Pt dendritic nanoparticles which reached a stable conversion of about 19% for the last 4 h of operation. A similar nitrosobenzene selectivity was reported in the work of Kataoka *et al.* using platinum nanoparticles immobilised in a coated capillary microreactor [236]. The authors used an inlet concentration of nitrobenzene of 50 mM, a liquid flowrate of 10 µL/min and a hydrogen flowrate of 100 µL/min.
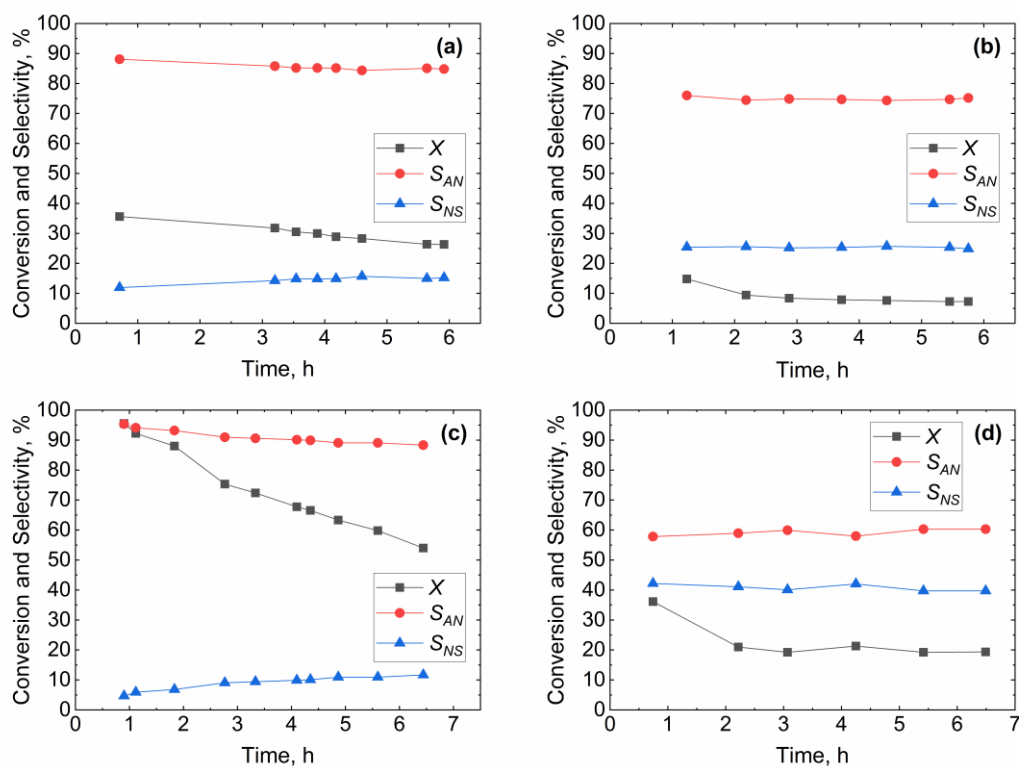
Figure 4.9. Nitrobenzene conversion, X, aniline selectivity, S_{AN} and nitrosobenzene selectivity, S_{NS}, in the hydrogenation of nitrobenzene for different nanoparticle systems. Reactions were carried out using (a) Pd spheres, (b) Pd truncated octahedra, (c) Pd cubes and (d) Pt-Pd dendrites. Nitrobenzene inlet concentration: 100 mM, liquid flowrate: 15 μL/min, liquid pressure: 6 bar, hydrogen pressure: 5 bar, temperature: 30 °C.

Elemental analysis of platinum and palladium metal loadings of each catalytic membrane was performed before and after reaction using ICP-MS and the results are reported in Table 4.2. As it is possible to observe, the metal loading ranged between 0.12 and 12.18 μg per each cm^2 of membrane inner surface. The catalytic membrane hosting Pd spheres had an initial metal loading of 1.09 μg/cm^2 and an initial nitrobenzene *TOF* of 629 h^{-1}. However, after 6 h of continuous reaction the metal loading dropped to 0.96 μg/cm^2 corresponding to a drop of 12% of the initial loading. Since nitrobenzene conversion dropped by 28%, the deactivation cannot be only explained as an effect of the catalyst leaching, but as a possible consequence of poisoning or particle restructuring.

Table 4.2. Palladium and platinum metal loading per internal membrane surface, nitrobenzene conversion, X, average turnover frequency, TOF, and turnover frequency based on surface atoms, TOF_p, at the start and at the end of the nitrobenzene hydrogenation for the different adsorbed nanoparticles.

Nanoparticle	Metal loading on the membrane, µg/cm^2		X, %		TOF, h^{-1}		TOF_p [a], h^{-1}	
	Start	End	Start	End	Start	End	Start	End
Pd spheres	1.09	0.96	36	26	629	515	1628	1332
Pd truncated octahedra	0.56	0.53	15	7	538	239	1457	647
Pd cubes	12.18	4.08	96	54	150	252	2293	3854
Pt-Pd dendrites (Pt)	3.38	2.37	36	19	341	257	1414	1067
Pt-Pd dendrites (Pd)	0.17	0.12	36	19				

[a] Calculated with respect to the surface atoms (see Appendix B).

The reactor hosting Pd truncated octahedra had half the initial catalyst loading (0.56 µg/cm^2) compared to the Pd spheres, but it achieved a similar *TOF* of 538 h^{-1}, possibly due to their smaller size. Furthermore, unlike the spherical nanoparticles, Pd truncated octahedra did not show leaching and their deactivation can be attributed to other effects.

The Pd-Pt dendrites displayed a *TOF* of approx. 340 h^{-1} which decreased to approximately 260 h^{-1} at the end of the reaction time. After reaction, a leaching of 29% from the initial platinum loading of 3.38 µg/cm^2 was detected, corresponding to a similar drop in palladium, which might represent a possible cause for the conversion relative decrease (-47%). However, considering the surface reaction of the nanoparticle atoms (see Appendix B), the calculated initial average turnover frequency (*TOF*) for the Pd-Pt dendrites was about 1414 h^{-1}, similar in magnitude with that of the Pd spheres (1628 h^{-1}) and truncated octahedra (1457 h^{-1}).

Batch hydrogenations of nitrobenzene reported in previous studies show similar results of nitrobenzene hydrogenation rates. Huang *et al.* reported a nitrobenzene average turnover frequency of 245 h^{-1} after 2 h reaction time using 2.6 nm Pd nanoparticles stabilised by P123 micelles in water at 45 °C and 30 bar [239]. A reaction rate of 126 h^{-1} was reported after 180 min by Harraz *et al.* using 4 nm Pd nanoparticles at room temperature and 1 bar pressure [240].

The turnover frequency analysis of the nanoparticles revealed that the Pd cubes had the highest calculated surface activity (*TOF$_p$*) of *ca.* 3000 h^{-1}, which was approximately two times higher than that of the other nanoparticles. However, the reactor hosting the palladium cubes showed a conversion drop of 44%, possibly attributable to the 66% loss of material with respect to the initial loading of 12.18 µg/cm^2. The metal loading achieved with the Pd cubes was 12-times higher than that achieved with the Pd spheres, while the ratio between the volume of a cube having a height of 25 nm and a sphere with a diameter of 4 cm is about 244. This indicates that a lower number of cubes were adsorbed on the membrane with respect to the Pd spheres. However, to explain their highest *TOF$_p$*, XPS results need to be brought back to the discussion. The cubes' lower degree of oxidation, compared to the other nanoparticles, as evidenced by the 0.3 eV shift of the Pd 3d peaks to lower

energies, might be the reason why they showed the highest TOF_p. In fact, palladium metal is known to be able to dissociate and provide surface-reactive hydrogen [241, 242]. The large particle size of the Pd cubes and their resulting lower dispersion might have also contributed to the highest TOF_p. In a work by Carturan *et al.* it is shown that large palladium particles favoured hydrogen dissociation and reduction of the catalytic surface which was oxidised by the adsorption of nitrobenzene [243].

The use of palladium nanoparticles supported in a modified tubular membrane is a suitable solution to overcome the internal mass transfer resistances that can be found in packed-bed reactors, as demonstrated in a work conducted in Prof Gavriilidis' group, in which Au-Pd/TiO_2 catalyst was packed in an identical Teflon AF-2400 tubular membrane for the aerobic oxidation of benzyl alcohol [185]. Examples of flow reactors with immobilised Pd nanoparticles for the nitrobenzene hydrogenation can be found in the work of Liu *et al.* [244]. In that study, PDA was used to modify the external surface of a polypropylene hollow fibre membrane, for the sequential adsorption of poly(sodium 4-styrenesulfonate) and PAH. Palladium nanoparticles were synthesised on the modified surface after adsorption and reduction of the palladium precursor, achieving an initial catalyst loading of *ca.* 57 µg. Assembled in a tube-in-tube configuration, similarly to this work, the reactor was pressurised with hydrogen inside the tubular membrane and a conversion of 100% was achieved before deactivation, at 10 µL/min and 30 mM inlet concentration. The *TOF* was 35 h^{-1}, which is much lower than that achieved by the spherical nanoparticles of this work, owing possibly to the larger size of Pd nanoparticles (100 nm) achieved by the researchers.

Using a flat PDMS membrane as support for 5.5 wt% Pd/γ-Al_2O_3 catalyst, Liu *et al.* performed the nitrobenzene hydrogenation with an inlet flowrate of 10 µL/min and hydrogen flowing on the other side of the membrane [245]. Results showed that 52% conversion was achieved with 110 mM nitrobenzene inlet concentration and 1.9 mg of coated catalyst. The catalyst layer depth was *ca.* 1 µm and could possibly decrease the catalyst availability and generate non-negligible internal mass transfer resistances.

4.4. Summary and conclusions

Layer-by-layer adsorption of polyelectrolytes was performed on the inner surface of a Teflon AF-2400 tubular membrane for the deposition of *ex situ* synthesised palladium-based nanoparticles with different shapes and size. The catalytic membrane was assembled inside a PTFE tube in a tube-in-tube configuration and tested for the hydrogenation of nitrobenzene to aniline in flow. Atomic force microscopy showed adsorbed nanoparticles on the modified inner surface of the membrane along with a wavy morphology that increased the available surface area for nanoparticle adsorption. X-ray photoelectron spectroscopy revealed a 0.3 eV shift to low energies for the palladium cubes which might be indicative of a lower oxidation state compared to the other nanoparticles.

Results from the continuous nitrobenzene hydrogenation showed that the 4 nm Pd spheres exhibited a stable conversion close to 100% for 6 h of continuous operation, using 30 mM of substrate inlet concentration. However, when the inlet concentration was increased to 100 mM deactivation was observed. A comparative study of the different nanoparticles during nitrobenzene hydrogenation showed that the highest *TOF* of 600 h^{-1} was achieved by the Pd spheres, possibly due to their small size. However, if the reactivity by the number of surface atoms is normalised, the highest turnover frequency per surface atoms was obtained by the Pd cubes ($\sim$3000 h^{-1}). One of the possible causes can be their lower oxidation state compared to the other nanoparticles. Nevertheless, the cubes also exhibited the highest leaching rate during operation, while almost no losses were detected for the Pd truncated octahedra.

These results show that the LbL-modified tube-in-tube Teflon AF-2400 membrane reactor with adsorbed Pd nanoparticles can be implemented as a platform for gas-liquid reactions. The catalytic membrane reactor allowed operation at high liquid pressures without forming gas bubbles in the liquid and provided improved process safety due to the small volume of pressurised gas.

Chapter V. Slurry loop tubular membrane reactor for the catalysed aerobic oxidation of benzyl alcohol
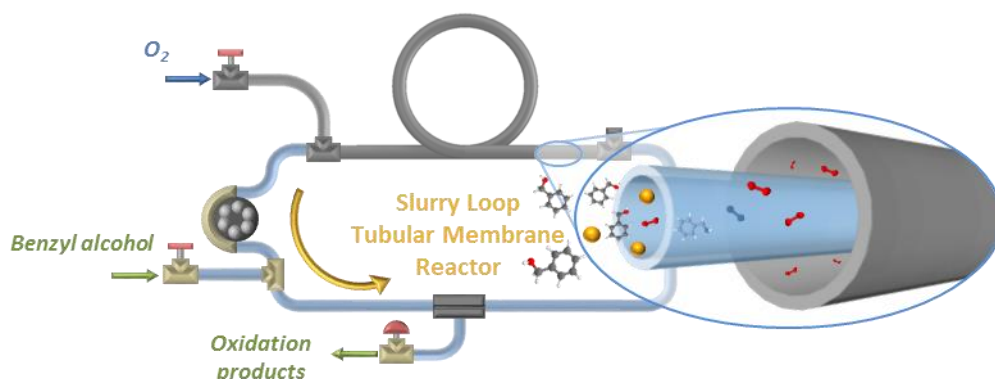
A novel reactor that combines the use of a catalyst slurry flowing in a loop, and a tubular Teflon AF-2400 membrane for oxygen delivery was demonstrated in the aerobic oxidation of benzyl alcohol using a 1 wt% Au-Pd/TiO$_2$ powder catalyst. Process safety was guaranteed by using a membrane that separated the organic slurry phase from the oxygen, while controlling the oxygen dosing by means of the transmembrane differential pressure. Owing to the presence of a crossflow filter, the reactor could either operate in batch or continuous mode. Similar *TOF* (20000 - 25000 h^{-1}) with comparable benzaldehyde selectivity were achieved by the reactor operated in batch mode compared to that from a conventional autoclave. Using a 60 cm long tubular membrane, with the slurry circulating at 10 mL/min, continuous oxidations were performed at 100 - 120 °C, 0 - 5 bar oxygen pressure and 1.2 - 5.0 g/L catalyst loading. The slurry loop tubular membrane reactor showed significantly higher *TOF* than that of a packed-bed membrane microchannel reactor using the same catalyst, and similar performance to that of a trickle-bed capillary reactor.

5.1. Introduction

The use of a suspension of fine catalyst particles in a liquid medium offers more advantages with respect to packed-bed catalysts [246]. Continuous slurry reactors for bulk chemical production are well established and can be found in hydrogenation processes or in petrochemical industries [3, 81, 246-248]. The advantages of using slurry reactors over fixed beds include the enhanced catalyst efficiency, owing to smaller catalyst particles, improved degree of mixing and temperature homogenisation [2, 246, 247]. An example of a reaction carried out using a slurry reactor is the isophorone hydrogenation to trimethyl cyclohexanone in a tubular slurry reactor, where reaction rates were found to be seven times higher than those achieved from an autoclave [249]. Another example includes the work of Sanofi-Aventis on a gas-liquid-solid slurry hydrogenation of a pharmaceutical molecule using the Corning Advanced Flow reactor [62]. Results showed a similar performance to batch and 0.43 kg/h of product could be continuously produced.

Despite their improved performance, slurry reactors suffer from scalability issues and difficult handling of catalyst particles in motion, along with product filtration [246, 247]. In some applications, such as in photocatalytic processes [250-252], submerged membranes were placed inside the continuously stirred slurry mixture and used as filters for the continuous withdrawal of pure liquid. However, slurry solid-liquid mixtures with particles smaller than 10 µm are usually difficult to separate with conventional methods. The use of polymeric microfiltration membranes in the dead-end configuration usually works but the performance diminishes as the membrane experiences progressive fouling [253]. There are different techniques by which fouling can be hindered and these include the use of turbulence promoters (*e.g.* modification of the filter geometry), backwashes with gas or liquid permeates, use of impellers with blades close to the filter, or appropriate filtration modes, such as the crossflow filtration [254, 255].

In this chapter, a continuous reactor that uses a catalyst slurry flowing inside a loop with a tubular membrane Teflon AF-2400 as oxygen saturator was developed and presented. The reactor was demonstrated in the solvent-free aerobic oxidation of benzyl alcohol, and a crossflow filter was designed and

connected to the loop to ensure a continuous filtration of the slurry, while retaining the catalyst within the loop.

5.1.1. The reaction: Benzyl alcohol oxidation

A variety of reactions are involved in the oxidation of benzyl alcohol [256]: The oxidation of benzaldehyde to form benzoic acid and benzyl benzoate, the disproportionation of benzyl alcohol to form benzaldehyde, toluene and water, the dehydration to produce dibenzyl ether and the self-condensation to generate anthracene and stilbene [46, 256, 257]. Disregarding the generation of secondary by-products, which are produced in small quantities, benzyl alcohol aerobic oxidation can be described by two macroscopic reactions: the direct oxidation (O) and the disproportionation (D) reaction, shown in Scheme 5.1 [258]. These two reactions are the products of three reaction steps that have been proposed in a microkinetic model of benzyl alcohol oxidation by Galvanin *et al.*: the dehydrogenation (DH) and the hydrogenolysis (HL) of benzyl alcohol to produce benzaldehyde and the disproportionation (DP) reaction, mentioned before [259, 260].
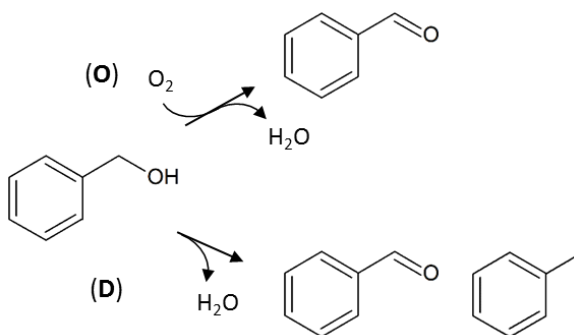
Scheme 5.1. Simplified benzyl alcohol oxidation reaction scheme.

5.2. Materials and methods

5.2.1. Reactor design and operation

The slurry loop tubular membrane (SLTM) reactor is a tubular reactor connected in a loop configuration. Inside the loop, a tube-in-tube membrane saturator provides the reactive gas. This is made of an external stainless steel tube (Swagelok, OD: 1/8'', tube wall: 0.035'') containing a tubular Teflon AF-2400 gas-permeable membrane (ID: 0.8 mm, OD: 1.0 mm, length: 60 cm, Biogeneral). The loop was connected to a recirculation peristaltic pump that continuously pumped a solid-liquid mixture made of the catalyst, the substrate and the reaction products at 10 mL/min. Figure 5.1 shows the schematic of the experimental setup.
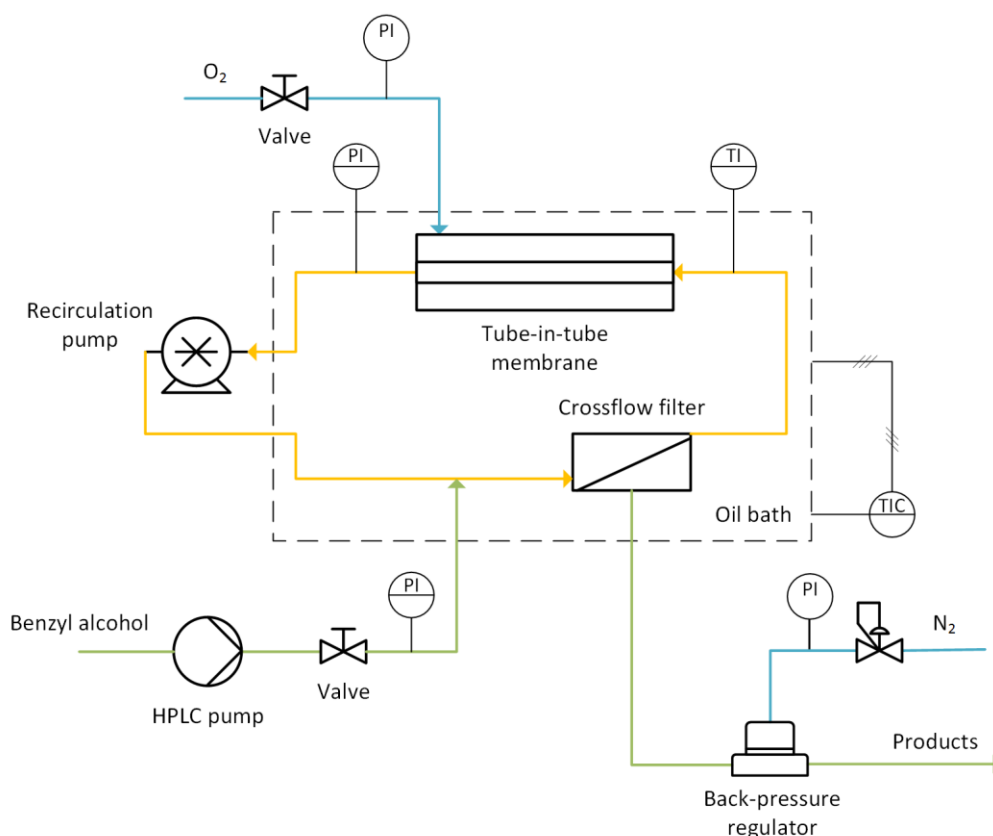
Figure 5.1. Setup schematic of the slurry tubular membrane reactor for the continuous catalytic aerobic oxidation of benzyl alcohol. PI: pressure indicator, TI: temperature indicator, TIC: temperature indicator and controller.

Pure oxygen (BOC, N5.5 grade) was pressurised and kept stagnant in the outer tube, permeated during reaction through the membrane and diffused

inside the slurry mixture flowing in the loop. A liquid inlet was connected to a T-junction in the loop, in order to provide fresh benzyl alcohol (99.0%, Sigma-Aldrich) by means of an HPLC pump (Knauer P2.1S, Germany). The liquid outlet was continuously withdrawn from a stainless crossflow filter (0.1 µm 316L, Mott), whose design details are presented in Appendix C. This was connected in the loop to the tubular membrane saturator and an outlet tube from the back of the filter was connected to a backpressure regulator (BPR-01, Zaiput) which kept a constant desired liquid pressure inside the loop. Pressure was measured using two pressure sensors (PX309, Omega), one at the reactor inlet and the other in the loop. The slurry pressure was always kept below 6 bar, since it was the maximum operating pressure of the recirculation pump. The pressure of oxygen was held at 1 bar lower than that of the slurry, to avoid its breakthrough into the slurry mixture during reaction.

To operate at high temperatures the whole loop reactor was immersed in a temperature bath (diameter: 230 mm, Boro 3.3, VWR International) containing a heat transfer fluid (Paratherm, NF) which was placed on top of a hotplate (US152, Stuart). The external temperature was monitored with a thermocouple dipped in the bath and connected to the hotplate, while an internal thermocouple was measuring the slurry temperature inside the loop at the inlet of the tube-in-tube membrane saturator. Since the recirculation pump was placed outside the temperature bath, complete isothermal conditions could not be fully guaranteed. However, simulations on the temperature profile of the loop reactor were performed using COMSOL Multiphysics® 5.3. Results demonstrated that, during reaction, the average temperature of the slurry in the loop was approximately 3 °C lower than the bath temperature (see Appendix D). For this reason, the reported temperature value in the experiments refers to the measured loop temperature at the inlet of the tube-in-tube contactor.

5.2.2. Macromixing study

Macromixing in the SLTM reactor was studied by performing a step injection of a tracer and studying its residence time distribution (RTD) (see Appendix E). The recirculation flowrate was set to 10 mL/min and the inlet to 0.025

mL/min, corresponding to a recycle-to-inlet flowrate ratio (recirculation ratio) of 400, similar to that used during reaction.

Equation (5.1) shows the convolution integral of the RTD of an ideal CSTR, with the experimental normalised concentration of the tracer at the inlet, $\hat{C}_{in}$, of the reactor equal to the outlet concentration, $\hat{C}_{out}$. The integral was iteratively solved using Python to fit the experimental outlet concentration, knowing the inlet concentration and assuming a CSTR behaviour of the loop [261]. Further details are reported in Appendix E.

$$\hat{C}_{out}(t) = \int_0^t \hat{C}_{in}(t - t')\, E_{CSTR}(t')\, dt' \tag{5.1}$$

5.2.3. Aerobic oxidation of benzyl alcohol

5.2.3.1. Catalyst preparation

The catalyst powder used in this study in a slurry form was a 1 wt% bimetallic Au-Pd/TiO$_2$, with a Au:Pd weight ratio of 1:19, provided by Johnson Matthey and used in other studies [186]. It was made by mixing titania (TiO$_2$, Evonik P25) with a HAuCl$_4\cdot$3H$_2$O and PdCl$_2$ solution. The resulting slurry mixture was spray-dried through a nozzle at a temperature of 220 °C and calcined in static air at 400 °C for 3 h. Analysis using laser diffraction (LS 13 320, Beckman Coulter) revealed a bimodal particle size distribution with two major peaks at 8.1 μm and 27.4 μm, an overall mean particle size of 9.3 μm and a standard deviation of 8.4 μm (see Figure D.1 in Appendix D). These values can be attributed to a possible agglomeration of the nanosized TiO$_2$ particles. TEM revealed a metal particle size in the range of 1 - 2 nm, while ICP-AES analysis showed a weight concentration of gold and palladium of 0.05% and 0.85%, respectively.

5.2.3.2. Reaction start-up and operation

The catalyst was mixed with pure benzyl alcohol (99.0%, Sigma-Aldrich) in the desired concentration. This was stirred under intense agitation in a beaker and gradually withdrawn into the loop using the recirculation pump. This operation was performed by disconnecting the pump inlet from the tube-in-tube

membrane saturator outlet and allowing the slurry mixture flow through the open loop. Subsequently, the recirculation pump was stopped, reconnected to the loop and restarted again in order to keep the slurry flowing in the loop. It was possible to determine the amount of catalyst inside the reactor, by knowing the initial catalyst concentration in benzyl alcohol and the internal volume of the reactor. The inlet pump was then switched on and neat benzyl alcohol was flowed in the reactor, with the back-pressure regulator ensuring a constant slurry pressure in the loop.

Batch reactions in the SLTM reactor were carried out without the crossflow filter and the resulting slurry mixture was discharged at the end of each reaction and filtered using a glass microfibre filter (Whatman, Grade GF/B). To ensure reproducibility of the experiments, cleaning of the reactor was performed by sequentially flowing acetone, water and small amounts of aqua regia to remove residual Au-Pd present in the reactor.

5.2.3.3. Reaction in the autoclave reactor

Batch aerobic oxidations of benzyl alcohol were carried out in a stainless steel Parr® autoclave reactor (50 mL, Parr 5500 Series compact reactor) for comparative studies with the batch SLTM reactor. The autoclave was loaded with 10 mL of pure benzyl alcohol and with the desired quantity of the same 1 wt% Au-Pd/TiO$_2$ catalyst used in the SLTM reactor experimental campaign. Before ramping the temperature, the autoclave was purged five times with oxygen at 5 bar while the impeller stirring rate was set to 1800 rpm. Oxygen pressure was then set to the desired value and the temperature to 120 °C. This was measured with an internal process thermocouple touching the slurry mixture and controlled by an external supervisory box that powered the electrical heaters on the reactor jacket. The reaction time was taken from the moment when the internal temperature reached 120 °C. After reaction, the stirring rate was set to zero and the reactor was cooled down inside an ice bath. Samples were withdrawn and filtered.

5.2.3.4. Reaction in a continuous trickle-bed capillary reactor

The aerobic oxidation of benzyl alcohol was carried out in a capillary packed reactor operated under trickle-bed mode. The 1 wt% Au-Pd/TiO$_2$ catalyst was pelletized, sieved to a size of 90-125 μm and inserted in a 60 cm long PTFE tube (ID: 1.0 mm, OD: 1.6 mm, Kinesis). Details of the experimental setup are presented in Appendix D. The capillary reactor was immersed in a temperature bath (Diameter: 230 mm, Boro 3.3, VWR International) containing a heat transfer fluid (Paratherm NF) at 120 °C on top of a hot plate (US152, Stuart). Benzyl alcohol was pumped at 0.025 mL/min using an 8 mL stainless steel syringe (Harvard Apparatus) driven by a syringe pump (PHD ULTRA, Harvard Apparatus), while oxygen (N5.5, BOC) was flowed at 2.5 NmL/min using a mass flow controller (SLA5850S, Brooks). Both the two feeds were pre-mixed in a T-junction and fed to the packed-bed reactor at 120 °C and 5 bar. Samples from the outlet were taken after 1 h of reaction from the moment the bath temperature reached the target temperature.

5.2.3.5. Product analysis

All the product samples were analysed using gas chromatography (GC, 7820A, Agilent Technologies) with a FID and a HP-INNOWAX (19091-133) capillary column and an auto-liquid sampler. For each experiment the carbon balance was calculated and found to be 96-104%. Furthermore, experiments that were repeated showed a maximum ±3% (absolute) variation of benzyl alcohol conversion and product selectivity. The conversion of benzyl alcohol, X, as well as selectivities towards benzaldehyde, S_{BzAl}, and toluene, S_{Tol}, were compared between reactors using the catalyst contact time, CCT, which in the case of continuous reactions it was calculated as the catalyst mass per inlet mass flowrate of substrate ($g_{cat} \cdot s/g_{ROH}$, where ROH refers to the alcohol substrate). For batch reactions, CCT was obtained by multiplying the catalyst mass and the reaction time, divided by the initial substrate mass. To quantify the catalyst performance, the average turnover frequency, TOF, was used, as described in Equation (3.2). For batch reactions, this was equal to the total molar amount of benzyl alcohol converted divided by the reaction time and by the molar amount of catalyst metal. In order to differentiate between the

contributions from the direct oxidation (TOF_O) and the disproportionation reaction (TOF_D), the corresponding turnover frequencies were calculated according to Equations (5.2) and (5.3).

$$TOF_O = TOF \ (S_{BzAl} - S_{Tol}) \tag{5.2}$$

$$TOF_D = 2 \ TOF \ S_{Tol} \tag{5.3}$$

5.3. Results and discussion

5.3.1. Batch reactions in the SLTM and autoclave reactors

The aerobic oxidation of benzyl alcohol using the 1 wt% Au-Pd/TiO$_2$ catalyst was performed under various conditions in a conventional autoclave reactor. A number of experiments was carried out at different oxygen pressures, ranging from 1 to 5 bar at 120 °C, and employing 5.0 g/L catalyst loading. Reactions were performed for 58 min and results are reported in Table 5.1.

Table 5.1. Effect of oxygen pressure, p_{O2}, on benzyl alcohol conversion, X, and on the selectivity to benzaldehyde, S_{BzAl}, toluene, S_{Tol}, benzoic acid, S_{BzAc}, and benzyl benzoate, S_{BzBz}, in an autoclave reactor during the aerobic oxidation of benzyl alcohol. Temperature: 120 °C, benzyl alcohol volume: 10 mL, catalyst mass: 50 mg, reaction time: 58 min, CCT: 17 g$_{cat}$·s/g$_{ROH}$.

p_{O2}, bar	X, %	S_{BzAl}, %	S_{Tol}, %	S_{BzAc}, %	S_{BzBz}, %
1	23	61	35	0.47	0.49
2	45	62	36	0.47	0.63
3	82	65	30	1.4	2.2
4	95	71	21	3.7	3.2
5	96	70	17	7.5	4.8

It is possible to observe that a visible increase in conversion followed the increase in the oxygen pressure from 1 to 3 bar. However, at higher pressures reaction reached almost completion. The maximum value of benzaldehyde selectivity (71%) was obtained at 4 bar, with a corresponding toluene selectivity of 21%. Similarly to this trend, Dimitratos *et al.* tested a 1 wt% Au-Pd/TiO$_2$ catalyst at 120 °C in a 100 mL autoclave, and found that at oxygen pressures higher than 3.4 bar and at a constant 10% conversion, benzaldehyde selectivity increased [45]. This suggested that the oxygen reacted quickly with the species adsorbed on the catalyst and its availability on the catalyst surface was dependent on the stirring rate.

Other by-products are produced in the aerobic oxidation of benzyl alcohol. These include benzoic acid and benzyl benzoate, whose selectivity increased

with the increasing oxygen pressure reaching 7.5% and 4.8%, respectively at 5 bar. This was experimentally observed by Cao *et al.*, where the same catalyst was tested in a micropacked bed reactor operated in a gas-liquid trickle mode at 120 °C [141]. At increasing oxygen pressures benzoic acid and benzyl benzoate selectivities reached maximum values of 2% and 3% respectively, at 5 bar.

Figure 5.2 shows conversion and selectivity to benzaldehyde and toluene as a function of the catalyst loading at 120 °C and 5 bar oxygen. Decreasing the catalyst loading, ρ_{cat}, from 5.0 to 2.5 g/L led to an increase to benzaldehyde selectivity to 76%, while conversion decreased to 82%. At 1.25 g/L, benzaldehyde selectivity reached 84% at the expense of toluene, while conversion was reduced to 27%. Furthermore, the selectivity of the second most produced by-products, namely benzyl benzoate and benzoic acid, did not show a large variation as the catalyst loading was varied (see Appendix D).
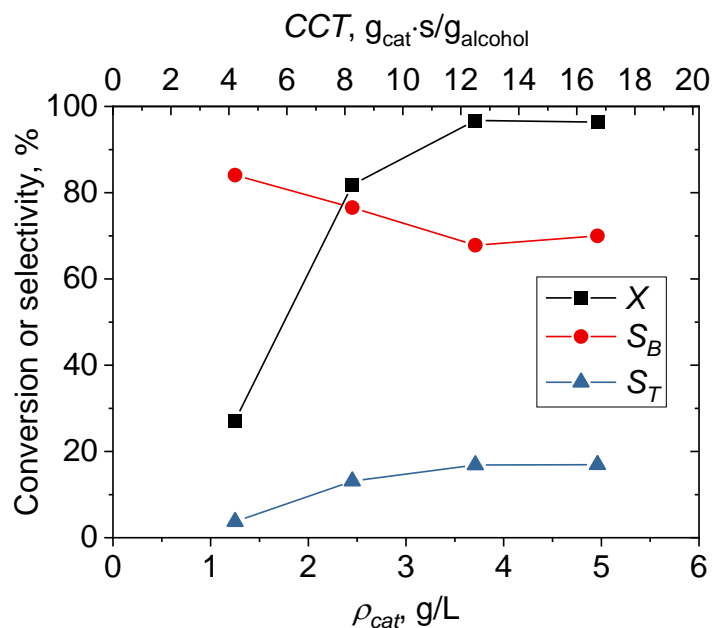
Figure 5.2. Benzyl alcohol conversion, *X*, benzaldehyde selectivity, S_{BzAl}, and toluene selectivity, S_{Tol}, in the autoclave reactor as a function of the catalyst loading, ρ_{cat}, during the aerobic oxidation of benzyl alcohol. Temperature: 120 °C, oxygen pressure: 5 bar, benzyl alcohol volume: 10 mL, reaction time: 58 min.

In their study, Dimitratos *et al.* oxidised 40 mL of benzyl alcohol and found that benzaldehyde and toluene selectivity were constant at approx. 72% and 23% for catalyst loadings below 1.3 g/L [45]. At higher catalyst concentrations, benzaldehyde selectivity decreased while the opposite happened with toluene selectivity, owing to the presence of mass transfer limitations.

The SLTM reactor was operated in batch without the crossflow filter and the results were compared to those obtained with the autoclave. A 200 cm long Teflon AF-2400 tubular membrane was employed in the tube-in-tube saturator, with the catalyst slurry circulating inside the loop at 10 mL/min at 120 °C and 5 bar oxygen pressure. Figure 5.3 shows the results with the catalyst contact time, *CCT*, used to compare the performance of the SLTM reactor to the autoclave. Benzyl alcohol conversion increased to *ca.* 69% in 1 h of reaction time, corresponding to a catalyst contact time of 17 $g_{cat} \cdot s/g_{ROH}$. For the same *CCT*, almost complete conversion was observed in the autoclave. Concerning benzaldehyde and toluene, they reached comparable selectivity values as in the autoclave reactions, and benzoic acid and benzyl benzoate selectivity did not exceed 3%.
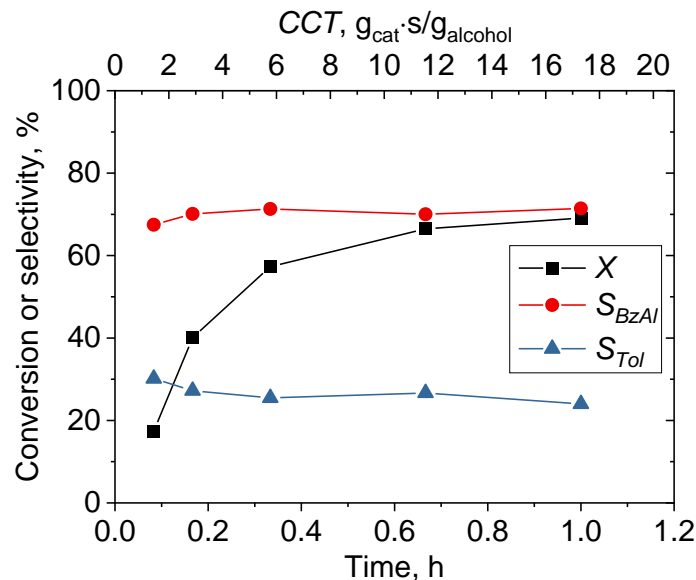
Figure 5.3. Benzyl alcohol conversion, *X*, benzaldehyde, S_{BzAl}, and toluene selectivity, S_{Tol}, as a function of reaction time in the SLTM reactor operating in a batch configuration during the aerobic oxidation of benzyl alcohol. Temperature: 120 °C, oxygen pressure: 5 bar, membrane length: 200 cm, catalyst loading: 5.0 g/L, reactor volume: 2.08 mL.

The activity of the catalyst can be compared between the two reactors by looking at the catalyst turnover frequency. Figure 5.4 shows the TOF_O and TOF_D for the autoclave and SLTM reactor at different values of the catalyst contact time. Between 2 and 6 $g_{cat}·s/g_{ROH}$ both reactors exhibited a similar turnover frequency for the direct oxidation of benzyl alcohol to benzaldehyde, TOF_O, which ranged between 20000 and 25000 h^{-1}. At CCT values near 17 $g_{cat}·s/g_{ROH}$, under which high conversions were obtained, the TOF_O decreased to 7300 h^{-1} for the SLTM reactor and to 15700 h^{-1} for the autoclave. The disproportionation reaction turnover frequency, TOF_D, had a similar value for both the two reactors at high CCT values, while at decreasing catalyst contact times the TOF_D increased for the SLTM reactor, reaching a value of $ca.$ 30000 h^{-1} at about 1 $g_{cat}·s/g_{ROH}$. However, at similar CCT values, disproportionation in the autoclave was suppressed. This might be ascribed to a better oxygen mass transfer in the autoclave. The CCT was decreased by decreasing the reaction time and by keeping the catalyst loading constant for the SLTM reactor, while the reverse was done for the autoclave.

Nevertheless, a TOF_O in the same order of magnitude is indicative of a similar direct oxidation performance of the catalyst, despite the possible presence of oxygen mass transfer bottle-necks in the SLTM reactor at high CCT values. Furthermore, while the SLTM reactor mostly produced benzaldehyde and toluene, reactions in the autoclave showed a cumulative selectivity to benzoic acid and benzyl benzoate of nearly 12%, even in the case of low catalyst loadings (1.3 g/L). This could be ascribed to a higher degree of oxygenation achieved in the autoclave, due to a high contact area between the reacting phases, which could not occur in the SLTM reactor given the fixed gas-liquid surface area provided by the membrane.
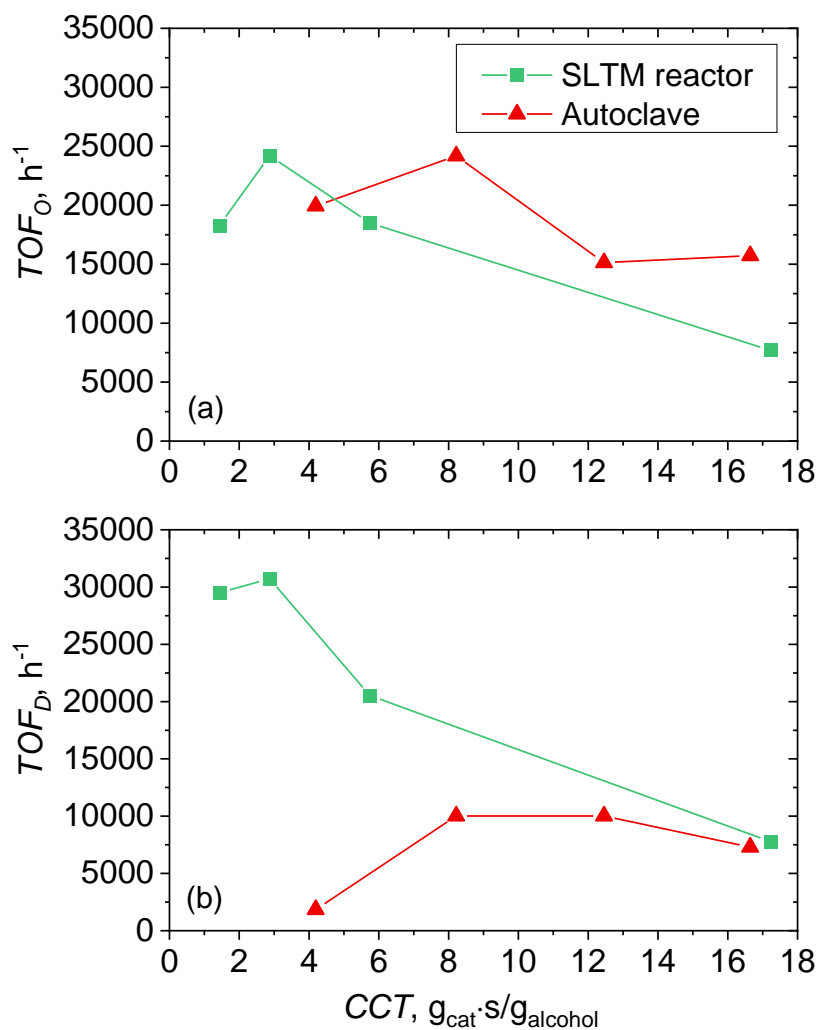
Figure 5.4. Turnover frequency as a function of the catalyst contact time, *CCT*, in the batch SLTM and autoclave reactors during the aerobic oxidation of benzyl alcohol. (a) Turnover frequency of the direct oxidation, TOF_O, and the (b) disproportionation reaction, TOF_D. Temperature: 120 °C, oxygen pressure: 5 bar. SLTM reactor: 200 cm membrane length, 5.0 g/L catalyst loading and 2.08 mL reactor volume. Autoclave: 10 mL benzyl alcohol volume and 58 min reaction time.

5.3.2. Residence time distribution in the slurry loop tubular membrane reactor

Continuous operation in the SLTM reactor could be performed using a crossflow filter connected to the loop. Before conducting reactions, macromixing was characterised in the continuous SLTM reactor by carrying out residence time distribution (RTD) experiments (see Appendix E).

The fitting of the convolution integral demonstrated that the ideal CSTR model could well describe the macromixing occurring in the loop reactor under a recycle ratio of 400. The mean residence time of the ideal CSTR that best fitted $\hat{C}_{out}$ was 60 min, close to the expected value of 58 min corresponding to the reactor space time. Furthermore, as shown in the work of Melo *et al.* [262], at relatively high recycle ratios the tracer outlet concentration from a loop reactor has a distinct decaying exponential trend, which is typical of that of an ideal CSTR.

5.3.3. Continuous aerobic oxidation of benzyl alcohol in the SLTM reactor

5.3.3.1. Stability test

A stability test was carried out in the continuous SLTM reactor, using a 60 cm long Teflon AF-2400 tubular membrane with oxygen pressurised at 4 bar and the reactor temperature at 120 °C. Benzyl alcohol flowrate was set to 0.025 mL/min with a catalyst slurry concentration of 5.0 g/L inside the loop. Figure 5.5 shows the result from a 4.5 h continuous experiment.
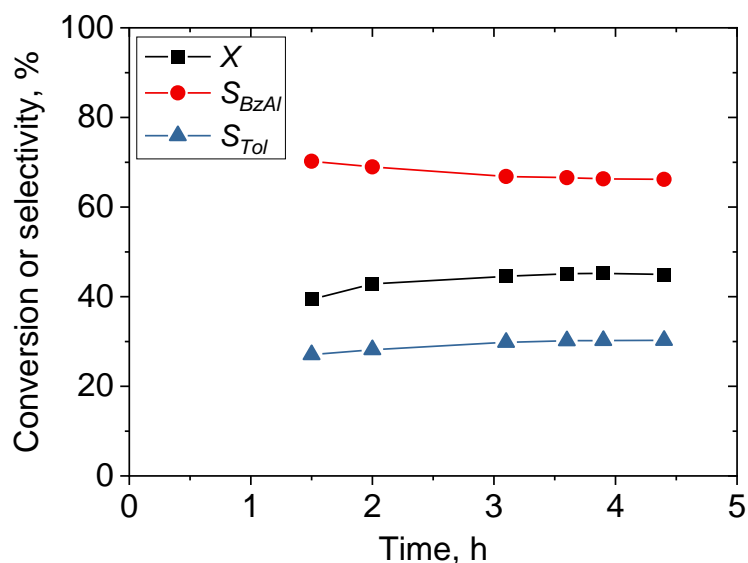
Figure 5.5. Benzyl alcohol conversion, X, benzaldehyde, S_{BzAl}, and toluene selectivity, S_{Tol}, in the continuous SLTM reactor during the aerobic oxidation of benzyl alcohol. Temperature: 120 °C, oxygen pressure: 4 bar, benzyl alcohol flowrate: 0.025 mL/min, catalyst concentration: 5.0 g/L, reactor volume: 1.46 mL, CCT: 17 $g_{cat} \cdot s/g_{ROH}$.

Approximately 45% of benzyl alcohol was oxidised to benzaldehyde and toluene, with a selectivity of 66% and 30% respectively. For 4.5 h the catalyst showed a stable conversion, enough to enable the reactor of a consistent catalyst testing at different operating conditions. In each parametric study involving a change in the operating condition, samples were collected after 2.5 h. Minor by-products, such as benzoic acid and benzyl benzoate had a selectivity of 1.4% and 1.2% respectively, and their cumulative selectivity was always less than 3% in all flow experiments.

5.3.3.2. Effect of the reaction temperature

It has been reported how benzyl alcohol oxidation is sensitive to the reaction temperature. As an example, selectivity to benzaldehyde generally drops as temperature increases, while toluene production is favoured [141, 263, 264]. The effect of temperature on benzyl alcohol oxidation was studied in the SLTM reactor, by conducting a series of experiments at 100 - 120 °C, with an oxygen pressure of 5 bar and at 17 $g_{cat} \cdot s/g_{ROH}$, corresponding to a 5.0 g/L catalyst

concentration and 0.025 mL/min benzyl alcohol inlet flowrate. The process temperature was recorded under steady-state conditions and simulations using COMSOL Multiphysics® 5.3a showed that the same temperature was reached inside each point of the loop, with the exception of the loop section outside the temperature bath. This decreased the average temperature of the slurry in the loop to 3 °C with respect to the measured temperature at the inlet of the tube-in-tube membrane saturator (see Appendix D).

Figure 5.6 shows the conversion and product selectivity as a function of the process temperature. As it is possible to observe, benzaldehyde selectivity decreased from 75% to 67% when the temperature was increased from 100 to 120 °C, with a corresponding rise in toluene selectivity.

According to the microkinetic model developed by Galvanin *et al.*, behind the production of toluene at higher temperatures there is the hydrogenolysis reaction, while the disproportionation is dominant at lower temperatures [259]. Nevertheless, when the temperature is increased both contributions are promoted, leading to a higher selectivity to toluene.
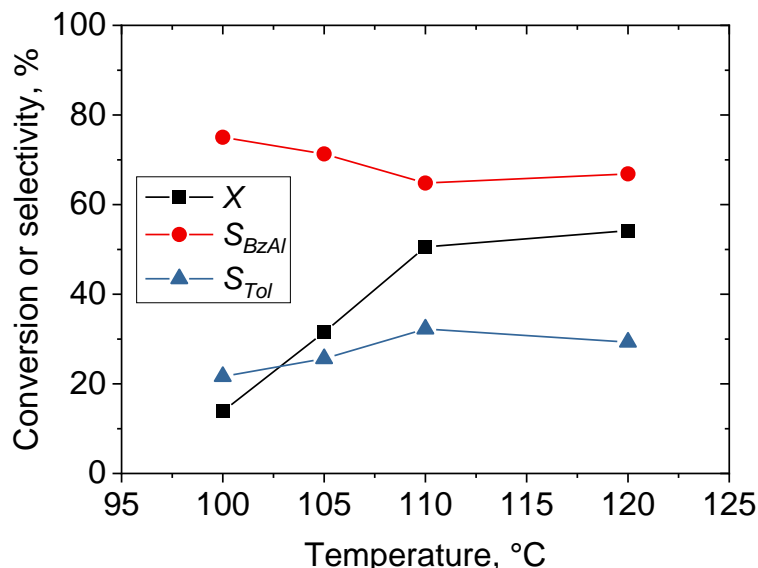
Figure 5.6. Benzyl alcohol conversion, X, benzaldehyde, S_{BzAl}, and toluene selectivity, S_{Tol}, as a function of the reaction temperature in the continuous SLTM reactor during the aerobic oxidation of benzyl alcohol. Oxygen pressure: 5 bar, benzyl alcohol flowrate: 0.025 mL/min, catalyst concentration: 5.0 g/L, volume of the reactor: 1.46 mL; CCT: 17 $g_{cat}·s/g_{ROH}$.

To assess how the reaction temperature impacted on the catalyst activity, the turnover frequency was calculated and reported in Figure 5.7. As it is possible to observe, the overall turnover frequency, TOF, increased from 3342 h^{-1} at 100 °C to 13057 h^{-1} at 120 °C. It is evident that the disproportionation reaction (TOF_D) becomes prevalent at higher temperatures with respect to the direct oxidation pathway (TOF_O). In their experiments conducted using the same 1 wt% Au-Pd/TiO$_2$ catalyst in a micro packed-bed reactor, Cao *et al.* observed a similar trend [265]. At 100 °C the two reactions had comparable turnover frequencies. However, at 120 °C the TOF_D was *ca.* 4300 h^{-1}, three times higher than the TOF_O (1400 h^{-1}), unlike in the SLTM reactor in which the TOF_O was approx. 5000 h^{-1} and 1.5 times lower than the TOF_D.
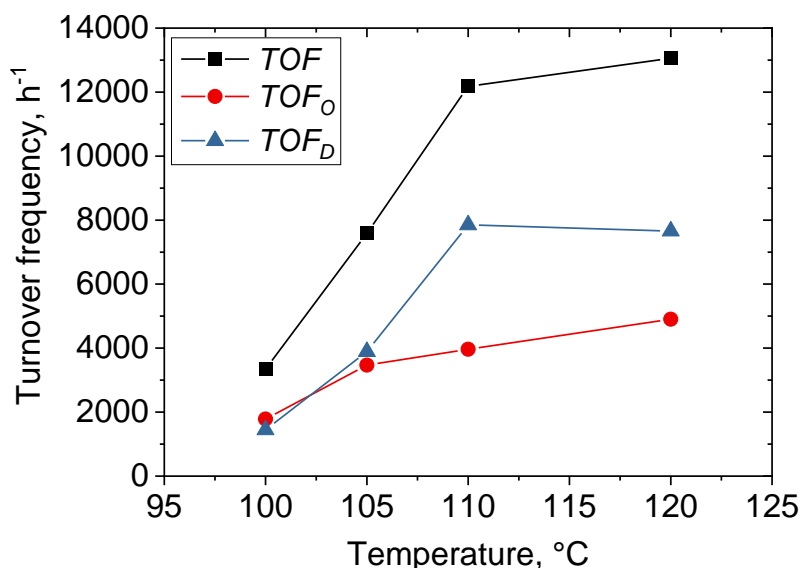
Figure 5.7. Turnover frequency of the overall, TOF, oxidation, TOF_O, and disproportionation, TOF_D, reaction as a function of the reaction temperature in the continuous SLTM reactor during the aerobic oxidation of benzyl alcohol. Oxygen pressure: 5 bar, benzyl alcohol flowrate: 0.025 mL/min, catalyst concentration: 5.0 g/L, volume of the reactor: 1.46 mL, CCT: 17 g$_{cat}$·s/g$_{ROH}$.

5.3.3.3.   Effect of the oxygen pressure

Oxygen pressure was increased from 0 to 5 bar and benzyl alcohol conversion and product selectivity are reported in Figure 5.8. At 0 bar oxygen pressure, under anaerobic conditions benzyl alcohol conversion was 2%, with 51% and 42% selectivity to benzaldehyde and toluene respectively. This could be

performed by pressurising the reactor with nitrogen at 3 bar. In the absence of oxygen, only the disproportionation and the hydrogenolysis reactions can take place, which lead to an equimolar production of benzaldehyde and toluene [265]. However, the slightly higher benzaldehyde selectivity is indicative of a possible contamination of air in the gas line.

At increasing oxygen pressures, both conversion and benzaldehyde selectivity were enhanced. Benzaldehyde selectivity increased to 62% at 3 bar and conversion reached 50%. However, only a marginal increase in benzaldehyde selectivity was observed at oxygen pressures higher than 3 bar. In fact, at 5 bar the selectivity to benzaldehyde was 68%, while benzyl alcohol conversion was still 50%.
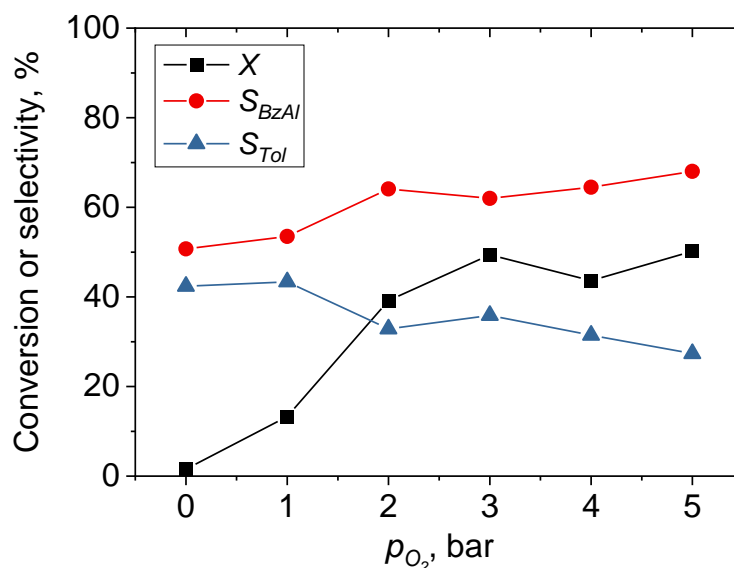
Figure 5.8. Benzyl alcohol conversion, X, benzaldehyde selectivity, S_{BzAl}, and toluene selectivity, S_{Tol}, as a function of the oxygen pressure, p_{O2}, in the continuous SLTM reactor during the aerobic oxidation of benzyl alcohol. Temperature: 120 °C, benzyl alcohol flowrate: 0.025 mL/min, catalyst concentration: 5.0 g/L, volume of the reactor: 1.46 mL, CCT: 17 $g_{cat}·s/g_{ROH}$.

These findings are in agreement with the work of Dimitratos *et al.*, who observed that at oxygen pressures higher than 50 psi (3.4 bar), the selectivity of benzaldehyde was 65% and increased to 70% at 100 psi [45]. Similarly, Cao *et al.* observed that the overall *TOF* for the same 1 wt% Au-Pd/TiO$_2$

catalyst was constant at 4 and 5 bar at 120 °C, using pre-mixed oxygen and benzyl alcohol flowing inside a micro packed-bed reactor [265].

5.3.3.4. Effect of the reactor loop length and the catalyst concentration

A second SLTM reactor with a longer tubular membrane (120 cm) and thus a larger volume (1.84 mL) was built in order to better understand the role of the oxygen availability. An experiment was performed at 120 °C, 5 bar oxygen pressure and 17 $g_{cat} \cdot s/g_{ROH}$ catalyst contact time and the result was compared to that form a 60 cm long tubular membrane. The result is shown in Table 5.2 and it is possible to observe that a longer membrane did not have a large impact on the overall *TOF*, indicating that there was no limitation in the oxygen supply.

Table 5.2. Benzyl alcohol conversion, X, benzaldehyde, S_{BzAl}, and toluene selectivity, S_{Tol}, along with turnover frequencies of the overall, *TOF*, oxidation, TOF_O, and disproportionation, TOF_D, reactions for two membrane lengths, L_m, and reactor volumes, V_R, in the continuous SLTM reactor during the aerobic oxidation of benzyl alcohol. Temperature: 120 °C, oxygen pressure: 5 bar, benzyl alcohol flowrate: 0.025 mL/min, catalyst concentration: 5.0 g/L, *CCT*: 17 $g_{cat} \cdot s/g_{ROH}$.

L_m, cm	V_R, mL	X (S_{BzAl}, S_{Tol}), %	*TOF*, h^{-1}	TOF_O, h^{-1}	TOF_D, h^{-1}
60	1.46	50 (68, 27)	12092	4921	6612
120	1.84	44 (70, 27)	10504	4449	5732

To assess whether the SLTM reactor was limited by external gas-liquid mass transfer resistances, the catalyst loading in the reactor was varied, whilst maintaining the same inlet flowrate (0.025 mL/min), temperature of 120 °C and oxygen pressure of 5 bar. Figure 5.9 shows the results. A blank test was conducted without catalyst (0 g/L) and the recorded conversion was only 3% with a benzaldehyde selectivity of 56%. Once the Au-Pd catalyst was

employed, the selectivity to benzaldehyde increased to 69% using 1.3 g/L of catalyst, while conversion reached 10%. Increasing the catalyst loading to 5.0 g/L, led to a five-fold increase in conversion (50%), while benzaldehyde and toluene selectivity did not change significantly.
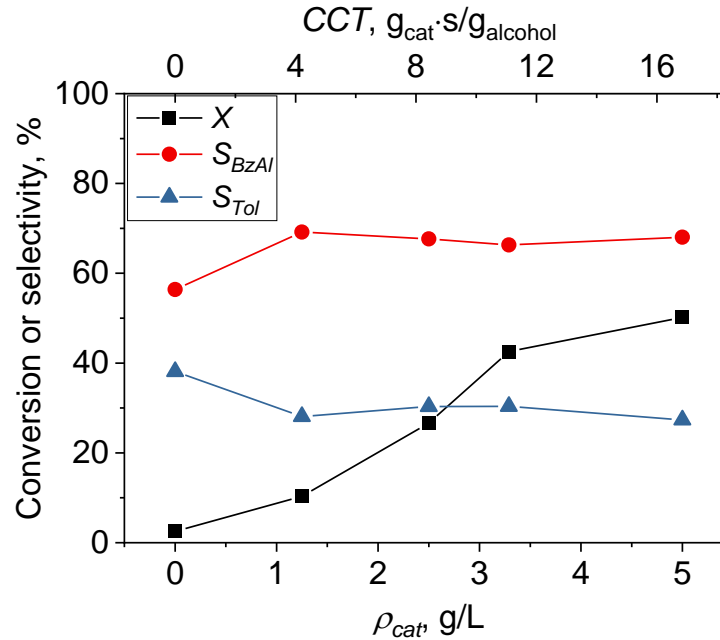
Figure 5.9. Benzyl alcohol conversion, X, benzaldehyde, S_{BzAl}, and toluene selectivity, S_{Tol}, as a function of the catalyst loading, ρ_{cat}, in the continuous SLTM reactor during the aerobic oxidation of benzyl alcohol. Temperature: 120 °C, oxygen pressure: 5 bar, benzyl alcohol flowrate: 0.025 mL/min, reactor volume: 1.46 mL.

The oxygen consumption rate, OCR, was calculated from conversion and product selectivity according to Equation (5.4), where $\tilde{V}_{O2}$ is the oxygen molar volume (22.414 L/mol) at standard temperature and pressure conditions (STP, 0 °C and 1 atm).

$$OCR = \frac{1}{2} F_{BzOH,in} \, X \, (S_{BzAl} - S_{Tol}) \, \tilde{V}_{O_2} \tag{5.4}$$

Figure 5.10 shows the OCR as a function of the catalyst loading, which was fitted with a linear model ($R^2 = 0.979$). At 5.0 g/L the oxygen consumption rate was 0.55 mL/min, while this decreased to 0.27 mL/min when the catalyst

loading was halved. This linearity possibly indicates the absence of gas-liquid mass transfer resistances while liquid-solid ones might still be present.
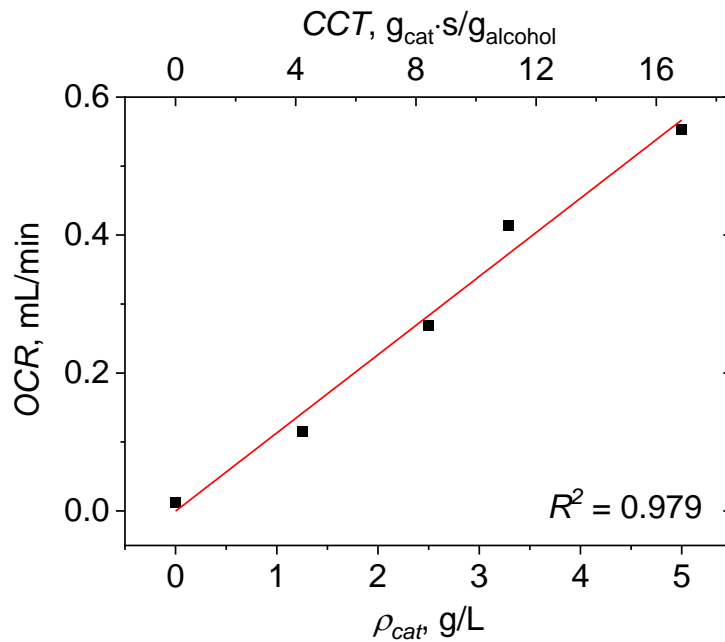
Figure 5.10. Oxygen consumption rate, *OCR*, at standard temperature and pressure conditions as a function of catalyst loading, ρ_{cat}, in the continuous SLTM reactor during the aerobic oxidation of benzyl alcohol. Temperature: 120 °C, oxygen pressure: 5 bar, benzyl alcohol flowrate: 0.025 mL/min, reactor volume: 1.46 mL.

5.3.4. Comparison with other reactor configurations

The aerobic oxidation of benzyl alcohol was performed in a packed-bed capillary reactor under trickle flow of oxygen and benzyl alcohol, using the same 1 wt% Au-Pd/TiO$_2$ catalyst, and the results are compared to that achieved with the SLTM reactor. An amount of 7 mg of catalyst was used, at a catalyst contact time of 17 g$_{cat}$·s/g$_{ROH}$ in order to ensure a proper comparison with the SLTM reactor.

Table 5.3 shows the results, along with those from previous works conducted using a flat membrane packed-bed reactor and a micro trickle-bed reactor operated under high gas-to-liquid ratios [186, 266]. The catalyst contact time and the specific surface area of the membrane per catalyst mass, a_m, are also included for comparison.

The reaction in the flat membrane packed-bed reactor was conducted using particles with sizes ranging between 90 and 125 µm packed inside a rectangular microchannel (length: 75 mm; width: 3 mm; depth: 1 mm) [186]. A flat Teflon AF-2400 membrane (length: 85 mm; width: 30 mm; thickness: 0.07 mm) was sealed on one of the sides of the channel and provided oxygen for reaction. Despite operating at a substantially higher catalyst contact time (577 $g_{cat} \cdot s/g_{ROH}$) and oxygen pressure (6.3 bar), conversion (43%) and benzaldehyde selectivity (62%) in the flat membrane packed-bed reactor did not exceed those obtained with the SLTM reactor, where the membrane area per catalyst mass was 93 times higher. The reason of a smaller TOF_O (< 143 h^{-1}) can be ascribed to the oxygen mass transfer resistances within the packed bed. The highest recorded benzaldehyde selectivity achieved in the packed-bed reactor was 70% at 8.4 bar and at a catalyst contact time of 1150 $g_{cat} \cdot s/g_{ROH}$ [186].

Owing to its plug flow-like conditions and to the direct contact of oxygen with benzyl alcohol at a gas-to-liquid ratio, G/L, of 100, the trickle-bed capillary reactor achieved a higher conversion (68%) compared to the SLTM reactor. Yet, a lower benzaldehyde selectivity of 62% was achieved and the TOF_O was in the same order of magnitude of the SLTM reactor (4900 - 5400 h^{-1}). The lower conversion achieved in the SLTM reactor compared to the capillary reactor could be possibly ascribed to the slightly lower average temperature of the catalyst slurry in the loop with respect to the set point, suggesting that an improved thermal insulation of the loop could enhance the performance of the SLTM reactor. Furthermore, a possible deposition of catalyst particles in the crossflow filter might reduce the concentration of catalyst in the slurry. Nevertheless, unlike the flat membrane packed-bed reactor and the SLTM reactor, other by-products including benzyl benzoate were detected with a selectivity of 5% (see Appendix D), possibly due to the oxidation of the main product.

Table 5.3. Benzyl alcohol conversion, X, benzaldehyde, S_{BzAl}, and toluene selectivity, S_{Tol}, along with the turnover frequency of the oxidation, TOF_O, and disproportionation reaction, TOF_D, for different reactor configurations with various catalyst contact times, CCT, and specific membrane surface areas, a_m, during the aerobic oxidation of benzyl alcohol. Temperature: 120 °C. SLTM reactor: 5 bar oxygen pressure, 15 cm^2 membrane inner surface area and 0.025 mL/min benzyl alcohol flowrate. Flat membrane packed-bed reactor [186]: 6.3 bar oxygen pressure, 2.25 cm^2 membrane surface area, 90-125 µm catalyst particle size and 0.1 g catalyst mass. Trickle-bed capillary reactor: 5 bar oxygen pressure, 2.5 NmL/min oxygen flowrate, 90-125 µm catalyst particle size and 0.025 mL/min benzyl alcohol flowrate. Micro trickle-bed reactor [266]: 2 bar oxygen pressure, 4 NmL/min oxygen flowrate, 63-75 µm catalyst particle size and 0.75 µL/min benzyl alcohol inlet flowrate. Autoclave: 5 bar oxygen pressure, 5 g/L catalyst concentration and G/L is volumetric gas-to-liquid ratio.

Reactor	X (S_{BzAl}, S_{Tol}), %	TOF_O, h^{-1}	TOF_D, h^{-1}	CCT, g$_{cat}$·s/g$_{ROH}$	a_m, cm^2/g$_{cat}$
SLTM (continuous)	50 (68, 27)	4921	6612	17	2094
Flat membrane packed-bed (6.3 bar) [186]	43 (62, 37)	76	209	577	22.5
Trickle-bed capillary (G/L = 100, STP)	68 (62, 30)	5388	9749	17	-
Micro trickle-bed (G/L= 3577, STP) [266]	97 (82, 13)	3221	1213	76	-
Autoclave	96 (70, 17)	11674	7457	17	-

Table 5.3 also reports the results from the work of Al-Rifai *et al.* on the aerobic oxidation of benzyl alcohol conducted in a silicon-glass microreactor operated in a trickle-bed mode at a G/L of 3577 [266]. From their work, it was suggested that the thinning of the contacting liquid on the catalyst particles at high gas superficial velocities was responsible for the gas-liquid mass transfer enhancement. The reported data refer to the gas dominated regime with sufficiently wetted catalyst, which led to a 97% conversion and 82% benzaldehyde selectivity, higher than that achieved in the autoclave (70%) despite the much lower oxygen pressure. Nevertheless, both the two reactors showed similar conversion (96 - 97%), suggesting that the liquid film shear and liquid/oxygen and oxygen/solid contact can play an important role in boosting conversion and selectivity.

5.4. Summary and conclusions

This work shows for the first time a novel slurry loop reactor with a tubular Teflon AF-2400 membrane as oxygen saturator for the safe catalytic aerobic oxidation of benzyl alcohol. The catalyst slurry circulated in a loop while oxygen was provided from the membrane saturator in a tube-in-tube configuration. The reactor proved to be a flexible tool that can be operated in a range of oxygen pressures and temperatures in both batch and continuous operation. A comparative study with a conventional autoclave (Parr® reactor) showed similar turnover frequencies at short catalyst contact times, proving that the slurry loop tubular membrane (SLTM) reactor is able to provide an intense oxygenation in the catalyst slurry. A crossflow filter inside the loop allowed the reactor to operate continuously, by providing an outlet where pure liquid was continuously filtered from the slurry. Under continuous operation, the reactor macromixing was similar to that of an ideal CSTR, as demonstrated by the residence time distribution study. High oxygen pressures and low reaction temperatures increased benzaldehyde selectivity, while conversion could be enhanced by increasing both the two parameters. Oxygen supply was found to be sufficient and not limited by gas-liquid mass transfer resistances, after doubling the available membrane surface area for oxygen diffusion. Furthermore, proportionality was observed between the oxygen consumption rate and the catalyst loading.

The SLTM reactor showed superior performance in terms of benzaldehyde selectivity and reaction rate compared to a reactor in which the same catalyst was packed in a channel and oxygen was provided using a flat Teflon AF-2400 membrane. When compared to a capillary reactor where pre-mixed oxygen and benzyl alcohol are flowed into a packed-bed catalyst under trickle-bed flow, the SLTM reactor achieved a similar turnover frequency for the direct oxidation of benzyl alcohol to benzaldehyde.

Other reactions involving a wider spectrum of powder catalysts can be performed using the SLTM reactor, with the additional benefits of providing small mass transport resistances and safe operation when using a gaseous oxidant.

Chapter VI. Slurry loop membrane reactor for the safe aerobic oxidation of primary and secondary alcohols
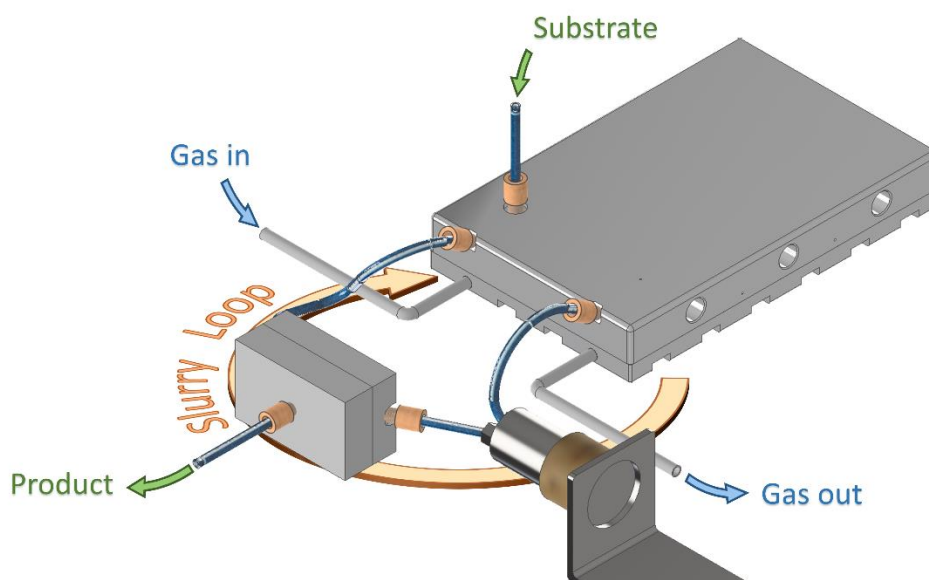
A novel slurry loop flat membrane reactor with a plug-and-play configuration was developed for the continuous and batch aerobic oxidation of various primary and secondary alcohols to aldehydes and ketones. The new loop reactor design, with a flat Teflon AF-2400 membrane, a serpentine channel in the saturator, and electrical heaters, allowed larger catalyst loadings to be used for reaction and improved heat management with respect to the SLTM reactor.

Macromixing studies showed a residence time distribution similar to that of an ideal CSTR, under recycle flowrates 100 times higher than the inlet. Styrene hydrogenation using 5 wt% Pd/C powder catalyst was performed to investigate the gas-liquid mass transfer resistance. A k_La of 1.2 s^{-1} was achieved under a moderate specific power input of 2.4 kW/m^3. The 1 wt% Au-Pd/TiO$_2$ catalyst was tested in the batch and continuous aerobic oxidation of different primary and secondary alcohols diluted in *tert*-butylbenzene with temperatures and oxygen pressures of 90 - 120 °C and 2 - 6 bar. By increasing the loop volume and operating at higher flowrates, 0.4 - 19 g of aldehydes were produced with only 88 mg of catalyst. Overall, the reactor demonstrated excellent performance in terms of catalyst usage and process safety during aerobic oxidations.

6.1. Introduction

In Chapter V, the SLTM reactor was demonstrated in the aerobic oxidation of benzyl alcohol in flow. The catalyst slurry was continuously pumped in a loop, to which a tubular Teflon AF-2400 membrane was connected and provided oxygen during reaction. It operated safely and effectively, and achieved similar turnover frequencies to those achieved in a conventional autoclave reactor. Furthermore, it showed superior performance compared to a flat membrane packed-bed reactor using only small amounts of catalyst and moderate oxygen pressures [186]. However, one of the problems was the difficult operation, due to the use of a bath filled with heat transfer oil where the reactor was submerged. Moreover, at high catalyst loadings clogging occurred in tubular restrictions. To overcome this problem, the use of a larger channel with a flat Teflon AF-2400 membrane can represent a suitable solution.

Mo *et al.* demonstrated a thin flat membrane reactor for aerobic oxidations and hydrogenations in flow [97]. The Teflon AF-2400 membrane was sandwiched between two porous carbon cloth layers, where the gas and the liquid phases were flowing separately. For heterogeneous reactions the authors embedded a catalyst in the carbon cloth and scale-up was performed by stacking membranes one over another. The catalyst amount was limited by the surface area available on the carbon cloth and high pressures had to be employed to achieve high yields. The use of fine catalyst particles suspended in the reaction medium can represent an alternative and attractive solution. As already described in the previous paragraphs, slurry reactors offer better temperature control, moderate pressure drops, and can boost the catalyst activity owing to the reduction of diffusional resistances, and to the enhanced mixing between the catalyst particles and the liquid [2, 267, 268].

In this chapter a novel slurry loop flat membrane reactor is presented, with a Teflon AF-2400 membrane film as a saturator, embedded with three heat cartridges for temperature control, and a plug-and-play configuration demonstrated in the heterogeneous aerobic oxidations of various primary and secondary alcohols.

6.2. Materials and methods

6.2.1. Slurry loop flat membrane reactor design and setup

The slurry loop flat membrane (SLFM) reactor was comprised of three main units: a gas saturator, a recirculation pump and a crossflow filter. These were connected in a loop, and the catalyst powder together with the liquid substrate and reaction products continuously circulated around the loop.

The heart of the loop was the saturator (see Figure 6.1). Here, the slurry flowed in a serpentine channel above which a flat Teflon AF-2400 membrane (0.023'' thickness, Biogeneral) was placed, separating the slurry flow from the gaseous reactant pressurised on the other side.
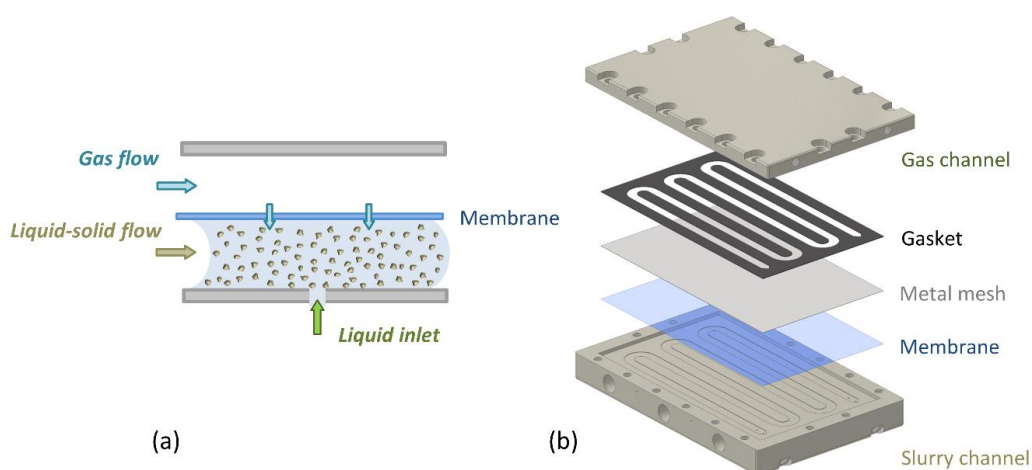
Figure 6.1. (a) Slurry-gas saturator schematic showing the Teflon AF-2400 membrane separating the catalyst slurry from the gaseous reactant. (b) Exploded assembly of the saturator unit (see Appendix F for details).

The slurry channel had a depth and width of 0.3 and 6 mm respectively, and a length of 808 mm with 4850 mm^2 surface area exposed to the membrane. Figure 6.1b shows the saturator assembly, comprising of a membrane, a 0.05 mm thick metal mesh (Industrial Netting) for mechanical support and a 0.5 mm-thick Kalrez® gasket (DuPont), sealing the liquid and the gas channel (see Appendix F for details). The membrane's selective permeability to gases allowed gas molecules to diffuse through the membrane and into the slurry mixture where they reacted on the catalyst particles. The saturator also

included an inlet port for the continuous feeding of neat liquid substrate during continuous operation.

The schematic of the setup is shown in Figure 6.2. Connected to the saturator, the recirculation pump was a microannular gear pump (mzr-4605, HNP Mikrosysteme) that pumped the slurry around the loop at a flowrate ranging between 5 and 20 mL/min. A crossflow filter was connected between the pump and the saturator and enabled the continuous withdrawal of pure liquid during continuous reactions, while keeping the catalyst flowing inside the loop. Polyfluoroalkoxy alkane (PFA) tubing (1/16'' OD x 1 mm ID, Idex) provided connection to these three units. The details on the design of the crossflow filter and the saturator are reported in Appendix C and F, respectively. The total volume of the slurry flowing in the loop reactor was 1.4 cm^3, which could be increased to 8.8 cm^3 for larger volume reactions that were performed to achieve higher productivity. This was done by adding extra tubing (PFA, 1/8'' OD x 0.062'' ID, volume 7.4 cm^3, Idex) to the loop (Loop extension in Figure 6.2).
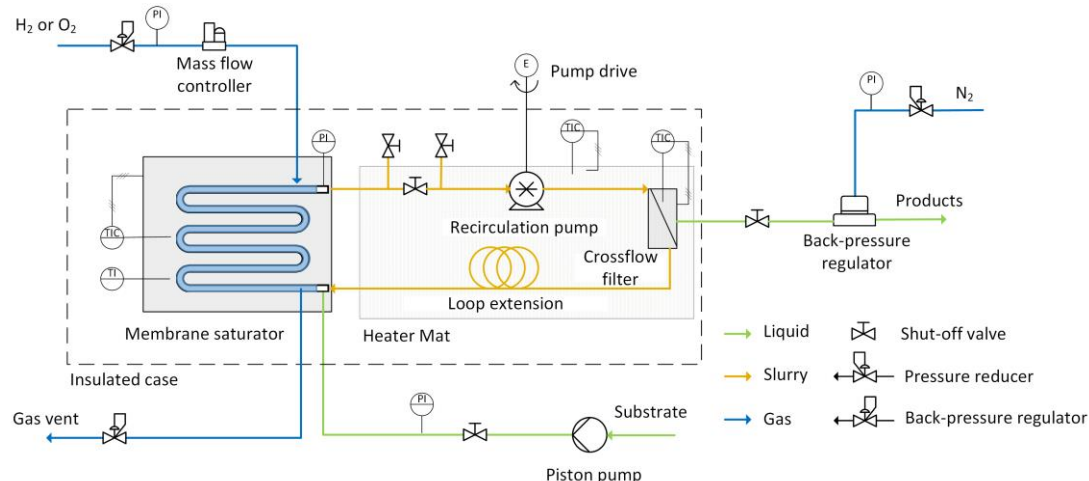
Figure 6.2. Schematic of the slurry loop flat membrane reactor setup for the aerobic oxidation of primary and secondary alcohols. The catalyst-liquid mixture is pumped around the loop through a crossflow filter and a membrane saturator, where the gas is pressurised. A set of valves between the recirculation pump and the saturator allows the easy loading and unloading of the catalyst slurry. PI: pressure indicator, TI: temperature indicator, TIC: temperature indicator and controller.

6.2.2. Continuous and batch operation modes

The setup could be operated either in batch or continuous mode. In both cases the catalyst slurry mixture was prepared outside the reactor inside a glass bottle (100 mL, Schott) with *ca.* 50 mL of substrate solution stirred together with the desired catalyst amount. Between the slurry outlet of the saturator and the slurry inlet of the recirculation pump, a series of three shut-off PEEK valves (0.04" ID hole, Kinesis) was installed to facilitate the introduction of the catalyst slurry in the loop prior to any reaction. This was continuously fed into the loop using a microannular gear pump, through the system of valves, until the whole loop was full of the slurry mixture.

For continuous reactions, the substrate inlet flowrate was provided by a dual piston pump (Azura P2.1S, Knauer) which pumped it to the inlet port in the slurry channel of the saturator. The outlet liquid flow was delivered from the crossflow filter, which was connected to a back-pressure regulator (BPR-01, Zaiput) that ensured a constant pressure upstream. This could be regulated using the pressure reducer on the nitrogen line that was connected to the liquid back-pressure regulator.

For batch reactions, once the slurry mixture was fed into the loop, the piston pump was used to deliver the liquid substrate (*e.g.* 100 µL/min for 2 min) and pressurise the slurry loop up to the desired pressure. After reaction, the system of valves between the pump and the saturator was used to withdraw the product mixture from the loop.

The slurry pressure across the saturator channel was measured using two pressure sensors (PX309, Omega), one connected to the liquid inlet and a second one to the other end of the serpentine channel. This was done to ensure that the gas pressure was always 0.5 bar lower than that of the slurry at any point in the saturator. Concerning the reacting gas, this was depressurised from the gas line using a gas pressure regulator (KPR, Swagelok) and its flowrate controlled by a mass flow controller (4850, Brooks). During experiments when the gas was stagnant, the mass flow controller was disconnected and the pressure reducer was directly connected to the saturator. The gas pressure in the saturator was controlled at the gas outlet by a gas back-pressure regulator (BP301, Pressure Tech) for both flowing and

stagnant gas operations. Stainless steel tubes of 1/16'' outer and 0.04'' internal diameter were used to deliver the gas at the inlet and vent it at the outlet. In order for the reactor to operate up to 120 °C the saturator and the crossflow filter were heated by electric heaters (see Appendix F for details). Figure 6.3 shows a picture of the setup with the reactor inside a case made of Delrin® acetal on the lowest level.

Figure 6.3. Picture of the slurry loop flat membrane reactor setup for the aerobic oxidation of primary and secondary alcohols. The reactor is inside the acetal case on the lowest shelf, the piston pump for the substrate delivery is on the middle shelf and the gas flowrate control box is on the top shelf. The temperature control boxes can be seen on the left and the vessels containing the alcohol substrate and those collecting the liquid products are on the right.

6.2.2.1.   Analysis of the products

Reaction products were analysed using a gas chromatograph (7820A, Agilent Technologies) equipped with an automatic liquid sampler, a HP-INNOWAX (19091-133) capillary column and a flame ionisation detector. Before the analysis of batch samples, the slurry mixture was filtered by means of glass microfibre filters (Grade GF/B, Whatman). For samples from continuous oxidations, filtration was continuously performed using the crossflow filter.

6.2.3. Macromixing study

Macromixing was characterised by a pulse-input injection of a tracer under different recycle-to-inlet flowrate ratios (recycle ratios). A volume of 100 µL of tracer (Basic Blue 3, Sigma-Aldrich) was injected at the inlet, while Ultraviolet-Visible (UV–Vis) spectroscopy (DH-2000BAL+UV-VIS-ES, Ocean Optics) was performed on the loop to monitor the tracer absorbance. Experimental details and derivation of the residence time distribution are presented in Appendix E. The recycle flowrate was set to 10 mL/min, while the inlet flowrate was varied in order to have recycle ratios, R, of 100, 50, 20 and 10.

6.2.4. Gas-liquid mass transfer study

The hydrogenation of styrene to ethylbenzene was performed to demonstrate the applicability of the SLFM reactor in hydrogenation reactions and to study the mass transport rate of hydrogen from the gas to the bulk liquid in the flowing slurry (see Scheme 6.1). Reactions were conducted using 2 M styrene (99%, containing 4-*tert*-butylcatechol as stabiliser), 0.5 M decane (99%) used as internal standard, dissolved in methanol (99.8%). All reagents were purchased from Sigma-Aldrich. The catalyst powder employed in the hydrogenation of styrene was a 5 wt% Pd/C (type 487, Alfa Aesar). Laser scattering analysis (LS 13 320, Beckman Coulter) showed a bimodal distribution of the catalyst particles with two peaks at 25.0 and 52.6 µm, and an overall mean particle size of 23.7 µm with a standard deviation of 17.0 µm (Figure F.7 in Appendix F).
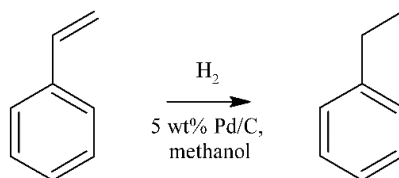
Scheme 6.1. Styrene hydrogenation to ethylbenzene using 5 wt% Pd/C in methanol.

Hydrogenations were performed at 21 °C and under a constant inlet styrene flowrate of 0.050 mL/min. The gas was delivered from a hydrogen generator (PH200, Peak Scientific) and was kept stagnant at 4 bar above the Teflon AF-

2400 membrane. A first set of experiments was performed to investigate the effect of the recycle ratio on styrene conversion under constant inlet flowrate and a catalyst concentration of 0.60 g/L. The recycle flowrate was set to 5, 10 and 20 mL/min, corresponding to an R of 100, 200 and 400. In a second set of experiments, the effect of catalyst concentration between 0.05 and 0.60 g/L was explored under a recycle flowrate of 10 mL/min. This was done to determine the volumetric gas-liquid mass transfer coefficient, $k_L a$. Equation (6.1) shows the ratio between the hydrogen concentration at the membrane-liquid interface, $C_{H2,i}$, and the hydrogen reaction rate, r_{H2} (mol/m^3/s), being equal to the sum of the gas-liquid, liquid-solid, catalyst internal diffusion and surface reaction resistances. By plotting $C_{H2,i}/r_{H2}$ against the inverse of the catalyst concentration, ρ_{cat}, the volumetric gas-liquid mass transfer coefficient, $k_L a$, can be determined by taking the inverse of the intercept on the graph. Details on the full derivation of Equation (6.1) are reported in Appendix F.

$$\frac{C_{H_2,i}}{r_{H_2}} = \frac{1}{k_L a} + \frac{1}{\rho_{cat}}\left(\frac{1}{k_{LS}a_p} + \frac{1}{\eta k'}\right) \tag{6.1}$$

6.2.5. Aerobic oxidation of alcohols

Benzyl alcohol (99.8%), cinnamyl alcohol (98%), geraniol (98%), 1-phenylethanol (98%), 1-phenyl-1-propanol (97%), piperonyl alcohol (98%) and 4-methylbenzyl alcohol (98%) were oxidised in *tert*-butylbenzene (99%), starting from a concentration of 0.1 M. Mesitylene (98%) was used as internal standard at a concentration of 0.05 M. All compounds were purchased from Sigma-Aldrich. The solvent was chosen based on its high boiling point and lower toxicity compared to other solvents (*e.g.* toluene [269]). Furthermore, to demonstrate a solvent-free aerobic oxidation, benzyl alcohol was also oxidised without solvent. Reactions were performed using the 1 wt% Au-Pd/TiO$_2$ catalyst reported in Chapter V, and, aiming to achieve high conversions, a catalyst concentration of 10 g/L, higher than those used in the hydrogenation of styrene, was employed. Batch and continuous reactions were conducted for 6 - 8 h using oxygen (N5.5, BOC) pressurised and kept stagnant above the membrane, except during continuous scaled-up experiments where oxygen

was continuously fed to the reactor *via* a mass flow controller at a constant flowrate of 30 NmL/min. The reaction temperature ranged between 90 and 120 °C and the inlet liquid flowrate was varied between 0.020 to 0.360 mL/min during continuous operations.

6.3. Results and discussion

6.3.1. Macromixing

As in Chapter V, the SLFM reactor was first characterised by studying its macromixing. The resulting normalised residence time distributions (RTD), $E(\theta)$, of the tracer are plotted in Figure 6.4 against the dimensionless time, θ. The RTDs are plotted along with that of an ideal CSTR as a reference (orange line) and the deviation between the two is calculated using the normalised residual sum of squares (*RSS*).
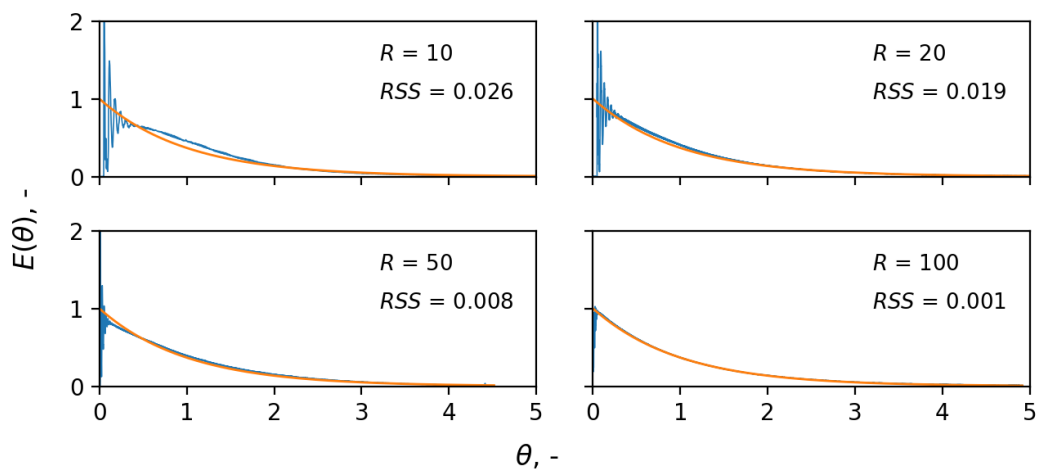
Figure 6.4. Normalised RTDs of a tracer in the slurry loop flat membrane reactor, $E(\theta)$, as a function of the dimensionless time, θ, under a constant recycle flowrate of 10 mL/min and different recycle ratios, *R*, of 10, 20, 50, 100. The orange line indicates the RTD of an ideal CSTR and its deviation from the experimental data (blue line) is highlighted using the normalised residual sum of squares, *RSS*.

It is possible to observe that under a recycle ratio, *R*, of 100, the RTD matches well with that of an ideal CSTR (*RSS* = 0.001). This result is in agreement with the work of Kiwi-Minsker *et al.*, in which the cumulative exit age distribution of a recycle loop reactor operating at a recycle ratio larger than 200 was equal to that of an ideal CSTR [270].

When decreasing the recycle ratio, the RTD started exhibiting more intense oscillations soon after the injection, and a growing deviation from the exponential trend of the ideal CSTR. This is clear for the case of a recycle ratio

of 10, in which periodic spikes of tracer concentrations were visible at earlier times for $\theta < 0.5$, indicating inhomogeneous macromixing. Appendix E reports details of the determination of the E curves and the RSS from the experimental data.

6.3.2. Gas-liquid mass transfer

Styrene hydrogenations were performed to highlight the role of mixing on the Pd/C catalyst performance. While still operating in a CSTR macromixing regime ($R > 100$), the slurry loop flat membrane reactor showed an increase in styrene conversion when the recycle flowrate was changed from 5 mL/min (28%) to 20 mL/min (45%). This could be attributed to an increased dispersion of hydrogen in the slurry flow and to an enhanced shear rate between the catalyst particles and the membrane surface. However, using a recycle flowrate of 10 mL/min conversion was 40%, only *ca.* 10% smaller than that obtained by doubling the recycle flowrate (see Figure F.8).

The catalyst concentration was varied to estimate the average gas-liquid mass transfer coefficient under a recycle flowrate of 10 mL/min (Figure F.9). The ratio between $C_{H2,i}$ and r_{H2} was calculated and plotted against the reciprocal of the catalyst concentration, and a linear fitting was obtained with a R^2 of 0.991 (see Figure 6.5). As expected, when the catalyst concentration was decreased, $C_{H2,i}/r_{H2}$ and thus the overall mass transfer resistance increased. However, the volumetric gas-liquid mass transfer coefficient is independent from the catalyst concentration and equals 1.2 s^{-1} (inverse of the intercept). This indicates that hydrogen had a characteristic diffusion time from the liquid-membrane surface to the bulk liquid of less than one second.

It is worth comparing this value with that of other gas-liquid contactors reported in the literature. Mo *et al.* reported a membrane reactor consisting of a Teflon AF-2400 membrane film sandwiched between two carbon cloth sheets, which separated the flowing liquid from the gas phase [97]. Simulations of the hydrogen transport through the membrane and into the liquid phase were performed to understand the role of the carbon cloth thickness in the gas-liquid mass transfer. It was found that a k_La of 0.3 s^{-1} was achieved with a 0.3 mm thick carbon cloth and in order to obtain a k_La of 1.2 s^{-1} a thickness smaller

than 0.2 mm would be necessary. In comparison, the SLFM reactor could deliver a higher volumetric gas-liquid mass transfer, with only a 0.3 mm deep saturator channel and the slurry being pumped at 10 mL/min. To assess the efficiency of mixing, the specific power input that the pump had to provide during operation, ε, was calculated. This is equal to the power dissipated by circulating the slurry, and can be determined using Equation (6.2) (see Appendix F for details), where Δp_{pump} is the pressure drop across the recirculation pump (0.2 bar) at a recycle flowrate, v_{rec}, of 10 mL/min, and V_R is the reactor volume (1.4 cm^3). This leads to a specific power input of 2.4 kW/m^3.

$$\varepsilon = \frac{\Delta p_{pump} \; v_{rec}}{V_R} \qquad (6.2)$$
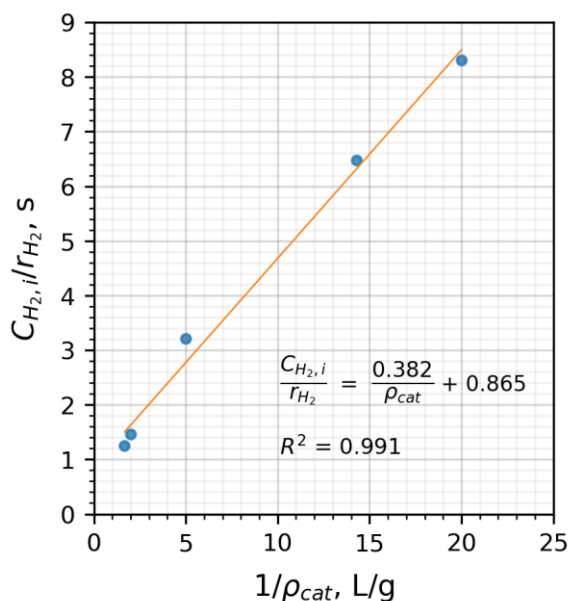
Figure 6.5. Hydrogen gas concentration at the membrane-liquid interface, $C_{H2,i}$, over reaction rate, r_{H2}, against the inverse of the catalyst concentration, ρ_{cat}, in the styrene hydrogenation to ethylbenzene in methanol using a 5 wt% Pd/C powder catalyst. Inlet flowrate: 0.050 mL/min, inlet styrene concentration: 2 M, internal standard: 0.5 M decane, recycle flowrate: 10 mL/min, hydrogen pressure: 4 bar, temperature: 21 °C, reactor volume: 1.4 cm^3.

For comparison, Table 6.1 shows the volumetric gas-liquid mass transfer coefficients and the specific power inputs of various gas-liquid contactors.

The k_La in the SLFM reactor lies within the upper range of the k_La achieved in a stirred slurry reactor [271], or a static mixer [272], but at a much lower volumetric power input. Vice versa, under a comparable specific power input, the SLFM reactor outperformed the reported loop reactor [273], bubble column [274] and Taylor-Couette reactor [275] in terms of gas-liquid mass transfer. Only the reported microreactor could deliver a much higher k_La. This was a micropacked-bed reactor in which gas-liquid mass transfer was investigated in the hydrogenation of cyclohexene over 50 μm Pt/Al_2O_3 catalyst particles under trickle-bed conditions [276]. However, the reactor required a relatively higher dissipation power than the SLFM reactor, due to the pressure drops across the packed-bed that the pump had to overcome.

Table 6.1. Comparison of volumetric gas-liquid mass transfer coefficients and specific power consumptions for different gas-liquid contactors.

Reference	Gas-liquid contactors	k_La, s^{-1}	ε, kW/m^3
Schmitz *et al.* [271]	Stirred slurry reactor	0.01 - 0.8	0.1 - 10
Dutta *et al.* [273]	Loop reactor	0.01 - 0.1	0.1 - 10
Heijnen *et al.* [274]	Bubble column reactor	0.02 - 0.15	0.5 - 3
Kang *et al.* [275]	Taylor-Couette reactor	0.002 - 0.005	1 - 7
Heyouni *et al.* [272]	Static mixer	0.1 - 5	10 - 100
Losey *et al.* [276]	Microreactor	5 - 15	2 - 5
This work	SLFM reactor	1.2	2.4

6.3.3. Continuous operation

To demonstrate the versatility in the operation and the applicability of the slurry loop flat membrane reactor to the aerobic oxidation of alcohols in flow, various primary and secondary alcohols were oxidised. The oxygen pressure was varied between 2 and 6 bar, while the temperature ranged between 90 and 120 °C. During the oxidations, the reactor operated nearly isothermally. As an example, during the solvent-free oxidation of benzyl alcohol performed at a set
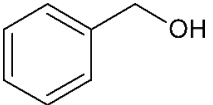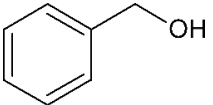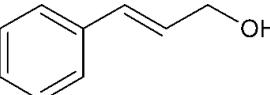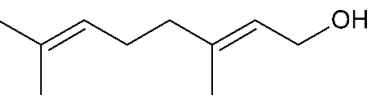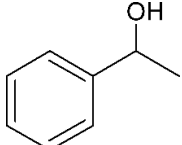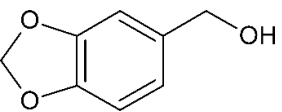
point temperature of 110 °C, the maximum temperature difference in the loop was 4 °C (see Table F.2 in Appendix F).

Table 6.2 shows the alcohol conversion, X, and the corresponding aldehyde or ketone selectivity, S, for each alcohol oxidation reaction. Benzyl alcohol (entry 1, Table 6.2) was oxidised with and without the solvent. In the case of the solvent-free oxidation, a conversion of 50% was achieved with a selectivity of 63% to benzaldehyde at a catalyst contact time of 7.8 $g_{cat} \cdot s/g_{ROH}$, corresponding to an alcohol inlet flowrate of 0.100 mL/min contacting 14 mg of catalyst. In Chapter V it was shown that using the slurry loop tube-in-tube membrane reactor and the same Au-Pd catalyst, 50% conversion and 66% benzaldehyde selectivity were achieved at 110 °C, 5 bar oxygen pressure and under a higher catalyst contact time (16.8 $g_{cat} \cdot s/g_{ROH}$), with a turnover frequency of 12200 h^{-1}. Conversion was similar to that achieved in this work, possibly due to a combination of lower oxygen pressure and higher catalyst contact time. Moreover, an isothermal temperature profile could not be attained within the SLTM reactor, owing to the recirculation pump being outside the oil bath where the reactor was placed. As a result of the different catalyst contact time and a lower average loop temperature, turnover frequency was also lower than 25000 h^{-1} compared to this work. More interestingly, no deactivation of the catalyst was observed during the solvent-free oxidation of benzyl alcohol (see Figure F.11 in Appendix F). Using an inlet concentration of 0.1 M in *tert*-butylbenzene and at 120 °C, benzyl alcohol conversion and benzaldehyde selectivity stabilised to 74% and 84%, respectively. The use of diluted benzyl alcohol hindered the disproportionation reaction to form toluene, which is enhanced at high concentrations of benzyl alcohol [259]. Selectivity to toluene was in fact below 3%, while the selectivity to benzoic acid, resulting from the oxidation of benzaldehyde, was around 5% (Figure F.12).

Cinnamyl alcohol was oxidised at 90 °C and 2 bar oxygen pressure for 7 h (Table 6.2, entry 2). No deactivation was observed in the last 5 h of the reaction and conversion was stable to 75%, while selectivity to cinnamaldehyde was 60% (Figure F.15).

Table 6.2. Continuous aerobic oxidation of various primary and secondary alcohols. Conversion, *X*, aldehyde or ketone selectivity, *S*, and turnover frequency, *TOF*, are presented for different liquid flowrates and catalyst contact times, *CCT*. Unless otherwise stated, reactions were carried out for 6 - 7 h time on stream using 0.1 M of alcohol in *tert*-butylbenzene with 0.05 M mesitylene as internal standard at 120 °C, 5 bar and 1 wt% Au-Pd/TiO$_2$ catalyst at a concentration of 10 g/L in a 1.4 cm^3 reactor volume.

Entry	Substrate		*v*, µL/min	*CCT*, $g_{cat} \cdot s/g_{ROH}$	*X*, % (*S*, %)	*TOF*, h^{-1}
1		solvent-free [a]	100	7.8	50 (63)	25000
		diluted	100	780	74 (84)	385
2[b]			100	600	75 (60)	390
3[c]			20	2700	28 (28)	30
4[d]			80	840	31 (100)	130
5			30	1860	17 (100[e])	27

[a] 110 °C, 6 bar. [b] 90 °C, 2 bar. [c, d] 6 bar. [e] Estimated using GC-MS (see Appendix F)

Wu *et al.* showed that under a similar catalyst contact time (450 $g_{cat} \cdot s/g_{ROH}$), 0.5 M cinnamyl alcohol in toluene was pre-mixed with flowing oxygen at 4 bar and fed into a packed-bed capillary microreactor containing 10 mg of the same Au-Pd/TiO$_2$ catalyst [277]. At 80 °C a stable conversion of 10% was achieved, corresponding to 6 mmol/h/g_{cat}, while at 100 °C conversion dropped from 40% (24 mmol/h/g_{cat}) to 20% (12 mmol/h/g_{cat}) during 7 h of continuous reaction. Selectivity to cinnamaldehyde was higher at 100 °C and equal to 65%. On the other hand, despite operating at a lower oxygen pressure (2 bar), the SLFM reactor could achieve a productivity of cinnamaldehyde of 32 mmol/h/g_{cat} at 90 °C, with a cinnamaldehyde selectivity of 60%. This indicates that when using a catalyst slurry an improvement in performance can be realised compared to packed-bed reactors, owing to the use of smaller catalyst particles that decrease intraparticle diffusional resistances and increase the contact surface area between the catalyst and the reacting liquid. The oxidation of the terpene geraniol (entry 3, Table 6.2) was more challenging. Selectivity to geranial was found to decrease and conversion to increase from the start to the end of the reaction until they both stabilised to 28% in the last three hours of the reaction (Figure F.17). Enache *et al.* found a similar selectivity-conversion trend using Au/SiO$_2$ catalyst in the oxidation of geraniol with and without solvent [44]. Regarding the catalyst activity, under steady-state the average turnover frequency was approximately 31 h^{-1}. This was smaller but of a similar order of magnitude to 71 h^{-1} relative to the overall amount of molar Pd catalyst supported on NaX zeolite, which was reported by Li *et al.* in the solvent-free batch oxidation of geraniol [278].
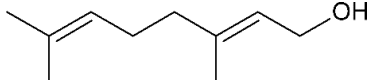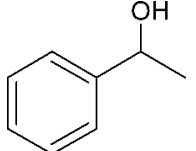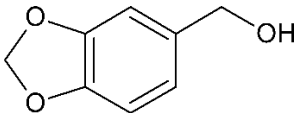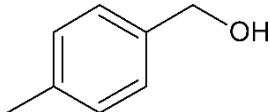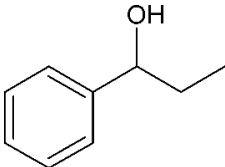
1-Phenylethanol oxidation (entry 4, Table 6.2) proceeded with 100% selectivity to acetophenone for 7 h with a conversion of 31% (see Figure F.18). In their batch oxidation of primary alcohols Enache *et al.* reported an average turnover frequency of 269000 h^{-1} for 1-phenylethanol using a Au-Pd/TiO$_2$ catalyst [46]. This is orders of magnitude higher than that achieved in this work, however the temperature employed was 160 °C. Pascanu *et al.* demonstrated the use of 2 - 3 nm palladium nanoparticles supported on metal organic frameworks, enclosed in a coating of silica nanoparticles for the continuous aerobic oxidation of 1-phenylethanol [279]. The reaction was conducted for 7 days inside a packed-bed reactor under a flowrate of 50 µL/min, and 80% of 0.1 M

of 1-phenylethanol in toluene was continuously converted at 110 °C and 1 bar air pressure using 0.0385 mmol of Pd metal. The *TOF* achieved here was 6 h^{-1} which is two orders of magnitude smaller than that reported in this work (130 h^{-1}), possibly due to a much larger catalyst molar amount (0.0012 mmol). Piperonyl alcohol (entry 5, Table 6.2) was continuously oxidised for 6.5 h with a conversion of 17% and 100% selectivity to piperonal, determined using GC-MS (Figure F.20). In the aerobic oxidations carried out in toluene by Zotova *et al.* in a XCube^{TM} flow reactor over 5% Ru/Al_2O_3 under 5 bar and 90 °C, both piperonyl alcohol and 1-phenylethanol were oxidised to 98% and >99% in 1 h, respectively [71]. Reactions were carried out using 0.29 g of catalyst packed in a cartridge and the alcohol solution was pumped and recirculated from the outlet to the inlet of the catalyst cartridge, in a differential batch reactor mode. The resulting average *TOF* was *ca.* 10 h^{-1} in both cases, lower than that achieved in the work presented here. This could be due to the larger amount of catalyst employed in their work.

6.3.4. Batch operation

In order to achieve higher conversions, the slurry loop flat membrane reactor was operated under batch mode using longer catalyst contact times (see Table 6.3). Geraniol (entry 1, Table 6.3) was oxidised after 7.8 h to 91% conversion, however with a small selectivity (5%) to geranial. Different by-products can result from the oxidation of geraniol, most of which are ascribed to isomerisation reactions [44, 280]. Selectivity to geranial could be improved at high conversion by using different catalysts such as chromium supported on mesoporous molecular sieves as presented by Dapurkar *et al.* [281], or by using small Pd nanoparticles as highlighted in the work of Li *et al.* [278]. 1-Phenylethanol was oxidised to completion after 6 h of batch reaction (entry 2, Table 6.3), with a selectivity of 72% to acetophenone, smaller than that achieved in the continuous mode (entry 4, Table 6.2). Similarly, piperonyl alcohol was oxidised to almost completion (98%), at a 6.6 times higher catalyst contact time with respect to the continuous reaction. Selectivity to piperonal was about 65% and by-products including piperonylic acid and 3,4-methylenedioxy toluene were also detected (Figure F.21).

Table 6.3. Batch aerobic oxidation of various primary and secondary alcohols. Conversion, X, and aldehyde or ketone selectivity, S, are presented for different reaction times and catalyst contact times, CCT. Unless otherwise stated, reactions were carried out using 0.1 M of alcohol in *tert*-butylbenzene with 0.05 M mesitylene as internal standard at 120 °C, 5 bar and 1 wt% Au-Pd/TiO$_2$ catalyst at a concentration of 10 g/L in a 1.4 cm^3 reactor volume.

Entry	Substrate	t, h	CCT, $g_{cat} \cdot s/g_{ROH}$	X, % (S, %)
1		7.8	18300	91 (5)
2		6.0	17580	98 (72)
3		5.2	12300	98 (65[a])
4		6.3	18420	72 (63)
5		6.4	16860	31 (22)

[a] Estimated using GC-MS (see Appendix F)
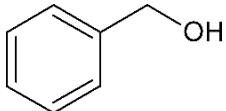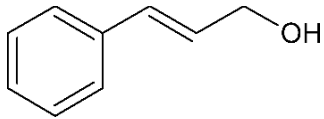
Two further molecules were oxidised in batch: 4-methylbenzyl alcohol (entry 4, Table 6.3) and 1-phenyl-1-propanol (entry 5, Table 6.3). The former was oxidised to 72% conversion, 63% of which to 4-methylbenzaldehyde, while the secondary alcohol reached a conversion of 31% with a selectivity to propiophenone of 22%.

6.3.5. Scaled-up continuous operation

Increase in productivity was demonstrated by using a larger reactor volume and higher inlet flowrates in the benzyl and cinnamyl alcohol aerobic oxidations (see Table 6.4).

The 7 h long solvent-free oxidation of benzyl alcohol (entry 1, Table 6.4) proceeded at a conversion of 35% and a selectivity to benzaldehyde of 59% (Figure F.13). The reaction was performed at a *CCT* of 22.8 $g_{cat} \cdot s/g_{ROH}$, 2.9 times higher than that shown in Table 6.2, entry 1. However, despite the longer catalyst contact time, a lower conversion was realised (*vide supra*). This could have been caused by a lower oxygen pressure employed in the reaction and also by an inadequate insulation of the loop extension, which in turn could have lowered the average reaction temperature. Nevertheless, a benzaldehyde amount of 19 g was achieved after 7 h. The benzaldehyde productivity resulting from this reactor can be compared to that from a scaled-up packed-bed flat membrane reactor where the same catalyst was used for the solvent-free aerobic oxidation of benzyl alcohol [186]. At 120 °C and 8.2 bar oxygen pressure, Wu *et al.* reported a 58% conversion with a 69% benzaldehyde selectivity using a flowrate of 50 µL/min and 1 g of packed catalyst. Comparing these results with the conversion, selectivity and flowrate employed in this work, the SLFM reactor achieved a 2.3 times higher benzaldehyde yield than that of the scaled-up packed-bed membrane reactor.

Table 6.4. Continuous aerobic oxidation of benzyl and cinnamyl alcohols. Conversion, X, aldehyde selectivity, S, and mass of final product, m_{CHO}, are presented for different liquid flowrates and catalyst contact times, CCT. Unless otherwise stated, reactions were carried out for 6 - 7 h time on stream using 0.1 M of alcohol in *tert*-butylbenzene with 0.05 M mesitylene as internal standard, 1 wt% Au-Pd/TiO$_2$ catalyst at a concentration of 10 g/L and using an oxygen flowrate of 30 NmL/min, in a 8.8 cm^3 reactor volume. Temperature and oxygen pressure: 120 °C and 5 bar (benzyl alcohol), and 100 °C and 2 bar (cinnamyl alcohol).

Entry	Substrate		v, μL/min	CCT, g$_{cat}$·s/g$_{ROH}$	X, % (S, %)	m_{CHO}, g
1	benzyl alcohol	solvent-free	220	22.8	35 (59)	19
		diluted	360	1380	84 (86)	1.2
2	cinnamyl alcohol		220	1980	65 (51)	0.4

Furthermore, if the outlet flowrate of benzaldehyde is related to the amount of catalyst in the reactor, the slurry loop flat membrane reactor produced 26 times higher yield of benzaldehyde per mg of Au-Pd/TiO$_2$ catalyst. This was due to the smaller amount of catalyst employed in this work, which shows again the superior performance of the SLFM reactor in terms of catalyst usage, compared to a membrane packed-bed reactor. As there are aerobic oxidations that require longer catalyst contact times, scaled-up continuous oxidations were also performed in *tert*-butylbenzene using an inlet concentration of 0.1 M. Benzyl alcohol reacted with 84% conversion and 86% selectivity (Figure F.14), yielding 1.2 g of benzaldehyde after 6 h reaction. Similarly, cinnamyl alcohol was oxidised (entry 2, Table 6.4) with a 65% conversion, 51% of which to 0.4 g cinnamaldehyde after 6.5 h continuous reaction (Figure F.16).

6.3.6. Safety considerations

Despite the presence of a membrane that prevented the direct contact between the gaseous oxidant and the organic substrates, explosive mixtures can form in the gas phase due to the pervaporation of organic molecules from the slurry, diffusing through the membrane and into the oxygen phase. During the scaled-up oxidations, oxygen was fed at 30 NmL/min and any organic vapours pervaporating through the membrane were condensed from the gas outlet using a cold trap, to measure their pervaporation rate. Using *tert*-butylbenzene as a solvent in both the benzyl and cinnamyl alcohol oxidation, no condensed organics were detected at the gas outlet. However, in the solvent-free oxidation of benzyl alcohol an average mass flowrate of 57 mg/h of organics pervaporated throughout the reaction time, showing that *ca.* 0.2% of organics was present on average at any time in the flowing oxygen (Table F.3 in Appendix F). This value is below the lower flammability limit (*LEL*) of toluene (1.1%) which is the lowest *LEL* in a mixture with benzyl alcohol and benzaldehyde in oxygen (see Appendix F). Therefore, it is possible to conclude that the continuous aerobic oxidation of benzyl alcohol was operated under safe conditions.

6.4. Summary and conclusions

This study demonstrates a novel slurry loop flat membrane reactor for the aerobic oxidation of various primary and secondary alcohols to aldehydes and ketones. The excellent performance, combined with a safe operation and plug-and-play configuration, makes this reactor an ideal platform for performing sustainable liquid phase aerobic oxidations. Homogeneity and perfect mixing behaviour were achieved at recycle ratios higher than 100, and an isothermal temperature profile was accomplished during reaction. Gas-liquid mass transfer was characterised in the hydrogenation of styrene in methanol with a Pd/C catalyst, and a k_La value of 1.2 s^{-1} was achieved under a moderate 2.4 kW/m^3 specific power consumption, which is relatively small compared to other gas-liquid contactors. The reactor could be operated under continuous mode using a crossflow filter that kept the catalyst flowing inside the loop while withdrawing liquid from the outlet. Continuous alcohol oxidations in this slurry loop flat membrane reactor showed enhanced turnover frequencies compared to those achieved in a packed-bed reactor, where oxygen was pre-mixed with the organic substrate. This was due to the smaller amount of catalyst employed and to the resulting reduction of intraparticle diffusion resistances. An example of solvent-free continuous oxidation was demonstrated with benzyl alcohol, achieving a turnover frequency of 25000 h^{-1}, higher than the previously reported slurry loop tube-in-tube membrane reactor. Under batch mode and longer catalyst contact times, higher conversions could be attained, yet this resulted in lower selectivities. Increased productivity was demonstrated by enlarging the loop volume and using higher inlet flowrates. A maximum of 19 g of aldehyde was obtained in the solvent-free oxidation of benzyl alcohol after 7 h of continuous reaction. This result is 26 times higher than the productivity per amount of catalyst achieved by a membrane packed-bed reactor employing the same Au-Pd catalyst. Safety hazards associated with the pervaporation of the organics were overcome by using 30 NmL/min of flowing oxygen, which reduced the concentration of volatile organics below their lower flammability limit in oxygen and allowed a safe operation.

Chapter VII. Taylor-vortex membrane reactor for continuous gas-liquid reactions
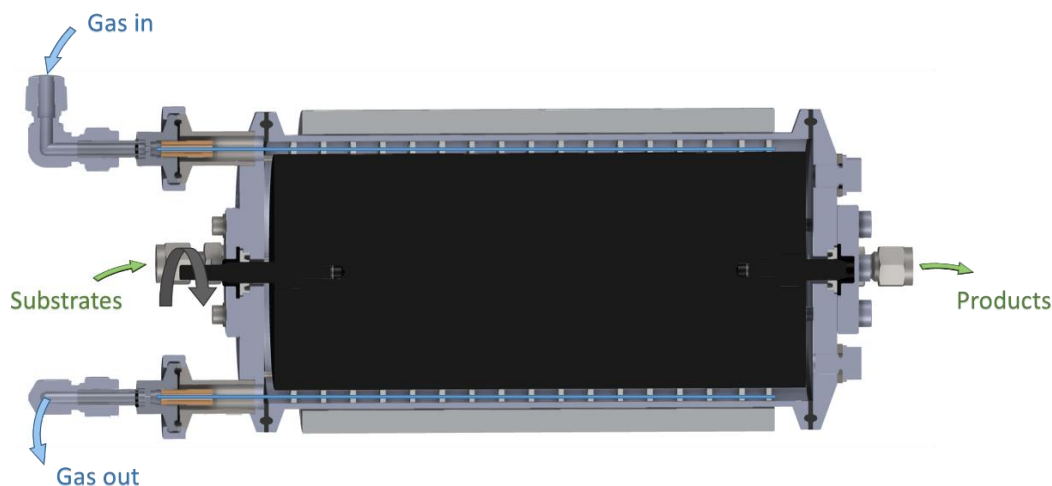
An intensified Taylor-vortex membrane reactor (TVMR) is presented for the first time, combining the benefits of a flexible baffle system that divides the annular gap in segregated compartments, hindering axial dispersion, and a supported tubular membrane for safe gas-liquid reactions. The annulus volume of approx. 330 mL between the PEEK rotor and the cylindrical stainless steel vessel was filled with 17 PTFE baffles, supported by 6 metallic rods and spaced by 10 mm. These covered the annular section and had holes for inserting the membrane along the rotor direction, which surrounded the rotor and bent in U-shapes at each end of the baffle system. The TVMR showed a plug-flow behaviour at 4 mL/min, outperforming the unbaffled reactor with a 5 - 12 times lower axial dispersion coefficient. At high rotor angular speeds, a narrower residence time distribution was observed compared to a reported ribbed-rotor Taylor-vortex reactor. In the continuous aerobic oxidation of benzyl alcohol using the $Pd(OAc)_2$/pyridine catalyst in toluene at 100 °C and 11 bar oxygen pressure, the reactor achieved a stable 30% conversion and 85% benzaldehyde selectivity, and was operated for 7 h. No pervaporation of organics through the membrane was detected, making this reactor a safe and scalable tool for continuous gas-liquid reactions.

7.1. Introduction

Multiphase reactions are omnipresent in industry and reactor design plays an important role in chemical process development, affecting interphase micromixing, reactant mass transfer and residence time distribution [3, 5]. When scaling out continuous reactors, flow patterns and transport phenomena vary differently as a function of the scale and need to be thoroughly assessed in order to preserve process performance and safety [10, 98, 282]. Furthermore, it is desirable to keep a low reaction space-time, while at the same time intensifying the micromixing to avoid compromising the catalyst performance and more generally the reaction rate.

Taylor-vortex reactors are continuous reactors characterised by efficient mass and heat transfer and whose mixing can be tuned by changing their operating conditions. For these reasons they have been successfully employed at different scales and in different applications such as in polymerisations [283, 284], photo- [285-287], electro- [288, 289], biochemistry [290, 291], crystallisation [292], graphene production [293, 294] and homogenous catalysis [295]. Mixing in a Taylor-vortex reactor under continuous axial flow has been the subject of many works [296-302]. A Taylor-vortex reactor consists of a cylindrical rotor inside a concentric cylindrical vessel and the fluid in the annulus can experience different fluid dynamic conditions depending on the rotational speed of the rotor. In particular, above a critical value of the rotor angular speed the hydrodynamic instability of the centrifugal fluid flow generates toroidal vortices around the rotor [303]. These can enlarge the specific contact surface between reacting phases and form a series of CSTRs that can narrow the residence time distribution. At a low rotor speed, the reactor is characterised by a low inter-vortex (macromixing) and intra-vortex mixing (mesomixing). However, at increasing rotational speeds, the degree of mixing gradually increases at all scales until full backmixing is achieved.

An attempt to decrease the axial dispersion at high rotor angular speeds by modifying the rotor geometry has been demonstrated in the works of Richter *et al.* [304, 305]. The rotor was segmented by horizontal ribs and their effect on mixing was compared to a conventional cylindrical rotor. The ribbed rotor increased vortex segregation, enabled toroidal vortices to be immobilised,

shifted the onset of turbulence to higher rotor speeds and eventually narrowed the liquid residence time distribution. However, a gap between the outer surface of the rotor ribs and the inner surface of the vessel can facilitate fluid bypass. Furthermore, an irreversible modification on the rotor leaves the operator with no option of flexibility.

In this work, the first example of a Taylor-vortex reactor with a tubular membrane is demonstrated for gas-liquid reactions. This consists of a basic cylindrical rotor rotating concentrically in a cylindrical vessel, but with a flexible and replaceable system of horizontal baffles in the annulus. The baffles completely fill the annular gap and divide the annulus into several axially segragated compartments, hindering inter-vortex bypass. At the same time, this baffle system supports a tubular gas membrane that is wound in the annulus around the rotor to maximise the surface area for gas delivery in gas-liquid reactions.

7.2. Materials and methods

7.2.1. Reactor design

The Taylor-vortex membrane reactor (TVMR, Figure 7.1) was developed in collaboration with Autichem Ltd, and it is based on a cylindrical rotor that rotates around its axis inside a cylindrical vessel. The vessel has an internal diameter of 97.6 mm and a length of 202 mm, and it is sealed on two flanges using 4'' high-pressure tri-clamps (Advanced Couplings Limited) and a PTFE envelope gasket on each side. Inside the vessel, a 196 mm-long carbon-filled poly ether ketone (PEEK) cylindrical rotor with a diameter of 87.6 mm is fitted in the inlet flange *via* a Kefloy rotary seal (MupuSeal) (Figure 7.2). The inlet flange has four ports, two of which are designed for the gas inlet and outlet. The gas ports are 33.5 mm long with an inner diameter of 9.5 mm, and a PEEK 1/4 28 UNF nut is hosted in each port for sealing the tubular membrane (see Figure 7.2). These nuts are screwed inside two outer clamp ferrules, that contain the gas for reaction, and which are sealed with the two gas ports using ½'' high pressure tri-clamps (Advanced Couplings Limited) and PTFE envelope gaskets. The other two ports on the inlet flange are ¼'' Swagelok connections that can be used for introducing the liquid reactants. Similarly and symmetrically to the inlet flange, the outlet side of the reactor hosts only two ports for the liquid outlet.
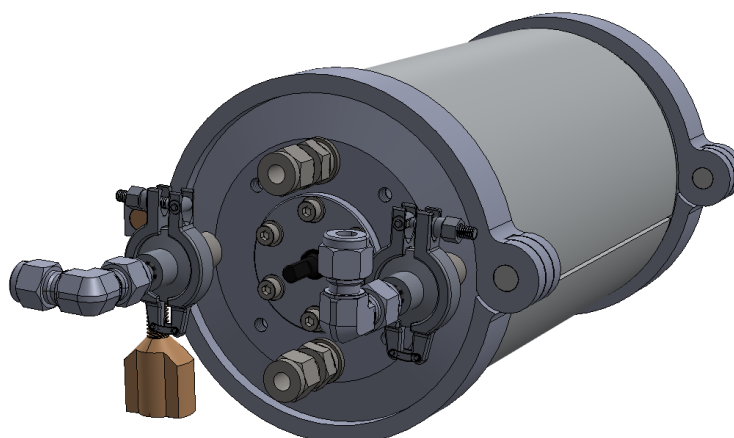
Figure 7.1. Perspective view of the Taylor-vortex membrane reactor.
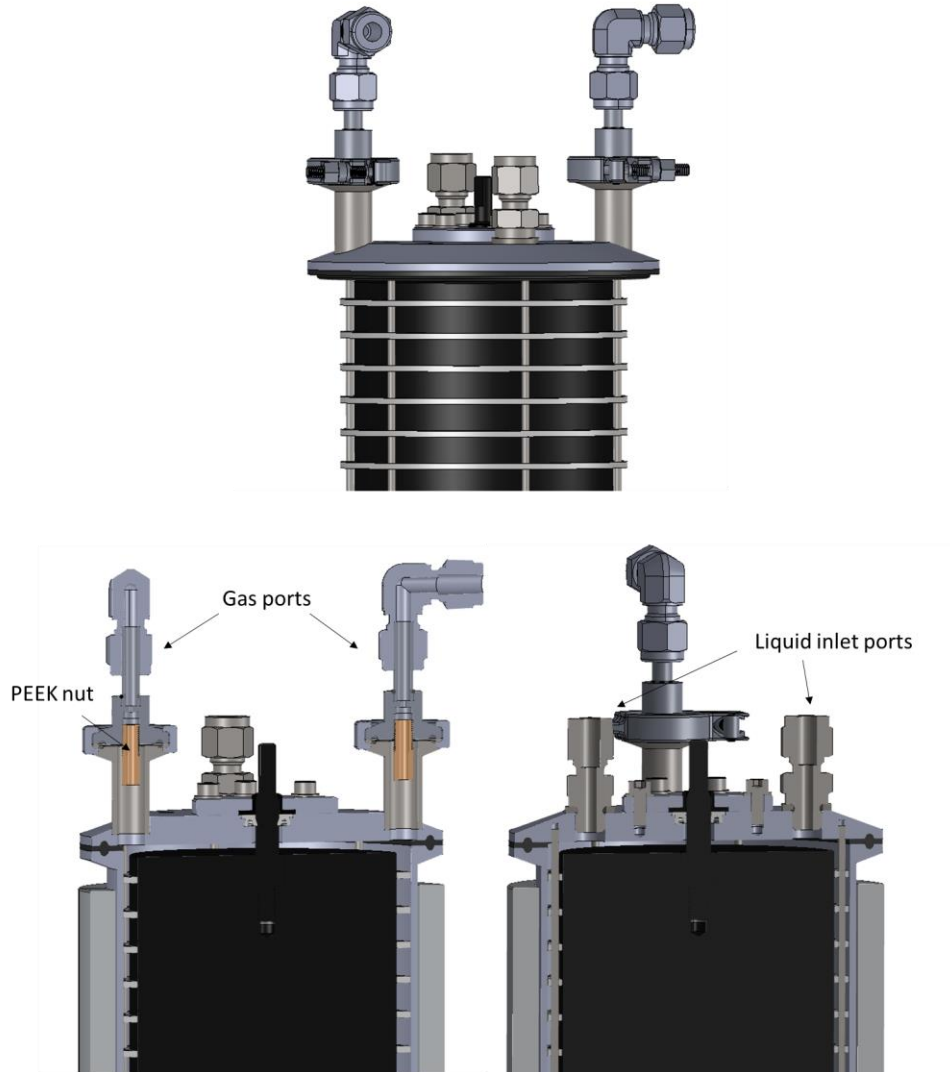
Figure 7.2. Inlet side of the Taylor-vortex membrane reactor (top), with sections of the gas inlet and outlet (bottom left) and the liquid inlet ports (bottom right).

Surrounding the rotor, six equispaced stainless steel threaded studs (M2.5 x 196 mm) are screwed on the liquid side of the inlet flange. They support a system of 17 horizontal baffles that divide the annulus in 18 axially segregated sections. The baffles are rings made of PTFE, with a thickness of 1.3 mm, and an inner and outer diameter of 87.6 and 97.5 mm. To avoid friction between the baffles and the rotor, which would cause them to twist during operation, the PTFE rings are polished on the inner diameter with sandpaper.

The baffles can have different features according to the membrane that needs to be fitted (see Figure 7.3). Each baffle is separated by 10 mm using stainless

steel hollow cylinder spacers (2.5 mm ID, 3 mm OD, 10 mm long), inserted in each threaded stud and between adjacent baffles. The reason for having an interbaffle spacing-to-annulus gap ratio of 2:1, with the baffle spacing being 10 mm and the annulus gap of 5 mm, is to maximise the Taylor vortex velocity, as informed by COMSOL Multiphysics® 5.5 simulations (see Appendix G).
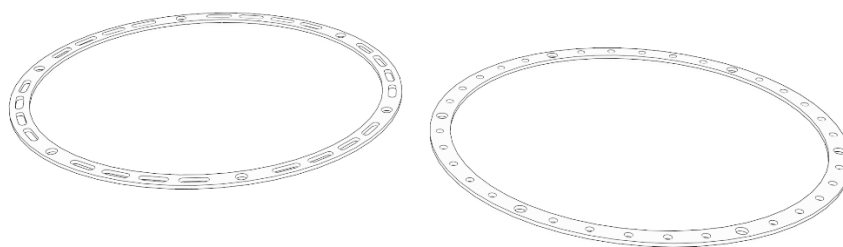
Figure 7.3. PTFE baffle ring with slots (left) and circular holes (right) used to support the membrane in the Taylor-vortex membrane reactor.

To demonstrate the use of a membrane in a gas-liquid reaction, a 6 m long polyfluoro alkoxy (PFA, 1/16'' OD x 0.040'' ID, Idex) tube was inserted inside the structrure of baffles around the rotor. The type of baffle used to support the PFA membrane is shown in Figure 7.3 (right). This had 36 equidistributed holes, 6 of which with a diameter of 2.7 mm and the remaining 30 with a 1.5 mm wide hole. In the larger holes the threaded studs were inserted to provide mechanical support to the baffles, while the smaller ones were used to insert and weave the gas membrane inside the annulus and around the rotor.

PFA has been successfully used in a previous study as a tubular membrane for oxygen delivery inside a stainless steel vessel containing the liquid substrate during gas-liquid aerobic oxidation of alcohols [171]. For this reason and for ease of installation, the PFA tubular membrane was selected to be tested in the TVMR. However, the reactor offers the possibility to install any flexible tubular membrane by using baffles with different hole diameters. To seal the membrane, the two high pressure tri-clamps were opened and the PFA tube was connected to the two PEEK 1/4''-28 UNF nuts present in each gas port (see Figure 7.2), which were screwed on the outer clamp ferrules to ensure the sealing and the separation of the liquid from the gas phase. The tri-clamps were then reconnected to seal the liquid from the outside. Figure

7.4 shows a picture of the reactor with and without the outer vessel, and the PFA tubular membrane inserted through the baffles along the axial direction, bending in U-shapes at each end of the baffle system. Once the wound membrane spanned the whole azimuthal coordinate around the rotor, it was bent around the baffles at 180° to connect to the outlet gas port.
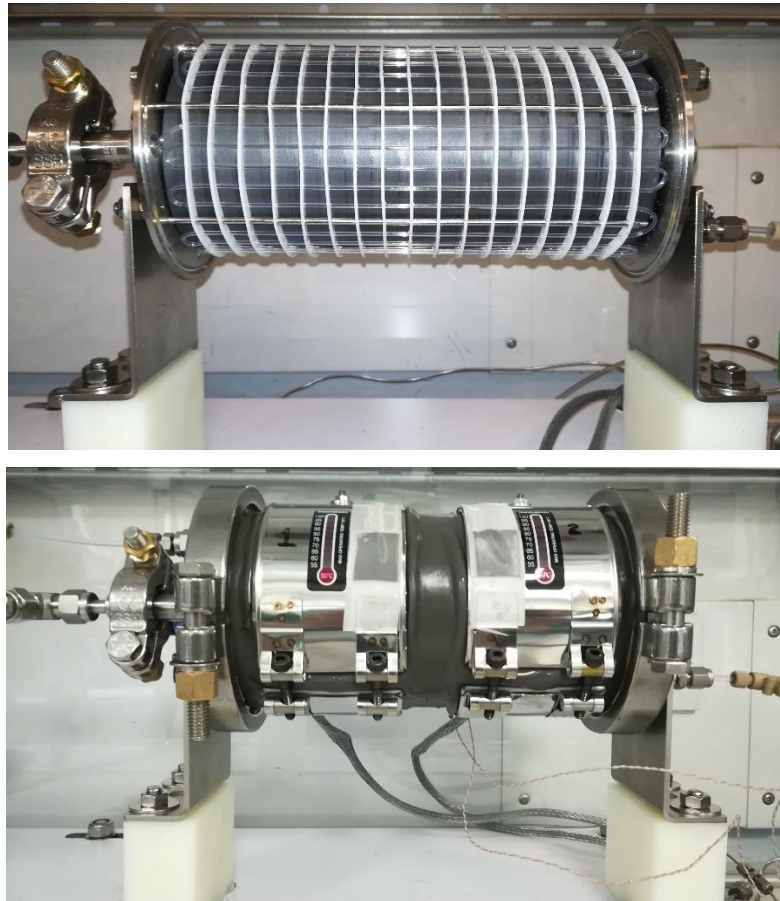
Figure 7.4. Taylor-vortex membrane reactor without the outer vessel, showing the tubular membrane wound around the rotor (top), and with the outer vessel together with the two external heaters (bottom).

The reactor was manufactured using off-the-shelf industrially tried and tested components, with only the rotor and baffles being bespoke designs. Therefore, the TVMR design benefits from an established and cost effective manufacture methods and offers a viable route to larger scales.

7.2.2. Setup description and operation

The schematic and the picture of the setup are shown in Figure 7.5 and 7.6. The rotor was connected to a drive (Masterflex L/S 7524-55, Cole Parmer) with adjustable speed *via* a flexible coupling. The substrate and catalyst solutions were separately delivered using high pressure dual piston pumps. The Azura P2.1S Knauer for the catalyst and the Vapourtec R2 pump for the substrate solution, were both connected to the two inlet ports on the reactor flange. On the outlet flange, one of the two liquid outlet ports was connected to a liquid back-pressure regulator (BPR, Zaiput), while the second one was closed with the process thermocouple (T type, RS Components). The BPR maintained the desired liquid pressure upstream using a gas pressure regulator (KPR, Swagelok) on the nitrogen line connected to the BPR. Liquid products were collected in a 250 mL glass vessel (Schott) which was occasionally emptied to avoid overfilling. The liquid pressure was constantly monitored using a pressure sensor (PX309, Omega) connected to the substrate inlet line. This was kept 1 bar higher than the gas pressure, in order to avoid breakthrough of the gas into the organic solution inside the reactor.
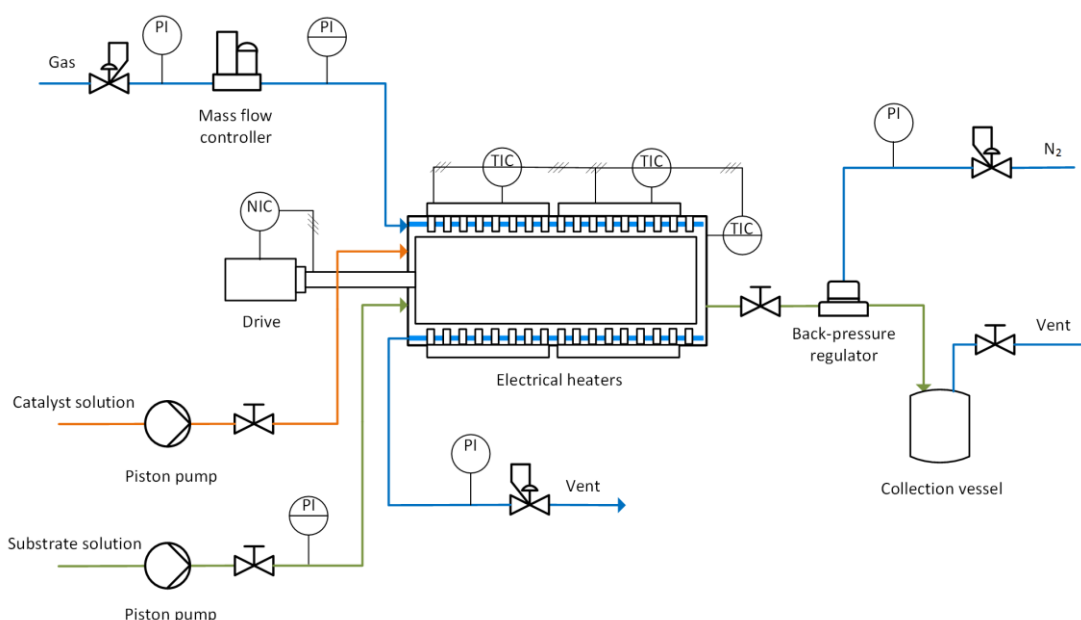
Figure 7.5. Schematic diagram of the Taylor-vortex membrane reactor setup for continuous gas-liquid reactions. PI: pressure indicator, TIC: temperature indicator and controller, NIC: angular speed indicator and controller.

Gas was fed into the membrane inlet port after having reduced its pressure using a gas pressure regulator (KPR, Swagelok) and adjusted its flowrate with a mass flow controller (4850, Brooks). The gas outlet port on the reactor inlet flange was connected to a gas back-pressure regulator (KBP, Swagelok) to maintain a constant gas pressure upstream.
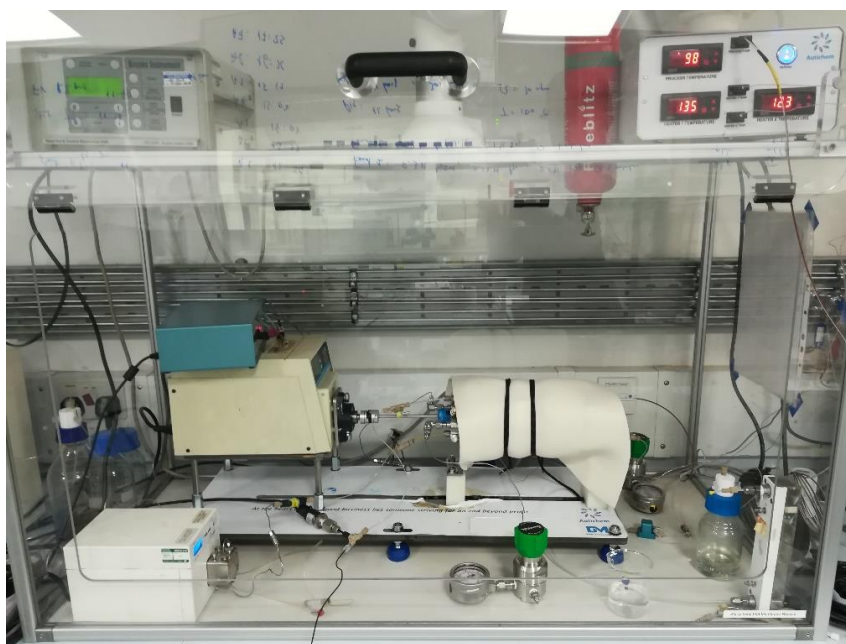
Figure 7.6. Picture of the Taylor-vortex membrane reactor setup for continuous gas-liquid reactions.

High temperature could be attained using two Mica band heaters (500 W, Elmatic) that surrounded the outer vessel of the reactor. Their power was controlled by a supervisory control box to which the process thermocouple (T type, RS Components) was connected and plugged inside the reactor outlet flange to measure the outlet temperature. As the two heaters could reach a maximum temperature of 300 °C, an additional thermocouple was embedded under each of them to control and limit their output power, by measuring the jacket temperature. Along with the target process temperature, the supervisory box required to specify the maximum differential temperature between the jacket, measured by the two heater thermocouples, and the process temperature, measured by the process thermocouple. This avoided exposing the reactor to excessively high wall temperatures. Furthermore, between the Mica band heaters and the reactor vessel a 2 mm silicon thermal interface pad

(4.5 W/m/K, RS components) was used to fill the gap and increase heat transfer on the reactor walls. Finally, to provide external insulation, a 6.35 mm thick silicone rubber sheet (Silex Silicones) was wrapped around the reactor.

7.2.3. Macromixing study

Macromixing was evaluated by studying the residence time distribution (RTD) of a tracer in the Taylor-vortex membrane reactor. Experiments were conducted by performing a pulse-input injection of a tracer (see Appendix E for details on macromixing studies). The Taylor-vortex membrane reactor was run at an agitation speed of 10 - 80 rpm and the RTD was studied at a pump flowrate of 4 and 6 mL/min. Furthermore, for comparison and to understand the effect of the baffles and the membrane on mixing, the RTD was studied in the reactor with neither the baffles nor the membrane at a similar flowrate of 4 mL/min.

Appendix E reports the derivation of the $E(t)$ function and the mean residence time and Equation (7.1) shows the tracer concentration variance, σ^2, determined by integrating the second moment of $E(t)$. Using the closed-closed vessel boundary conditions, and assuming a perfect pulse at the liquid inlet, the dispersion number, D_{ax}/uL, which describes the extent of the axial mixing, can be calculated by solving the non-linear Equation (7.2), which is valid for large deviations from plug-flow ($D_{ax}/uL > 0.01$) [306]. The dispersion number is a dimensionless number defined as the ratio between the dispersion coefficient D_{ax}, and the product between u, the average axial velocity, and L, the distance between the inlet and the outlet.

$$\sigma^2 = \int_0^\infty (t - \tau)^2 \, E(t) dt \tag{7.1}$$

$$\frac{\sigma^2}{\tau^2} = 2 \left(\frac{D_{ax}}{uL}\right) - 2 \left(\frac{D_{ax}}{uL}\right)^2 \left(1 - e^{-\frac{uL}{D_{ax}}}\right) \tag{7.2}$$

In order to describe the fluid dynamic regime occuring in the Taylor-vortex system, dimensionless numbers can be used. The Taylor number, Ta, defined in Equation (7.3) describes the ratio between rotational inertial and viscous forces [304]. In this equation, Ω is the rotational speed (rad/s), r_i the rotor

radius, r_o the internal radius of the vessel and v the kinematic viscosity of the fluid. The axial inertial forces are characterised by the axial Reynolds number, Re, defined in Equation (7.4).

$$Ta = \frac{\Omega r_i (r_o - r_i)}{v} \tag{7.3}$$

$$Re = \frac{u(r_o - r_i)}{v} \tag{7.4}$$

The dispersion number also depends on the physical properties of the liquid, which are generally characterised by the Schmidt number, Sc, defined in Equation (3.7). Table 7.1 reports the reactor geometrical and fluid properties for this work.

Table 7.1. Reactor and fluid properties in the Taylor-vortex membrane reactor during the macromixing studies, including the tracer molecular diffusivity, D_m, water viscosity, v, rotor, r_o, and inner vessel radius, r_i.

Property	Value
r_i, m	0.0438
r_o, m	0.0488
v, m^2/s	10^{-6}
D_m [307], m^2/s	$6.4 \cdot 10^{-10}$

7.2.4. Continuous aerobic oxidation

The reactor was tested in the continuous aerobic oxidation of benzyl alcohol using the Pd(OAc)$_2$/pyridine homogeneous catalyst system, developed and used in other works [100, 308, 309]. Reaction was conducted at 100 °C and 11 bar oxygen pressure in toluene for 7 h, 2 h of which was required for start-up and 1 h for shut-down.

Prior to reaction, the reactor was placed vertically and loaded with a toluene solution of 0.15 M benzyl alcohol (99.8%, Sigma-Aldrich) and 0.1 M mesitylene (98%, Sigma-Aldrich), used as internal standard. After connecting the reactor to the gas and liquid lines, the drive was switched on and the angular speed was set to 30 rpm. Two solutions were pumped into the reactor, one containing

the substrate and the other the homogeneous catalyst. The substrate solution was made of 0.3 M benzyl alcohol, 0.12 M pyridine (> 99.5%, Alfa Aesar) and 0.1 M mesitylene, dissolved in toluene (HPLC grade, Fisher Scientific). The second solution was made of 0.03 M $Pd(OAc)_2$ (47.5% Pd, ACROS Organics) and 0.1 M mesitylene in toluene. The two solutions were pumped separately at 2 mL/min each and mixed inside the reactor, generating a total flowrate of 4 mL/min. The Zaiput back-pressure regulator was set to 12 bar and after the liquid pressure reached that value, oxygen (N5.5, BOC) was fed at a constant flowrate of 30 NmL/min and pressure of 11 bar into the 6 m long PFA tubular membrane (1/16'' OD x 0.040'' ID, Idex) [171]. The gas back-pressure regulator was venting the outlet oxygen gas in a GC vial immersed in an ice bath, in order to condense any volatile organics pervaporating through the membrane during reaction. The heaters were switched on and the process temperature setpoint was set to 100 °C, with a maximum allowed temperature for the heaters of 140 °C. Gas chromatography (7820A, Agilent Technologies) was used to analyse the liquid products using an automatic liquid sampler, a HP-INNOWAX (19091-133) capillary column and a flame ionisation detector.

7.3. Results and discussion

7.3.1. Macromixing study

The residence time distribution of the tracer in the TVMR was characterised at different angular speeds and compared to the unbaffled Taylor-vortex reactor (u-TVR) at 4 mL/min inlet flowrate. Figure 7.7 shows two examples of normalised RTDs, one for the TVMR and the other relative to the u-TVR, plotted against the dimensionless time residence time. The two RTDs were obtained at 10 rpm (Ta = 229) and 4 mL/min inlet flowrate (Re = 0.23) and it is possible to observe that a much larger variance characterised the u-TVR.
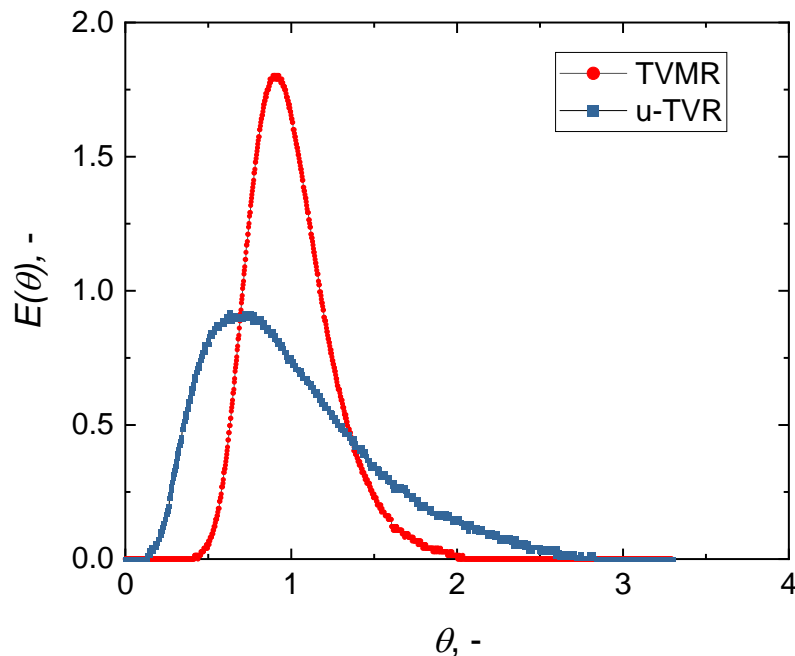
Figure 7.7. Residence time distribution, $E(\theta)$, in the Taylor-vortex membrane reactor (TMVR) and in the unbaffled Taylor-vortex reactor (u-TVR). Inlet flowrate: 4 mL/min (Re = 0.23), rotor angular speed: 10 rpm (Ta = 229).

For each inlet flowrate, the average residence time for the TVMR was determined at different agitation speeds, which was 71 min at 4 mL/min, corresponding to a liquid volume of approx. 280 mL. On the other hand, the tracer in the u-TVR had an average residence time of 83 min, which corresponded to a volume occupied by the liquid of *ca.* 330 mL, 50 mL higher then the TVMR due to the absence of the baffles and the membrane.

From the analysis of all the RTDs, the average residence time for the various agitation speeds varied within ±6.1%.

Figure 7.8 shows the dispersion number of the TVMR and the u-TVR for a range of Taylor numbers. As a reference, the dispersion numbers for 10 and 20 CSTRs in series are reported. The number of CSTRs in series, N, can be correlated to the dimensionless variance, σ^2/τ^2, of Equation (7.2) using Equation (7.5) [306].

$$\frac{\sigma^2}{\tau^2} = \frac{1}{N} \tag{7.5}$$
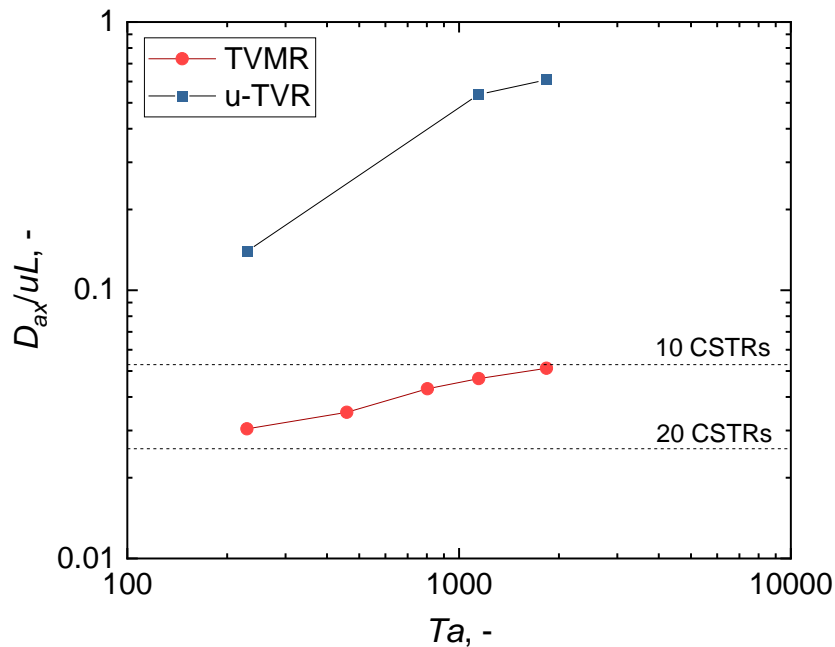
Figure 7.8. Dispersion number, D_{ax}/uL, in the Taylor-vortex membrane reactor (TMVR) and in the unbaffled Taylor-vortex reactor (u-TVR). The dispersion numbers for 10 CSTRs and 20 CSTRs in series are reported as a reference. Inlet flowrate: 4 mL/min ($Re = 0.23$).

It is possible to observe that the dispersion number for the TVMR increased almost linearly in a log-log plot at increasing angular speed, from 0.030 ($N = 16.9$) at $Ta = 229$ (10 rpm) to 0.051 ($N = 10.3$) for $Ta = 1835$. The discrepancy between the TVMR and the unbaffled reactor (u-TVR) is of one order of magnitude. In fact, the dispersion number for the u-TVR increased rapidly from

0.140 ($N = 4.2$) to 0.609 ($N = 1.6$) for the same values of Taylor number. It is interesting to observe that the highest equivalent number of CSTRs achieved in the TVMR was 17 (16.9) at 10 rpm, which is similar to the number of the actual 18 compartments that axially divide the reactor.

To explain these differences, it is important to note that mixing in a Taylor-vortex reactor is closely bound to the fluid dynamic regime inside the annulus [298, 310]. At a low angular speed of the rotor, the fluid in the annulus of an unbaffled TVR is characterised by a laminar Couette flow [311]. This consists of a purely azimuthal laminar flow around the rotor. At increasing speed of the rotor, this flow transitions into a laminar Taylor-vortex flow, defined by the presence of laminar counter-rotating toroidal vortices surrounding the rotor and stacked on one another. For higher values of the Taylor number, the flow regime changes into a wavy vortex flow which is time-dependent and the stacked Taylor vortices transition into azimuthal waves. At even higher Taylor numbers, the flow becomes modulated and finally turbulent [310, 312]. In the study of Dusting *et al.* conducted in an unbaffled TVR, at $Ta = 330$ the intravortex mixing times were found to be shorter than the intervortex ones and the azimuthal mixing was faster than that in the meridian plane inside the vortex. However, at $Ta = 950$, near the onset of a wavy-flow regime, intervortex mixing times were reduced due to possible axial fluctuations [303]. This explains why an increase in the Taylor number is associated with an increase in the axial dispersion coefficient. Recktenwald *et al.* derived the critical Taylor numbers, Ta_c, above which the first flow instability between a laminar Couette and a Taylor-vortex flow occurs [311]. The Ta_c is a function of the axial Reynolds number and the ratio between the rotor diameter and the vessel inner diameter. Given a 0.90 diameter ratio and a $Re = 0.23$, the unbaffled reactor of this work has a critical Ta_c of 130, corresponding to an agitation speed of 5.7 rpm. Using the fluid dynamic intervals reported by Nemri *et al.* for a ratio between the rotor diameter and the vessel inner diameter of 0.85, the u-TVR would experience a wavy vortex flow regime for Ta between 172 and 707 [310]. However, for Ta values up to 1192 the flow regime would lie within the modulated wavy flow, while above this value the flow would be turbulent. Therefore, it is possible to assume that the dispersion numbers for the unbaffled TVR (see Figure 7.8) were obtained in three different flow regimes:

a wavy vortex flow regime at $Ta = 229$ ($D_{ax}/uL = 0.134$), a modulated wavy vortex flow regime ($D_{ax}/uL = 0.537$) at $Ta = 1147$ and a turbulent Taylor-vortex flow at a $Ta = 1835$ ($D_{ax}/uL = 0.609$).

Axial dispersion in the TVMR was reduced compared to the unbaffled TVR, possibly due to a stabilisation effect of the vortices induced by the baffles and to a decreased intervortex mass transfer. This result can be connected to what Richter *et al.* found in their work [304]. The authors studied the liquid residence time distribution inside a Taylor-vortex reactor with a ribbed rotor. Compared to a conventional cylindrical rotor, the ribbed Taylor-vortex reactor increased vortex segregation, immobilised the toroidal vortices between the rotor ribs and decreased axial dispersion. The authors also investigated the flow patterns in the gap between the rotor and the vessel at increasing Taylor numbers, and they discovered that the onset to turbulence was shifted to higher rotor speeds compared to the unribbed reactor. However, unlike in this study, the axial dispersion in the ribbed Taylor-vortex reactor did not show a monotonic increase as the rotor increased speed, but rather showed a minimum. This corresponded to the transition between the laminar Couette flow and the laminar vortex flow in the gap created between the rib and the vessel.

In the case of the TVMR, it is difficult to assess what fluid dynamic pattern characterises the interbaffle area. It is certain that axial dispersion is a function of the axial flowrate and the rotor angular speed. However, with a tubular membrane wound around the rotor and baffles at a short distance between each other, it is not possible to exclude that the fluid dynamics in the annulus is characterised by a Couette flow with the presence of azimuthal vortices in the fluid trailings behind the tubular membrane which may be responsible for the enhanced micromixing.

Mixing experiments at a higher axial Reynolds number equal to 0.34 were performed in the TVMR and the results are reported in Figure 7.9. For comparison, the experimental results from Richter *et al.* are also reported [304]. These are derived from solving the transport equations of the tracer in the annulus and inside the 20 mixing cells created by the rotor ribs, and the axial dispersion was calculated based on the fitted mass transfer coefficients.

The authors' results refer to a 60 m% glycerol/water solution ($Sc = 13507$) and a $Re = 0.04$.
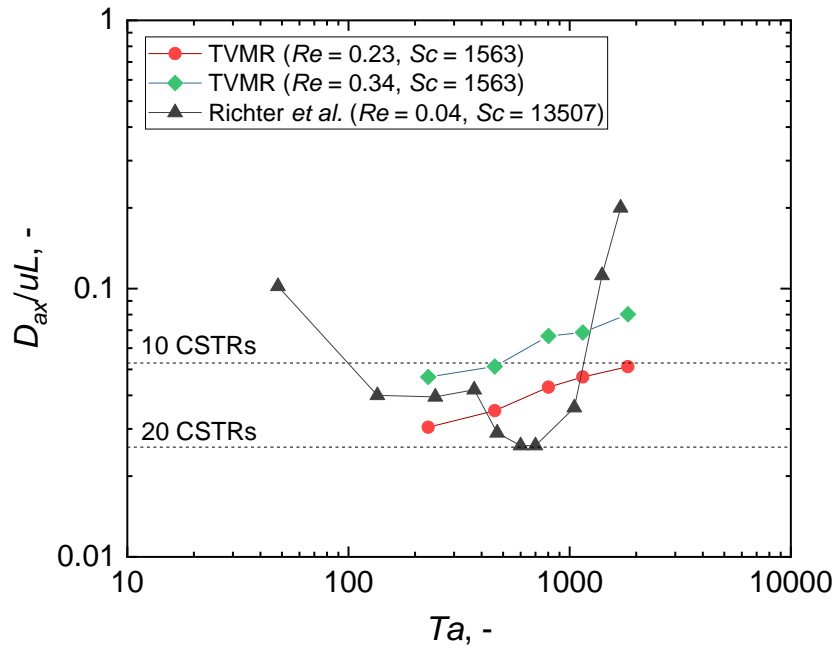
Figure 7.9. Dispersion number, D_{ax}/uL, in the Taylor-vortex membrane reactor (TMVR) and in the ribbed rotor Taylor-vortex reactor reported by Richter *et al.* [304]. The dispersion numbers for 10 CSTRs and 20 CSTRs in series are reported as a reference.

From the graph, it is possible to observe that at a $Re = 0.34$, corresponding to a flowrate of 6 mL/min, the dispersion number increased almost linearly from 0.047 ($N = 11.2$) at $Ta = 229$ to 0.080 ($N = 6.7$) at a $Ta = 1835$, deviating from the 10 CSTRs in series. Differently from the relation of Moore and Cooney that predicts a -0.83 exponent on the Re in the formula to calculate D_{ax}/uL [298], axial dispersion in the TVMR increased as the Re increased from 0.23 to 0.34. The reason may be attributed to a by-pass of the tracer in the small gaps created by the tubular membrane and the baffle holes, or between the baffles and the rotor or the vessel, which can be promoted at higher axial flowrates and in less developed vortices. This conclusion was reached by Richter *et al.*, who in their study observed an increase in the axial dispersion for values of Ta below the dispersion minima [304].

For the range of Ta = 500 - 700 the Taylor-vortex reactor with a ribbed rotor reached even lower dispersion numbers, equivalent to 20 CSTRs in series, which is close to the number of mixing cells created by the rotor. However, for increasing values of Ta, the reported reactor showed a steep increase in the dispersion number above 0.05 and up to 0.2 at Ta = 1700. This corresponded to the transition from a laminar vortex to a turbulent vortex flow in the gap between the rotor and the vessel. Despite operating at a higher axial Reynolds number, the TVMR suppressed backmixing and was able to keep a lower dispersion number than the ribbed Taylor-vortex reactor, for Ta > 1100. A possible explanation for the reduced backmixing can be attributed to the absence of a wide gap between the baffles and the vessel in the TVMR, which might have hindered a turbulent transition. Furthermore, the presence of a tubular membrane inside the annulus can create disruption of the vortices and enhance the tracer mesomixing inside the interbaffle annular zone.

Disruption of the Taylor vortex can also be induced by an oscillatory angular speed of the rotor. Appendix G reports the simulation results from COMSOL Multiphysics® 5.5 showing the beneficial effect that this can have on mesomixing.

7.3.2. Continuous aerobic oxidation reaction

The oxidation of benzyl alcohol was performed in the TVMR and results are presented in Figure 7.10. The reaction proceeded with 30% benzyl alcohol conversion and 85% selectivity to benzaldehyde, corresponding to the production of 5 g of benzaldehyde after 7 h of continuous operation. As mentioned in Chapter II, Ye *et al.* used the same $Pd(OAc)_2$/pyridine catalyst system for the aerobic oxidation of various alcohols [100]. Benzyl alcohol was oxidised at 100 °C and 500 psig (34 bar) using a flowrate of 0.9 mmol/min for benzyl alcohol, the palladium catalyst and the oxygen gas, and a substrate residence time of 2.5 h. A yield of 87% to benzaldehyde was achieved, equivalent to 0.41 g/min of benzaldehyde produced per 1 g/min of flowing $Pd(OAc)_2$, and to 8 g of benzaldehyde isolated at the end of the reaction.
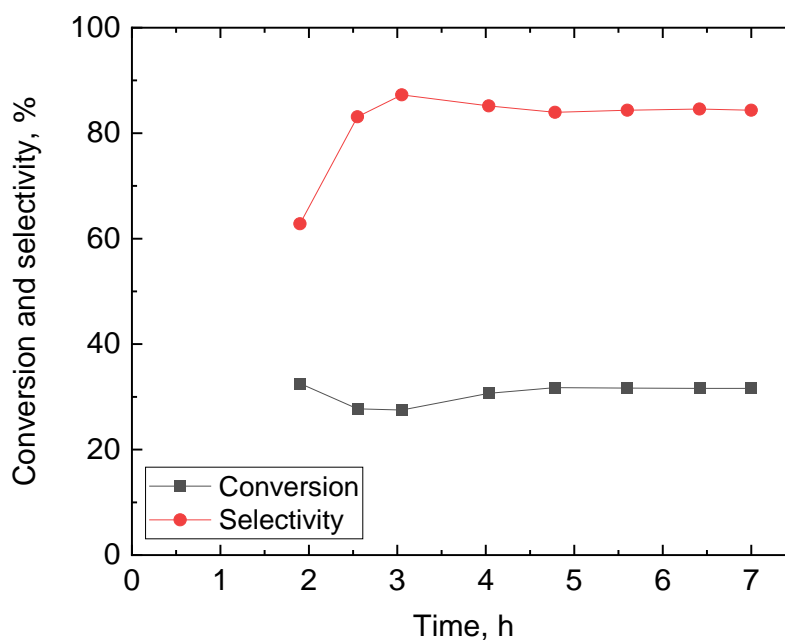
Figure 7.10. Benzyl alcohol conversion and benzaldehyde selectivity in the Taylor-vortex membrane reactor during the aerobic oxidation of benzyl alcohol. Substrate solution: 0.3 M benzyl alcohol, 0.1 M mesitylene and 0.12 M pyridine at 2 mL/min. Catalyst solution: 0.1 M mesitylene and 0.03 M Pd(OAc)$_2$ at 2 mL/min. Solvent: toluene, temperature: 100 °C, oxygen pressure: 11 bar.

In constrast, the TVMR operated with a shorter liquid residence time (*ca.* 70 min) and with a substrate and catalyst flowrate of 2 mL/min each. This corresponded to an inlet flowrate of 0.6 mmol/min of benzyl alcohol and 0.06 mmol/min of palladium, reacting to produce 1.26 g/min of benzaldehyde per 1 g/min of Pd(OAc)$_2$ catalyst. Furthermore, the use of a membrane allowed to control the oxygen dosing from the gas phase to the palladium catalyst in the bulk liquid. After 7 h of continuous operation, fouling of palladium metal was found at the entrance of the reactor. This might have been caused by the incomplete re-oxidation of the palladium catalyst, possibly due to the excess of benzyl alcohol as compared to oxygen, which kept the catalyst in its reduced form [100]. Nevertheless, the TVMR achieved a stable conversion and selectivity for 7 h under safe conditions due to the presence of a membrane that physically separated the oxidant from the organic substrate. During

reaction, no condensed organics were detected in the vial that was connected to the gas outlet and was immersed in an ice bath, indicating that the reaction was conducted safely without the risk of forming a flammable gas mixture. This could be ascribed to the PFA membrane hindering the pervaporation of the organics from the hot organic liquid in the reactor to the gas phase.

7.4. Summary and conclusions

The Taylor-vortex membrane reactor (TVMR) is a novel continuous reactor that combines the mixing benefits of a Taylor-vortex system and the presence of a gas permeable tubular membrane supported by horizontal baffles in the annulus for gas-liquid reactions. The reactor was demonstrated to have a robust and reliable design, with the potential to be reproduced at larger scales. Residence time distribution studies showed a plug-flow behaviour for an inlet flowrate of 4 mL/min and with rotor speeds ranging between 10 and 80 rpm ($Ta =$ 229 - 1835). Under these conditions the equivalent number of CSTRs in series ranged from a maximum of 17 ($Ta = 229$) to 10 ($Ta = 1835$). However, at 6 mL/min inlet flowrate, the equivalent number of CSTRs in series dropped below 10 for $Ta > 459$. Compared to the same reactor system without baffles and membrane, the TVMR showed a 4 - 6 times higher number of CSTRs in series. Furthermore, it outperformed a reported Taylor-vortex reactor with horizontal ribs on the rotor for $Ta > 1140$. This was possible owing to the horizontal baffles supporting the membrane that divided the annulus in segregated annular compartments.

To demonstrate the application of this reactor to continuous gas-liquid reactions, the aerobic oxidation of benzyl alcohol was performed using the $Pd(OAc)_2$/pyridine catalyst system in toluene at 11 bar oxygen pressure and 100 °C. Conversion and selectivity remained constant at 30% and 85% respectively, and 5 g benzaldehyde were produced after 7 h continuous reaction. The risks associated with oxygen forming a flammable mixture with the organic substrate were overcome by using a perfluoro alkoxy membrane that separated the gas from the liquid phase.

Chapter VIII. Conclusions and Future Outlook

Different reactor designs at various scales have been proposed in this thesis as safe and process intensified solutions to continuous oxidation and hydrogenation reactions. In this chapter, summary and conclusions from this research are presented along with an outlook on the future work.

8.1. Reactor designs for catalyst studies

One of the objectives of this thesis was to design safe and intensified reactors that can be applied in studying and testing catalysts. This goal was pursued by developing and demonstrating reactors of different scales and with various process intensification features ranging from the reduced reactor size of the silicon microreactor to the use of a membrane reactor that separated the reacting gas and liquid phases during studies on the catalyst performance.

The silicon microreactor presented in **Chapter III** of this thesis was demonstrated in the catalytic combustion of methane using a 2 wt% Pd/Al_2O_3 and in the oxidation of carbon monoxide with a 1 wt% Pt/Al_2O_3 catalyst. The silicon-glass design and the reactor configuration ensured isothermal operation. In fact, the maximum temperature variation along the micropacked bed was 2 °C at a temperature setpoint of 400 °C. During the catalytic combustion of methane, the reactor operated without external or internal mass transfer resistances and under a plug-flow regime, owing to the small catalyst particles employed in the microchannel with respect to its cross sectional area. These features made this reactor a suitable, compact and versatile tool for investigating gas phase catalytic oxidations, allowing the study of the reaction intrinsic kinetics. The activation energy of the combustion of methane over the Pd/Al_2O_3 catalyst was calculated to be 80.7 kJ/mol, while that of carbon monoxide oxidation on Pt/Al_2O_3 was 48.4 kJ/mol. Both values were similar in magnitude to those reported in previous studies.

The use of spectroscopic techniques such as X-ray absorption and diffuse reflectance infrared Fourier transform spectroscopy, alongside mass spectrometry, allowed the study of the catalyst oxidation state and the reactive adsorbed species under operating conditions. XAS showed that palladium was in its oxidised state at all temperatures during the combustion of methane, while DRIFTS showed the presence of linearly adsorbed CO molecules on the platinum sites in the carbon monoxide oxidation.

Due to the absence of dead volumes and high space velocities that were employed, transient response experiments could be performed, such as the temperature-resolved reduction of palladium catalyst using methane or CO oxidation over Pt/Al_2O_3, showing the catalyst oxidation state changing during

reaction. Moreover, due to its large silicon window, the catalyst packed bed could be axially probed by IR in nine different positions during CO oxidation at 310 °C, showing the axial profile of CO species along the catalyst bed.

Several difficulties were encountered in this work. One amongst them was the X-ray and IR beam alignment, which was necessary prior to starting the analysis. This was due to the small geometry of the microchannel, which was designed to ensure a reduced catalyst volume. Furthermore, the microreactor was fragile and could easily break if the clamps were overtightened. Possible design improvements can be implemented, such as etching reference points on the reactor surface for the beam alignment, or using clamps with gaskets that would distribute the force and prevent damages to the reactor. Furthermore, the glass type used in the reactor currently limits the reactor operation below 400 °C and could be replaced with one rated for higher temperatures.

Recent developments in the automation of continuous flow systems and its coupling with online analysis for the fast identification of kinetic models and parameters have benefited from the use of microreactors, due to their reduced volumes and suitability to fast response experiments [313-315]. In this context, model based design of experiments (MBDoE) techniques have been successfully employed [314, 316]. A potential future work would be to use this silicon microreactor for rapidly identifying kinetic models and parameters using MBDoE while performing *operando* studies on the catalyst. Both the results from spectroscopic analyses on the catalyst and the composition at the outlet could be fed back to the automated system to decide what experimental conditions to employ. This would allow a deeper understanding of the dynamic performance of the catalyst and its structure-activity relationships under different steady-state and transient conditions.

The use of a membrane as a capillary reactor represents a safety feature that can be used in reactors that are larger than a microreactor and employed for gas-liquid continuous reactions. In **Chapter IV** the work on a tubular membrane reactor for nitrobenzene hydrogenation was presented. A tubular Teflon AF-2400 membrane was modified with a novel technique for the adsorption of polyelectrolyte multilayers above which palladium-based

nanoparticles of different size and shape could be adsorbed and tested in the hydrogenation of nitrobenzene to aniline.

Atomic force microscopy before reaction revealed the presence of singularly adsorbed nanoparticles and a wavy surface topography of the modified membrane that increased the surface area for nanoparticle adsorption. The membrane was assembled in a tube-in-tube configuration with hydrogen pressurised in the outer tube and nitrobenzene flowing in the inner membrane tube. The comparative performance study between the nanoparticles revealed that the 4 nm palladium nanospheres showed the highest average turnover frequency of nitrobenzene, equal to 600 h^{-1}. However, the highest turnover frequency based on the surface atoms was 3000 h^{-1}, exhibited by the 25 nm nanocubes, possibly due to their lower oxidation state revealed by XPS analysis.

The main problem encountered in this research was the deactivation of nanoparticles. Leaching was among the responsible causes and this was extensive when palladium nanocubes were used, of which almost 66% of their initial loading was lost, affecting conversion which dropped by 44% after 6 h of continuous reaction.

This novel technique for adsorbing catalytic nanoparticles onto membranes was proven to be inexpensive and could be performed at room temperature, unlike conventional processes for making catalysts [19]. However, it did not offer full adhesion of the nanoparticles to the surface, possibly because of the weak electrostatic interactions of the nanoparticles with the polyelectrolytes. A possible solution could be the adsorption and polymerisation of a further layer of dopamine on top of the nanoparticles, which could hinder their detachment, as demonstrated in the work of Feng *et al.* [317]. The authors also took advantage of the resulting rugged and increased surface area to adsorb a second layer of palladium nanoparticles, thus increasing the catalyst loading and achieving a higher and longer-lasting nitrobenzene conversion.

A possible application would be to use the layer-by-layer modified membrane in the aerobic oxidation of alcohols. However, it is important to ensure that the adsorbed polycation employed in the membrane modification, such as polyallylamine, does not react with oxygen, thus losing its functionality, and

that the whole supporting polyelectrolyte structure can withstand higher temperatures.

To minimise deactivation, higher catalyst loadings can be adsorbed, as demonstrated in the work of Liu *et al.* [245]. In this study, a PDMS membrane was functionalised with polydopamine and coated with Pd/Al_2O_3 particles, and the resulting membrane reactor was tested for the nitrobenzene hydrogenation. However, if on one hand a thick catalyst coating can guarantee a more durable and robust reaction, on the other hand it can be characterised by internal diffusion resistances that can make catalyst testing unreliable.

An alternative solution to coating is the use of supported catalyst particles in a slurry form, mixed with the reaction substrate, in order to minimise internal mass transfer resistances. **Chapter V** presented the work on a tube-in-tube Teflon AF-2400 membrane reactor that used a catalyst slurry flowing in a loop to which the membrane was connected and delivered oxygen during the aerobic oxidation of benzyl alcohol. The reactor could be operated either in batch or continuous mode, by means of a crossflow filter connected to the loop that allowed the continuous withdrawal of filtered liquid products. A $Au-Pd/TiO_2$ catalyst was tested and its turnover frequency was found to be comparable to that of the same catalyst tested in a conventional autoclave where oxygen, benzyl alcohol and the catalyst were mixed together. Parametric studies showed that the increase in temperature favoured catalyst activity but also decreased benzaldehyde selectivity, while the increase in oxygen pressure enhanced benzaldehyde selectivity and suppressed the production of toluene. The membrane reactor efficiently delivered oxygen to the catalyst slurry, showing superior performance compared to a membrane reactor where the catalyst was used in a packed bed under a flat Teflon AF-2400 membrane.

Given the importance of studying catalysts under operating conditions, a potential future work could aim to perform *operando* spectroscopic studies in this slurry loop tubular membrane reactor. Infrared spectroscopy has been employed for mechanistic and kinetic studies of reactions with catalysts suspended in solution [318-320]. This would allow the detection of transient chemical species during reaction in the liquid and on the catalyst surface, and could be performed using attenuated total reflectance (ATR) probes in contact with the flowing slurry.

One of the problems encountered in this research was the occasional clogging of the loop by catalyst particles, especially at high catalyst loadings and near tubular restrictions. Moreover, the use of a bath filled with heat transfer oil was not user-friendly. Design improvements were made to overcome these issues and a new slurry loop membrane reactor was designed and presented in **Chapter VI**.

8.2. Reactor designs for lab-scale continuous production

In **Chapter VI**, a novel slurry loop flat membrane reactor design consisting of a flat Teflon AF-2400 membrane as a gas saturator was presented. This reactor was employed in the oxidation of various primary and secondary alcohols to aldehydes and ketones using molecular oxygen and a 1 wt% Au-Pd/TiO$_2$ catalyst slurry. Thanks to the wide serpentine channel in the gas saturator unit, catalyst concentrations up to 10 g/L could be used without the risk of clogging the loop. The reactor was heated using cartridge heaters and insulated inside a box that made it a plug-and-play system, suitable for performing safe gas-liquid-solid reactions in flow and batch. Process intensification was realised by achieving an overall 1.2 s^{-1} volumetric gas-liquid mass transfer coefficient ($k_L a$) at 2.4 kW/m^3, overcoming that of other common gas-liquid contactors. Furthermore, the aerobic oxidation of alcohols was performed with enhanced turnover frequencies compared to packed-bed reactors, in which oxygen was pre-mixed with the organic substrate, and in the solvent-free aerobic oxidation of benzyl alcohol the catalyst achieved a turnover frequency of 25000 h^{-1}, higher than in the slurry loop tubular membrane reactor. After 7 h of continuous reaction, 19 g of benzaldehyde were produced, which corresponded to more than 26 times the productivity per amount of the same catalyst obtained with a flat membrane packed-bed reactor.

The risk of forming flammable organic vapours mixtures with oxygen was prevented by using 30 NmL/min of flowing oxygen, which reduced the concentration of volatile organics at the outlet of the gas port below their lower flammability limit in oxygen.

Despite its demonstration in a continuous reaction, the amount of product from the membrane reactor cannot meet the multi-tonne productivity demands of a fine chemicals production. Nevertheless, the use of a membrane in combination with a slurry loop reactor configuration has never been demonstrated before and can represent a viable solution to process intensification and process safety for production at a small scale.

Competitiveness and success of a reactor depend on its capital cost, and in the case of the slurry loop flat membrane reactor a substantial contribution

comes from the flat Teflon AF-2400 membrane. Teflon AF-2400 is a high performance membrane, with one of the highest permeability to light gases and an exceptional chemical inertness and temperature resistance [168, 169]. However, its cost ($25000/kg in 2015) is more than three orders of magnitude higher than that of other fluoropolymers, including PTFE and PFA [171]. A potential future work could be aimed at investigating the use of inexpensive polymeric membranes that are permeable to gases and that can also limit pervaporation of liquid organics during reaction.

In **Chapter VII** the Taylor-vortex membrane reactor was presented and it is the largest continuous membrane reactor demonstrated in this thesis. The reactor was designed in collaboration with Autichem Ltd and proved to be a robust and reliable design, which has the potential to be used for large scale gas-liquid reactions. Its configuration consisted of a cylindrical rotor surrounded by 17 annular ring baffles that segregated the annular space between the rotor and the outer cylindrical vessel in axial compartments. Mixing studies showed that the Taylor-vortex membrane reactor (TVMR) could achieve a PFR macromixing at inlet flowrates between 4 and 6 mL/min, outperforming the same reactor without baffles and a similar Taylor-vortex reactor with a ribbed rotor. An inexpensive PFA tube was supported by the annular baffles and was used as a membrane to deliver oxygen in the homogeneously catalysed aerobic oxidation of benzyl alcohol in flow. Using the Pd(OAc)$_2$/pyridine catalyst system in toluene at a rotor agitation speed of 30 rpm, 11 bar oxygen pressure and 100 °C temperature, a stable 30% conversion with 85% selectivity to benzaldehyde was achieved for 7 h of continuous reaction. No pervaporation of organics through the membrane was observed during reaction and gas breakthrough was avoided by holding the liquid pressure 1 bar higher than the gas phase.

The main issue encountered after reaction in the TVMR was the palladium catalyst fouling near the liquid inlet section, which could be ascribed to the lack of oxygen dissolved in the area. Addressing this problem can represent the basis for future work, in which other types of homogeneous catalysts that are less prone to fouling, and different semi-permeable membranes can be used. Moreover, heterogeneous catalysts can be employed in the form of slurry in the TVMR upon modifications of the baffles and the rotor design to avoid

clogging the annular section. This would enable to perform many gas-liquid-solid transformations that find utility in the fine chemical production.

References

1.	M. Poliakoff, J.M. Fitzpatrick, T.R. Farren, and P.T. Anastas, *Green Chemistry: Science and Politics of Change,* Science, 2002, **297**(5582), 807-810.

2.	V.G. Pangarkar, *Process intensification in multiphase reactors: from concept to reality,* Chemical Engineering and Processing: Process Intensification, 2017, **120**, 1-8.

3.	P.L. Mills and R.V. Chaudhari, *Multiphase catalytic reactor engineering and design for pharmaceuticals and fine chemicals,* Catalysis Today, 1997, **37**(4), 367-404.

4.	R.V. Chaudhari and P.L. Mills, *Multiphase catalysis and reaction engineering for emerging pharmaceutical processes,* Chemical Engineering Science, 2004, **59**(22), 5337-5344.

5.	P.L. Mills, P.A. Ramachandran, and R.V. Chaudhari, *Multiphase reaction engineering for fine chemicals and pharmaceuticals,* Reviews in Chemical Engineering, 1992, **8**(1-2), 1-176.

6.	A. Stankiewicz and J.A. Moulijn, *Process Intensification,* Industrial & Engineering Chemistry Research, 2002, **41**(8), 1920-1924.

7.	J.C. Etchells, *Process Intensification: Safety Pros and Cons,* Process Safety and Environmental Protection, 2005, **83**(2), 85-89.

8.	K.F. Jensen, *Flow chemistry—Microreaction technology comes of age,* AIChE Journal, 2017, **63**(3), 858-869.

9.	J. Yue, J.C. Schouten, and T.A. Nijhuis, *Integration of Microreactors with Spectroscopic Detection for Online Reaction Monitoring and Catalyst Characterization,* Industrial & Engineering Chemistry Research, 2012, **51**(45), 14583-14609.

10.	N. Kockmann, M. Gottsponer, and D.M. Roberge, *Scale-up concept of single-channel microreactors from process development to industrial production,* Chemical Engineering Journal, 2011, **167**(2), 718-726.

11.	N. Kockmann, P. Thenee, C. Fleischer-Trebes, G. Laudadio, and T. Noel, *Safety assessment in development and operation of modular continuous-flow processes,* Reaction Chemistry & Engineering, 2017, **2**(3), 258-280.

12. C. Wiles and P. Watts, *Continuous flow reactors: a perspective,* Green Chemistry, 2012, **14**(1), 38-54.

13. A. Gavriilidis, A. Constantinou, K. Hellgardt, K.K. Hii, G.J. Hutchings, G.L. Brett, S. Kuhn, and S.P. Marsden, *Aerobic oxidations in flow: opportunities for the fine chemicals and pharmaceuticals industries,* Reaction Chemistry & Engineering, 2016, **1**(6), 595-612.

14. A. Stankiewicz and J.A. Moulijn, *Process intensification: Transforming Chemical Engineering,* Chemical Engineering Progress, 2000, **96**, 22-34.

15. P.J. Dunn, A.S. Wells, and M.T. Williams, *Green Chemistry in the Pharmaceutical Industry*, Wiley-VCH, Weinheim, 2010.

16. D.J.C. Constable, P.J. Dunn, J.D. Hayler, G.R. Humphrey, J.J.L. Leazer, R.J. Linderman, K. Lorenz, J. Manley, B.A. Pearlman, A. Wells, A. Zaks, and T.Y. Zhang, *Key green chemistry research areas - A perspective from pharmaceutical manufacturers,* Green Chemistry, 2007, **9**(5), 411-420.

17. W.J.W. Watson, *How do the fine chemical, pharmaceutical, and related industries approach green chemistry and sustainability?,* Green Chemistry, 2012, **14**(2), 251-259.

18. M. Poliakoff and P. Licence, *Green chemistry,* Nature, 2007, **450**(7171), 810-812.

19. C.H. Bartholomew and R.J. Farrauto, *Fundamentals of Industrial Catalytic Processes*, John Wiley & Sons, Hoboken, New Jersey, 2005.

20. F. Cavani and J.H. Teles, *Sustainability in Catalytic Oxidation: An Alternative Approach or a Structural Evolution?,* ChemSusChem, 2009, **2**(6), 508-534.

21. P.N. Rylander, *Hydrogenation Methods*, Academic Press, New York, 1990.

22. P.N. Rylander, *Catalytic Hydrogenations in Organic Synthesis*, Academic Press, New York, 1979.

23. R.A. Sheldon and J.K. Kochi, *Metal-Catalyzed Oxidations of Organic Compounds in the Liquid Phase: A Mechanistic Approach,* Advances in Catalysis, 1976, **25**, 272-413.

24. S. Caron, R.W. Dugger, S.G. Ruggeri, J.A. Ragan, and D.H.B. Ripin, *Large-scale oxidations in the pharmaceutical industry,* Chemical Reviews, 2006, **106**(7), 2943-2989.

25. K. Kaizuka, K.-Y. Lee, H. Miyamura, and S. Kobayashi, *Multiphase Flow Systems for Selective Aerobic Oxidation of Alcohols Catalyzed by Bimetallic Nanoclusters,* Journal of Flow Chemistry, 2012, **2**(1), 1-4.

26. J.-E. Bäckvall, *Modern Oxidation Methods*, John Wiley & Sons, Weinheim, 2011.

27. J.S. Carey, D. Laffan, C. Thomson, and M.T. Williams, *Analysis of the reactions used for the preparation of drug candidate molecules,* Organic & Biomolecular Chemistry, 2006, **4**(12), 2337-2347.

28. B. Gutmann, D. Cantillo, and C.O. Kappe, *Continuous-flow technology — A tool for the safe manufacturing of active pharmaceutical ingredients,* Angewandte Chemie International Edition, 2015, **54**(23), 6688-6728.

29. M. Hudlicky, *Oxidations in Organic Chemistry*, American Chemical Society, Washington DC, 1990.

30. T. Mallat and A. Baiker, *Oxidation of alcohols with molecular oxygen on solid catalysts,* Chemical Reviews, 2004, **104**(6), 3037-3058.

31. C.A. Hone and C.O. Kappe, *The use of molecular oxygen for liquid phase aerobic oxidations in continuous flow,* Topics in Current Chemistry, 2019, **377**(1), 2.

32. B. Gutmann, U. Weigl, D.P. Cox, and C.O. Kappe, *Batch- and continuous-flow aerobic oxidation of 14-hydroxy opioids to 1,3-oxazolidines — A concise synthesis of noroxymorphone,* Chemistry – A European Journal, 2016, **22**(30), 10393-10398.

33. C.A. Hone, A. O'Kearney-McMullan, R. Munday, and C.O. Kappe, *A continuous-flow process for palladium-catalyzed olefin cleavage by using oxygen within the explosive regime,* ChemCatChem, 2017, **9**(17), 3298-3302.

34. Z. Guo, B. Liu, Q. Zhang, W. Deng, Y. Wang, and Y. Yang, *Recent advances in heterogeneous selective oxidation catalysis for sustainable chemistry,* Chemical Society Reviews, 2014, **43**(10), 3480-3524.

35. C.A. Hone, D.M. Roberge, and C.O. Kappe, *The use of molecular oxygen in pharmaceutical manufacturing: is flow the way to go?*, ChemSusChem, 2017, **10**(1), 32-41.

36. R.A. Sheldon, I.W.C.E. Arends, G.-J. ten Brink, and A. Dijksman, *Green, Catalytic Oxidations of Alcohols,* Accounts of Chemical Research, 2002, **35**(9), 774-781.

37. S.S. Stahl and P.L. Alsters, *Liquid Phase Aerobic Oxidation Catalysis*, Wiley-VCH, New York, 2016.

38. J.R. Parikh and W.v.E. Doering, *Sulfur trioxide in the oxidation of alcohols by dimethyl sulfoxide,* Journal of the American Chemical Society, 1967, **89**(21), 5505-5507.

39. I.W.C.E. Arends and R.A. Sheldon, *Modern Oxidation of Alcohols Using Environmentally Benign Oxidants*, in *Modern Oxidation Methods*, ed. J.-E. Bäckvall, Wiley-VCH Verlag GmbH & Co. KGaA, Weinheim, 2010, pp. 147-185.

40. B. Pieber and C.O. Kappe, *Aerobic Oxidations in Continuous Flow*, in *Organometallic Flow Chemistry*, ed. T. Noël, Springer, Cham, 2016, pp. 97-136.

41. P.T. Anastas and J.C. Warner, *Green chemistry: Theory and Practice*, Oxford University Press, New York, 1998.

42. P.T. Anastas and M.M. Kirchhoff, *Origins, Current Status, and Future Challenges of Green Chemistry,* Accounts of Chemical Research, 2002, **35**(9), 686-694.

43. P.T. Anastas, M.M. Kirchhoff, and T.C. Williamson, *Catalysis as a foundational pillar of green chemistry,* Applied Catalysis A: General, 2001, **221**(1), 3-13.

44. D.I. Enache, D.W. Knight, and G.J. Hutchings, *Solvent-free Oxidation of Primary Alcohols to Aldehydes using Supported Gold Catalysts,* Catalysis Letters, 2005, **103**(1), 43-52.

45. N. Dimitratos, J.A. Lopez-Sanchez, D. Morgan, A.F. Carley, R. Tiruvalam, C.J. Kiely, D. Bethell, and G.J. Hutchings, *Solvent-free oxidation of benzyl alcohol using Au-Pd catalysts prepared by sol immobilisation,* Physical Chemistry Chemical Physics, 2009, **11**(25), 5142-5153.

46. D.I. Enache, J.K. Edwards, P. Landon, B. Solsona-Espriu, A.F. Carley, A.A. Herzing, M. Watanabe, C.J. Kiely, D.W. Knight, and G.J. Hutchings, *Solvent-free oxidation of primary alcohols to aldehydes using Au-Pd/TiO₂ catalysts,* Science, 2006, **311**(5759), 362.

47. M. Morad, M. Sankar, E. Cao, E. Nowicka, T.E. Davies, P.J. Miedziak, D.J. Morgan, D.W. Knight, D. Bethell, A. Gavriilidis, and G.J. Hutchings, *Solvent-free aerobic oxidation of alcohols using supported gold palladium nanoalloys prepared by a modified impregnation method,* Catalysis Science & Technology, 2014, **4**(9), 3120-3128.

48. M. Sankar, Q. He, M. Morad, J. Pritchard, S.J. Freakley, J.K. Edwards, S.H. Taylor, D.J. Morgan, A.F. Carley, D.W. Knight, C.J. Kiely, and G.J. Hutchings, *Synthesis of Stable Ligand-free Gold–Palladium Nanoparticles Using a Simple Excess Anion Method,* ACS Nano, 2012, **6**(8), 6600-6613.

49. A.T. Bell, *The Impact of Nanoscience on Heterogeneous Catalysis,* Science, 2003, **299**(5613), 1688-1691.

50. D. Astruc, F. Lu, and J.R. Aranzaes, *Nanoparticles as Recyclable Catalysts: The Frontier between Homogeneous and Heterogeneous Catalysis,* Angewandte Chemie International Edition, 2005, **44**(48), 7852-7872.

51. D. Astruc, *Transition-metal Nanoparticles in Catalysis: From Historical Background to the State-of-the Art*, in *Nanoparticles and Catalysis*, ed. D. Astruc, Wiley-VCH Verlag, Weinheim, 2008, pp. 1-48.

52. B. Roldan Cuenya, *Metal Nanoparticle Catalysts Beginning to Shape-up,* Accounts of Chemical Research, 2013, **46**(8), 1682-1691.

53. F. Zaera, *New Challenges in Heterogeneous Catalysis for the 21st Century,* Catalysis Letters, 2012, **142**(5), 501-516.

54. M. Crespo-Quesada, A. Yarulin, M. Jin, Y. Xia, and L. Kiwi-Minsker, *Structure Sensitivity of Alkynol Hydrogenation on Shape- and Size-Controlled Palladium Nanocrystals: Which Sites Are Most Active and Selective?,* Journal of the American Chemical Society, 2011, **133**(32), 12787-12794.

55. K. An and G.A. Somorjai, *Size and Shape Control of Metal Nanoparticles for Reaction Selectivity in Catalysis,* ChemCatChem, 2012, **4**(10), 1512-1524.

56. S. Mostafa, F. Behafarid, J.R. Croy, L.K. Ono, L. Li, J.C. Yang, A.I. Frenkel, and B.R. Cuenya, *Shape-Dependent Catalytic Properties of Pt Nanoparticles,* Journal of the American Chemical Society, 2010, **132**(44), 15714-15719.

57. H.-J. Freund, *Model Studies in Heterogeneous Catalysis,* Chemistry - A European Journal, 2010, **16**(31), 9384-9397.

58. S. Cheong, J.D. Watt, and R.D. Tilley, *Shape control of platinum and palladium nanoparticles for catalysis,* Nanoscale, 2010, **2**(10), 2045-2053.

59. P. Sonström and M. Bäumer, *Supported colloidal nanoparticles in heterogeneous gas phase catalysis: on the way to tailored catalysts,* Physical Chemistry Chemical Physics, 2011, **13**(43), 19270-19284.

60. N. Semagina and L. Kiwi-Minsker, *Palladium Nanohexagons and Nanospheres in Selective Alkyne Hydrogenation,* Catalysis Letters, 2009, **127**(3), 334-338.

61. Z. Sun, Y. Zhao, Y. Xie, R. Tao, H. Zhang, C. Huang, and Z. Liu, *The solvent-free selective hydrogenation of nitrobenzene to aniline: an unexpected catalytic activity of ultrafine Pt nanoparticles deposited on carbon nanotubes,* Green Chemistry, 2010, **12**(6), 1007-1011.

62. B. Buisson, S. Donegan, D. Wray, A. Parracho, J. Gamble, P. Caze, J. Jorda, and C. Guermeur, *Slurry hydrogenation in a continuous flow reactor for pharmaceutical application,* Chimica Oggi - Chemistry Today, 2009, **27**, 12-19.

63. C. Parmeggiani and F. Cardona, *Transition metal based catalysts in the aerobic oxidation of alcohols,* Green Chemistry, 2012, **14**(3), 547-564.

64. K.P. Peterson and R.C. Larock, *Palladium-Catalyzed Oxidation of Primary and Secondary Allylic and Benzylic Alcohols,* The Journal of Organic Chemistry, 1998, **63**(10), 3185-3189.

65. K.R. Seddon and A. Stark, *Selective catalytic oxidation of benzyl alcohol and alkylbenzenes in ionic liquids,* Green Chemistry, 2002, **4**(2), 119-123.

66. T. Nishimura, T. Onoue, K. Ohe, and S. Uemura, *Pd(OAc)$_2$-catalyzed oxidation of alcohols to aldehydes and ketones by molecular oxygen,* Tetrahedron Letters, 1998, **39**(33), 6011-6014.

67. Q. Cao, L.M. Dornan, L. Rogan, N.L. Hughes, and M.J. Muldoon, *Aerobic oxidation catalysis with stable radicals,* Chemical Communications, 2014, **50**(35), 4524-4543.

68. M. Irfan, T.N. Glasnov, and C.O. Kappe, *Heterogeneous Catalytic Hydrogenation Reactions in Continuous-Flow Reactors,* ChemSusChem, 2011, **4**(3), 300-316.

69. P.M. Osterberg, J.K. Niemeier, C.J. Welch, J.M. Hawkins, J.R. Martinelli, T.E. Johnson, T.W. Root, and S.S. Stahl, *Experimental Limiting Oxygen Concentrations for Nine Organic Solvents at Temperatures and Pressures Relevant to Aerobic Oxidations in the Pharmaceutical Industry,* Organic Process Research & Development, 2015, **19**(11), 1537-1543.

70. H.P.L. Gemoets, Y. Su, M. Shang, V. Hessel, R. Luque, and T. Noël, *Liquid phase oxidation chemistry in continuous-flow microreactors,* Chemical Society Reviews, 2016, **45**(1), 83-117.

71. N. Zotova, K. Hellgardt, G.H. Kelsall, A.S. Jessiman, and K.K. Hii, *Catalysis in flow: the practical and selective aerobic oxidation of alcohols to aldehydes and ketones,* Green Chemistry, 2010, **12**(12), 2157-2163.

72. T. Kahl, K.-W. Schröder, F.R. Lawrence, W.J. Marshall, H. Höke, and R. Jäckh, *Aniline*, in *Ullmann's Encyclopedia of Industrial Chemistry*, 2012, vol. 3, pp. 465-478.

73. E.H. Stitt, *Alternative multiphase reactors for fine chemicals: A world beyond stirred tanks?,* Chemical Engineering Journal, 2002, **90**(1), 47-60.

74. H. Freund and K. Sundmacher, *Process Intensification, 3. Process Unit Level*, in *Ullmann's Encyclopedia of Industrial Chemistry*, Wiley-VCH Verlag GmbH & Co. KGaA, Weinheim, 2011.

75. T. Van Gerven and A. Stankiewicz, *Structure, Energy, Synergy, Time— The Fundamentals of Process Intensification,* Industrial & Engineering Chemistry Research, 2009, **48**(5), 2465-2474.

76. H. Freund and K. Sundmacher, *Towards a methodology for the systematic analysis and design of efficient chemical processes: Part 1. From unit operations to elementary process functions,* Chemical Engineering and Processing: Process Intensification, 2008, **47**(12), 2051-2060.

77. H. Freund and K. Sundmacher, *Process Intensification, 1. Fundamentals and Molecular Level*, in *Ullmann's Encyclopedia of Industrial Chemistry*, Wiley-VCH Verlag GmbH & Co. KGaA, Weinheim, 2011.

78. P. Oxley, C. Brechtelsbauer, F. Ricard, N. Lewis, and C. Ramshaw, *Evaluation of Spinning Disk Reactor Technology for the Manufacture of Pharmaceuticals,* Industrial & Engineering Chemistry Research, 2000, **39**(7), 2175-2182.

79. H. Freund and K. Sundmacher, *Process Intensification, 4. Plant Level*, in *Ullmann's Encyclopedia of Industrial Chemistry*, Wiley-VCH Verlag GmbH & Co. KGaA, Weinheim, 2011.

80. L.L. van Dierendonck, J. Zahradník, and V. Linek, *Loop venturi reactor - A feasible alternative to stirred tank reactors?,* Industrial & Engineering Chemistry Research, 1998, **37**(3), 734-738.

81. L.K. Doraiswamy, *Organic Synthesis Engineering*, Oxford University Press, New York, 2001.

82. R.J. Malone, *Loop reactor technology improves catalytic hydrogenations,* Chemical Engineering Progress, 1980, **53**

83. S.G. Newman and K.F. Jensen, *The role of flow in green chemistry and engineering,* Green Chemistry, 2013, **15**(6), 1456-1472.

84. D. Dallinger and C.O. Kappe, *Why flow means green – Evaluating the merits of continuous processing in the context of sustainability,* Current Opinion in Green and Sustainable Chemistry, 2017, **7**, 6-12.

85. M. Movsisyan, E.I.P. Delbeke, J.K.E.T. Berton, C. Battilocchio, S.V. Ley, and C.V. Stevens, *Taming hazardous chemistry by continuous flow technology,* Chemical Society Reviews, 2016, **45**(18), 4892-4928.

86. C. Wiles and P. Watts, *Continuous process technology: a tool for sustainable production,* Green Chemistry, 2014, **16**(1), 55-62.

87. L. Malet-Sanz and F. Susanne, *Continuous Flow Synthesis. A Pharma Perspective,* Journal of Medicinal Chemistry, 2012, **55**(9), 4062-4098.

88. R.L. Hartman, J.P. McMullen, and K.F. Jensen, *Deciding Whether To Go with the Flow: Evaluating the Merits of Flow Reactors for Synthesis,* Angewandte Chemie International Edition, 2011, **50**(33), 7502-7519.

89. M. Berton, J.M. de Souza, I. Abdiaj, D.T. McQuade, and D.R. Snead, *Scaling continuous API synthesis from milligram to kilogram: extending the enabling benefits of micro to the plant,* Journal of Flow Chemistry, 2020, **10**(1), 73-92.

90. C.J. Mallia and I.R. Baxendale, *The use of gases in flow synthesis,* Organic Process Research & Development, 2016, **20**(2), 327-360.

91. J.A. Moulijn, A. Tarfaoui, and F. Kapteijn, *General aspects of catalyst testing,* Catalysis Today, 1991, **11**(1), 1-12.

92. T. Osako, K. Torii, A. Tazawa, and Y. Uozumi, *Continuous-flow hydrogenation of olefins and nitrobenzenes catalyzed by platinum nanoparticles dispersed in an amphiphilic polymer,* RSC Advances, 2015, **5**(57), 45760-45766.

93. X. Fan, A.A. Lapkin, and P.K. Plucinski, *Liquid phase hydrogenation in a structured multichannel reactor,* Catalysis Today, 2009, **147**, S313-S318.

94. D.V. Bavykin, A.A. Lapkin, S.T. Kolaczkowski, and P.K. Plucinski, *Selective oxidation of alcohols in a continuous multifunctional reactor: ruthenium oxide catalysed oxidation of benzyl alcohol,* Applied Catalysis A: General, 2005, **288**(1), 175-184.

95. D.S. Mannel, S.S. Stahl, and T.W. Root, *Continuous flow aerobic alcohol oxidation reactions using a heterogeneous $Ru(OH)_x/Al_2O_3$ catalyst,* Organic Process Research & Development, 2014, **18**(11), 1503-1508.

96. D. Obermayer, A.M. Balu, A.A. Romero, W. Goessler, R. Luque, and C.O. Kappe, *Nanocatalysis in continuous flow: supported iron oxide nanoparticles for the heterogeneous aerobic oxidation of benzyl alcohol,* Green Chemistry, 2013, **15**(6), 1530-1537.

97.   Y. Mo, J. Imbrogno, H. Zhang, and K.F. Jensen, *Scalable thin-layer membrane reactor for heterogeneous and homogeneous catalytic gas–liquid reactions,* Green Chemistry, 2018, **20**(16), 3867-3874.

98.   G. Donati and R. Paludetto, *Scale up of chemical reactors,* Catalysis Today, 1997, **34**(3), 483-533.

99.   J. Wegner, S. Ceylan, and A. Kirschning, *Ten key issues in modern flow chemistry,* Chemical Communications, 2011, **47**(16), 4583-4592.

100. X. Ye, M.D. Johnson, T. Diao, M.H. Yates, and S.S. Stahl, *Development of safe and scalable continuous-flow methods for palladium-catalyzed aerobic oxidation reactions,* Green Chemistry, 2010, **12**(7), 1180-1186.

101. J.F. Greene, J.M. Hoover, D.S. Mannel, T.W. Root, and S.S. Stahl, *Continuous-flow aerobic oxidation of primary alcohols with a copper(I)/TEMPO catalyst,* Organic Process Research & Development, 2013, **17**(10), 1247-1251.

102. J. Keil Frerich, *Process intensification,* Reviews in Chemical Engineering, 2018, **34**(2), 135.

103. K.F. Jensen, *Microreaction engineering — is small better?,* Chemical Engineering Science, 2001, **56**(2), 293-303.

104. E.R. Delsman, A. Pierik, M.H.J.M. De Croon, G.J. Kramer, and J.C. Schouten, *Microchannel Plate Geometry Optimization for Even Flow Distribution at High Flow Rates,* Chemical Engineering Research and Design, 2004, **82**(2), 267-273.

105. J. Kobayashi, Y. Mori, K. Okamoto, R. Akiyama, M. Ueno, T. Kitamori, and S. Kobayashi, *A Microfluidic Device for Conducting Gas-Liquid-Solid Hydrogenation Reactions,* Science, 2004, **304**(5675), 1305.

106. H. Löwe and W. Ehrfeld, *State-of-the-art in microreaction technology: concepts, manufacturing and applications,* Electrochimica Acta, 1999, **44**(21), 3679-3689.

107. S.L. Lee, T.F. O'Connor, X. Yang, C.N. Cruz, S. Chatterjee, R.D. Madurawe, C.M.V. Moore, L.X. Yu, and J. Woodcock, *Modernizing Pharmaceutical Manufacturing: from Batch to Continuous Production,* Journal of Pharmaceutical Innovation, 2015, **10**(3), 191-199.

108. A. Kavara, D. Sokolowski, M. Collins, and M. Schofield, *Chapter 4 - Recent advances in continuous downstream processing of antibodies*

and related products, in *Approaches to the Purification, Analysis and Characterization of Antibody-Based Therapeutics*, ed. A. Matte, Elsevier, Amsterdam, 2020, pp. 81-103.

109. T. von Keutz, J.D. Williams, and C.O. Kappe, *Continuous Flow C-Glycosylation via Metal–Halogen Exchange: Process Understanding and Improvements toward Efficient Manufacturing of Remdesivir,* Organic Process Research & Development, 2020, **24**(10), 2362-2368.

110. A. Adamo, R.L. Beingessner, M. Behnam, J. Chen, T.F. Jamison, K.F. Jensen, J.-C.M. Monbaliu, A.S. Myerson, E.M. Revalor, D.R. Snead, T. Stelzer, N. Weeranoppanant, S.Y. Wong, and P. Zhang, *On-demand continuous-flow production of pharmaceuticals in a compact, reconfigurable system,* Science, 2016, **352**(6281), 61.

111. D.M. Roberge, L. Ducry, N. Bieler, P. Cretton, and B. Zimmermann, *Microreactor Technology: A Revolution for the Fine Chemical and Pharmaceutical Industries?,* Chemical Engineering & Technology, 2005, **28**(3), 318-323.

112. B.J. Doyle, P. Elsner, B. Gutmann, O. Hannaerts, C. Aellig, A. Macchi, and D.M. Roberge, *Mini-Monoplant Technology for Pharmaceutical Manufacturing,* Organic Process Research & Development, 2020, **24**(10), 2169-2182.

113. A.R. Bogdan, S.L. Poe, D.C. Kubis, S.J. Broadwater, and D.T. McQuade, *The Continuous-Flow Synthesis of Ibuprofen,* Angewandte Chemie International Edition, 2009, **48**(45), 8547-8550.

114. P. Watts and S.J. Haswell, *Continuous flow reactors for drug discovery,* Drug Discovery Today, 2003, **8**(13), 586-593.

115. J. Hogan, *A little goes a long way,* Nature, 2006, **442**(7101), 351-352.

116. A. Turley. *Industrial nitroglycerin made fast and safe.* https://www.chemistryworld.com/news/industrial-nitroglycerin-made-fast-and-safe/5135.article (accessed 11 November 2021).

117. B. Tidona, A. Urakawa, and P. Rudolf von Rohr, *High pressure plant for heterogeneous catalytic CO_2 hydrogenation reactions in a continuous flow microreactor,* Chemical Engineering and Processing: Process Intensification, 2013, **65**, 53-57.

118. J.-i. Yoshida, A. Nagaki, and T. Yamada, *Flash Chemistry: Fast Chemical Synthesis by Using Microreactors,* Chemistry – A European Journal, 2008, **14**(25), 7450-7459.

119. B. Gutmann and C.O. Kappe, *Forbidden Chemistries — Paths to a Sustainable Future Engaging Continuous Processing,* Journal of Flow Chemistry, 2017, **7**(3), 65-71.

120. J.M. Thomas, C.R.A. Catlow, and G. Sankar, *Determining the structure of active sites, transition states and intermediates in heterogeneously catalysed reactions,* Chemical Communications, 2002, 2921-2925.

121. M.A. Newton and W. van Beek, *Combining synchrotron-based X-ray techniques with vibrational spectroscopies for the in situ study of heterogeneous catalysts: a view from a bridge,* Chemical Society Reviews, 2010, **39**(12), 4845-4863.

122. M.A. Bañares, *Operando methodology: combination of in situ spectroscopy and simultaneous activity measurements under catalytic reaction conditions,* Catalysis Today, 2005, **100**(1), 71-77.

123. B.M. Weckhuysen, *Preface: recent advances in the in-situ characterization of heterogeneous catalysts,* Chemical Society Reviews, 2010, **39**(12), 4557-4559.

124. C.M.A. Parlett, C.V. Gaskell, J.N. Naughton, M.A. Newton, K. Wilson, and A.F. Lee, *Operando synchronous DRIFTS/MS/XAS as a powerful tool for guiding the design of Pd catalysts for the selective oxidation of alcohols,* Catalysis Today, 2013, **205**, 76-85.

125. Y. Zhou, D.E. Doronkin, M. Chen, S. Wei, and J.-D. Grunwaldt, *Interplay of Pt and Crystal Facets of TiO_2: CO Oxidation Activity and Operando XAS/DRIFTS Studies,* ACS Catalysis, 2016, **6**(11), 7799-7809.

126. A.M. Abdel-Mageed, G. Kučerová, J. Bansmann, and R.J. Behm, *Active Au Species During the Low-Temperature Water Gas Shift Reaction on Au/CeO2: A Time-Resolved Operando XAS and DRIFTS Study,* ACS Catalysis, 2017, **7**(10), 6471-6484.

127. E.K. Gibson, E.M. Crabb, D. Gianolio, A.E. Russell, D. Thompsett, and P.P. Wells, *Understanding the role of promoters in catalysis: operando*

XAFS/DRIFTS study of CeO$_x$/Pt/Al$_2$O$_3$ during CO oxidation, Catalysis, Structure & Reactivity, 2017, **3**(1-2), 5-12.

128. E.K. Dann, E.K. Gibson, R.A. Catlow, P. Collier, T. Eralp Erden, D. Gianolio, C. Hardacre, A. Kroner, A. Raj, A. Goguet, and P.P. Wells, *Combined In Situ XAFS/DRIFTS Studies of the Evolution of Nanoparticle Structures from Molecular Precursors,* Chemistry of Materials, 2017, **29**(17), 7515-7523.

129. G. Sankar and J.M. Thomas, *In situ combined X-ray absorption spectroscopic and X-ray diffractometric studies of solid catalysts,* Topics in Catalysis, 1999, **8**(1), 1-21.

130. G. Sankar, J.M. Thomas, and C.R.A. Catlow, *Combining X-ray absorption with X-ray diffraction for the structural elucidation of catalysts,* Topics in Catalysis, 2000, **10**(3), 255-264.

131. N.-Y. Topsøe, *In situ FTIR: A versatile tool for the study of industrial catalysts,* Catalysis Today, 2006, **113**(1), 58-64.

132. J. Ryczkowski, *IR spectroscopy in catalysis,* Catalysis Today, 2001, **68**(4), 263-381.

133. N.S. Marinkovic, Q. Wang, and A.I. Frenkel, *In situ diffuse reflectance IR spectroscopy and X-ray absorption spectroscopy for fast catalytic processes,* Journal of Synchrotron Radiation, 2011, **18**(3), 447-455.

134. K.A. Beyer, H. Zhao, O.J. Borkiewicz, M.A. Newton, P.J. Chupas, and K.W. Chapman, *Simultaneous diffuse reflection infrared spectroscopy and X-ray pair distribution function measurements,* Journal of Applied Crystallography, 2014, **47**(1), 95-101.

135. S. Yao, K. Mudiyanselage, W. Xu, A.C. Johnston-Peck, J.C. Hanson, T. Wu, D. Stacchiola, J.A. Rodriguez, H. Zhao, K.A. Beyer, K.W. Chapman, P.J. Chupas, A. Martínez-Arias, R. Si, T.B. Bolin, W. Liu, and S.D. Senanayake, *Unraveling the Dynamic Nature of a CuO/CeO$_2$ Catalyst for CO Oxidation in Operando: A Combined Study of XANES (Fluorescence) and DRIFTS,* ACS Catalysis, 2014, **4**(6), 1650-1661.

136. A. Chakrabarti, M.E. Ford, D. Gregory, R. Hu, C.J. Keturakis, S. Lwin, Y. Tang, Z. Yang, M. Zhu, M.A. Bañares, and I.E. Wachs, *A decade+ of operando spectroscopy studies,* Catalysis Today, 2017, **283**, 27-53.

137. N. Al-Rifai, E. Cao, V. Dua, and A. Gavriilidis, *Microreaction technology aided catalytic process design,* Current Opinion in Chemical Engineering, 2013, **2**(3), 338-345.

138. F.C. Meunier, *The design and testing of kinetically-appropriate operando spectroscopic cells for investigating heterogeneous catalytic reactions,* Chemical Society Reviews, 2010, **39**(12), 4602-4614.

139. J.D. Grunwaldt, M. Caravati, S. Hannemann, and A. Baiker, *X-ray absorption spectroscopy under reaction conditions: suitability of different reaction cells for combined catalyst characterization and time-resolved studies,* Physical Chemistry Chemical Physics, 2004, **6**(11), 3037-3047.

140. E. Cao, S. Firth, P.F. McMillan, and A. Gavriilidis, *Application of microfabricated reactors for operando Raman studies of catalytic oxidation of methanol to formaldehyde on silver,* Catalysis Today, 2007, **126**(1), 119-126.

141. E. Cao, M. Sankar, S. Firth, K.F. Lam, D. Bethell, D.K. Knight, G.J. Hutchings, P.F. McMillan, and A. Gavriilidis, *Reaction and Raman spectroscopic studies of alcohol oxidation on gold-palladium catalysts in microstructured reactors,* Chemical Engineering Journal, 2011, **167**(2-3), 734-743.

142. D.E. Doronkin, S. Baier, T. Sheppard, F. Benzi, and J.D. Grunwaldt, *Lithographically fabricated silicon microreactor foroperandoQEXAFS studies in exhaust gas catalysis during simulation of a standard driving cycle,* Journal of Physics: Conference Series, 2016, **712**, 012030.

143. S.J.A. Figueroa, D. Gibson, T. Mairs, S. Pasternak, M.A. Newton, M. Di Michiel, J. Andrieux, K.C. Christoforidis, A. Iglesias-Juez, M. Fernandez-Garcia, and C. Prestipino, *Innovative insights in a plug flow microreactor for operando X-ray studies,* Journal of Applied Crystallography, 2013, **46**(5), 1523-1527.

144. G. Sankar, E. Cao, and A. Gavriilidis, *A microstructured reactor based in situ cell for the study of catalysts by X-ray absorption spectroscopy under operating conditions,* Catalysis Today, 2007, **125**(1), 24-28.

145. S. Zhao, Y. Li, E. Stavitski, R. Tappero, S. Crowley, M.J. Castaldi, D.N. Zakharov, R.G. Nuzzo, A.I. Frenkel, and E.A. Stach, *Operando*

Characterization of Catalysts through use of a Portable Microreactor, ChemCatChem, 2015, **7**(22), 3683-3691.

146. B.A. Rizkin, F.G. Popovic, and R.L. Hartman, *Review Article: Spectroscopic microreactors for heterogeneous catalysis,* Journal of Vacuum Science & Technology A, 2019, **37**(5), 050801.

147. P. Beato, R. Kraehnert, S. Engelschalt, T. Frank, and R. Schlögl, *A micro-structured quartz reactor for kinetic and in situ spectroscopic studies in heterogeneous catalysis,* Chemical Engineering Journal, 2008, **135**, S247-S253.

148. A. Urakawa, F. Trachsel, P.R. von Rohr, and A. Baiker, *On-chip Raman analysis of heterogeneous catalytic reaction in supercritical CO_2: phase behaviour monitoring and activity profiling,* Analyst, 2008, **133**(10), 1352-1354.

149. C. Daniel, M.O. Clarté, S.P. Teh, O. Thinon, H. Provendier, A.C. Van Veen, B.J. Beccard, Y. Schuurman, and C. Mirodatos, *Spatially resolved catalysis in microstructured reactors by IR spectroscopy: CO oxidation over mono- and bifunctional Pt catalysts,* Journal of Catalysis, 2010, **272**(1), 55-64.

150. C.K.C. Tan, W.N. Delgass, and C.D. Baertsch, *Spatially resolved in situ FTIR analysis of CO adsorption and reaction on Pt/SiO_2 in a silicon microreactor,* Applied Catalysis B: Environmental, 2009, **93**(1), 66-74.

151. E. Gross, X.-Z. Shu, S. Alayoglu, H.A. Bechtel, M.C. Martin, F.D. Toste, and G.A. Somorjai, *In Situ IR and X-ray High Spatial-Resolution Microspectroscopy Measurements of Multistep Organic Transformation in Flow Microreactor Catalyzed by Au Nanoclusters,* Journal of the American Chemical Society, 2014, **136**(9), 3624-3629.

152. S. Baier, A. Rochet, G. Hofmann, M. Kraut, and J.-D. Grunwaldt, *Lithographically fabricated silicon microreactor for in situ characterization of heterogeneous catalysts - Enabling correlative characterization techniques,* Review of Scientific Instruments, 2015, **86**(6), 065101.

153. J.-D. Grunwaldt and B.S. Clausen, *Combining XRD and EXAFS with on-Line Catalytic Studies for in situ Characterization of Catalysts,* Topics in Catalysis, 2002, **18**(1), 37-43.

154. J.-D. Grunwaldt, B. Kimmerle, S. Hannemann, A. Baiker, P. Boye, and C.G. Schroer, *Parallel structural screening of solid materials,* Journal of Materials Chemistry, 2007, **17**(25), 2603-2606.

155. C. Liebner, J. Fischer, S. Heinrich, T. Lange, H. Hieronymus, and E. Klemm, *Are micro reactors inherently safe? An investigation of gas phase explosion propagation limits on ethene mixtures,* Process Safety and Environmental Protection, 2012, **90**(2), 77-82.

156. J. Fischer, C. Liebner, H. Hieronymus, and E. Klemm, *Maximum safe diameters of microcapillaries for a stoichiometric ethene/oxygen mixture,* Chemical Engineering Science, 2009, **64**(12), 2951-2956.

157. S. Heinrich, F. Edeling, C. Liebner, H. Hieronymus, T. Lange, and E. Klemm, *Catalyst as ignition source of an explosion inside a microreactor,* Chemical Engineering Science, 2012, **84**, 540-543.

158. M. Gödde, C. Liebner, and H. Hieronymus, *Sicherheit in der Mikroreaktionstechnik,* Chemie Ingenieur Technik, 2009, **81**(1-2), 73-78.

159. H. Jiang, Y. Liu, W. Xing, and R. Chen, *Porous Membrane Reactors for Liquid-Phase Heterogeneous Catalysis,* Industrial & Engineering Chemistry Research, 2021, **60**(25), 8969-8990.

160. T. Noël and V. Hessel, *Membrane Microreactors: Gas–Liquid Reactions Made Easy,* ChemSusChem, 2013, **6**(3), 405-407.

161. H.C. Aran, H. Klooster, J.M. Jani, M. Wessling, L. Lefferts, and R.G.H. Lammertink, *Influence of geometrical and operational parameters on the performance of porous catalytic membrane reactors,* Chemical Engineering Journal, 2012, **207–208**, 814-821.

162. A. Julbe, D. Farrusseng, and C. Guizard, *Porous ceramic membranes for catalytic reactors - Overview and new ideas,* Journal of Membrane Science, 2001, **181**(1), 3-20.

163. A. Cassano and A. Basile, *7 - Integrating different membrane operations and combining membranes with conventional separation techniques in industrial processes*, in *Handbook of Membrane Reactors*, ed. A. Basile, Woodhead Publishing Limited, Sawston, Cambridge, 2013, vol. 2, pp. 296-343.

164. R. Dittmeyer, V. Höllein, and K. Daub, *Membrane reactors for hydrogenation and dehydrogenation processes based on supported palladium,* Journal of Molecular Catalysis A: Chemical, 2001, **173**(1), 135-184.

165. J. Coronas and J. Santamaría, *Catalytic reactors based on porous ceramic membranes,* Catalysis Today, 1999, **51**(3–4), 377-389.

166. I.F.J. Vankelecom, L.E.M. Gevers, T. Schäfer, and J.G. Crespo, *Membrane Processes*, in *Green Separation Processes*, ed. C.A.M.C. Alfonso, J. G., Wiley-VCH Verlag GmbH & Co. KGaA, Weinheim, 2006, pp. 251-289.

167. A. Constantinou, G. Wu, A. Corredera, P. Ellis, D. Bethell, G.J. Hutchings, S. Kuhn, and A. Gavriilidis, *Continuous Heterogeneously Catalyzed Oxidation of Benzyl Alcohol in a Ceramic Membrane Packed-Bed Reactor,* Organic Process Research and Development, 2015, **19**(12), 1973-1979.

168. T.C. Merkel, I. Pinnau, R. Prabhakar, and B.D. Freeman, *Gas and Vapor Transport Properties of Perfluoropolymers*, in *Materials Science of Membranes for Gas and Vapor Separation*, ed. Y. Yampolskii, I. Pinnau, and B.D. Freeman, John Wiley & Sons, Chichester, 2006, pp. 251-270.

169. I. Pinnau and L.G. Toy, *Gas and vapor transport properties of amorphous perfluorinated copolymer membranes based on 2,2-bistrifluoromethyl-4,5-difluoro-1,3-dioxole/tetrafluoroethylene,* Journal of Membrane Science, 1996, **109**(1), 125-133.

170. M. O'Brien, I.R. Baxendale, and S.V. Ley, *Flow ozonolysis using a semipermeable Teflon AF-2400 membrane to effect gas−liquid contact,* Organic Letters, 2010, **12**(7), 1596-1598.

171. J.F. Greene, Y. Preger, S.S. Stahl, and T.W. Root, *PTFE-Membrane Flow Reactor for Aerobic Oxidation Reactions and Its Application to Alcohol Oxidation,* Organic Process Research & Development, 2015, **19**(7), 858-864.

172. *Properties Bulletin - Tefzel EFTE, fluoropolymer film. Chemours.*

173. R.A. Pasternak, M.V. Christensen, and J. Heller, *Diffusion and Permeation of Oxygen, Nitrogen, Carbon Dioxide, and Nitrogen Dioxide through Polytetrafluoroethylene,* Macromolecules, 1970, **3**(3), 366-371.

174. *Properties Bulletin - Teflon PFA, fluorocarbon film. DuPont.*

175. W.J. Koros, G.K. Fleming, S.M. Jordan, T.H. Kim, and H.H. Hoehn, *Polymeric membrane materials for solution-diffusion based permeation separations,* Progress in Polymer Science, 1988, **13**(4), 339-401.

176. M. Brzozowski, M. O'Brien, S.V. Ley, and A. Polyzos, *Flow Chemistry: Intelligent Processing of Gas–Liquid Transformations Using a Tube-in-Tube Reactor,* Accounts of Chemical Research, 2015, **48**(2), 349-362.

177. S.L. Bourne, M. O'Brien, S. Kasinathan, P. Koos, P. Tolstoy, D.X. Hu, R.W. Bates, B. Martin, B. Schenkel, and S.V. Ley, *Flow Chemistry Syntheses of Styrenes, Unsymmetrical Stilbenes and Branched Aldehydes,* ChemCatChem, 2013, **5**(1), 159-172.

178. A. Polyzos, M. O'Brien, T.P. Petersen, I.R. Baxendale, and S.V. Ley, *The continuous-flow synthesis of carboxylic acids using CO_2 in a tube-in-tube gas permeable membrane reactor,* Angewandte Chemie International Edition, 2011, **50**(5), 1190-1193.

179. P. Koos, U. Gross, A. Polyzos, M. O'Brien, I. Baxendale, and S.V. Ley, *Teflon AF-2400 mediated gas-liquid contact in continuous flow methoxycarbonylations and in-line FTIR measurement of CO concentration,* Organic & Biomolecular Chemistry, 2011, **9**(20), 6903-6908.

180. M.A. Mercadante, C.B. Kelly, C. Lee, and N.E. Leadbeater, *Continuous Flow Hydrogenation Using an On-Demand Gas Delivery Reactor,* Organic Process Research & Development, 2012, **16**(5), 1064-1068.

181. M. O'Brien, N. Taylor, A. Polyzos, I.R. Baxendale, and S.V. Ley, *Hydrogenation in flow: Homogeneous and heterogeneous catalysis using Teflon AF-2400 to effect gas–liquid contact at elevated pressure,* Chemical Science, 2011, **2**(7), 1250-1257.

182. F. Mastronardi, B. Gutmann, and C.O. Kappe, *Continuous Flow Generation and Reactions of Anhydrous Diazomethane Using a Teflon AF-2400 Tube-in-Tube Reactor,* Organic Letters, 2013, **15**(21), 5590-5593.

183. D. Dallinger, V.D. Pinho, B. Gutmann, and C.O. Kappe, *Laboratory-Scale Membrane Reactor for the Generation of Anhydrous Diazomethane,* The Journal of Organic Chemistry, 2016, **81**(14), 5814-5823.

184. S.R. Chaudhuri, J. Hartwig, L. Kupracz, T. Kodanek, J. Wegner, and A. Kirschning, *Oxidations of Allylic and Benzylic Alcohols under Inductively-Heated Flow Conditions with Gold-Doped Superparamagnetic Nanostructured Particles as Catalyst and Oxygen as Oxidant,* Advanced Synthesis & Catalysis, 2014, **356**(17), 3530-3538.

185. G. Wu, A. Constantinou, E. Cao, S. Kuhn, M. Morad, M. Sankar, D. Bethell, G.J. Hutchings, and A. Gavriilidis, *Continuous heterogeneously catalyzed oxidation of benzyl alcohol using a tube-in-tube membrane microreactor,* Industrial & Engineering Chemistry Research, 2015, **54**(16), 4183-4189.

186. G. Wu, E. Cao, P. Ellis, A. Constantinou, S. Kuhn, and A. Gavriilidis, *Development of a flat membrane microchannel packed-bed reactor for scalable aerobic oxidation of benzyl alcohol in flow,* Chemical Engineering Journal, 2019, **377**, 120086.

187. D.W. Green and R.H. Perry, *Perry's Chemical Engineers' Handbook*, McGraw-Hill, New York, Oct. 2007.

188. I.A. Zlochower and G.M. Green, *The limiting oxygen concentration and flammability limits of gases and gas mixtures,* Journal of Loss Prevention in the Process Industries, 2009, **22**(4), 499-505.

189. C.V. Mashuga and D.A. Crowl, *Derivation of Le Chatelier's mixing rule for flammable limits,* Process Safety Progress, 2000, **19**(2), 112-117.

190. S.K. Matam, O. Korsak, L. Bocher, D. Logvinovich, P. Hug, A. Weidenkaff, and D. Ferri, *Lab Scale Fixed-Bed Reactor for Operando X-Ray Absorption Spectroscopy for Structure Activity Studies of Supported Metal Oxide Catalysts,* Topics in Catalysis, 2011, **54**(16), 1213.

191. G.L. Chiarello, M. Nachtegaal, V. Marchionni, L. Quaroni, and D. Ferri, *Adding diffuse reflectance infrared Fourier transform spectroscopy capability to extended x-ray-absorption fine structure in a new cell to*

study solid catalysts in combination with a modulation approach, Review of Scientific Instruments, 2014, **85**(7), 074102.

192. E.K. Dann, E.K. Gibson, C.R.A. Catlow, V. Celorrio, P. Collier, T. Eralp, M. Amboage, C. Hardacre, C. Stere, A. Kroner, A. Raj, S. Rogers, A. Goguet, and P.P. Wells, *Combined spatially resolved operando spectroscopy: New insights into kinetic oscillations of CO oxidation on Pd/γ-Al$_2$O$_3$,* Journal of Catalysis, 2019, **373**, 201-208.

193. G. Agostini, D. Meira, M. Monte, H. Vitoux, A. Iglesias-Juez, M. Fernandez-Garcia, O. Mathon, F. Meunier, G. Berruyer, F. Perrin, S. Pasternak, T. Mairs, S. Pascarelli, and B. Gorges, *XAS/DRIFTS/MS spectroscopy for time-resolved operando investigations at high temperature,* Journal of Synchrotron Radiation, 2018, **25**(6), 1745-1752.

194. M.A. Newton, *Applying Dynamic and Synchronous DRIFTS/EXAFS to the Structural Reactive Behaviour of Dilute (≤1 wt%) Supported Rh/Al$_2$O$_3$ Catalysts using Quick and Energy Dispersive EXAFS,* Topics in Catalysis, 2009, **52**(10), 1410-1424.

195. N. Richards, J.H. Carter, E. Nowicka, L.A. Parker, S. Pattisson, Q. He, N.F. Dummer, S. Golunski, and G.J. Hutchings, *Structure-sensitivity of alumina supported palladium catalysts for N$_2$O decomposition,* Applied Catalysis B: Environmental, 2020, **264**, 118501.

196. A.J. Dent, G. Cibin, S. Ramos, S.A. Parry, D. Gianolio, A.D. Smith, S.M. Scott, L. Varandas, S. Patel, M.R. Pearson, L. Hudson, N.A. Krumpa, A.S. Marsch, and P.E. Robbins, *Performance of B18, the Core EXAFS Bending Magnet beamline at Diamond,* Journal of Physics: Conference Series, 2013, **430**, 012023.

197. R. Burch, F.J. Urbano, and P.K. Loader, *Methane combustion over palladium catalysts: The effect of carbon dioxide and water on activity,* Applied Catalysis A: General, 1995, **123**(1), 173-184.

198. P. Briot and M. Primet, *Catalytic oxidation of methane over palladium supported on alumina: Effect of aging under reactants,* Applied Catalysis, 1991, **68**(1), 301-314.

199. R. Burch and P.K. Loader, *Investigation of Pt/Al$_2$O$_3$ and Pd/Al$_2$O$_3$ catalysts for the combustion of methane at low concentrations,* Applied Catalysis B: Environmental, 1994, **5**(1), 149-164.

200. N. Mouaddib, C. Feumi-Jantou, E. Garbowski, and M. Primet, *Catalytic oxidation of methane over palladium supported on alumina: Influence of the oxygen-to-methane ratio,* Applied Catalysis A: General, 1992, **87**(1), 129-144.

201. S.K. Matam, G.L. Chiarello, Y. Lu, A. Weidenkaff, and D. Ferri, *PdO$_x$/Pd at Work in a Model Three-Way Catalyst for Methane Abatement Monitored by Operando XANES,* Topics in Catalysis, 2013, **56**(1), 239-242.

202. L. Kiwi-Minsker and A. Renken, *Microstructured Reactors*, in *Handbook of Heterogeneous Catalysis*, ed. G. Ertl*, et al.*, Wiley-VCH, Weinheim, 2008, vol. 1, ch. 10, pp. 2248-2264.

203. E.L. Cussler, *Diffusion: Mass Transfer in Fluid Systems*, Cambridge University Press, Cambridge, 2009.

204. H.S. Fogler, *Elements Of Chemical Reaction Engineering*, Prentice Hall, Upper Saddle River, New Jersey, 2016.

205. J. Kestin and W. Leidenfrost, *The viscosity of helium,* Physica, 1959, **25**(1), 537-555.

206. F. Kapteijn and J.A. Moulijn, *Laboratory Catalytic Reactors: Aspects of Catalyst Testing*, in *Handbook of Heterogeneous Catalysis*, ed. G. Ertl*, et al.*, Wiley-VCH, Weinheim, 2008, vol. vol. 1, ch. ch. 9, pp. 2019-2045.

207. J.M.P.Q. Delgado, *A critical review of dispersion in packed beds,* Heat and Mass Transfer, 2006, **42**(4), 279-310.

208. H. Gierman, *Design of laboratory hydrotreating reactors: Scaling Down of Trickle-flow Reactors,* Applied Catalysis, 1988, **43**(2), 277-286.

209. D.E. Mears, *Tests for Transport Limitations in Experimental Catalytic Reactors,* Industrial & Engineering Chemistry Process Design and Development, 1971, **10**(4), 541-547.

210. J.C. van Giezen, F.R. van den Berg, J.L. Kleinen, A.J. van Dillen, and J.W. Geus, *The effect of water on the activity of supported palladium catalysts in the catalytic combustion of methane,* Catalysis Today, 1999, **47**(1), 287-293.

211. F.H. Ribeiro, M. Chow, and R.A. Dallabetta, *Kinetics of the Complete Oxidation of Methane over Supported Palladium Catalysts,* Journal of Catalysis, 1994, **146**(2), 537-544.

212. W.R. Schwartz, D. Ciuparu, and L.D. Pfefferle, *Combustion of Methane over Palladium-Based Catalysts: Catalytic Deactivation and Role of the Support,* The Journal of Physical Chemistry C, 2012, **116**(15), 8587-8593.

213. M. Schmal, M.M.V.M. Souza, V.V. Alegre, M.A.P. da Silva, D.V. César, and C.A.C. Perez, *Methane oxidation – effect of support, precursor and pretreatment conditions – in situ reaction XPS and DRIFT,* Catalysis Today, 2006, **118**(3), 392-401.

214. H. Na, Z. Liu, and T. Zhu, *In situ DRIFTS investigation of the promoting effect of Zr on Pd/Al$_2$O$_3$ catalyst for the catalytic combustion of methane,* Reaction Kinetics, Mechanisms and Catalysis, 2014, **111**(1), 137-148.

215. O. Demoulin, M. Navez, and P. Ruiz, *Investigation of the behaviour of a Pd/γ-Al$_2$O$_3$ catalyst during methane combustion reaction using in situ DRIFT spectroscopy,* Applied Catalysis A: General, 2005, **295**(1), 59-70.

216. C. Brieger, J. Melke, N. van der Bosch, U. Reinholz, H. Riesemeier, A. Guilherme Buzanich, M.K. Kayarkatte, I. Derr, A. Schökel, and C. Roth, *A combined in-situ XAS–DRIFTS study unraveling adsorbate induced changes on the Pt nanoparticle structure,* Journal of Catalysis, 2016, **339**, 57-67.

217. S.K. Matam, E.V. Kondratenko, M.H. Aguirre, P. Hug, D. Rentsch, A. Winkler, A. Weidenkaff, and D. Ferri, *The impact of aging environment on the evolution of Al$_2$O$_3$ supported Pt nanoparticles and their NO oxidation activity,* Applied Catalysis B: Environmental, 2013, **129**, 214-224.

218. M. Bowker, *Automotive catalysis studied by surface science,* Chemical Society Reviews, 2008, **37**(10), 2204-2211.

219. A.D. Allian, K. Takanabe, K.L. Fujdala, X. Hao, T.J. Truex, J. Cai, C. Buda, M. Neurock, and E. Iglesia, *Chemisorption of CO and Mechanism*

of CO Oxidation on Supported Platinum Nanoclusters, Journal of the American Chemical Society, 2011, **133**(12), 4498-4517.

220. R.H. Nibbelke, M.A.J. Campman, J.H.B.J. Hoebink, and G.B. Marin, *Kinetic Study of the CO Oxidation over Pt/γ-Al$_2$O$_3$ and Pt/Rh/CeO$_2$/γ-Al$_2$O$_3$ in the Presence of H$_2$O and CO$_2$,* Journal of Catalysis, 1997, **171**(2), 358-373.

221. M. Campman, *PhD thesis*, 1996, University of Eindhoven.

222. N.W. Cant, P.C. Hicks, and B.S. Lennon, *Steady-state oxidation of carbon monoxide over supported noble metals with particular reference to platinum,* Journal of Catalysis, 1978, **54**(3), 372-383.

223. C. Daniel, M.-O. Clarté, H. Provendier, A.C. Van Veen, Y. Schuurman, B.J. Beccard, and C. Mirodatos, *Spatially resolved operando infrared analysis of a microstructured catalytic surface for CO oxidation over Pt based catalysts,* Comptes Rendus Chimie, 2009, **12**(6), 647-653.

224. H.H. Kung and E.I. Ko, *Preparation of oxide catalysts and catalyst supports - a review of recent advances,* The Chemical Engineering Journal and the Biochemical Engineering Journal, 1996, **64**(2), 203-214.

225. C. Jiang and V.V. Tsukruk, *Freestanding Nanostructures via Layer-by-Layer Assembly,* Advanced Materials, 2006, **18**(7), 829-840.

226. V.V. Tsukruk, V.N. Bliznyuk, D. Visser, A.L. Campbell, T.J. Bunning, and W.W. Adams, *Electrostatic Deposition of Polyionic Monolayers on Charged Surfaces,* Macromolecules, 1997, **30**(21), 6615-6625.

227. D.M. Dotzauer, A. Abusaloua, S. Miachon, J.-A. Dalmon, and M.L. Bruening, *Wet air oxidation with tubular ceramic membranes modified with polyelectrolyte/Pt nanoparticle films,* Applied Catalysis B: Environmental, 2009, **91**(1), 180-188.

228. J. Liu, X. Zhu, Q. Liao, R. Chen, D. Ye, H. Feng, M. Liu, and G. Chen, *Layer-by-layer self-assembly of palladium nanocatalysts with polyelectrolytes grafted on the polydopamine functionalized gas-liquid-solid microreactor,* Chemical Engineering Journal, 2018, **332**(Supplement C), 174-182.

229. Y. Piao, Y. Jang, M. Shokouhimehr, I.S. Lee, and T. Hyeon, *Facile Aqueous-Phase Synthesis of Uniform Palladium Nanoparticles of Various Shapes and Sizes,* Small, 2007, **3**(2), 255-260.

230. B. Lim, M. Jiang, P.H.C. Camargo, E.C. Cho, J. Tao, X. Lu, Y. Zhu, and Y. Xia, *Pd-Pt Bimetallic Nanodendrites with High Activity for Oxygen Reduction,* Science, 2009, **324**(5932), 1302-1305.

231. B. Lim, M. Jiang, J. Tao, P.H.C. Camargo, Y. Zhu, and Y. Xia, *Shape-Controlled Synthesis of Pd Nanocrystals in Aqueous Solutions,* Advanced Functional Materials, 2009, **19**(2), 189-200.

232. H. Lee, S.M. Dellatore, W.M. Miller, and P.B. Messersmith, *Mussel-Inspired Surface Chemistry for Multifunctional Coatings,* Science, 2007, **318**(5849), 426-430.

233. J.H. Ryu, P.B. Messersmith, and H. Lee, *Polydopamine Surface Chemistry: A Decade of Discovery,* ACS Applied Materials & Interfaces, 2018, **10**(9), 7523-7540.

234. D.M. Dotzauer, J. Dai, L. Sun, and M.L. Bruening, *Catalytic Membranes Prepared Using Layer-by-Layer Adsorption of Polyelectrolyte/Metal Nanoparticle Films in Porous Supports,* Nano Letters, 2006, **6**(10), 2268-2272.

235. A. Corma, P. Concepción, and P. Serna, *A Different Reaction Pathway for the Reduction of Aromatic Nitro Compounds on Gold Catalysts,* Angewandte Chemie International Edition, 2007, **46**(38), 7266-7269.

236. S. Kataoka, Y. Takeuchi, A. Harada, T. Takagi, Y. Takenaka, N. Fukaya, H. Yasuda, T. Ohmori, and A. Endo, *Microreactor containing platinum nanoparticles for nitrobenzene hydrogenation,* Applied Catalysis A: General, 2012, **427-428**, 119-124.

237. E.A. Gelder, S.D. Jackson, and C.M. Lok, *The hydrogenation of nitrobenzene to aniline: a new mechanism,* Chemical Communications, 2005, 522-524.

238. S. Mondini, A.M. Ferretti, A. Puglisi, and A. Ponti, *Pebbles and PebbleJuggler: software for accurate, unbiased, and fast measurement and analysis of nanoparticle morphology from transmission electron microscopy (TEM) micrographs,* Nanoscale, 2012, **4**(17), 5356-5372.

239. C. Huang, X. Wang, F. Yu, B. Yuan, C. Xie, and S. Yu, *Water-soluble palladium nanoparticles as an active catalyst for highly selective hydrogenation of nitrobenzene to aniline,* Research on Chemical Intermediates, 2018, **44**(1), 13-26.

240. F.A. Harraz, S.E. El-Hout, H.M. Killa, and I.A. Ibrahim, *Palladium nanoparticles stabilized by polyethylene glycol: Efficient, recyclable catalyst for hydrogenation of styrene and nitrobenzene,* Journal of Catalysis, 2012, **286**, 184-192.

241. B.D. Adams and A. Chen, *The role of palladium in a hydrogen economy,* Materials Today, 2011, **14**(6), 282-289.

242. M. Guo, H. Li, Y. Ren, X. Ren, Q. Yang, and C. Li, *Improving Catalytic Hydrogenation Performance of Pd Nanoparticles by Electronic Modulation Using Phosphine Ligands,* ACS Catalysis, 2018, **8**(7), 6476-6485.

243. G. Carturan, G. Facchin, G. Cocco, G. Navazio, and G. Gubitosa, *Hydrogenation of nitrocompounds with supported palladium catalysts: Influence of metal dispersion and nitrocompound nature,* Journal of Catalysis, 1983, **82**(1), 56-65.

244. M. Liu, X. Zhu, R. Chen, Q. Liao, D. Ye, B. Zhang, J. Liu, G. Chen, and K. Wang, *Tube-in-tube hollow fiber catalytic membrane microreactor for the hydrogenation of nitrobenzene,* Chemical Engineering Journal, 2018, **354**, 35-41.

245. M. Liu, X. Zhu, R. Chen, Q. Liao, H. Feng, and L. Li, *Catalytic membrane microreactor with Pd/γ-Al$_2$O$_3$ coated PDMS film modified by dopamine for hydrogenation of nitrobenzene,* Chemical Engineering Journal, 2016, **301**, 35-41.

246. T.K. Sherwood and E.J. Farkas, *Studies of the slurry reactor,* Chemical Engineering Science, 1966, **21**(6), 573-582.

247. T. Wang, J. Wang, and Y. Jin, *Slurry reactors for gas-to-liquid processes: a review,* Industrial & Engineering Chemistry Research, 2007, **46**(18), 5824-5847.

248. Y.T. Shah, *Gas-Liquid-Solid Reactor Design*, McGraw-Hill, New York,, 1979.

249. D.I. Enache, G.J. Hutchings, S.H. Taylor, and E.H. Stitt, *The hydrogenation of isophorone to trimethyl cyclohexanone using the downflow single capillary reactor,* Catalysis Today, 2005, **105**(3), 569-573.

250. S. Laohaprapanon, J. Matahum, L. Tayo, and S.-J. You, *Photodegradation of Reactive Black 5 in a ZnO/UV slurry membrane reactor,* Journal of the Taiwan Institute of Chemical Engineers, 2015, **49**, 136-141.

251. R. Janssens, M.K. Mandal, K.K. Dubey, and P. Luis, *Slurry photocatalytic membrane reactor technology for removal of pharmaceutical compounds from wastewater: Towards cytostatic drug elimination,* Science of The Total Environment, 2017, **599-600**, 612-626.

252. R.C. Asha and M. Kumar, *Sulfamethoxazole in poultry wastewater: Identification, treatability and degradation pathway determination in a membrane-photocatalytic slurry reactor,* Journal of Environmental Science and Health, Part A, 2015, **50**(10), 1011-1019.

253. J.F. Richardson, J.H. Harker, and J.R. Backhurst, *Chapter 8 - Membrane Separation Processes*, in *Chemical Engineering, fifth ed.*, Butterworth-Heinemann, Oxford, 2002.

254. F. Carstensen, A. Apel, and M. Wessling, *In situ product recovery: Submerged membranes vs. external loop membranes,* Journal of Membrane Science, 2012, **394-395**, 1-36.

255. R. Field, *Fundamentals of Fouling*, in *Membrane Technology*, ed. K.-V. Peinemann and S. Pereira Nunes, Wiley-VCH Verlag, Weinheim, 2010.

256. M. Sankar, E. Nowicka, R. Tiruvalam, Q. He, S.H. Taylor, C.J. Kiely, D. Bethell, D.W. Knight, and G.J. Hutchings, *Controlling the duality of the mechanism in liquid-phase oxidation of benzyl alcohol catalysed by supported Au-Pd nanoparticles,* Chemistry - A European Journal, 2011, **17**(23), 6524-6532.

257. A. Savara, C.E. Chan-Thaw, I. Rossetti, A. Villa, and L. Prati, *Benzyl alcohol oxidation on carbon-supported Pd nanoparticles: elucidating the reaction mechanism,* ChemCatChem, 2014, **6**(12), 3464-3473.

258. S. Meenakshisundaram, E. Nowicka, P.J. Miedziak, G.L. Brett, R.L. Jenkins, N. Dimitratos, S.H. Taylor, D.W. Knight, D. Bethell, and G.J. Hutchings, *Oxidation of alcohols using supported gold and gold-palladium nanoparticles,* Faraday Discussions, 2010, **145**(0), 341-356.

259. F. Galvanin, M. Sankar, S. Cattaneo, D. Bethell, V. Dua, G.J. Hutchings, and A. Gavriilidis, *On the development of kinetic models for solvent-free benzyl alcohol oxidation over a gold-palladium catalyst,* Chemical Engineering Journal, 2018, **342**, 196-210.

260. F. Galvanin, N. Al-Rifai, E. Cao, M. Sankar, G. Hutchings, A. Gavriilidis, and V. Dua, *Merging information from batch and continuous flow experiments for the identification of kinetic models of benzyl alcohol oxidation over Au-Pd catalyst,* Computer Aided Chemical Engineering, 2016, **38**, 961-966.

261. T.E. Oliphant, *Python for scientific computing,* Computing in Science & Engineering, 2007, **9**(3), 10-20.

262. P.A. Melo, J.C. Pinto, and E.C. Biscaia, *Characterization of the residence time distribution in loop reactors,* Chemical Engineering Science, 2001, **56**(8), 2703-2713.

263. D.I. Enache, D. Barker, J.K. Edwards, S.H. Taylor, D.W. Knight, A.F. Carley, and G.J. Hutchings, *Solvent-free oxidation of benzyl alcohol using titania-supported gold–palladium catalysts: effect of Au–Pd ratio on catalytic performance,* Catalysis Today, 2007, **122**(3), 407-411.

264. P.J. Miedziak, Q. He, J.K. Edwards, S.H. Taylor, D.W. Knight, B. Tarbit, C.J. Kiely, and G.J. Hutchings, *Oxidation of benzyl alcohol using supported gold–palladium nanoparticles,* Catalysis Today, 2011, **163**(1), 47-54.

265. E. Cao, M. Sankar, E. Nowicka, Q. He, M. Morad, P.J. Miedziak, S.H. Taylor, D.W. Knight, D. Bethell, C.J. Kiely, A. Gavriilidis, and G.J. Hutchings, *Selective suppression of disproportionation reaction in solvent-less benzyl alcohol oxidation catalysed by supported Au–Pd nanoparticles,* Catalysis Today, 2013, **203**, 146-152.

266. N. Al-Rifai, F. Galvanin, M. Morad, E. Cao, S. Cattaneo, M. Sankar, V. Dua, G. Hutchings, and A. Gavriilidis, *Hydrodynamic effects on three phase micro-packed bed reactor performance – Gold–palladium*

catalysed benzyl alcohol oxidation, Chemical Engineering Science, 2016, **149**, 129-142.

267. I.K. Stamatiou and F.L. Muller, *Determination of mass transfer resistances of fast reactions in three-phase mechanically agitated slurry reactors,* AIChE Journal, 2017, **63**(1), 273-282.

268. R.V. Chaudhari and P.A. Ramachandran, *Three phase slurry reactors,* AIChE Journal, 1980, **26**(2), 177-201.

269. D. Prat, A. Wells, J. Hayler, H. Sneddon, C.R. McElroy, S. Abou-Shehada, and P.J. Dunn, *CHEM21 selection guide of classical- and less classical-solvents,* Green Chemistry, 2016, **18**(1), 288-296.

270. L. Kiwi-Minsker, E. Joannet, and A. Renken, *Loop reactor staged with structured fibrous catalytic layers for liquid-phase hydrogenations,* Chemical Engineering Science, 2004, **59**(22), 4919-4925.

271. M. Schmitz, A. Steiff, and P.-M. Weinspach, *Gas/liquid interfacial area per unit volume and volumetric mass transfer coefficient in stirred slurry reactors,* Chemical Engineering & Technology, 1987, **10**(1), 204-215.

272. A. Heyouni, M. Roustan, and Z. Do-Quang, *Hydrodynamics and mass transfer in gas–liquid flow through static mixers,* Chemical Engineering Science, 2002, **57**(16), 3325-3333.

273. N.N. Dutta and K.V. Raghavan, *Mass transfer and hydrodynamic characteristics of loop reactors with downflow liquid jet ejector,* The Chemical Engineering Journal, 1987, **36**(2), 111-121.

274. J.J. Heijnen and K. Van't Riet, *Mass transfer, mixing and heat transfer phenomena in low viscosity bubble column reactors,* The Chemical Engineering Journal, 1984, **28**(2), B21-B42.

275. S.H. Kang, S.G. Lee, W.M. Jung, M.C. Kim, W.-S. Kim, C.K. Choi, and R.S. Feigelson, *Effect of Taylor vortices on calcium carbonate crystallization by gas–liquid reaction,* Journal of Crystal Growth, 2003, **254**(1), 196-205.

276. M.W. Losey, M.A. Schmidt, and K.F. Jensen, *Microfabricated Multiphase Packed-Bed Reactors: Characterization of Mass Transfer and Reactions,* Industrial & Engineering Chemistry Research, 2001, **40**(12), 2555-2562.

277. G. Wu, G.L. Brett, E. Cao, A. Constantinou, P. Ellis, S. Kuhn, G.J. Hutchings, D. Bethell, and A. Gavriilidis, *Oxidation of cinnamyl alcohol using bimetallic Au–Pd/TiO$_2$ catalysts: a deactivation study in a continuous flow packed bed microreactor,* Catalysis Science & Technology, 2016, **6**(13), 4749-4758.

278. F. Li, Q. Zhang, and Y. Wang, *Size dependence in solvent-free aerobic oxidation of alcohols catalyzed by zeolite-supported palladium nanoparticles,* Applied Catalysis A: General, 2008, **334**(1), 217-226.

279. V. Pascanu, A. Bermejo Gómez, C. Ayats, A.E. Platero-Prats, F. Carson, J. Su, Q. Yao, M.À. Pericàs, X. Zou, and B. Martín-Matute, *Double-Supported Silica-Metal–Organic Framework Palladium Nanocatalyst for the Aerobic Oxidation of Alcohols under Batch and Continuous Flow Regimes,* ACS Catalysis, 2015, **5**(2), 472-479.

280. C. Bäcktorp, L. Hagvall, A. Börje, A.-T. Karlberg, P.-O. Norrby, and G. Nyman, *Mechanism of Air Oxidation of the Fragrance Terpene Geraniol,* Journal of Chemical Theory and Computation, 2008, **4**(1), 101-106.

281. S.E. Dapurkar, H. Kawanami, M. Chatterjee, C.V. Rode, T. Yokoyama, and Y. Ikushima, *Selective catalytic oxidation of geraniol to citral with molecular oxygen in supercritical carbon dioxide,* Applied Catalysis A: General, 2011, **394**(1), 209-214.

282. K.D. Nagy, B. Shen, T.F. Jamison, and K.F. Jensen, *Mixing and Dispersion in Small-Scale Flow Systems,* Organic Process Research & Development, 2012, **16**(5), 976-981.

283. T. Imamura, K. Saito, S. Ishikura, and M. Nomura, *A new approach to continuous emulsion polymerization,* Polymer International, 1993, **30**(2), 203-206.

284. X. Wei, H. Takahashi, S. Sato, and M. Nomura, *Continuous emulsion polymerization of styrene in a single Couette–Taylor vortex flow reactor,* Journal of Applied Polymer Science, 2001, **80**(11), 1931-1942.

285. T.K. Sengupta, M.F. Kabir, and A.K. Ray, *A Taylor Vortex Photocatalytic Reactor for Water Purification,* Industrial & Engineering Chemistry Research, 2001, **40**(23), 5268-5281.

286. J.G. Sczechowski, C.A. Koval, and R.D. Noble, *A Taylor vortex reactor for heterogeneous photocatalysis,* Chemical Engineering Science, 1995, **50**(20), 3163-3173.

287. P.K. Dutta and A.K. Ray, *Experimental investigation of Taylor vortex photocatalytic reactor for water purification,* Chemical Engineering Science, 2004, **59**(22), 5249-5259.

288. E.P. Rivero, P. Granados, F.F. Rivera, M. Cruz, and I. González, *Mass transfer modeling and simulation at a rotating cylinder electrode (RCE) reactor under turbulent flow for copper recovery,* Chemical Engineering Science, 2010, **65**(10), 3042-3049.

289. F. Coeuret and J. Legrand, *Mass transfer at the electrodes of concentric cylindrical reactors combining axial flow and rotation of the inner cylinder,* Electrochimica Acta, 1981, **26**(7), 865-872.

290. J.E. Weaver, H. Hong, J.J. Ducoste, and F.L. de los Reyes, *Controlling aerobic biological floc size using Couette-Taylor Bioreactors,* Water Research, 2018, **147**, 177-183.

291. E.K. Hill, B. Krebs, D.G. Goodall, G.J. Howlett, and D.E. Dunstan, *Shear Flow Induces Amyloid Fibril Formation,* Biomacromolecules, 2006, **7**(1), 10-13.

292. A.A. Barresi, D. Marchisio, and G. Baldi, *On the role of micro- and mesomixing in a continuous Couette-type precipitator,* Chemical Engineering Science, 1999, **54**(13), 2339-2349.

293. T.S. Tran, S.J. Park, S.S. Yoo, T.-R. Lee, and T. Kim, *High shear-induced exfoliation of graphite into high quality graphene by Taylor-Couette flow,* RSC Advances, 2016, **6**(15), 12003-12008.

294. K.-H. Nam, U. Jung Kim, M. Hee Jeon, T.-R. Lee, J. Yu, N.-H. You, Y.-K. Kim, J. Won Suk, and B.-C. Ku, *Green, fast, and scalable production of reduced graphene oxide via Taylor vortex flow,* Chemical Engineering Journal, 2019, **391**, 123482.

295. T. Färber, O. Riechert, T. Zeiner, G. Sadowski, A. Behr, and A.J. Vorholt, *Homogeneously catalyzed hydroamination in a Taylor–Couette reactor using a thermormorphic multicomponent solvent system,* Chemical Engineering Research and Design, 2016, **112**, 263-273.

296. K. Kataoka, H. Doi, T. Kongo, and M. Futagawa, *Ideal plug-flow properties of Taylor vortex flow,* Journal of Chemical Engineering of Japan, 1975, **8**(6), 472-476.

297. B. Judat, A. Racina, and M. Kind, *Macro- and Micromixing in a Taylor-Couette Reactor with Axial Flow and their Influence on the Precipitation of Barium Sulfate,* Chemical Engineering & Technology, 2004, **27**(3), 287-292.

298. C.M.V. Moore and C.L. Cooney, *Axial dispersion in Taylor-Couette flow,* AIChE Journal, 1995, **41**(3), 723-727.

299. P.I. Pudjiono, N.S. Tavare, J. Garside, and K.D.P. Nigam, *Residence time distribution from a continuous Couette flow device,* The Chemical Engineering Journal, 1992, **48**(2), 101-110.

300. S.S.S. Yim, M.Y.A. Lo, N. Titchener-Hooker, and P.A. Shamlou, *The dependence of residence time distribution on flow in co-axial cylinder devices,* Bioprocess Engineering, 1998, **19**(3), 221-227.

301. Y. Enokida, K. Nakata, and A. Suzuki, *Axial turbulent diffusion in fluid between rotating coaxial cylinders,* AIChE Journal, 1989, **35**, 1211-1214.

302. M. Schrimpf, J. Esteban, H. Warmeling, T. Färber, A. Behr, and A.J. Vorholt, *Taylor-Couette reactor: Principles, design, and applications,* AIChE Journal, 2021, **67**(5), e17228.

303. J. Dusting and S. Balabani, *Mixing in a Taylor–Couette reactor in the non-wavy flow regime,* Chemical Engineering Science, 2009, **64**(13), 3103-3111.

304. O. Richter, H. Hoffmann, and B. Kraushaar-Czarnetzki, *Effect of the rotor shape on the mixing characteristics of a continuous flow Taylor-vortex reactor,* Chemical Engineering Science, 2008, **63**(13), 3504-3513.

305. O. Richter, M. Menges, and B. Kraushaar-Czarnetzki, *Investigation of mixing in a rotor shape modified Taylor-vortex reactor by the means of a chemical test reaction,* Chemical Engineering Science, 2009, **64**(10), 2384-2391.

306. O. Levenspiel, *Chemical Reactor Engineering*, John Wiley & Sons, New York, 1999.

307. D. Rossi, L. Gargiulo, G. Valitov, A. Gavriilidis, and L. Mazzei, *Experimental characterization of axial dispersion in coiled flow inverters,* Chemical Engineering Research and Design, 2017, **120**, 159-170.

308. T. Nishimura, T. Onoue, K. Ohe, and S. Uemura, *Palladium(II)-Catalyzed Oxidation of Alcohols to Aldehydes and Ketones by Molecular Oxygen,* The Journal of Organic Chemistry, 1999, **64**(18), 6750-6755.

309. B.A. Steinhoff, I.A. Guzei, and S.S. Stahl, *Mechanistic Characterization of Aerobic Alcohol Oxidation Catalyzed by Pd(OAc)$_2$/Pyridine Including Identification of the Catalyst Resting State and the Origin of Nonlinear [Catalyst] Dependence,* Journal of the American Chemical Society, 2004, **126**(36), 11268-11278.

310. M. Nemri, E. Climent, S. Charton, J.-Y. Lanoë, and D. Ode, *Experimental and numerical investigation on mixing and axial dispersion in Taylor–Couette flow patterns,* Chemical Engineering Research and Design, 2013, **91**(12), 2346-2354.

311. A. Recktenwald, M. Lücke, and H.W. Müller, *Taylor vortex formation in axial through-flow: Linear and weakly nonlinear analysis,* Physical Review E, 1993, **48**(6), 4444-4454.

312. C.D. Andereck, S.S. Liu, and H.L. Swinney, *Flow regimes in a circular Couette system with independently rotating cylinders,* Journal of Fluid Mechanics, 1986, **164**, 155-183.

313. B.J. Reizman and K.F. Jensen, *An Automated Continuous-Flow Platform for the Estimation of Multistep Reaction Kinetics,* Organic Process Research & Development, 2012, **16**(11), 1770-1782.

314. C. Waldron, A. Pankajakshan, M. Quaglio, E. Cao, F. Galvanin, and A. Gavriilidis, *An autonomous microreactor platform for the rapid identification of kinetic models,* Reaction Chemistry & Engineering, 2019, **4**(9), 1623-1636.

315. B.J. Reizman and K.F. Jensen, *Feedback in Flow for Accelerated Reaction Development,* Accounts of Chemical Research, 2016, **49**(9), 1786-1796.

316. G. Franceschini and S. Macchietto, *Model-based design of experiments for parameter precision: State of the art,* Chemical Engineering Science, 2008, **63**(19), 4846-4872.

317. H. Feng, B. Zhang, X. Zhu, R. Chen, Q. Liao, D.-d. Ye, J. Liu, M. Liu, and G. Chen, *Multilayered Pd nanocatalysts with nano-bulge structure in a microreactor for multiphase catalytic reaction,* Chemical Engineering Research and Design, 2018, **138**, 190-199.

318. G. Richner, J.A. van Bokhoven, Y.-M. Neuhold, M. Makosch, and K. Hungerbühler, *In situ infrared monitoring of the solid/liquid catalyst interface during the three-phase hydrogenation of nitrobenzene over nanosized Au on TiO$_2$,* Physical Chemistry Chemical Physics, 2011, **13**(27), 12463-12471.

319. A. Pintar, R. Malacea, C. Pinel, G. Fogassy, and M. Besson, *In situ monitoring of catalytic three-phase enantioselective hydrogenation using FTIR/ATR spectroscopy,* Applied Catalysis A: General, 2004, **264**(1), 1-12.

320. L. Negahdar, C.M.A. Parlett, M.A. Isaacs, A.M. Beale, K. Wilson, and A.F. Lee, *Shining light on the solid–liquid interface: in situ/operando monitoring of surface catalysis,* Catalysis Science & Technology, 2020, **10**(16), 5362-5385.

321. B. Ravel and M. Newville, *ATHENA, ARTEMIS, HEPHAESTUS: data analysis for X-ray absorption spectroscopy using IFEFFIT,* Journal of Synchrotron Radiation, 2005, **12**(4), 537-541.

322. B. Loganathan and B. Karthikeyan, *Au core Pd/Pt shell in trimetallic Au/Pd/Pt colloidal nanocomposites – Physicochemical characterization study,* Colloids and Surfaces A: Physicochemical and Engineering Aspects, 2013, **436**, 944-952.

323. Mott Corporation Porous Metal Products. *Porous metal solutions. Filtration flow control, sparging, dispersion, and shapes of porous metal.* https://mottcorp.com (accessed 11 November 2021).

324. K.-D. Chen, Y.-F. Lin, and C.-H. Tu, *Densities, viscosities, refractive indexes, and surface tensions for mixtures of ethanol, benzyl acetate, and benzyl alcohol,* Journal of Chemical & Engineering Data, 2012, **57**(4), 1118-1127.

325. F.P. Incropera, *Fundamentals of Heat and Mass Transfer*, John Wiley & Sons, New York, 2011.

326. S. van der Walt, S.C. Colbert, and G. Varoquaux, *The NumPy array: a structure for efficient numerical computation,* Computing in Science & Engineering, 2011, **13**(2), 22-30.

327. A.D. Jorgensen, K.C. Picel, and V.C. Stamoudis, *Prediction of gas chromatography flame ionization detector response factors from molecular structures,* Analytical Chemistry, 1990, **62**(7), 683-689.

328. C.-C. Chen, *A Study on Estimating Flammability Limits in Oxygen,* Industrial & Engineering Chemistry Research, 2011, **50**(17), 10283-10291.

329. D. Kong, D.J. am Ende, S.J. Brenek, and N.P. Weston, *Determination of flash point in air and pure oxygen using an equilibrium closed bomb apparatus,* Journal of Hazardous Materials, 2003, **102**(2), 155-165.

330. D. Tromans, *Temperature and pressure dependent solubility of oxygen in water: a thermodynamic analysis,* Hydrometallurgy, 1998, **48**(3), 327-342.

331. F. Brühne and E. Wright, *Benzyl Alcohol*, in *Ullmann's Encyclopedia of Industrial Chemistry*, Wiley-VCH, Weinheim, 2012, vol. 5, pp. 357-366.

332. F. Brühne and E. Wright, *Benzaldehyde*, in *Ullmann's Encyclopedia of Industrial Chemistry*, Wiley-VCH, Weinheim, 2012, vol. 5, pp. 223-236.

333. P.V. Danckwerts, *The definition and measurement of some characteristics of mixtures,* Applied Scientific Research, Section A, 1952, **3**(4), 279-296.

Appendix A. Silicon microeactor design and data post-processing

A.1. Microfabricated silicon-glass reactor

Pictures of the silicon-glass microreactor are presented in Figure A.1. It is possible to observe in the top pictures of both the back and the front side, the thermocouple wells used to insert the thermocouples and the larger X-ray slits, through which X-ray beams were shone. The DRIFTS window is visible on the front side, while the back side shows the catalyst bed with silica beads.
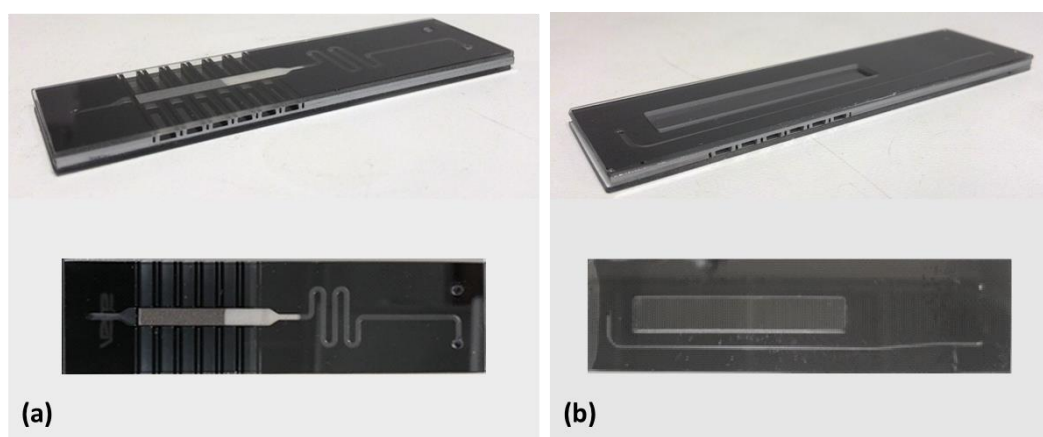

Figure A.1. Pictures of the silicon-glass microreactor: (a) back side and (b) front side

Figure A.2 shows the microreactor in an in-house made heating unit. This comprised of a ceramic heater which was fitted into a stainless steel holder.

## A.2. Data post-processing and linear combination fitting

The raw XAS data were post-processed using the Athena software [321]. Pre-edge subtraction and normalisation to the post-edge background were performed on the X-ray absorption near edge structure (XANES) spectra. The normalised XANES data were fitted around the Pd K-edge (24150 - 24986 eV) using the linear combination fitting (LCF) technique with the Athena software. As reference spectra, the XANES related to the Pd metal foil and the PdO component at the inlet during calcination, were used for the Pd^0 and PdO weightings in the LCF, respectively. Their value was constrained between 0 and 1 and their sum to be equal to 1. The quality of the fitting was quantified using the R-factor, which was constantly low for all the fittings (R-factor = 0.00083 ± 0.00021). Figure A.2 shows an example of LCF for a XANES spectrum taken at the inlet of the catalyst bed at 250 °C. The fitting was achieved with weightings for PdO and Pd^0 of 0.923 and 0.077 respectively, and a resulting R-factor of 0.00016. Concerning the EXAFS data, their Fourier transform (FT) was performed on the k^3-weighted functions between 2.7 and 10 $Å^{-1}$.
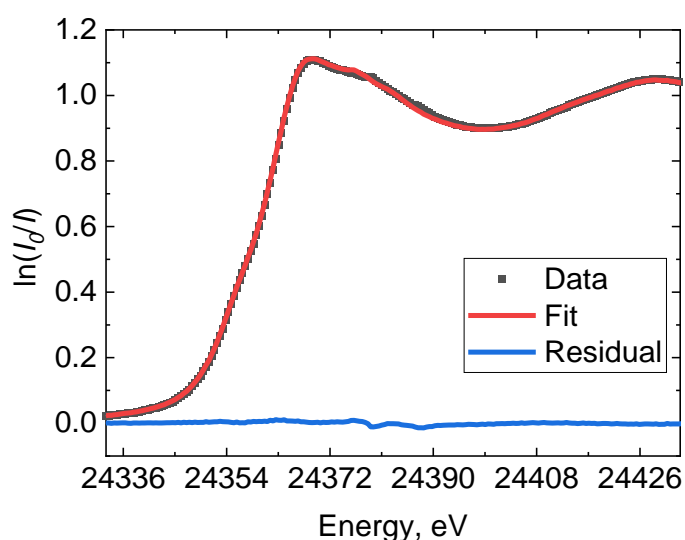
Figure A.2. Example of linear combination fitting (red line) of the experimental XANES spectrum (black dots) and resulting residual (blue line) for the 2 wt% Pd/Al_2O_3 at the inlet of the catalyst bed at 250 °C. Gas inlet composition: 1% CH_4 and 4% of O_2 in He, flowrate: 40 NmL/min, atmospheric pressure, catalyst amount: 27.7 mg (53 - 63 µm).

A.3. Fourier Transform of the EXAFS

Fourier Transform (FT) of the corresponding EXAFS is presented in Figure A.3. This shows the contribution of oxygen in the first coordination shell of the PdO structure at 1.5 Å (phase shift uncorrected) and the Pd-Pd pair in the second coordination shell at about 3 Å. A small contribution from Pd-Pd metal (*ca.* 2.4 Å) at 250 °C is visible, indicating once more a predominant presence of palladium oxide in the catalyst.
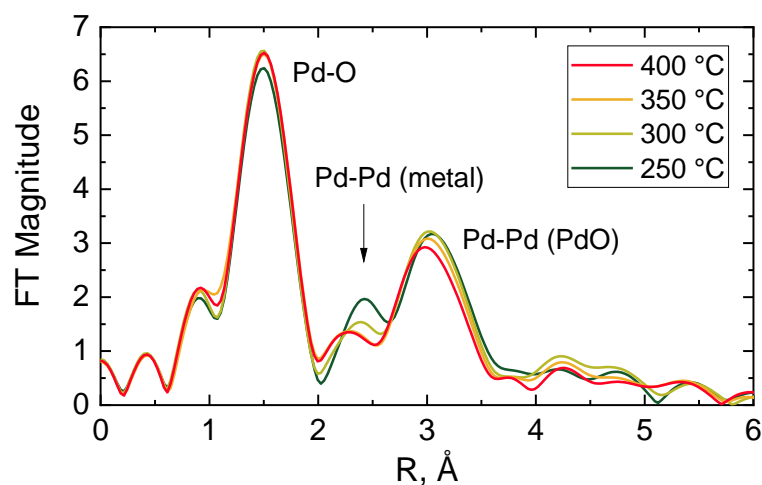
Figure A.3. Phase shift uncorrected Fourier Transform magnitude of the Pd K-edge EXAFS of the 2 wt% Pd/Al$_2$O$_3$ during methane combustion.

Appendix B. Membrane reactor with adsorbed catalytic nanoparticles

B.1. Estimation of the catalytic activity of surface atoms

The estimation of the ratio, α_p, between the number of bulk atoms below the first external atomic layer, $N_{sub,p}$, and the total amount of metal atoms in the nanoparticle, N_p, is given in Equation (B.1). It can be assumed that all the nanoparticles have a spherical shape, whose average diameter, d_p, is determined by the TEM analysis. α_p can be seen the ratio between two spheres. The first sphere is obtained by subtracting from the entire nanoparticle diameter two times the atom covalent diameter, cd (metal atom diameter in a covalent bonding). The second sphere corresponds to the entire nanoparticle. The covalent radius used for the palladium nanoparticles was 0.139 nm [322]. For the dendritic nanoparticles, the platinum covalent radius was used due to its larger amount. This is equal to 0.136 nm [322]. The calculation of the ratio between the number of surface atoms, $N_{sup,p}$, and the total number of atoms for each nanoparticle, $1 - \alpha_p$, is presented in Equation (B.2) and the estimated values are shown in Table B.1.

$$\alpha_p = \frac{N_{sub,p}}{N_p} = \frac{(d_p - 2\,cd)^3}{d_p^3} \tag{B.1}$$

$$1 - \alpha_p = \frac{N_p - N_{sub,p}}{N_p} = \frac{N_{sup,p}}{N_p} \tag{B.2}$$

Table B.1. Ratio between the number of superficial atoms and the total number of atoms, $1 - \alpha_p$, for the Pd spherical, Pd truncated octahedral, Pd cubical and Pt-Pd dendritic nanoparticles.

	Pd spheres	Pd truncated octahedral	Pd cubes	Pt-Pd Dendrites
$1 - \alpha_p$	0.39	0.37	0.07	0.24

B.2. Hydrogen supply and maximum consumption rate

The hydrogen supply rate, $v_{H2,sup}$, and the hydrogen demand rate, $v_{H2,dem}$, at standard temperature and pressure (STP, 0 °C and 1 atm) were determined according to Equation (B.3).

$$v_{H_2,sup} = \frac{P_{m,H_2} \, A_m \, \Delta p}{\delta_m} \tag{B.3}$$

The hydrogen permeability in the Teflon AF-2400, $P_{m,H2}$, is 2090 barrer at 35 °C (see Chapter II). The membrane area, A_m, was 3.78 cm^2, Δp is the gas pressure difference across the membrane, which assuming full consumption of hydrogen at the catalyst location to evaluate its maximum possible value is 5 bar, and δ_m, the membrane thickness, 0.1 mm. The hydrogen demand rate at STP was estimated considering maximum conversion and selectivity to aniline. This is presented in Equation (B.4), where v is the stoichiometric ratio between the consumed hydrogen and nitrobenzene, 3, and $\tilde{V}_{H2}$ is the molar volume of hydrogen at STP, 22.414 L/mol.

$$v_{H_2,dem} = v \, X \, F_{NB,in} \, \tilde{V}_{H_2} \tag{B.4}$$

Appendix C. Crossflow filter design

Tangential flow filtration, also known as crossflow filtration, is a filtration technique that occurs perpendicularly to a filtration surface on top of which a solid-liquid flows tangentially [253, 255]. The benefits deriving from a crossflow filtration include a higher permeate flux at relatively low transmembrane pressures, owing to the reduced bed thickness of the solid cake [253]. Furthermore, increasing the tangential flow of the solid-liquid mixture, more concentrated slurry mixtures can be filtered [253]. However, since the applications can vary there is no unique design for crossflow filters. In this work a crossflow filter was designed to allow continuous filtration of a circulating slurry flow inside a loop that could prevent accumulation and progressive fouling of the filter.
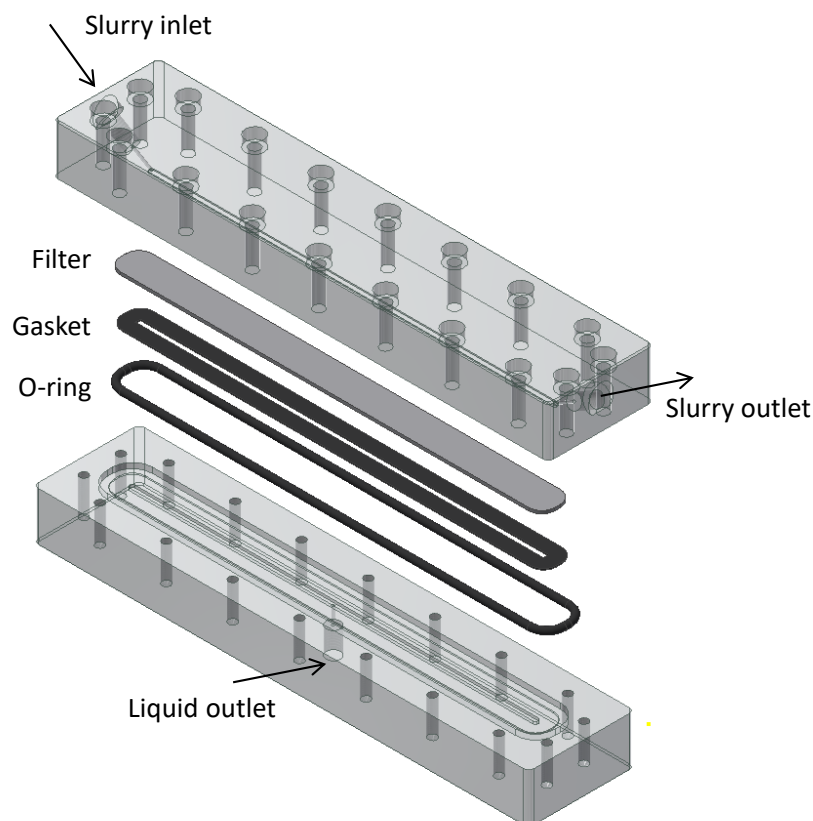
C.1. Filter in the slurry loop tubular membrane reactor

A stainless steel sintered filter (0.1 µm, 316 L, Mott) was chosen for the crossflow filter of the slurry tubular membrane reactor, owing to its mechanical and chemical resistance and ability to deal with particles larger than 0.1 µm. Figure C.1 shows the trans-filter pressure drop of the Mott filter versus the liquid flux for a range of viscosities [323].
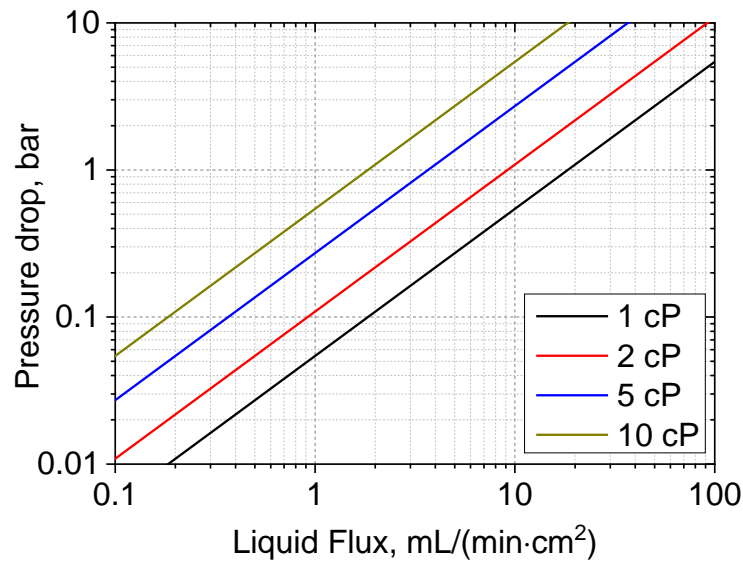
Figure C.1. Pressure drop across the Mott 0.1 316L SS filter surface as function of the liquid flux for four different viscosities: 1 cP, 2 cP, 5 cP and 10 cP [323].

With a benzyl alcohol viscosity of 5.4 cP at 20 °C [324], the liquid flux that corresponding to a pressure drop of 0.1 bar across the filter is *ca.* 0.3 mL/(min·cm^2). This pressure value is enough to avoid over pressurisation of the loop with respect to the desired back pressure set on the liquid back-pressure regulator. Assuming a maximum operating inlet flowrate of 1 mL/min of benzyl alcohol, the required surface area that matches the 0.3 mL/(min·cm^2) flux would be 3 cm^2. Nevertheless, using half the filtration area would only create 0.5 bar pressure drop with 1 mL/min trans-filter flowrate. The CAD drawing of the filter assembly is displayed in Figure C.2.

Figure C.2. Schematic of the crossflow filter used in the slurry loop tubular membrane reactor. The filter consists of a top channel for the inlet and outlet flow of the catalyst slurry, a bottom channel for the filtered liquid, a sintered stainless steel filter for the filtration and a Kalrez® gasket and O-ring for sealing.

This is a cassette-type assembly made of a top and bottom 316 stainless steel parts. The top block had an inlet, an outlet port and a channel for the slurry flow. This channel has a length of 156 mm, a width of 2 mm and a cross sectional area of 1 mm^2 (2 mm x 0.5 mm), which created an average velocity of 16.7 cm/s at 10 mL/min. The bottom block had a 156 mm long channel with a width of 2 mm and depth of 1 mm, facing the slurry channel on the top part. In the middle a hole allows the filtered liquid to exit. The sintered filter (0.1 µm, 316L, Mott) was shaped to fit between the two channels, with a length, width and thickness of 166 mm, 12 mm and 1 mm respectively. To ensure proper sealing of the filter with the bottom block, a Kalrez® gasket (thickness: 0.50 mm, DuPont) of the same shape as the filter was placed between the filter and the bottom part. To seal the filter to the top part, a Kalrez® O-ring (cross section

diameter: 2.62 mm, DuPont) was fitted inside the groove in the bottom unit that surrounded the filter. The crossflow filter unit was then screwed with 18 bolts (M4 x 25 mm, RS Components) in order to compress the filter to the gasket and the O-ring around the filter.

C.2. Filter in the slurry loop flat membrane reactor

A smaller filter unit was chosen for the slurry loop flat membrane reactor setup. The filter unit was made of the same cassette-type design of Figure C.2, consisting of two blocks of stainless steel 316L, a top and a bottom part. The former hosted the slurry channel and was connected to the loop, while the bottom part collected the pure liquid from the slurry and was connected to the outlet of the reactor. Figure C.3 shows the assembly of the crossflow filter. The sintered stainless steel filter (0.1 µm 316L, Mott) was placed between the two blocks and was sealed using a Kalrez® O-ring (cross section diameter: 2.62 mm, DuPont) and a Kalrez® gasket (thickness: 0.50 mm, DuPont). Fourteen M2.5x20 bolts (ISO 4762) ensured that the filter was tightened enough to withstand the operating pressure of the slurry in the loop. The characteristic feature of the filter top part was the 30° angle at which the inlet and the outlet ports were connected to the loop and this was done to hinder clogging of the channel by catalyst particles. Design details of the top and bottom parts are reported in Figure C.4 and C.5, respectively. The top part shows that both the inlet and the outlet holes (1/4-28 UNF) were made at 30° with respect to the plane of the slurry channel. This was 0.5 mm deep, 2 mm wide and 25 mm long, leading to an average slurry velocity of 16.7 cm/s, when a recycle flowrate of 10 mL/min was used. An O-ring was fitted in the groove of the bottom part, while the gasket and the stainless steel filter were placed on the area surrounded by the groove. A hole of 1 mm diameter was drilled to connect the channel for the collection of pure liquid to the hole (1/4-28 UNF) of the outlet (see Figure C.5).

The surface area of the channel (0.5 cm^2) allowed a transversal flow of 0.5 mL/min for 0.5 bar pressure drop with benzyl alcohol at room temperature, according to Figure C.1. However, the small design allowed the whole setup components to be inserted inside the acetal box (see Appendix F).
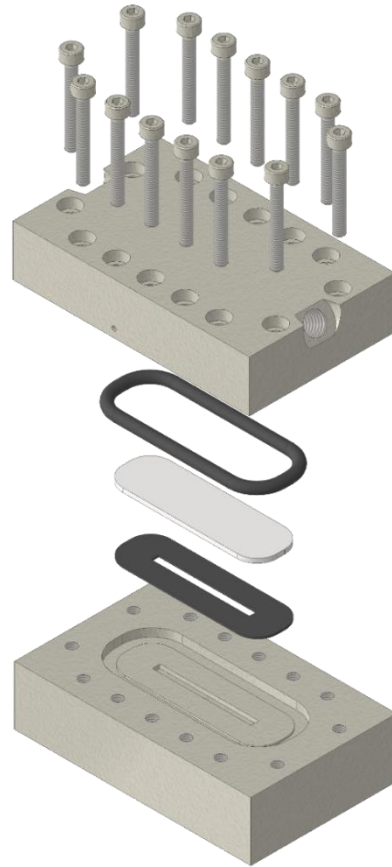
Figure C.3. Exploded assembly of the crossflow filter used in the slurry loop flat membrane reactor.
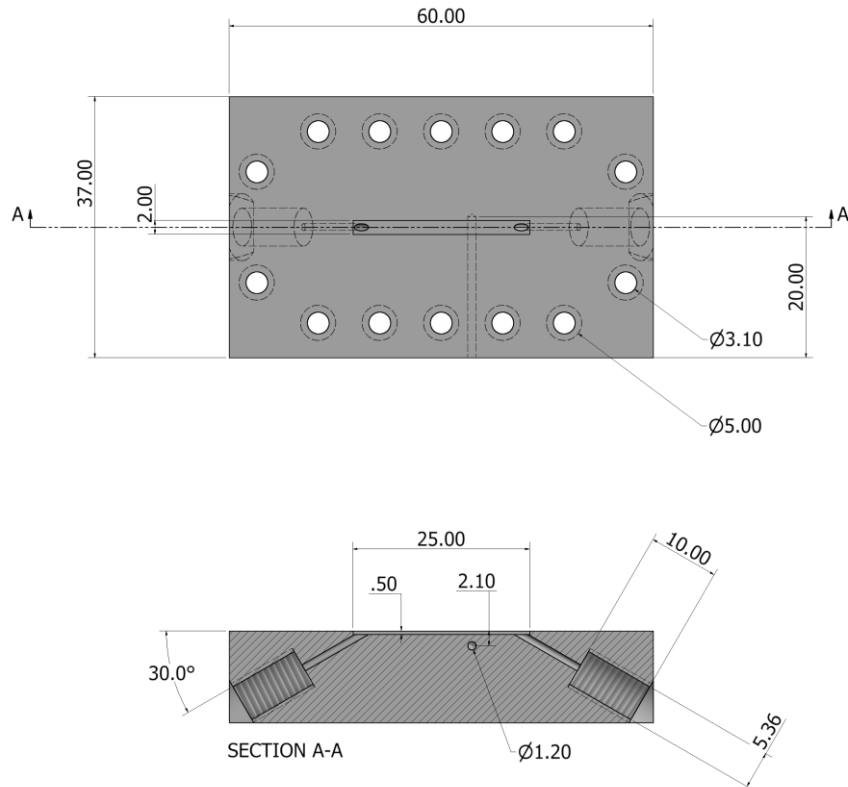
Figure C.4. Technical drawing of the crossflow filter top part.
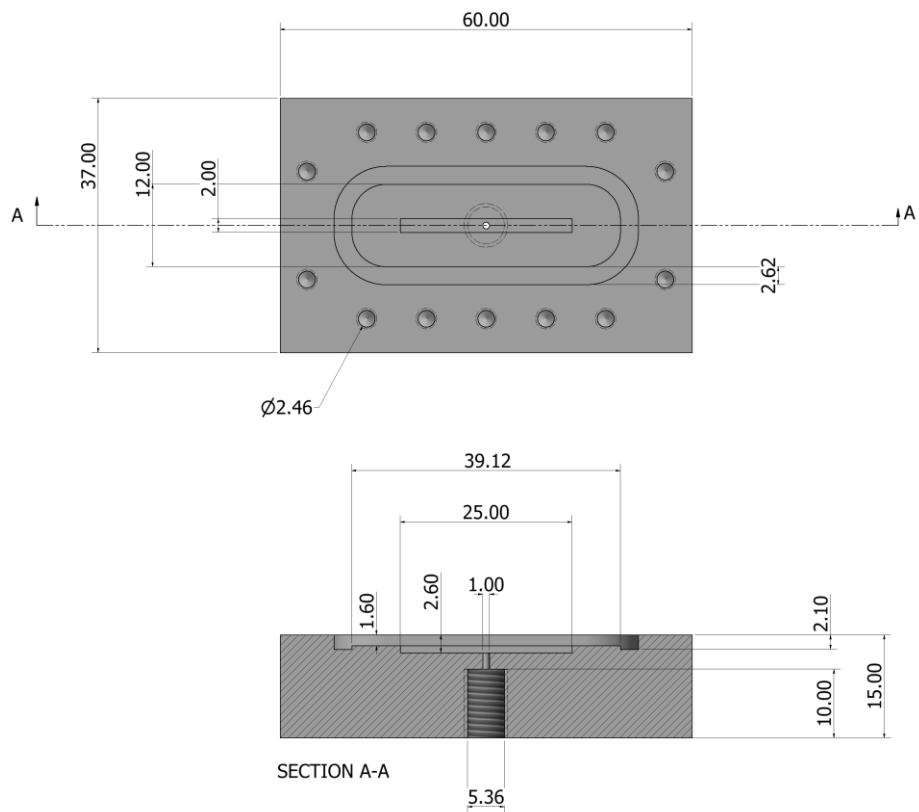
Figure C.5. Technical drawing of the crossflow filter bottom part.

Appendix D. Slurry loop tubular membrane reactor characterisation and comparative reaction studies

D.1. Catalyst particle size distribution

The 1 wt% Au-Pd/TiO$_2$ catalyst (Johnson Matthey) employed in this thesis was characterised *via* laser scattering (LS 13 320, Beckman Coulter) and the particle size distribution is shown in Figure D.1.
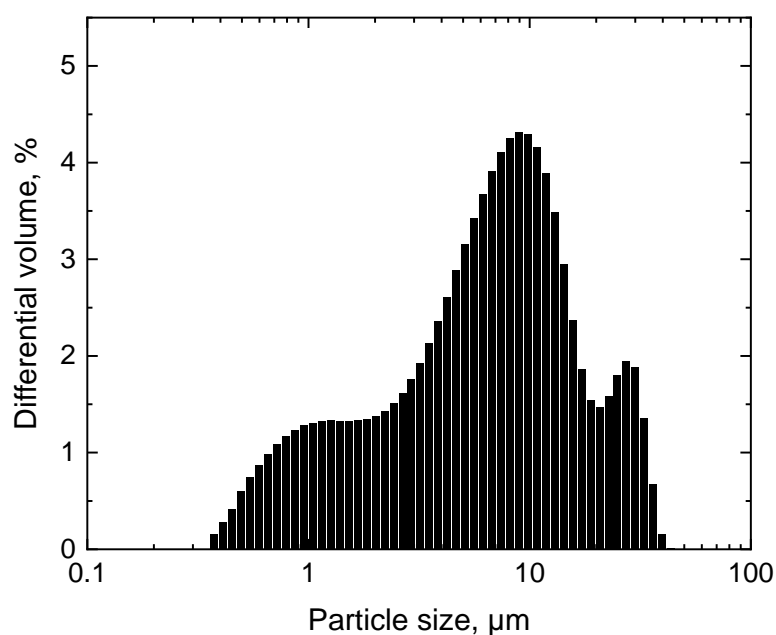
Figure D.1. Particle size distribution of the 1% Au-Pd/TiO$_2$ employed in the aerobic oxidation of alcohols in the two slurry loop membrane reactors.

D.2. Benzoic acid and benzyl benzoate selectivity in the autoclave experiments

The selectivity to benzoic acid and benzyl benzoate from the autoclave aerobic oxidation of benzyl alcohol, which were the second most produced by-products after benzaldehyde and toluene, are reported in Table D.1. As it is is possible to observe, they did not vary much as a function of the catalyst loading, except for the large benzoic acid selectivity (9.2%) at a catalyst concentration of 3.7 g/L.

Table D.1. Benzoic acid, S_{BzAc}, and benzyl benzoate, S_{BzBz}, selectivity as a function of the catalyst concentration, ρ_{cat}, in the autoclave reactor. Temperature: 120 °C, oxygen pressure: 5 bar, benzyl alcohol volume: 10 mL, reaction time: 58 min.

ρ_{cat}, g/L	CCT, $g_{cat}{\cdot}s/g_{ROH}$	S_{BzAc}, %	S_{BzBz}, %
1.3	4	3.7	6.3
2.5	8	4.8	4.9
3.7	12	9.2	5.3
5.0	17	7.5	4.8

D.3. Simulation of the fluid temperature in the SLTM reactor

Simulations using the finite element modelling software COMSOL Multiphysics® 5.3a were performed to estimate the time needed for the slurry flow inside the loop to reach 120 °C and to assess the average liquid temperature. The simulations took into account a section of the loop (recirculation pump) outside the temperature bath, and only the heat transfer between the oil, the loop material and the slurry flow, without considering any chemical reaction. The loop tube was modelled as axisymmetric and was comprised of different domains: pump section, various tubular connections and the oxygen saturator section (see Figure D.2). The model consisted of the tube bore and its walls. The bore of each tube section was modelled assuming it contained pure benzyl alcohol, since the catalyst slurry only contained < 1 v% of suspended particles.
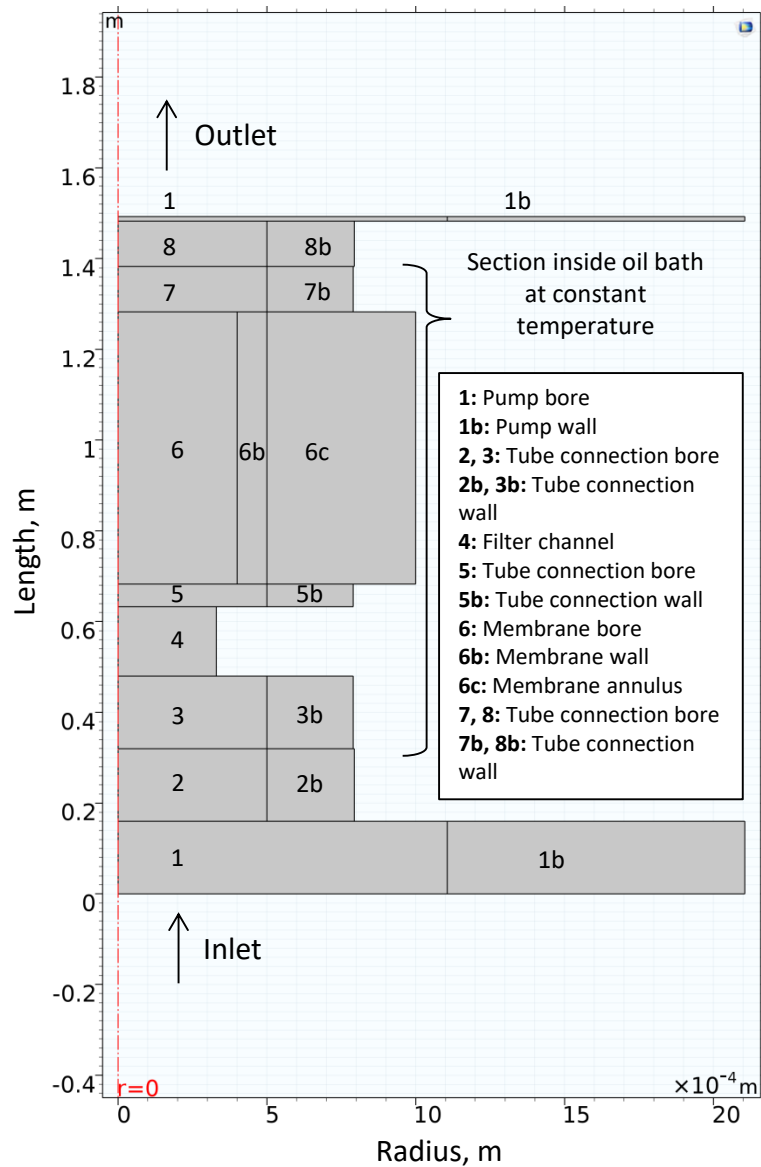
Figure D.2. Length and radial dimensions of the different sections forming the axisymmetric model geometry of the slurry loop tubular system.

Table D.2 shows the dimensions and the material for each tube wall section, including the pump, connections and membrane. For the crossflow filter and the outer tube of the tube-in-tube saturator, no wall was included in the model as these were made of stainless steel.

Table D.2. Dimensions and materials in the different sections of the loop reactor model.

Domain	Section	Material	Length, m	Width, 10^{-4} m
1b	Pump wall	PTFE	0.16	10
2b	Tube wall	PTFE	0.16	2.9
3b	Tube wall	PTFE	0.16	2.9
5b	Tube wall	PTFE	0.05	2.9
6b	Membrane wall	PTFE	0.6	1
6c	Membrane annulus	Oxygen	0.6	5
7b	Tube wall	PTFE	0.1	2.9
8b	Tube wall	PTFE	0.1	2.9

A section of the pump tube (1, 1b) in the model was placed on top of the loop geometry (8, 8b) in order to simulate the loop configuration of the tube. No external inlet or outlet were simulated, given the high ratio of 400 between the recirculation rate and the inlet flowrate during the experiments. Therefore, the energy and momentum balance contribution from the inlet were considered to be negligible.

The mesh was set to "fine", corresponding to 139585 elements, with a maximum and minimum size of 0.0791 m and $4.48 \cdot 10^{-4}$ m. A steady-state momentum balance of Equation (D.1) was solved along with the continuity Equation (D.2). In parallel, the time-dependent energy balance of Equation (D.3) was solved by coupling the "laminar flow" with the "heat transfer in fluids" model provided by COMSOL.

$$\rho(\boldsymbol{u} \cdot \nabla)\boldsymbol{u} = -\nabla p + \mu \nabla^2 \boldsymbol{u} + \rho \boldsymbol{g} \qquad \text{(D.1)}$$

$$\rho \nabla \cdot \boldsymbol{u} = 0 \qquad \text{(D.2)}$$

$$\rho C_p \frac{DT}{Dt} = k \, \nabla^2 T + Q \qquad \text{(D.3)}$$

The boundary conditions are mentioned below. The inlet velocity and the pressure were set equal to the outlet velocity and pressure at any time, as in Equation (D.4) and (D.5), and non-slip velocity was assumed on the inner

walls, as described in Equation (D.6). The flowrate was set equal to 10 mL/min and the pressure increase in the pump was modelled by setting a pressure increase between section 1 and 2.

$$\boldsymbol{u_{in}} = \boldsymbol{u_{out}} \tag{D.4}$$

$$p_{in} = p_{out} \tag{D.5}$$

$$\boldsymbol{u}|_{int-wall} = 0 \tag{D.6}$$

Periodic boundary conditions were set also for the energy balance. In particular the inlet and the outlet temperatures were set equal to each other, as shown in Equation (D.7). Moreover, the external wall temperature, in contact with the oil, was set to 120 °C for section 3, 4, 5, 6 and 7 (see Figure D.2). For the remaining sections, heat loss to the environment was simulated, as described in Equation (D.8), by assuming an external temperature, T_{ext}, of 20 °C and a heat transfer coefficient, U, of 5 W/(m²·K) corresponding to mild natural convection [325].

$$T_{in} = T_{out} \tag{D.7}$$

$$Q = UA\left(T_{ext} - T\right) \tag{D.8}$$

Figure D.3 depicts the temperature distribution after 1 min of simulation time. The maximum value of temperature was 120 °C, reached in section 5, 6 and 7 (Figure D.2), while the minimum temperature was equal to 99 °C at the pump wall and 112 °C inside the tube connection to the pump. Steady-state conditions were reached after 1 s of simulation time, indicating that despite the presence of heat losses, the small diameter of the tube sections inside the temperature bath enhanced heat transfer.

Equation (D.9) shows how the average volumetric temperature in the liquid inside the loop was calculated, assuming constant specific heat capacity.

$$\bar{T} = \frac{\int_0^L \int_0^R T(r,z)\rho(T)2\pi r\,dr\,dz}{m_R} \tag{D.9}$$

In Equation (D.9) $T(r,z)$ is the temperature along the radial and axial position, $\rho(T)$ is the liquid density as a function of temperature and m_R is the total mass of flowing liquid. With an oil bath temperature of 120 °C, the average volumetric temperature of the liquid was *ca.* 117 °C. Simulations were

performed for other target temperatures and the resulting average liquid temperatures are reported in Table D.3. It is possible to observe, that these are consistently 3 °C lower than the oil bath temperature for all the target set point values.
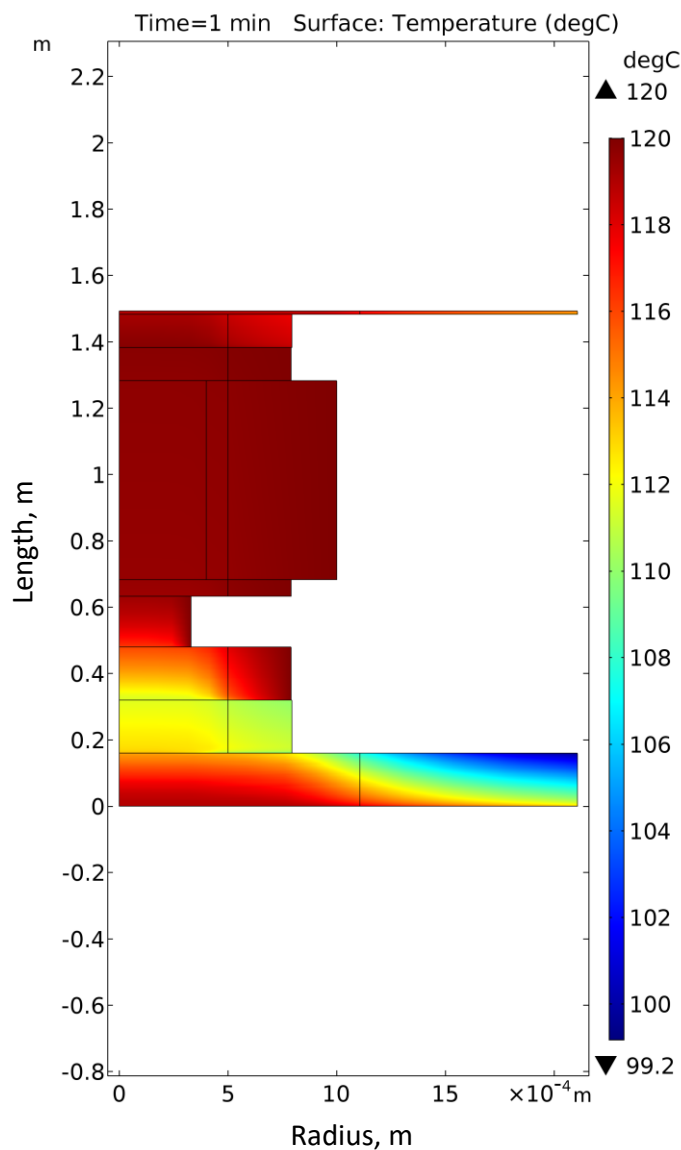
Figure D.3. Temperature profile in the slurry loop tubular membrane system. Recycle flowrate: 10 mL/min, wall temperature: 120 °C in the oil bath, natural convection at room temperature for the section outside the oil bath.

Table D.3. Average volumetric temperature inside the slurry loop tubular membrane assembly as function of the external oil bath temperature. Recycle flowrate: 10 mL/min, wall temperature: 120 °C in the oil bath, natural convection and room temperature for the section outside the oil bath.

| Oil bath temperature, °C	Average temperature in the loop, °C
100	97
105	102
110	107

D.4. Trickle-bed capillary reactor setup and by-product formation

The 1 wt% Au-Pd/TiO$_2$ powder catalyst was pelletized, crushed and sieved to reach an average particle size between 90 and 120 µm. An amount of 7 mg of the resulting catalyst was packed in a 60 cm long PTFE capillary tube (ID: 1 mm, OD: 1.6 mm, Kinesis) using a vacuum pump (KNF labs) connected on the other end of the tube. A picture of the reactor is shown in Figure D.4. A nickel mesh (25 µm, Tecan) placed between a PEEK union (Upchurch) and the PEEK ferrule fitting (Upchurch) was used to retain the catalyst.

Figure D.4. Picture of the trickle-bed capillary reactor made of PTFE tube (ID: 1 mm) containing 7 mg of packed 1 wt% Au-Pd/TiO$_2$ catalyst with a particle size 90-125 µm.

The setup schematic is shown in Figure D.5. An oil bath was used to keep a constant temperature of 120 °C with a thermocouple connected to the hotplate underneath (Type T, RS Components), immersed and measuring the temperature of the oil. The capillary reactor was placed in the bath and benzyl alcohol (99.0%, Sigma-Aldrich) was pumped at 0.025 mL/min using an 8 mL stainless steel syringe (Harvard Apparatus) driven by a syringe pump (PHD ULTRA, Harvard Apparatus). Pressure was measured at the inlet of the reactor using a pressure sensor (Hastelloy/PFA wetted parts, Zaiput) and controlled by means of a back pressure regulator (BPR-01, Zaiput). Oxygen was fed using a mass flow controller (SLA5850S, Brooks) which kept a constant flowrate of 2.5 NmL/min.
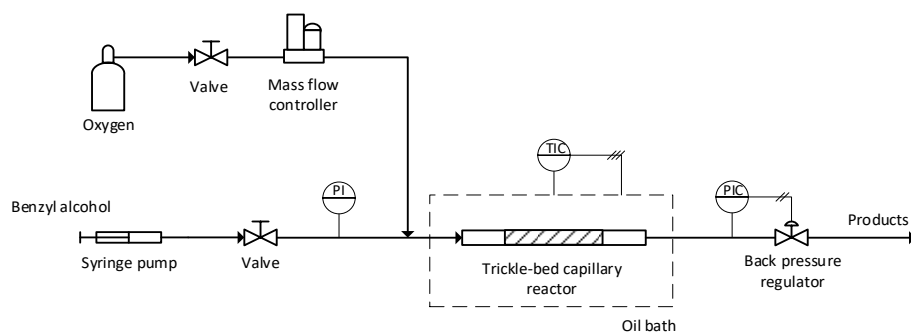
Figure D.5. Experimental setup of the trickle-bed capillary reactor used for the aerobic oxidation of benzyl alcohol in flow using a packed-bed of Au-Pd/TiO$_2$ catalyst through which premixed benzyl alcohol and oxygen were fed. PI: pressure indicator, PIC: pressure indicator and controller (back pressure regulator), TIC: temperature indicator and controller.

The pressure in the reactor was kept at 5 bar and results from the aerobic oxidation of benzyl alcohol are reported in Table D.4. A repetition of the experiment was performed and a maximum variation of ±2% (absolute) was observed for both conversion and product selectivity. The second most produced by-product after toluene was benzyl benzoate with a selectivity of 5%. This suggests the presence of a highly oxygenated environment, which could lead to the further oxidation of benzaldehyde.

Table D.4. Benzyl alcohol conversion, X, and product selectivity in the aerobic oxidation of benzyl alcohol in a trickle-bed capillary reactor. Temperature: 120 °C, pressure: 5 bar, oxygen flowrate: 2.5 NmL/min, benzyl alcohol flowrate: 0.025 mL/min, catalyst mass: 7 mg, CCT: 17 g$_{cat}$·s/g$_{ROH}$.

X, %	Selectivity, %				
	Benzaldehyde	Toluene	Benzoic acid	Dibenzyl ether	Benzyl benzoate
68	62	30	1.1	1.4	4.6

Appendix E. Macromixing studies

Macromixing characterisations were carried out in the reactors by performing a residence time distribution (RTD) analysis. All experiments were conducted at room temperature (20 °C) and atmospheric pressure, using DI water and a tracer (Basic Blue 3, Sigma-Aldrich) that was always introduced at the inlet and analysed at the outlet of the reactor, or in the loop in the case of loop reactors.

Optical fibres were used to direct the light through the reactor tubes, where the flow cells were installed allowing the transmitted light to be analysed by a spectrophotometer (Ocean Optics USB2000 + UV-VIS-ES).

The concentration of the tracer can be related to the absorbance according to the Beer-Lambert law shown in Equation (E.1), where A_L stands for the light absorbance, I_t and I_0 the transmitted and incident light intensity respectively, ψ the extinction coefficient, L the absorption length and C the tracer concentration. Calibration of the spectrophotometer was performed to make sure that the tracer concentration in the loop lied within the range where absorbance and tracer concentration are linearly proportional. The transmitted light intensity was averaged between 645 and 660 nm as this corresponds to the blue colour wavelength range. The integration time was set to 4 ms for the two loop reactors and to 30 ms for the Taylor-vortex membrane reactor (see below). The background absorbance resulting from the water and the PFA walls was subtracted from the tracer absorbance before the RTD study. Data analysis was performed using the spectrophotometer software Ocean Optics Spectra Suite.

$$A_L = -\log\left(\frac{I_t}{I_0}\right) = \psi L C \qquad\qquad \text{(E.1)}$$

Given the proportionality between the absorbance and the concentration, the residence time distribution, $E(t)$, can be derived according to Equation (E.2). The average residence time, τ, was determined by integrating the first moment of $E(t)$, see Equation (E.3). The dimensionless residence time distribution, $E(\theta)$, and time, θ, can be determined using Equation (E.4).

$$E(t) = \frac{C(t)}{\int_0^\infty C(t)\, dt} = \frac{A_L(t)}{\int_0^\infty A_L(t)\, dt} \tag{E.2}$$

$$\tau = \int_0^\infty t\, E(t)\, dt \tag{E.3}$$

$$E(\theta) = \tau\, E(t); \quad \theta = t/\tau \tag{E.4}$$

In the case of the slurry loop flat membrane (SLFM) reactor, the RTD data from the macromixing study were compared to the residence time distribution of a CSTR, E_{CSTR}, shown in Equation (E.5). The discrepancy between the two was calculated using the normalised residual sum of squares (*RSS*). Equation (E.6) shows the *RSS*, where *N* is the total number of experimental points.

$$E_{CSTR}(\theta) = e^{-\theta} \tag{E.5}$$

$$RSS = \frac{1}{N} \sum_i^N (E(\theta_i) - E_{CSTR}(\theta_i))^2 \tag{E.6}$$

## E.1. Slurry loop tubular membrane reactor

The RTD setup schematic of the slurry loop tubular membrane (SLTM) reactor is shown in Figure E.1. Prior to the RTD, deionised water was filled in all the reactor. At the inlet, one glass syringe (SGE) was filled with deionised water and a second one with an aqueous solution of the tracer (75 mg/L). Before the injection, the one containing the water was pumped using a syringe pump (PHD 2000, Harvard Apparatus) flowing water inside the reactor, where a recycle ratio of 400 was ensured by the recirculation pump. At the moment of the injection the valve of the water syringe was closed and that of the tracer syringe was opened, letting the tracer start flowing inside the reactor.
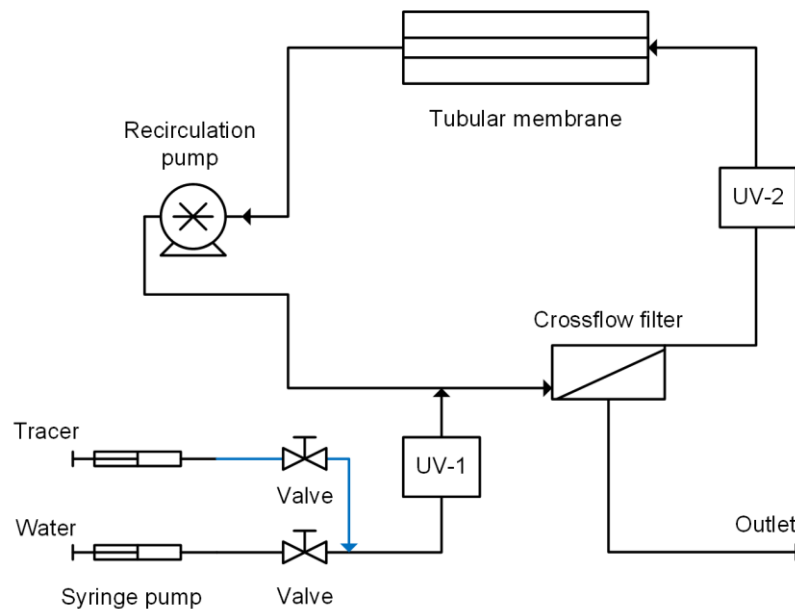

Figure E.1. Schematic of the experimental rig used for the residence time distribution study of the SLTM reactor. The flow cells of the spectrophotometers in which the capillary was inserted were installed in the loop (UV-2) and at the inlet of the reactor loop (UV-1).

The normalised tracer concentration of the inlet, $\hat{C}_{in}$, and the outlet (from the loop), $\hat{C}_{out}$, are presented in Figures E.2 and E.3 respectively. A Python code was developed to solve the convolution integral relating $\hat{C}_{out}$ to $\hat{C}_{in}$ *via* the assumed ideal CSTR behaviour [326]. By fitting the convolution integral to the experimental $\hat{C}_{out}$ it was possible to estimate the mean residence time of the

ideal CSTR representing the loop reactor. This was 60 min and close to the 58 min corresponding to the volume of the reactor divided by the inlet flowrate. The fitting was accomplished using the Nelder-Mead minimisation function provided by the package "SciPy" [261].
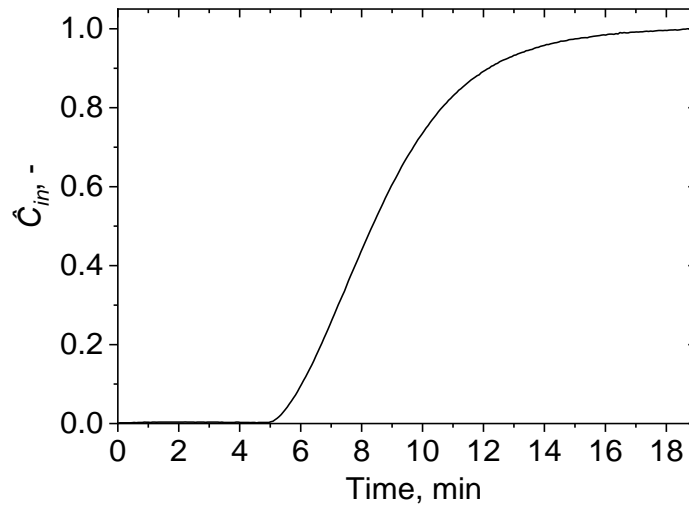

Figure E.2. Normalised tracer concentration at the inlet of the loop reactor (measured at UV-1) in the step-input RTD experiment at an inlet flowrate of 0.025 mL/min.
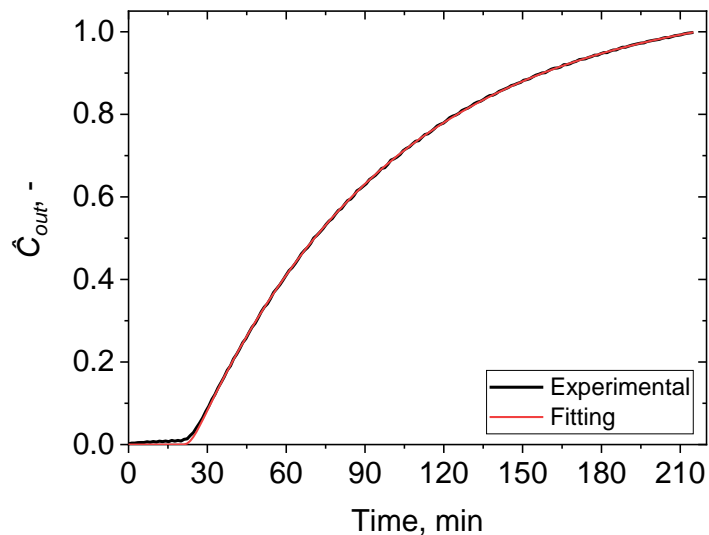
Figure E.3. Normalised tracer concentration in the loop reactor (measured at UV-2) in the step-input RTD experiment and the fitting obtained from the convolution integral of the normalised inlet tracer concentration profile with the RTD of an ideal CSTR. Inlet flowrate: 0.025 mL/min, recycle ratio: 400.
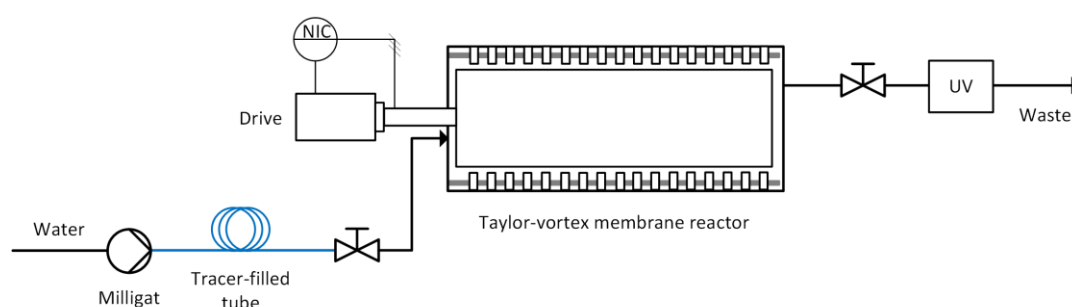
E.2. Slurry loop flat membrane reactor

The RTD setup schematic of the slurry loop flat membrane (SLFM) reactor is shown in Figure E.4. A syringe pump (Harvard Apparatus PHD 2000) was used to flow DI water, contained in a syringe (50 mL, SHE). Connected to the syringe was a perfluoro alkoxy capillary tube (PFA, 1/16'' OD x 0.040'' ID, Idex) filled with 100 µL of 7.5 g/L of tracer and closed at the outlet and inlet by two shut-off valves (0.04'' ID hole, Kinesis). Before the tracer injection, all the tubings were filled with DI water, including the loop. The recirculation flowrate was set to 10 mL/min and the two valves at the ends of the tracer-filled tubing were opened and the syringe pump was switched on. The inlet flowrate was varied from 0.1 mL/min to 1 mL/min and the elapsed time was taken from the moment the tracer entered the loop.
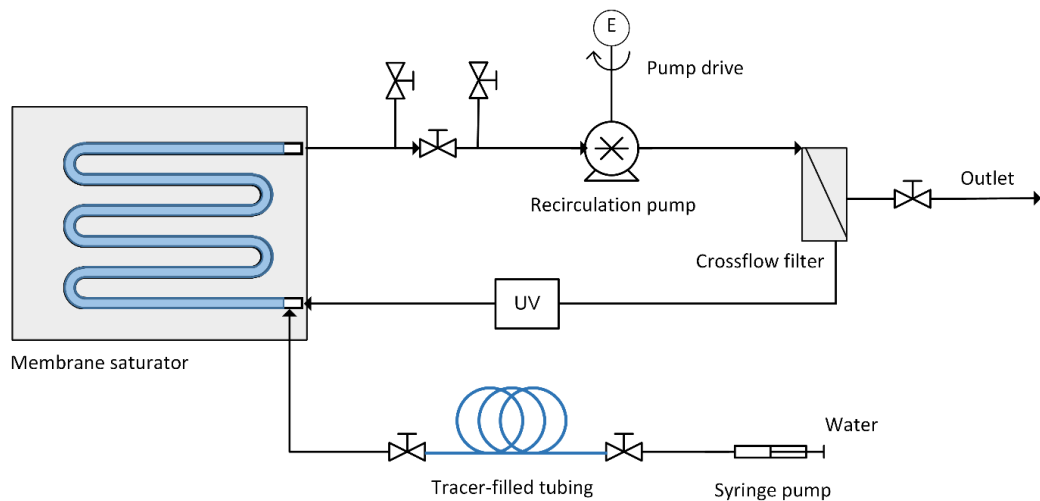
Figure E.4. Setup schematic of the SLFM reactor for the macromixing study. The tracer was introduced by a pulse-input injection. The flow cell of the UV-vis (UV) spectrophotometer was installed directly in the loop.

E.3. Taylor-vortex membrane reactor

The RTD setup schematic of the Taylor-vortex membrane reactor (TVMR) is shown in Figure E.5. A volume of 3 mL of the tracer at a concentration of 7.5 g/L in deionised water was filled in a PFA capillary tube (1/16'' OD x 0.040'' ID, Idex). This was connected to the liquid inlet port of the reactor and to a milligat LF pump (VICI Valco) that provided water at a constant flowrate. The integration time was set to 30 ms and scans were taken approx. every 6.03 s for the experiments at 6 mL/min inlet flowrate, and 12.06 s for those ones at 4 mL/min.


Figure E.5. Setup schematic of the TVMR for the macromixing study. The tracer was introduced by a pulse-input injection. The flow cell of the UV-vis (UV) spectrophotometer was installed directly in the loop (UV).

# Appendix F. Slurry loop flat membrane reactor design, characterisation and reactions

F.1. Design of the setup components

F.1.1. Saturator

The saturator was made of two parts in stainless steel (316L), one hosting the serpentine channel for the slurry flow and a second one designed for delivering the gaseous reactants. Between the two, a Teflon AF-2400 membrane (0.023" thickness, Biogeneral US) was sandwiched and in direct contact with the slurry flow. Figure F.1 shows the saturator part with the serpentine channel for the slurry and Figure F.2 reveals the technical details and dimensions of this block. There are three lateral holes for three cartridge heaters. The slurry mixture entered and left the saturator *via* two holes (1/4-28 UNF) at 30° to prevent clogging of the channel by the catalyst particles in the slurry (see section A-A in Figure F.2). Two further holes on both ends of the serpentine channel were designed for pressure measurements, one of which was also used to introduce the neat liquid substrate in the loop. The serpentine channel was 0.30 mm deep, 6 mm wide and each channel was separated by 7.7 mm distance between each other. The channel had 5 U-turns, a length of 808 mm and a surface area of 4850 mm^2.
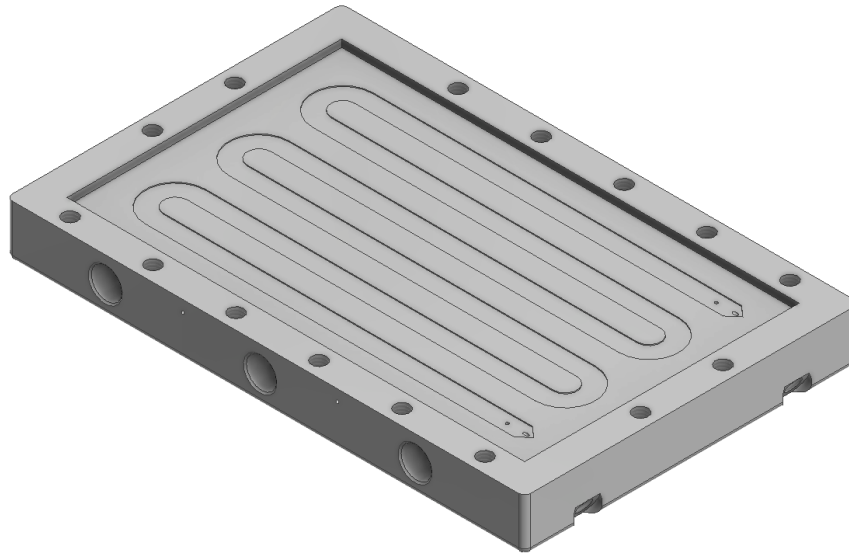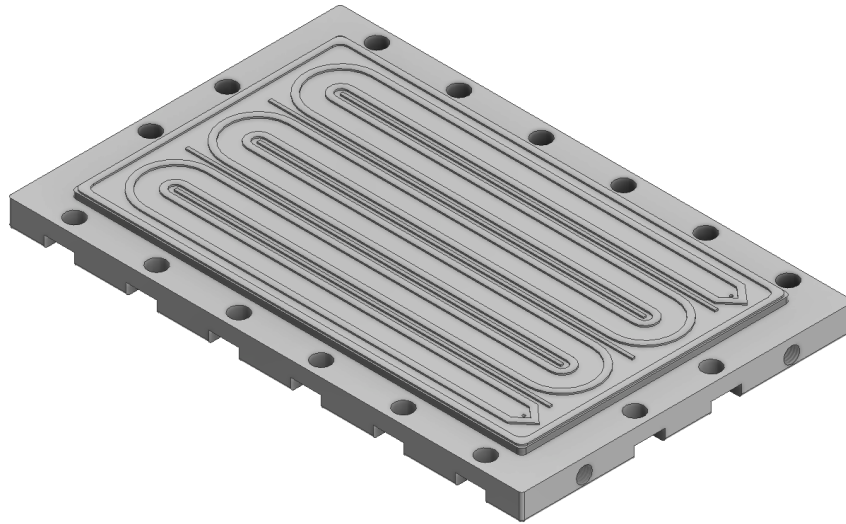
Figure F.1. Top part of the saturator hosting the channel for the slurry flow.
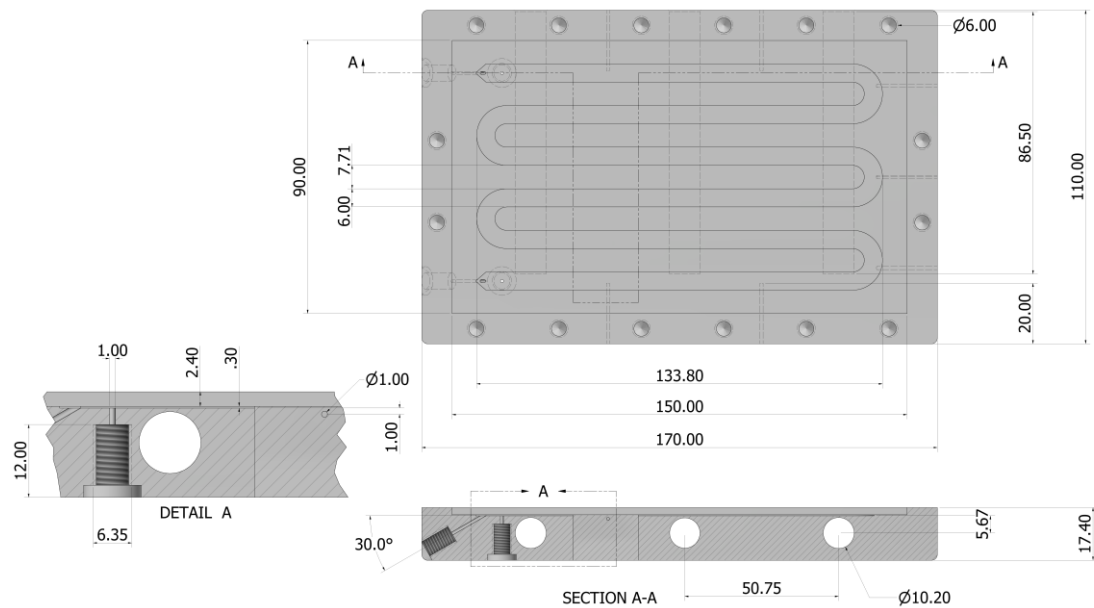
Figure F.2. Technical drawing of the saturator slurry side (top part) with section and detailed zoomed-in picture of one thermowell.

The Teflon AF-2400 membrane was placed over an area of 90 mm x 150 mm at the centre of the block, covering the whole serpentine channel. The part of the saturator hosting the gas channel is featured in Figure F.3 and Figure F.4. The channel was surrounded by a 2 mm thick edge and in between each channel a series of fins of 1 mm x 124 mm were designed. Both the edge and the fins were 0.50 mm higher compared to the channel surface and were

devised in order to exert pressure on the gasket around the slurry channel in order to prevent internal bypasses. The 2 mm thick edge was designed to enclose the whole serpentine in order to hinder external leakage. The gas inlet and outlet ports were perpendicular to the serpentine gas channel (see section A-A and detail A in Figure F.4).

Figure F.3. Bottom part of the saturator hosting the channel for the gas.
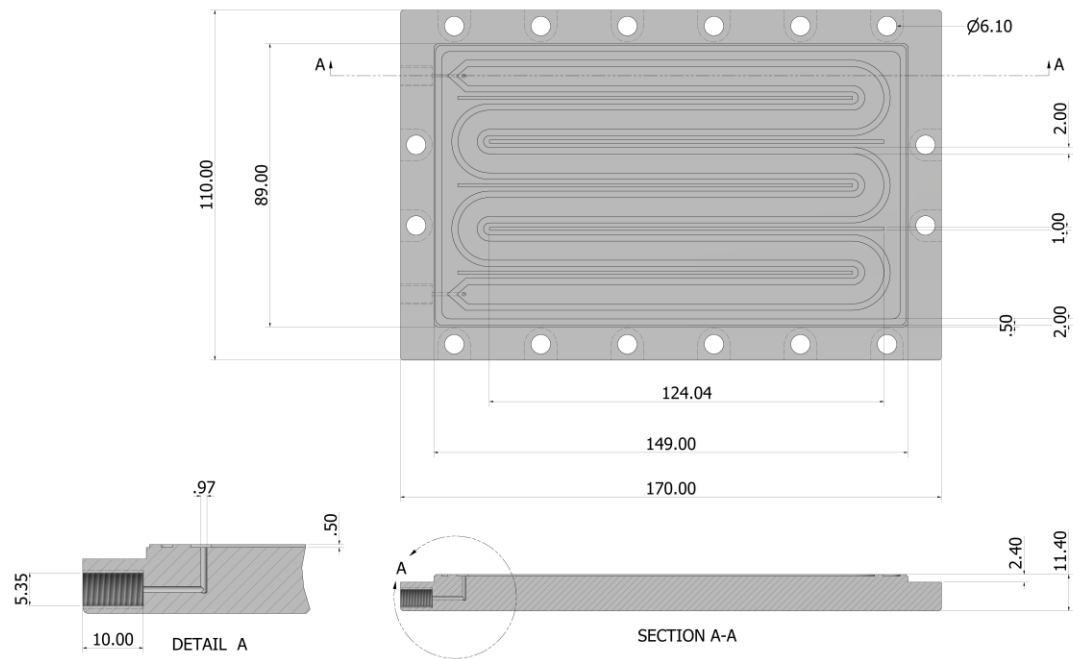
Figure F.4. Technical drawing of the saturator side hosting the gas channel (bottom part) with section and detailed zoomed-in picture of the inlet/outlet ports.

The saturator assembly is presented in Figure F.5. On the left-hand side it is possible to see the single parts inside the saturator. Above the Teflon AF-2400 membrane, a 304 stainless steel mesh (Industrial Netting) was placed to provide mechanical stability to the membrane. This had the same length (150 mm) and width (90 mm) of the membrane, but had a thickness of 0.05 mm. Furthermore, it was covered by microholes for 23% of the total area, with an average diameter of 76 µm. In order to seal the membrane and the mesh onto the slurry channel, a Kalrez® gasket (DuPont) with a thickness of 0.5 mm was cut and shaped according to the same geometry of the slurry channel and used on top of the metal mesh. The saturator was then tightened with sixteen M6x50 bolts (ISO 4762), flipped over and further tightened with two clamps held together by four M8 x 60 bolts (ISO 4762). The clamps had a set of ten pillars on one side that exerted pressure on the center of the saturator and avoided internal bypasses between the slurry channels. In Figure F.5 (right) it is possible to see two holes (1/4-28 UNF) on the top part of the saturator, to measure the slurry pressure across the serpentine. As stated before, the hole

on the left was also used as inlet port for introducing the reaction substrates during continuous operation.
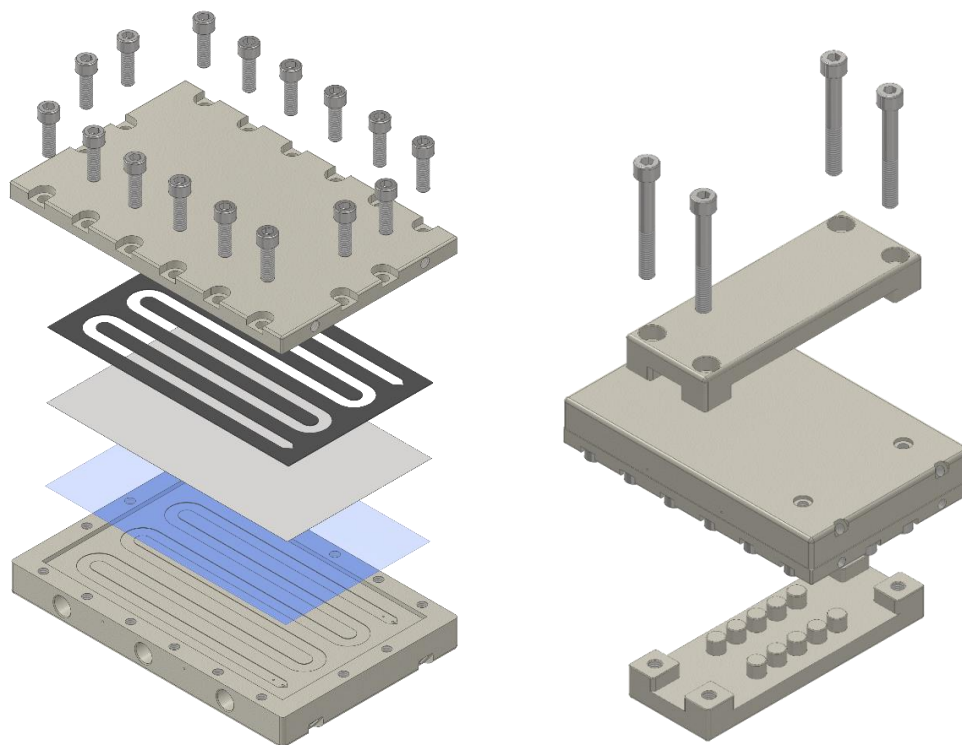
Figure F.5. Exploded assemblies of the saturator. On the left: The Teflon AF-2400 membrane (blue), metal mesh (light grey) and gasket (black) were assembled inside the saturator. On the right: The saturator is turned upside down and tightened with two clamps.

Pictures of the saturator are shown in Figure F.6. Holes for the thermocouples were distributed around the saturator while the cartridge heaters were inserted from one side and the wires collected outside the Delrin® acetal box.
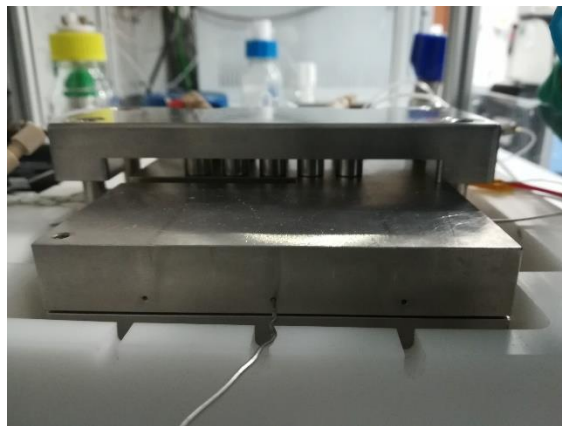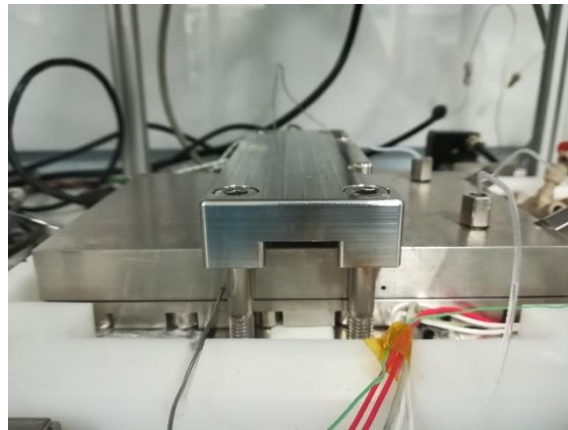
Figure F.6. Pictures of the saturator showing where thermocouples and cartridge heaters were inserted.

F.1.2. Heating units

In order for the reactor to operate up to 120 °C the saturator had three cartridge heaters (10 mm x 70 mm, 250 W, RS Components) inserted inside and covered by thermal grease (10 W/m/K, RS Components). Furthermore a silicon heater mat (100 mm x 150 mm, 15 W, RS Components) was placed below the crossflow filter and the pump head, and a polyimide flexible heater (10 W/in^2, Omega) was attached on the crossflow filter. Seven holes for thermocouples (T type, RS Components) were drilled around the saturator and one hole in the filter at 1 - 2 mm underneath the slurry channel, in order to measure the temperature profile and allow for heating control. The process thermocouple was inserted in the saturator (see below section F.3.1) and connected to a temperature control box, which controlled the power of the heaters according to the desired temperature setpoint.

The whole loop reactor was covered in a calcium-magnesium silicate thermal insulating sheets (6 mm thick, RS Components) and placed inside a Delrin$^®$ acetal box to decrease heat losses.

F.2. Styrene hydrogenation and gas-liquid mass transfer

F.2.1. Catalyst particle size distribution

The particle size distribution of the 5 wt% Pd/C catalyst (type 487, Alfa Aesar) was determined *via* laser scattering (LS 13 320, Beckman Coulter) and the result is shown in Figure F.7.
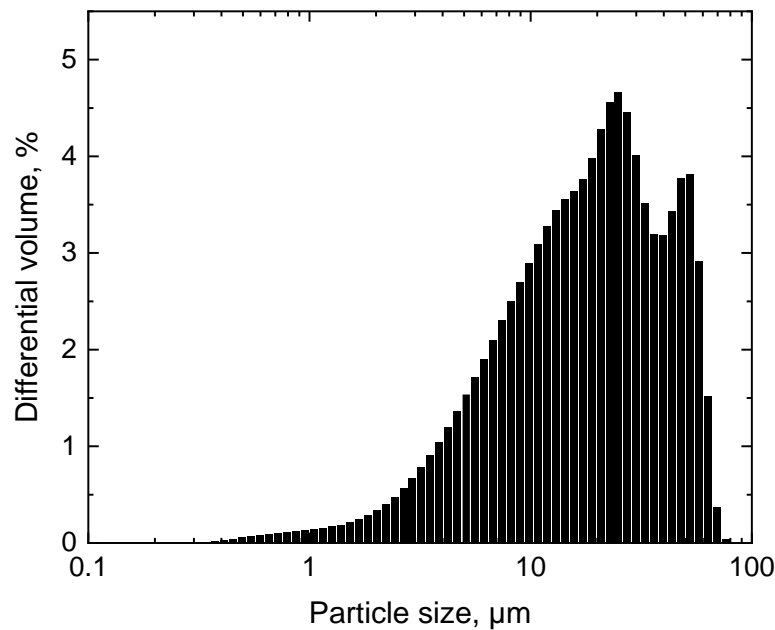
Figure F.7. Particle size distribution of the 5 wt% Pd/C employed in the gas-liquid mass transfer study in the slurry loop flat membrane reactor

F.2.2. $k_L a$ determination

Equation (6.1) in Chapter VI is derived considering all the steps in the transport of hydrogen from the bulk gas to the reaction on the catalyst particles in the slurry. In this derivation it is assumed that the mass transport of styrene is not limited by resistances, due to its relatively high concentration (2 M). The diffusion of hydrogen from the gas phase to the membrane is governed by Equation (F.1), where r_{H2} is the volumetric rate of transport, k_{GL} the external gas-liquid mass transfer coefficient, a the surface membrane area-to-reactor volume ratio, $p_{H2,bG}$ the pressure of hydrogen in the bulk gas phase, $p_{H2,iG}$ the

pressure of hydrogen on the surface of the membrane and H_E the Henry constant of hydrogen.

$$r_{H_2} = k_{GL}a \left(\frac{p_{H_2,bG}}{H_E} - \frac{p_{H_2,iG}}{H_E} \right)$$

(F.1)

However, for pure gases or slightly soluble gases, the adsorption and dissolution of hydrogen onto the membrane is improbable to be the rate limiting step [267]. As pure hydrogen was employed in this work, $p_{H2,bG}$ and $p_{H2,iG}$ can be assumed equal to each other (4 bar).

The mass transport of hydrogen across the Teflon-AF 2400 membrane can be written as in Equation (F.2). Here $P_{m,H2}$ is the hydrogen permeability across the membrane, $C_{H2,i}$ the hydrogen concentration on the membrane-liquid interface and δ_m the membrane thickness.

$$r_{H_2} = \frac{P_{m,H_2} \, a \, (p_{H_2,iG} - C_{H_2,i}H_E)}{\delta_m}$$

(F.2)

In certain cases this transport can be rate limiting. However, assuming the concentration of hydrogen at the membrane-liquid interface equal to zero, the maximum molar flowrate of hydrogen that can be delivered by the membrane would be $2.5 \cdot 10^{-6}$ mol/s, which translates into 0.074 mL/min of 2 M styrene in methanol being converted. However, results from experiments performed at 0.050 mL/min didn't show full conversion (*vide infra*), suggesting that the rate limiting step was not the hydrogen transport across the membrane.

Table F.1 shows the membrane properties from which the hydrogen molar flow can be calculated using Equation (F.2), where $p_{H2,iG}$ is equal to 4 bar.

Table F.1. Properties of the Teflon AF-2400 membrane film used in this work.

Property	Value
$P_{m,H2}$, barrer	2090
δ_m, mm	0.58
A_m, mm^2	4850
a, m^{-1}	3460

It is now possible to set Equation (F.2) equal to zero and determine $C_{H2,i}$ as a ratio between $p_{H2,iG}$ and H_E. Under the temperature (21 °C) and pressure (4 bar) employed in this work, the Henry constant for the hydrogen-methanol system was calculated according to Equation (F.3) and a value of 674 MPa/M was determined [267]. The concentration of hydrogen at the interface of the membrane with the liquid, $C_{H2,i}$, at 4 bar was taken equal to $5.93 \cdot 10^{-4}$ M.

$$\ln(H_E) = 122.3 - \frac{4815.6}{T} - 17.5 \ln(T) + 1.4 \cdot 10^{-7} p_{H_2} \tag{F.3}$$

Once diffused through the membrane, hydrogen must diffuse into the bulk liquid and on the catalyst surface where it can react with styrene. The hydrogen transport in the liquid phase can be described using Equation (F.4). Here, $k_L a$ stands for the volumetric gas-liquid mass transfer coefficient on the liquid side and $C_{H2,b}$ is the hydrogen concentration in the bulk liquid. Equation (F.5) describes the hydrogen transport from the bulk liquid to the catalyst surface, $C_{H2,s}$, where k_{LS} is the external liquid-solid mass transfer coefficient, a_p the external surface area of the catalyst per unit mass and ρ_{cat} is the catalyst loading.

$$r_{H_2} = k_L a \left(C_{H_2,i} - C_{H_2,b} \right) \tag{F.4}$$

$$r_{H_2} = k_{LS} a_p \rho_{cat} \left(C_{H_2,b} - C_{H_2,s} \right) \tag{F.5}$$

The diffusion of hydrogen through the pores of the catalyst particles and the reaction on the surface can be summarised in Equation (F.6) assuming first-order with respect to the concentration of hydrogen on the catalyst surface, $C_{H2,s}$. Here, η is the effectiveness factor and k' the pseudo-first order rate constant per unit of catalyst mass.

$$r_{H_2} = \eta \rho_{cat} k' C_{H_2,s} \tag{F.6}$$

At steady-state the abovementioned equations are equal to each other as shown in Equation (F.7). Summing all the driving forces it is possible to relate the concentration of hydrogen at the membrane-liquid surface, $C_{H2,i}$, to the single mass transport resistances, as expressed in Equation (F.8). This can be further rearranged into Equation (F.9) which shows the overall mass transfer resistance as a function of the single mass transfer resistances.

$$r_{H_2} = k_L a \left(C_{H_2,i} - C_{H_2,b} \right) = k_{LS} a_p \rho_{cat} \left(C_{H_2,b} - C_{H_2,s} \right) = \eta \rho_{cat} k' C_{H_2,s} \qquad (F.7)$$

$$C_{H_2,i} = \frac{r_{H_2}}{k_L a} + \frac{r_{H_2}}{k_{LS} a_p \rho_{cat}} + \frac{r_{H_2}}{\eta \rho_{cat} k'} \qquad (F.8)$$

$$\frac{C_{H_2,i}}{r_{H_2}} = \frac{1}{k_L a} + \frac{1}{\rho_{cat}} \left(\frac{1}{k_{LS} a_p} + \frac{1}{\eta k'} \right) \qquad (F.9)$$
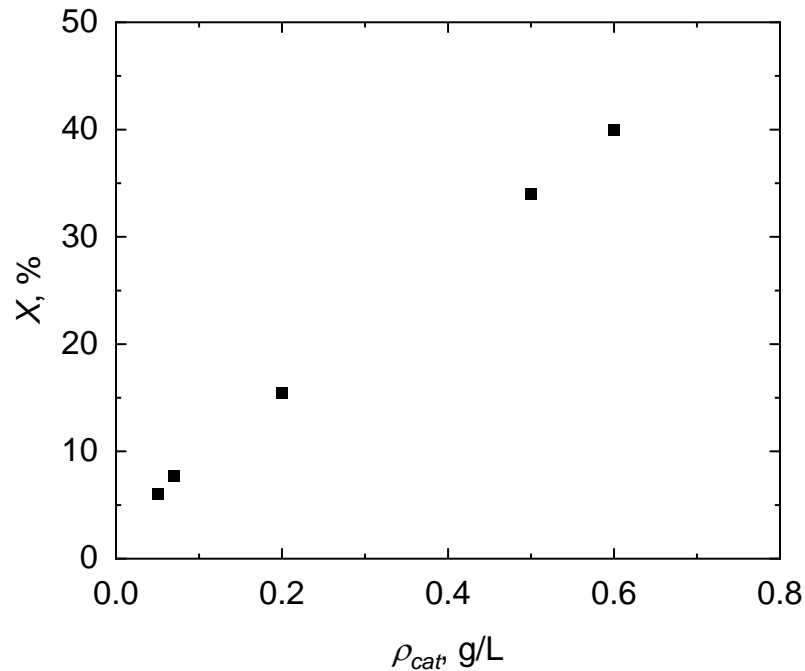
F.2.3. Styrene hydrogenation

At an inlet flowrate of 0.050 mL/min and a catalyst loading of 0.6 g/L, the recycle flowrate, v_{rec}, was varied from 5 to 20 mL/min. Hydrogen pressure above the membrane and the reactor temperature were kept constant at 4 bar and 21 °C. Figure F.8 shows the results from the experiment. In spite of the fact that the reactor was operating under CSTR conditions ($R > 100$), conversion increased by increasing the recycle flowrate. However, from 10 mL/min to 20 mL/min only a 5% conversion increment was observed.
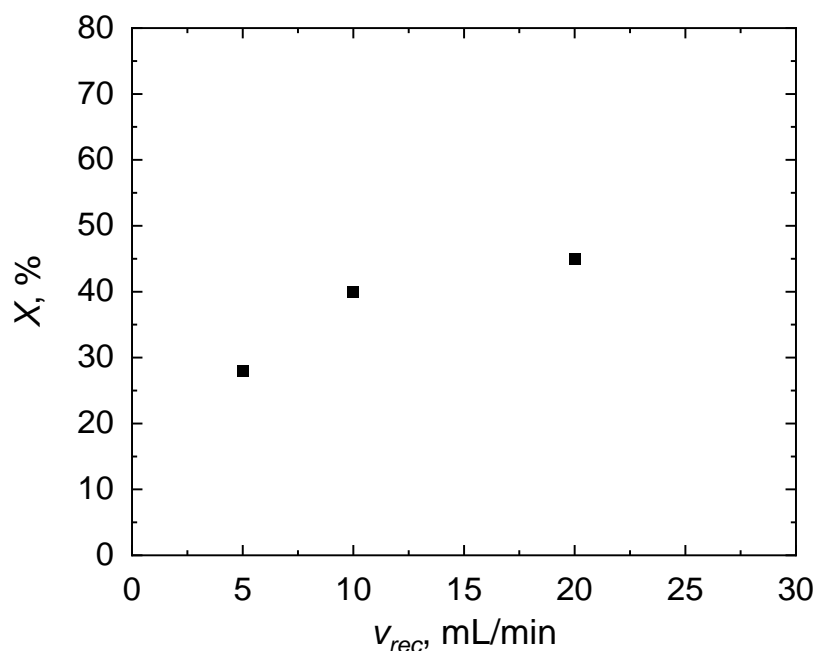
Figure F.8. Styrene conversion, X, as a function of the recycle flowrate, v_{rec}, in the styrene hydrogenation to ethylbenzene. Inlet flowrate: 0.050 mL/min, catalyst loading: 0.60 g/L, hydrogen pressure: 4 bar, temperature: 21 °C.

The catalyst loading was then varied in order to determine the value of k_La. Experiments were performed at 10 mL/min at 4 bar and 21 °C. Figure F.9 shows the experimetal results.

Figure F.9. Styrene conversion, X, as a function of the catalyst concentration, ρ_{cat}, in the styrene hydrogenation to ethylbenzene. Inlet flowrate: 0.050 mL/min, recycle flowrate: 10 mL/min, hydrogen pressure: 4 bar, temperature: 21 °C.

Calculation of the volumetric transport rate of hydrogen, used to determine the k_La was performed according to Equation (F.10). X is the styrene conversion, V_R is the reactor volume (1.4 mL) and v the inlet flowrate (0.050 mL/min).

$$r_{H_2} = \frac{v \, X \, C_{Sty,in}}{V_R} \tag{F.10}$$

F.2.4. Specific power input

The specific power input in the SLFM reactor can be derived from the Bernoulli equation. Equation (F.11) shows the Bernoulli equation applied to the recirculation pump, in the case of equal kinetic and potential energy at the inlet and the outlet of the pump and no dissipative energies within the pump. p_1 and p_2 stand for the inlet and outlet pressures, while H_{pump} is the pump head. The pressure drop on the pump, Δp_{pump}, can be written as the power provided by the pump, P_{pump}, divided by the recycle flowrate of the slurry, v_{rec}, as shown in Equation (F.12), and by definition the power is the product of the volumetric power input, ε, and the reactor volume, V_R.

$$p_1 + H_{pump} = p_2 \tag{F.11}$$

$$H_{pump} = p_2 - p_1 = \Delta p_{pump} = \frac{P_{pump}}{v_{rec}} = \frac{\varepsilon\, V_R}{v_{rec}} \tag{F.12}$$

F.3. Aerobic oxidation of alcohols

F.3.1. Temperature distribution in the loop

The loop reactor presented eight different positions between the saturator and the crossflow filter where temperature could be monitored. Figure F.10 shows the loop reactor inside the box and the areas of temperature measurement. Table F.2 reports temperature measurements during the solvent-free aerobic oxidation of benzyl alcohol at 6 bar oxygen pressure, 10 mL/min recycle flowrate and an overall temperature of 110 ± 1.4 °C. The process temperature was inserted in position number 4, where the highest temperature was measured.
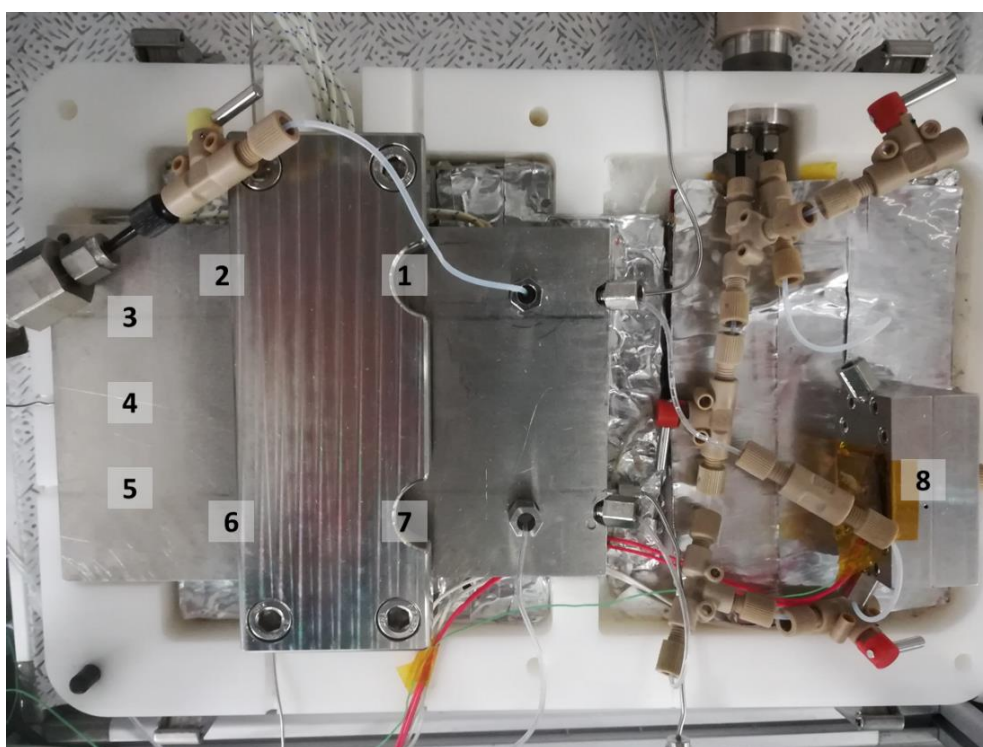
Figure F.10. Picture of the slurry loop flat membrane reactor without insulating sheets. Numbers indicate where thermocouples can be inserted for temperature measurements in the saturator (left) and the filter (right).

Table F.2. Temperature measurements in the saturator and the filter during the continuous solvent-free benzyl alcohol aerobic oxidation, referring to Figure F.10. The reaction was carried out at 6 bar oxygen pressure and using 14 mg of 1 wt% Au-Pd/TiO$_2$ catalyst.

| Component	Area	Temperature, °C
	1	111
	2	111
	3	112
Saturator	4	112
	5	108
	6	109
	7	109
Filter	8	110

F.3.2. Continuous operation

The conversion and product selectivity results from the continuous aerobic oxidation of benzyl alcohol, cinnamyl alcohol, geraniol, 1-phenylethanol and piperonyl alcohol are reported below.

F.3.3.1. Benzyl alcohol

The solvent-free oxidation of benzyl alcohol was performed for 7 h and Figure F.11 reports conversion and product selectivity during that period. No noticeable decrease in conversion was observed in the last 4 h of operation. In the case of the oxidation of diluted benzyl alcohol (Figure F.12) conversion was higher (74%) with a 82% selectivity to benzaldehyde and only 2% to toluene.
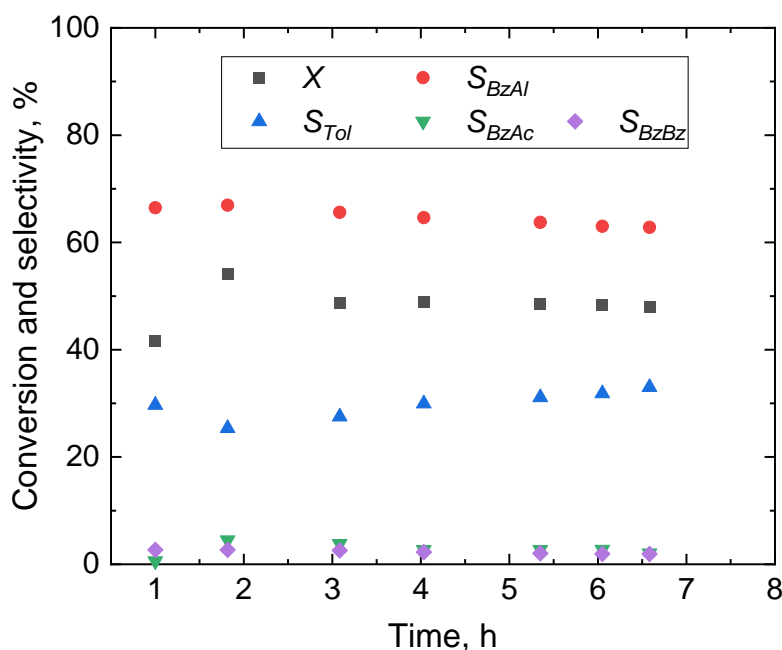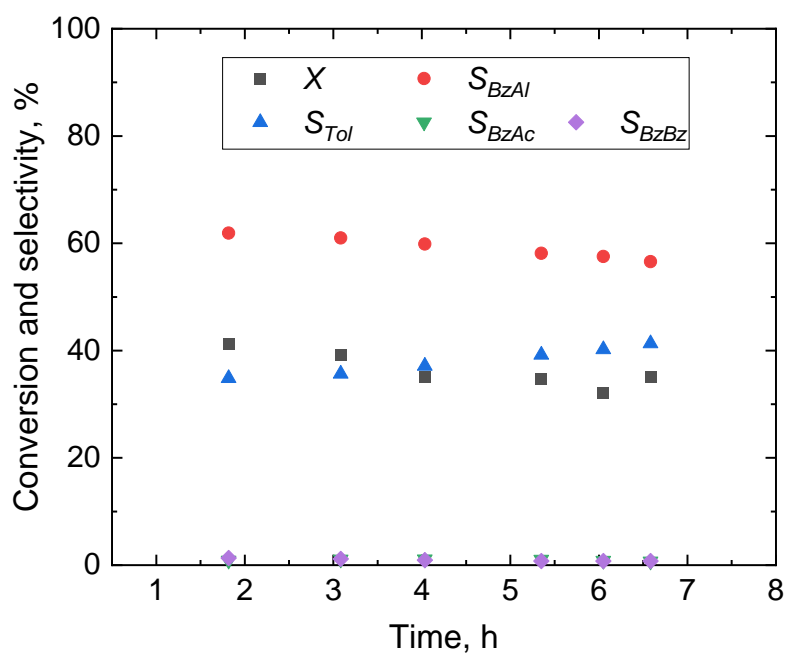

Figure F.11. Benzyl alcohol conversion, X, benzaldehyde, S_{BzAl}, toluene selectivity, S_{Tol}, benzoic acid selectivity, S_{BzAc}, and benzyl benzoate selectivity, S_{BzBz}, during 7 h of solvent-free continuous reaction. Inlet flowrate: 100 µL/min, oxygen pressure: 6 bar, temperature: 110 °C, reactor volume: 1.4 cm^3, 1 wt% Au-Pd/TiO$_2$ catalyst concentration: 10 g/L.
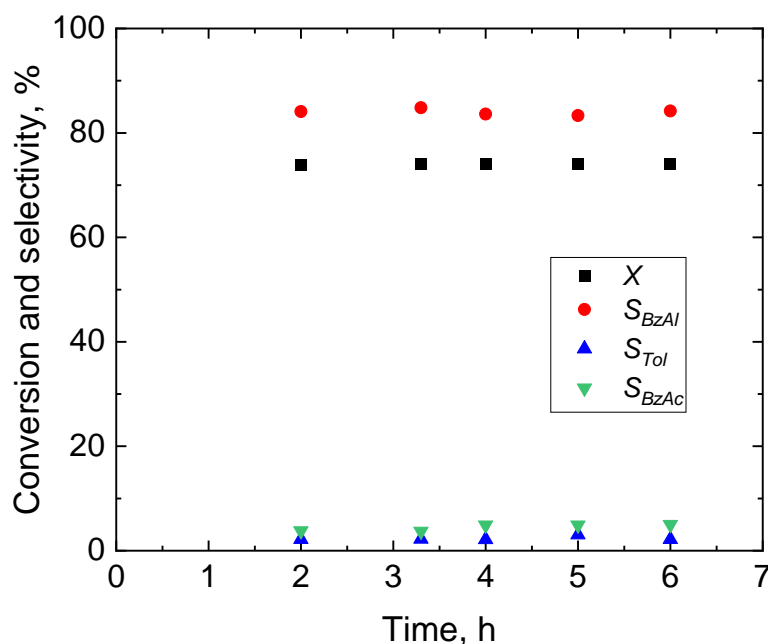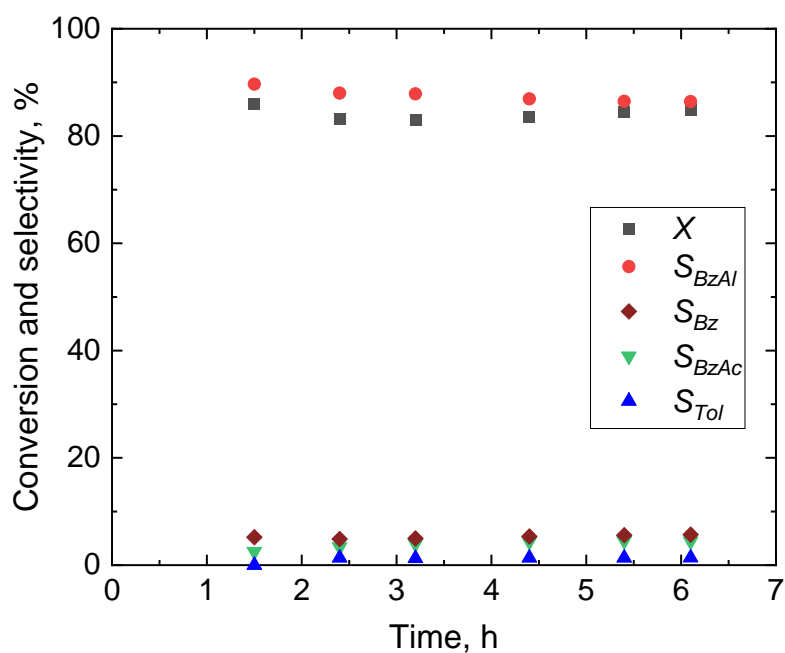
Figure F.12. Benzyl alcohol conversion, X, benzaldehyde, S_{BzAl}, toluene selectivity, S_{Tol} and benzoic acid selectivity, S_{BzAc}, during 6 h of continuous reaction. Benzyl alcohol inlet concentration: 0.1 M, inlet flowrate: 100 μL/min, oxygen pressure: 5 bar, temperature: 120 °C, reactor volume: 1.4 cm^3, 1 wt% Au-Pd/TiO$_2$ catalyst concentration: 10 g/L.

Conversion and product selectivity from the solvent-free benzyl alcohol oxidation performed in a 8.8 cm^3 reactor (scaled-up) are reported in Figure F.13. Conversion stabilised to 35% in the last 2 h, while benzaldehyde selectivity was about 60%. Selectivity to the main by-products (benzoic acid and benzyl benzoate) was lower than 5%. The scaled-up oxidation of benzyl alcohol was also performed in *tert*-butylbenzene and Figure F.14 shows the results. Benzyl alcohol conversion was 84%, 86% of which was converted to benzaldehyde while toluene selectivity was about 1%. The main by-products were benzoic acid whose selectivity was *ca.* 5% and benzene with a selectivity of 6%.

Figure F.13. Benzyl alcohol conversion, X, benzaldehyde, S_{BzAl}, toluene selectivity, S_{Tol}, benzoic acid selectivity, S_{BzAc}, and benzyl benzoate selectivity, S_{BzBz}, during 7 h of continuous solvent-free reaction. Inlet flowrate: 220 µL/min, oxygen pressure: 5 bar, temperature: 120 °C, reactor volume: 8.8 cm^3, 1 wt% Au-Pd/TiO$_2$ catalyst concentration: 10 g/L.

Figure F.14. Benzyl alcohol conversion, *X*, benzaldehyde, S_{BzAl}, benzoic acid selectivity, S_{BzAc}, and benzene selectivity, S_{Bz}, during 6 h of continuous reaction. Benzyl alcohol inlet concentration: 0.1 M, inlet flowrate: 360 µL/min, oxygen pressure: 5 bar, temperature: 120 °C, reactor volume: 8.8 cm^3, 1 wt% Au-Pd/TiO$_2$ catalyst concentration: 10 g/L.
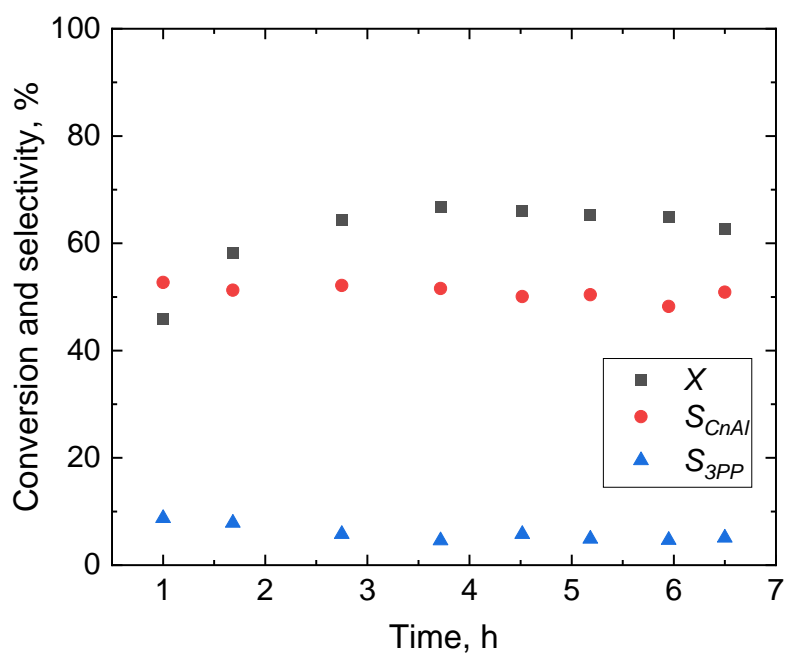
F.3.3.2. Cinnamyl alcohol

Diluted cinnamyl alcohol was oxidised at 90 °C and 2 bar oxygen pressure, and its conversion and selectivity to cinnamaldehyde and 3-phenyl-1-propanol are reported in Figure F.15. Figure F.16 shows results from the scaled-up reaction, performed in a 8.8 cm^3 reactor (88 mg catalyst).
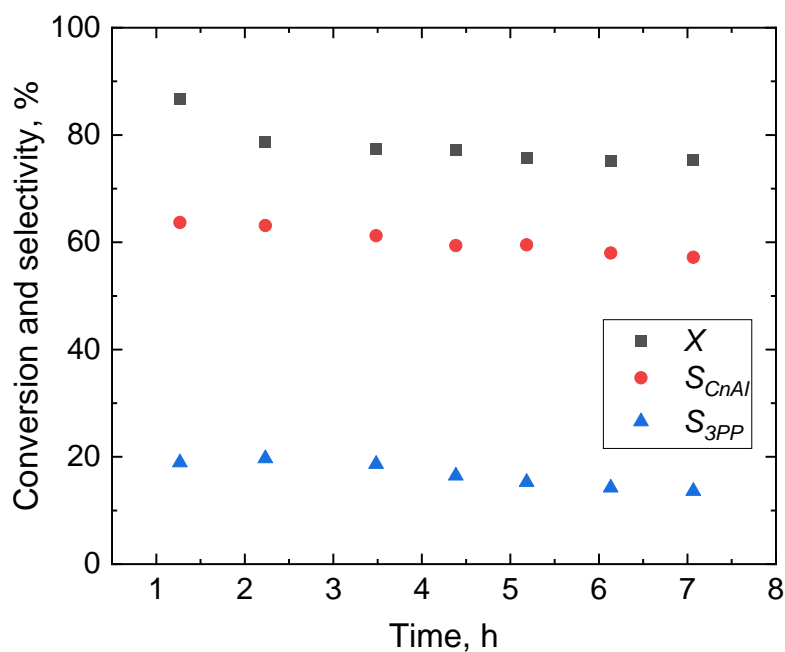
Figure F.15. Cinnamyl alcohol conversion, X, cinnamaldehyde, S_{CnAl}, and 3-phenyl-1-propanol selectivity, S_{3PP}, during 7 h continuous reaction. Inlet cinnamyl alcohol concentration: 0.1 M, inlet flowrate: 100 µL/min, oxygen pressure: 2 bar, temperature: 90 °C, reactor volume: 1.4 cm^3, 1 wt% Au-Pd/TiO$_2$ catalyst concentration: 10 g/L.

Figure F.16. Cinnamyl alcohol conversion, X, cinnamaldehyde, S_{CnAl}, and 3-phenyl-1-propanol selectivity, S_{3PP}, during 7 h continuous reaction. Inlet cinnamyl alcohol concentration: 0.1 M, inlet flowrate: 200 µL/min, oxygen pressure: 2 bar, temperature: 100 °C, reactor volume: 8.8 cm^3, 1 wt% Au-Pd/TiO$_2$ catalyst concentration: 10 g/L.

F.3.3.3. Geraniol

Geraniol was oxidised and its conversion and selectivity to geranial are reported in Figure F.17. Due to the lower inlet flowrate (20 µL/min), steady-state was reached after about 3 h from the start-up. Selectivity to geranial was found to be higher at low conversion and lower (*ca.* 28%) when conversion increased to approx. 28%.
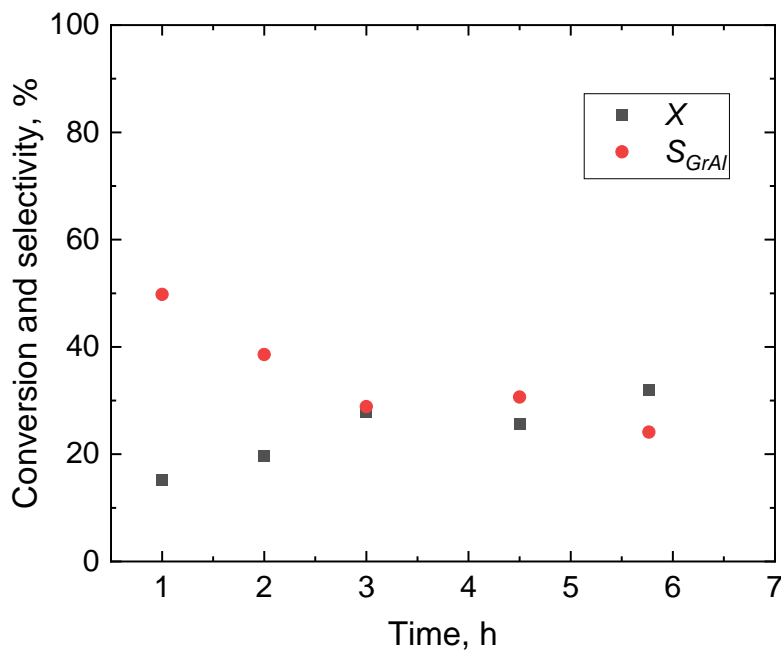
Figure F.17. Geraniol conversion, *X*, and geranial selectivity, S_{GrAl}, during 6 h continuous reaction. Inlet 1-geraniol concentration: 0.1 M, inlet flowrate: 20 µL/min, oxygen pressure: 6 bar, temperature: 120 °C, reactor volume: 1.4 cm^3, 1 wt% Au-Pd/TiO$_2$ catalyst concentration: 10 g/L.

F.3.3.4. 1-Phenylethanol

Conversion of 1-phenylethanol and its selectivity to acetophenone are reported in Figure F.18. The conversion stabilised to *ca.* 30% with 100% selectivity to acetophenone.
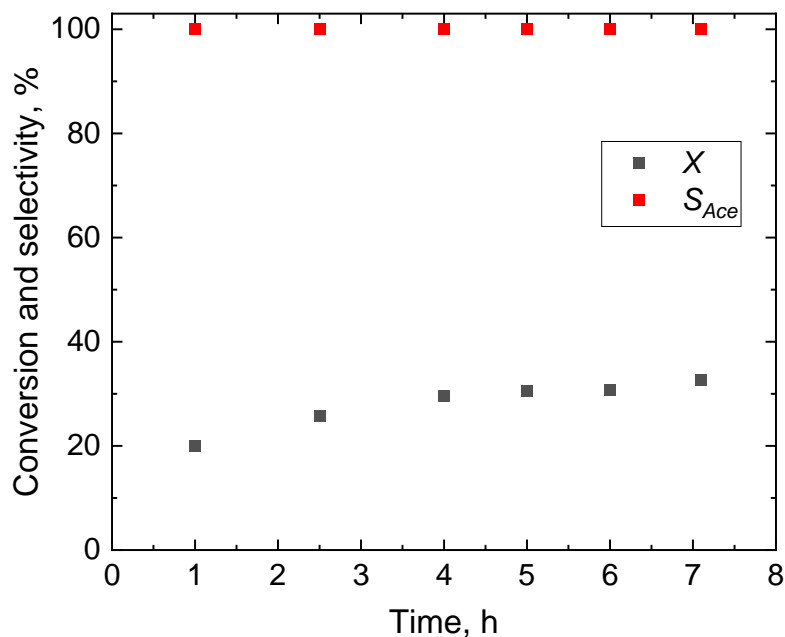
Figure F.18. 1-Phenylethanol conversion, *X*, and acetophenone selectivity, S_{Ace}, during 7 h continuous reaction. Inlet 1-phenylethanol concentration: 0.1 M, inlet flowrate: 80 µL/min, oxygen pressure: 6 bar, temperature: 120 °C, reactor volume: 1.4 cm^3, 1 wt% Au-Pd/TiO$_2$ catalyst concentration: 10 g/L.
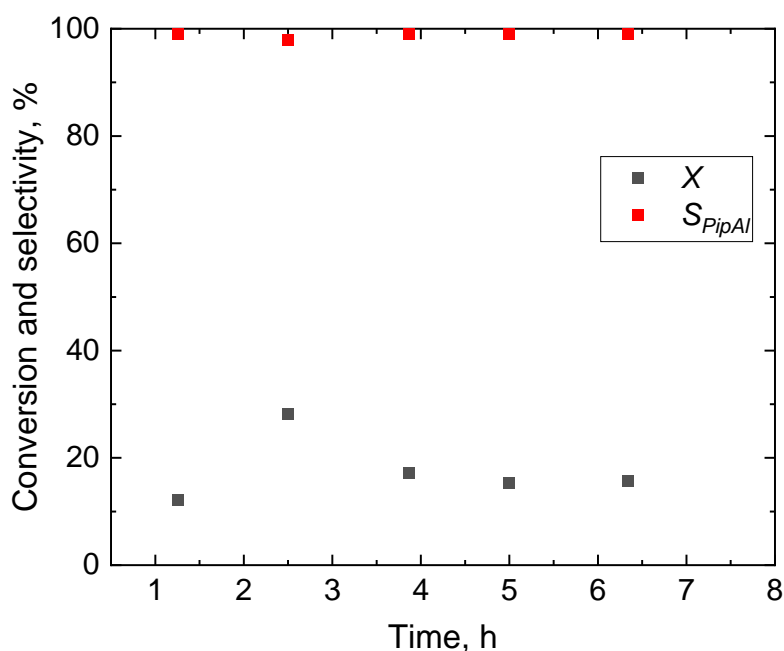
F.3.3.5. Piperonyl alcohol

The oxidation products of piperonyl alcohol were analysed by manually injecting the samples in a GC-MS (QP2010 SE, Shimadzu). A typical spectrum is shown in Figure F.19. At retention times of 7.7 min and 8 min, mesitylene, the internal standard, and the solvent *tert*-butylbenzene are observed. Piperonal was separated after 12 min and this was the only detected product, while piperonyl alcohol eluted after 12.3 min.
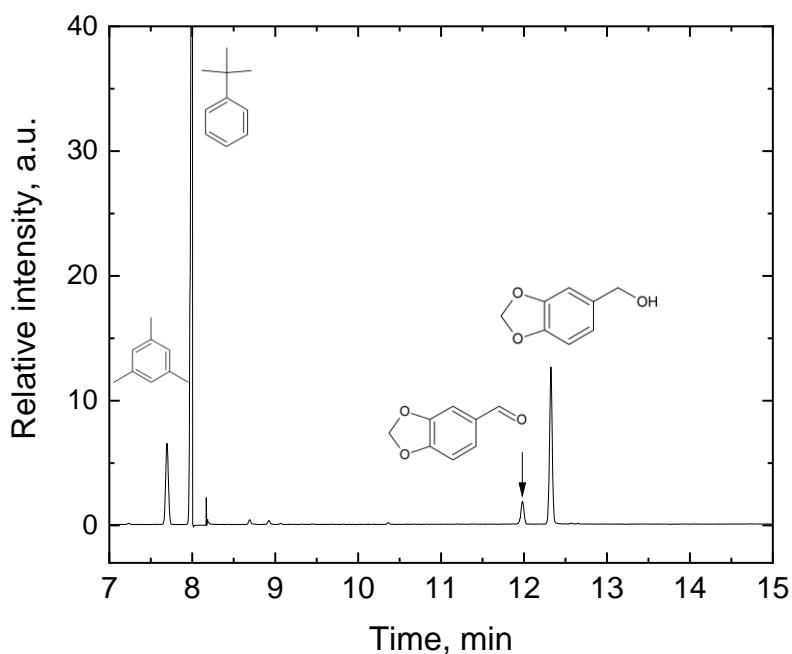
Figure F.19. Typical GC-MS spectrum for the piperonyl alcohol continuous aerobic oxidation products.

Piperonal concentration was estimated by dividing the area under its peak with that of piperonyl alcohol, multiplied by the known piperonyl alcohol concentration. This could be done assuming similar relative response factors between the two molecules. The response factor of a flame ionisation detector is mainly a function of the carbon number and the molecular weight of a molecule and its value does not differ much between molecules with a hydroxyl group and a corresponding carbonyl group [327].

Figure F.20 shows the piperonyl alcohol conversion and piperonal selectivity over 6.5 h continuous reaction.

Figure F.20. Piperonyl alcohol conversion, X, and piperonal selectivity, S_{PipAl}, during 6.5 h continuous reaction. Inlet piperonyl alcohol concentration: 0.1 M, inlet flowrate: 30 μL/min, oxygen pressure: 5 bar, temperature: 120 °C, reactor volume: 1.4 cm^3, 1 wt% Au-Pd/TiO$_2$ catalyst concentration: 10 g/L.

Unlike in the continuous reaction, the batch oxidation of piperonyl alcohol produced other products (Figure F.21). These include 1,3-benzodioxole (8.5 min), 3,4-methylenedioxy toluene (12.6 min) and piperonylic acid (14 min), the latter possibly resulting from the oxidation of piperonal. Piperonal concentration was estimated as described above and a selectivity of 65% was determined.
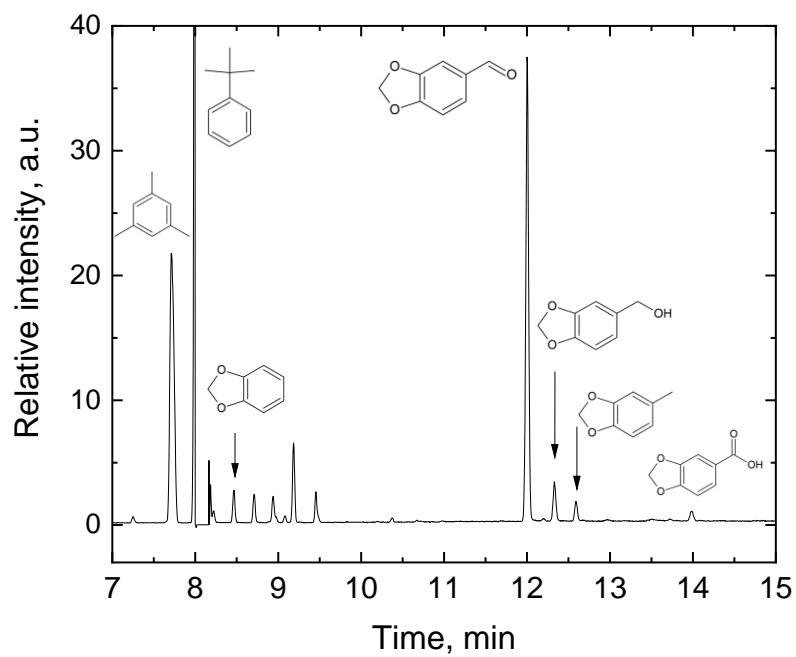
Figure F.21. GC-MS spectrum for the piperonyl alcohol batch aerobic oxidation products.

F.3.3.6. Pervaporation rate and safety considerations

In the scaled-up continuous oxidations, pure oxygen was flowing in the gas channel at a flowrate of 30 NmL/min (measured under normal conditions: 20 °C and 1 atm). A cold trap (0 °C, 1 atm) installed at the gas outlet ensured the condensation of the organic vapours entrained in the flowing gas. The condensed liquid was collected in a vial and the amount weighted at the end of the reaction. For reactions conducted in *tert*-butylbenzene, no organic vapour condensed in the vial. This could be ascribed to the high boiling point of the solvent (169 °C) and to the low concentration of alcohol substrates in the reaction. The choice of diluting the alcohols in *tert*-butylbenzene made the risk of creating flammables mixtures in the oxygen phase negligible.

However, in the solvent-free oxidation of benzyl alcohol an amount of 0.341 g of organics was collected after 6 h reaction. These were analysed at the GC and the first row of Table F.3 shows the molar fraction of each component in the collected liquid, x_i. Equation (F.13) was used to calculate the mass flowrate of each component, $\dot{m}_i$, where MM_i is the molar mass and $\dot{m}_{vap}$ the average mass flowrate of organics in the gas phase during 6 h of operation (57 mg/h). The molar concentration of each component in the gas phase, y_i, was derived using Equation (F.14), where v_{O2} is the oxygen flowrate (30 NmL/min), R_G the ideal gas constant (8.3145 J/mol/K), T the absolute temperature (393 K) and p_{O2} the oxygen pressure (5 bar).

$$\dot{m}_i = \frac{x_i \, MM_i}{\sum_i x_i \, MM_i} \, \dot{m}_{vap} \tag{F.13}$$

$$y_i = \frac{\dot{m}_i}{MM_i} \frac{R_G \, T}{p_{O_2} v_{O_2}} \tag{F.14}$$

Summing up the molar fractions of benzyl alcohol, benzaldehyde and toluene in the gas phase the organics concentration in the gas phase would be 0.2%. The lower flammability limit (*LEL*) of the organics in pure oxygen can be estimated using the approach developed by Chen [328]. Equation (F.15) was applied to benzaldehyde and benzyl alcohol, as the *LEL* of toluene in oxygen is reported to be 1.1% [329]. In the equation, $LEL_{i,O2}$ and $LEL_{i,air}$ are the lower flammability limit in oxygen and air of the i-th component, while $\hat{c}_{p,O2}$ and $\hat{c}_{p,N2}$

are the molar heat capacities of oxygen (30 J/mol/K, [330]) and nitrogen (31 J/mol/K, [328]), respectively.

$$LEL_{i,O_2} = \frac{LEL_{i,air}\ \hat{c}_{p,O_2}}{LEL_{i,air}\ \hat{c}_{p,O_2} + (1 - LEL_{i,air})(0.21\ \hat{c}_{p,O_2} + 0.79\ \hat{c}_{p,N_2})} \qquad (F.15)$$

Benzyl alcohol has an *LEL* in air of 1.3%, similar to the 1.4% of benzaldehyde [331, 332]. Applying Chen's method, the lower flammability limits in oxygen are 1.25% and 1.35% respectively, and still above toluene's *LEL*. Therefore, since the flammability limit of a mixture of benzyl alcohol, benzaldehyde and toluene vapours will never be lower than the lowest flammability limit of the components (1.1% in this case) [189], it is possible to conclude that the concentration of organics (0.2%) was below the flammability window and hence the continuous scaled-up aerobic oxidation of benzyl alcohol was operated under safe conditions.

Table F.3. Mass flowrates and molar fraction of benzyl alcohol, BzOH, benzaldehyde, BzAl, and toluene, Tol, in the liquid, x_i, and in oxygen, y_i, during the continuous scaled-up aerobic oxidation of benzyl alcohol. The total concentration of organics in oxygen is lower than the lower flammability limit, *LEL*.

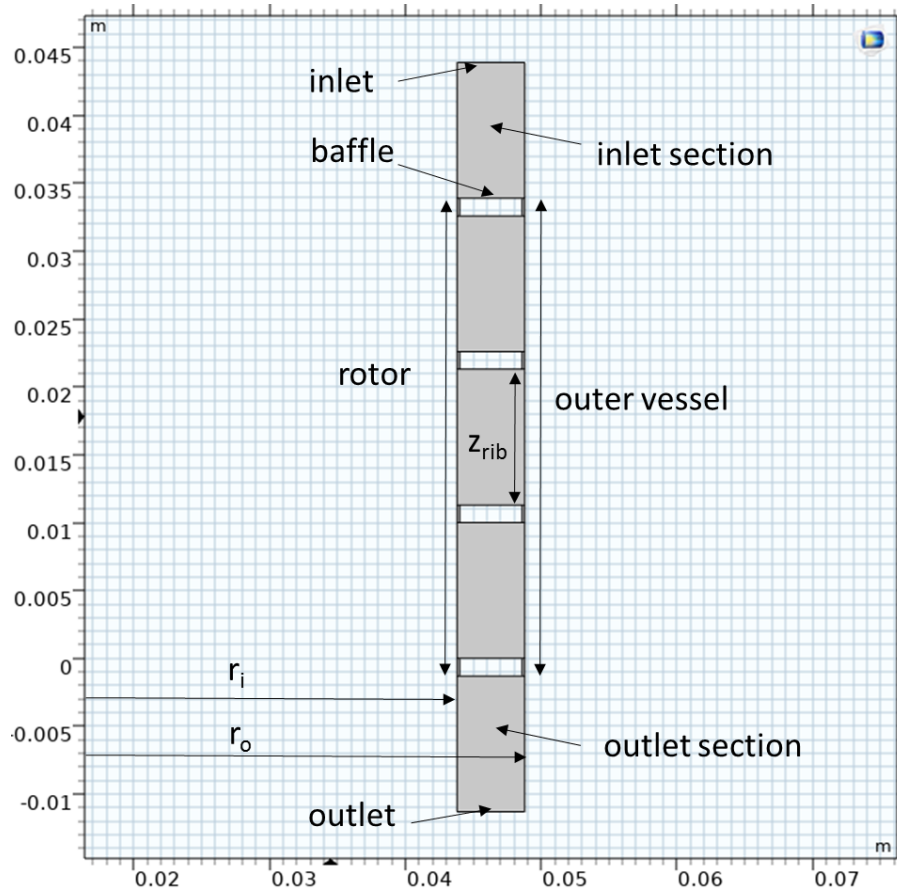|	BzOH	BzAl	Tol	Total
x_i, mol%	40	29	31	100
$\dot{m}_i$, mg/h	24	17	16	57
y_i, mol%	0.08	0.06	0.06	**0.2 (< *LEL* = 1.1)**

Appendix G. Taylor-vortex membrane reactor simulations

G.1. Interbaffle distance effect on vortex velocity

The effect of the interbaffle distance on the vortex properties was simulated using COMSOL Multiphysics® 5.5. The annulus of the Taylor-vortex membrane reactor was modelled by considering only three horizontal baffles and two interbaffle annular sections. The baffles were modelled without holes and without the tubular membrane inside the annulus, and the liquid was assumed flowing in the annulus through the 0.2 mm gap between the baffle and the outer vessel and the rotor. Figure G.1 shows the model geometry. Three interbaffle sections between the rotor and the outer vessel were simulated, while an inlet and an outlet section were included to simulate the liquid inlet and outlet streams outside the rotor zone. The rotor radius, r_i, the outer vessel radius, r_o, and the baffle thickness are reported in Chapter VII. The liquid was modelled as water with density, ρ, of 1000 kg/m^3 and viscosity, μ, of 1 mPa·s in the laminar regime. The time-dependent momentum balance, featured in Equation (G.1) and the continuity in Equation (G.2) were solved together. In these equations, $\boldsymbol{u}$ is the velocity vector, p the pressure and $\boldsymbol{g}$ the gravitational field.

$$\rho \frac{\partial \boldsymbol{u}}{\partial t} + \rho(\boldsymbol{u} \cdot \nabla)\boldsymbol{u} = -\nabla p + \mu \nabla^2 \boldsymbol{u} + \rho \boldsymbol{g} \tag{G.1}$$

$$\rho \nabla \cdot \boldsymbol{u} = 0 \tag{G.2}$$

Figure G.1. Axisymmetric model of 3 interbaffle sections in the Taylor-vortex membrane reactor.

The boundary conditions are presented below. The non-slip velocity condition in Equation (G.3) was considered at the surfaces of the baffles and the outer wall, while non-zero velocity (slip velocity) was assumed for the walls of both the inlet and the outlet section. This was done to facilitate convergence, and because these sections are fictitious, as they do not represent the real inlet and outlet of the reactor. The velocity magnitude of the fluid near the wall of the rotor was set equal to the tip speed of the rotor, as in Equation (G.4), where Ω is the rotor angular speed in rad/s, r_i is the rotor radius and *step(t)* is a smooth step function that increases from 0 to 1 in 1 s. This is done in order to simulate the ramping speed of the rotor with the fluid being still at t = 0 s.

$$u_{wall} = 0 \tag{G.3}$$

$$u_{rotor} = \Omega\, r_i\, step(t) \tag{G.4}$$

At the inlet, a normal inflow velocity was assumed with a magnitude equal to the volumetric flowrate, v, over the cross sectional area of the annulus, A, (Equation (G.5)) while at the outlet a constant pressure of 0 barg was assumed (Equation (G.6)).

$$u_{in} = v/A \tag{G.5}$$

$$p_{out} = 0 \tag{G.6}$$

The equations above were solved using the Backward Differentiation Formula (BDF) for the time stepping, with free steps taken by the solver and with a relative tolerance for the study of 0.001. The geometry was divided in a mapped mesh with 16300 elements, with a minimum and maximum mesh size of $1.5 \cdot 10^{-5}$ m and $3.35 \cdot 10^{-4}$ m, respectively. The simulation was repeated using a finer mesh with 32100 mesh elements, to ensure a mesh-independent solution. In fact, a maximum variation of 0.2% was calculated for the velocity magnitude.

Simulations were performed for different interbaffle distances, ranging between 5 and 15 mm and for a rotor angular speed of 10 rpm. The inlet flowrate was 2 mL/min. Figure G.2 shows the velocity magnitude of the Taylor vortices, u_{TV}, after 3 min at steady-state conditions. This velocity is calculated according to Equation (G.7), where u_r and u_z are the radial and axial components of the velocity.

$$u_{TV} = \sqrt{u_r^2 + u_z^2} \tag{G.7}$$
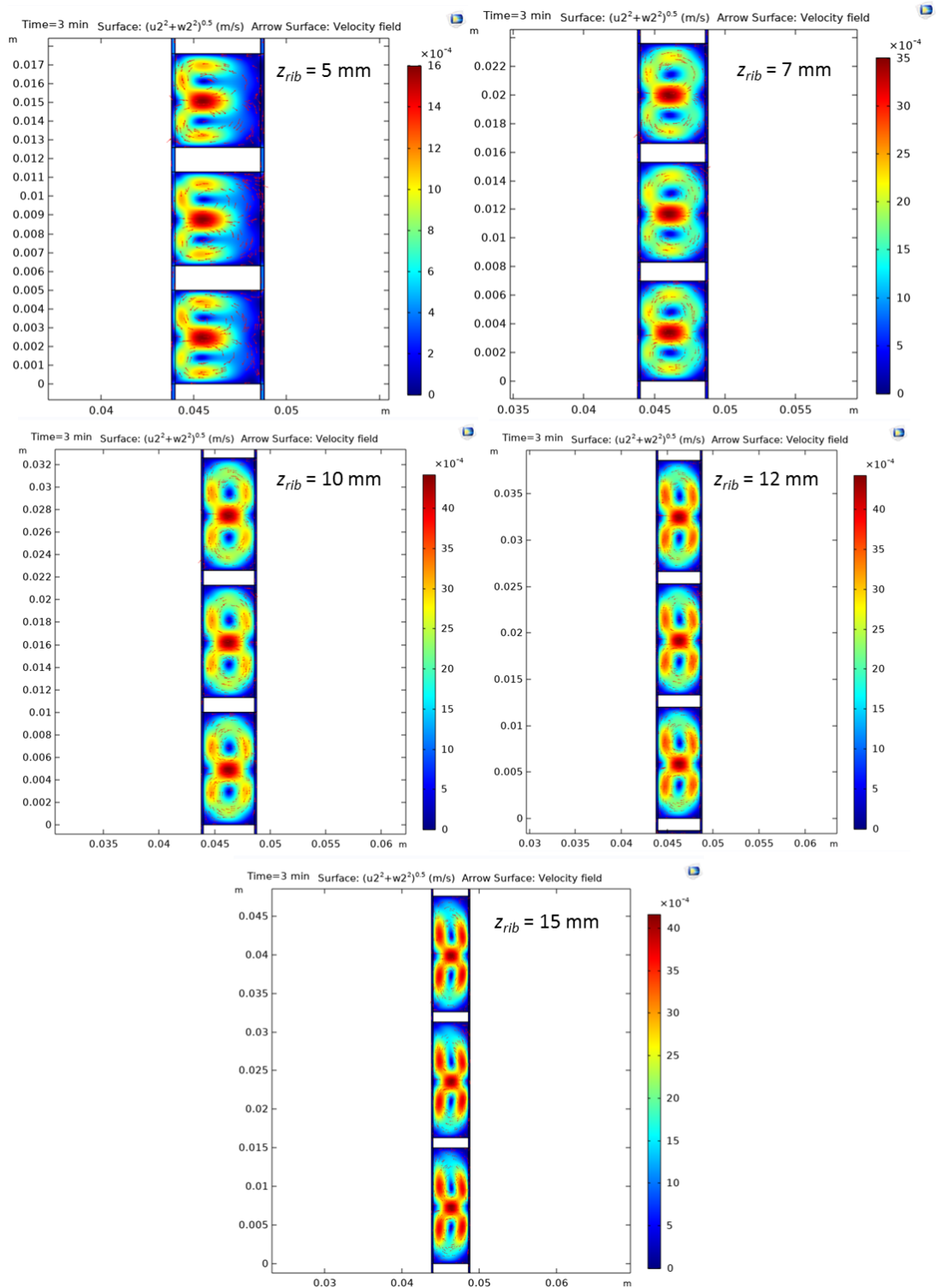
Figure G.2. Fluid velocity field in the meridian plane of the Taylor-vortex membrane reactor annulus at different interbaffle distances, z_{rib}, at a rotor angular speed of 10 rpm and after 3 min of steady-state conditions. Inlet flowrate: 2 mL/min.

Figure G.2 shows the coupled counter-rotating vortices between the baffles, which stretch or compress when the distance between two baffles increases or decreases. In Figure G.3, the average, $u_{TV,av}$, and the maximum value of the vortex velocity, $u_{TV,max}$, calculated inside the area between two consecutive baffles, are plotted as a function of the rotor speed and the interbaffle distance. It is possible to notice that for a constant rotational speed, both values of the Taylor vortex velocity increase when z_{rib} increases from 5 to 10 - 12 mm and decrease for larger values of the baffle distance. In particular, while $u_{TV,av}$ shows a maximum value for z_{rib} equal to 12 mm, $u_{TV,max}$ reaches its maximum for z_{rib} equal to 10 mm, corresponding to the "8" shape coupled vortex configuration (see Figure G.2). For this reason, the distance between two consecutive baffles was set to 10 mm, with the annulus gap being 5 mm.
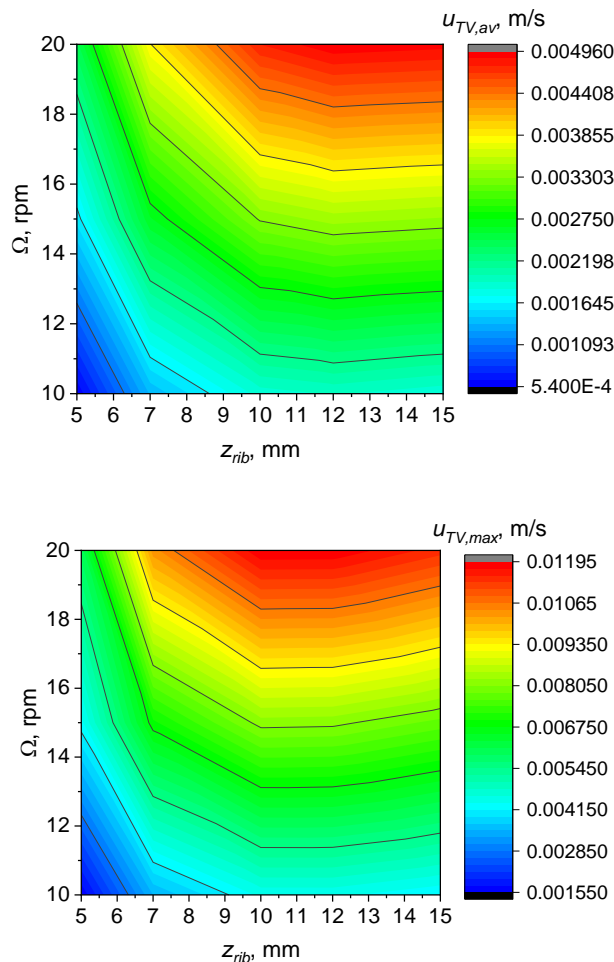

Figure G.3. Average, $u_{TV,av}$, and maximum velocity, $u_{TV,max}$, of the Taylor vortices as a function of the rotor angular speed, Ω, and the interbaffle distance, z_{rib}. The annulus gap is 5 mm.

G.2. Oscillatory angular speed effect on mesomixing

Simulations using COMSOL Multiphysics® 5.5 were performed on an axisymmetric model of a ribbed rotor featured in Figure G.4. The reactor in these simulations had two ribs on the rotor which created a gap with the outer vessel. The inlet and outlet sections were simulated in order to specify a flow of liquid that entered and left the system. However, these sections did not experience the rotation of the rotor.

The dimensions of the system are reported in Table G.1.
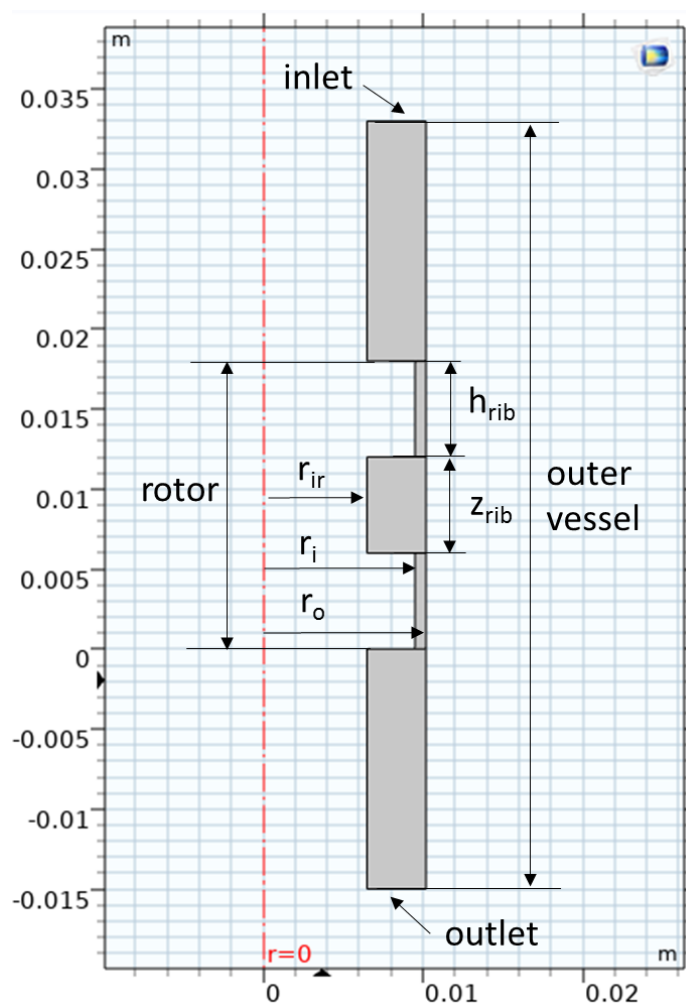
Figure G.4. Axisymmetric model of 2 interbaffle sections in a Taylor-vortex reactor with a ribbed rotor.

Table G.1. Dimensions of the simulated ribbed rotor.

Geometrical property	Value, mm
r_o	10.2
r_i	9.5
r_{ir}	6.5
h_{rib}	6.0
z_{rib}	6.0

The liquid was modelled as water with density, ρ, of 1000 kg/m³ and viscosity, μ, of 1 mPa·s in the laminar regime. Equations (G.1) and (G.2) were solved simultaneusly. However, the rotor agitation speed, and thus the velocity of the liquid at the rotor wall, was set equal to Equation (G.8), where ω is the oscillation frequency and Ω the rotor angular speed, equal to 80 rpm. The rotor angular speed rotates according to a sinusoidal function around 0 rpm, but with an amplitude of 80 rpm.

$$u_{rotor} = \Omega\, r_i \sin(\omega t) \tag{G.8}$$

The non-slip velocity boundary condition was adopted for the rest of the walls of the geometry with a zero inlet flowrate at the inlet. The system was therefore studied without a constant flow of liquid.

The objective of this simulation is to model the transport of a tracer inside the interrib area and observe its mixing with the existing fluid. To do so, the transport of diluted species in Equation (G.9) was solved, where C is the concentration of the tracer and D_m is 6.4·10⁻¹⁰ m²/s (see Chapter VII).

$$\frac{\partial C}{\partial t} + \boldsymbol{u} \cdot \nabla C = D_m \nabla^2 C \tag{G.9}$$

The zero flux boundary conditions of Equation (G.10) for the transport of the species was adopted for all the walls except for the wall segment on the outer vessel line corresponding to z_{rib} (see Figure G.4). In this section, an injection of a tracer was simulated with a gaussian function as described in Equation (G.11), where C_0 is equal to 1 M, σ is the standard deviation equal to 0.1, and t_0 the injection time equal to 1.5 s.

$$\nabla C_{wall} = 0 \tag{G.10}$$

$$C_{wall} = \frac{C_0}{\sigma\sqrt{2\pi}}\, e^{-\frac{(t-t_0)^2}{2\sigma^2}}$$

(G.11)

The Backward Differentiation Formula (BDF) for the time stepping was used to solve the equations above, with free steps taken by the solver and with a 0.005 relative tolerance for the study. A mapped mesh with 176000 elements was used, with a minimum and maximum mesh size of $3.3 \cdot 10^{-7}$ m and $2.86 \cdot 10^{-5}$ m.

The simulation was performed with an oscillation frequency, ω, of π/3 rad/s, corresponding to a period of time of 6 s in which the rotor started from 0 rpm, reached an angular speed of +80 rpm, decreased to 0 rpm, reached -80 rpm and then 0 rpm again. Figure G.5 shows the tracer diffusion in the interrib area. It is possible to observe that the tracer diffused from the point of the injection around the interrib area at a simulation time between 7 s and 9 s. However, at around 10 s and 13 s when the rotor reached the maximum speed in absolute value and it started to decelerate, the vortex broke forming a lamella with a reduced thickness flowing inside the vortex. This pattern periodically repeated itself.
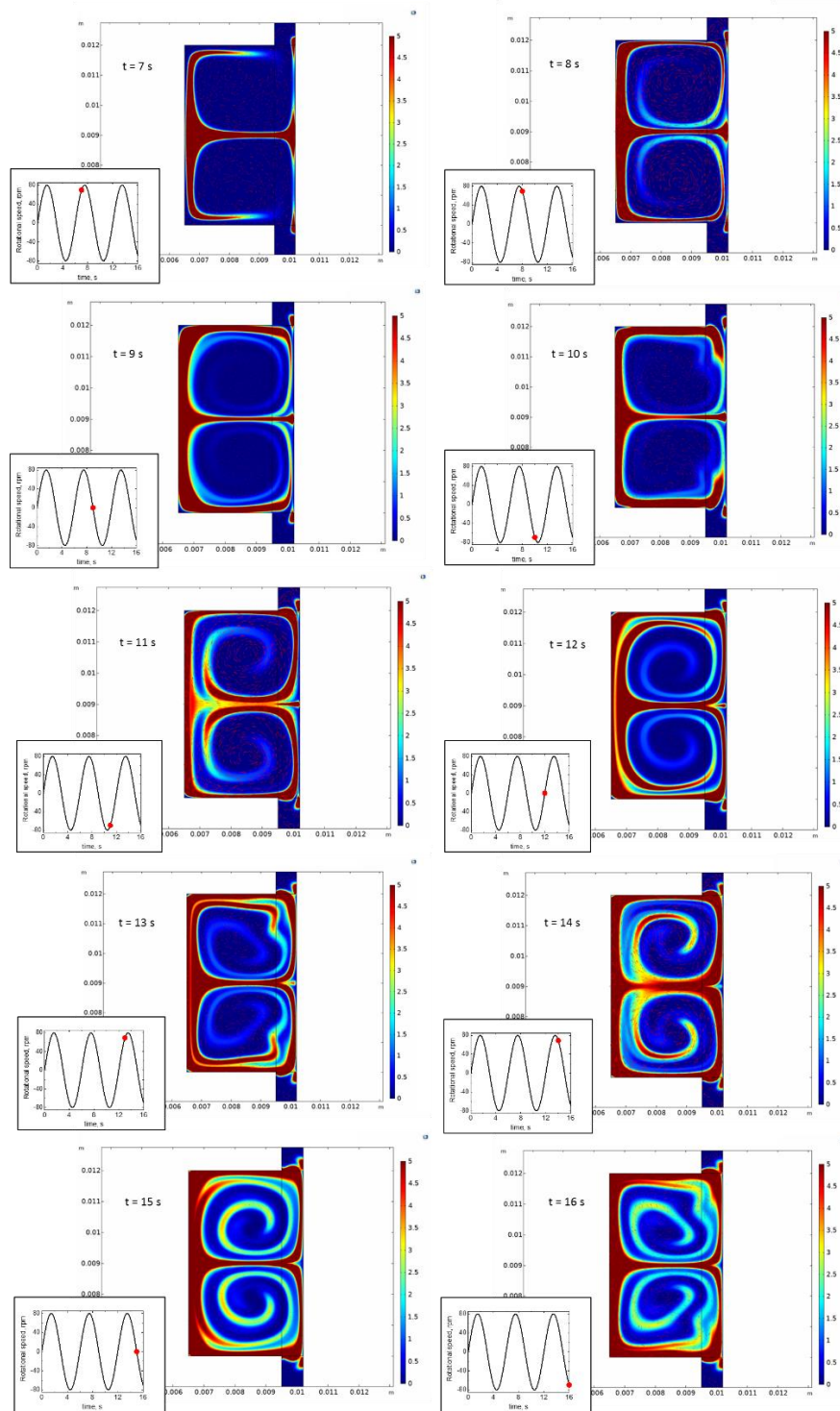
Figure G.5. Sequence of images showing the interrib area and the tracer diffusing inside the vortex when the rotor is perfoming an oscillatory rotation. At the bottom left of each image the agitation speed is shown. The tracer concentration (mol/m^3) legend is displayed in the column on the right of each image. The simulation time is shown on the left of each image, with the injection time being t = 0 s.

These results can be compared to the rotor with a steady angular speed of 80 rpm, and be better visualised using the Danckwerts intensity of segregation, I_s, which is calculated according to Equation (G.12), where σ_t^2 is the concentration variance at any time and $\sigma_{t,o}^2$ is the initial variance [333]. This quantity describes the degree of mixing and ranges between 0, corresponding to a uniform concentration and 1, equivalent to maximum segregation.

$$I_s = \frac{\sigma_t^2}{\sigma_{t,o}^2} \tag{G.12}$$

Figure G.6 shows the intensity of segregation for operation with a steady angular speed and the oscillatory asngular speed.
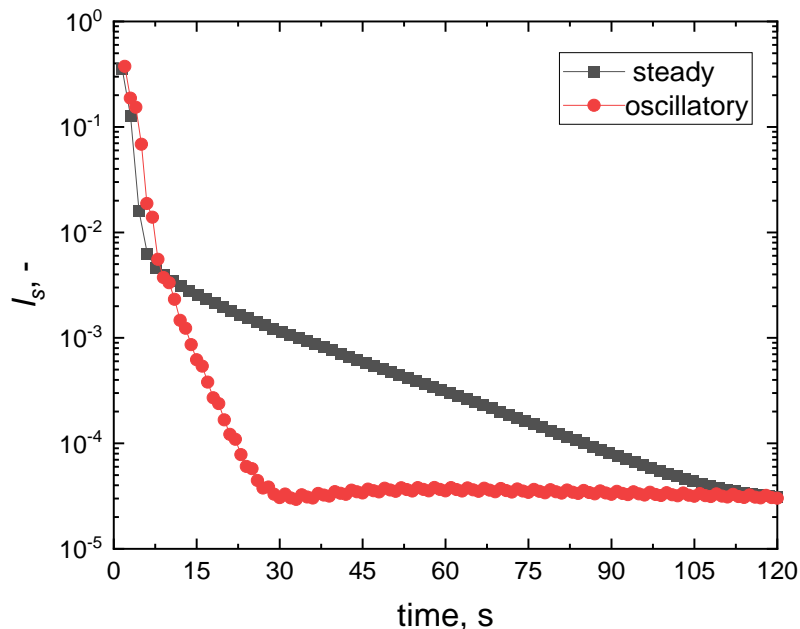
Figure G.6. Intensity of segregation in a ribbed Taylor-vortex reactor for the rotor with a steady angular speed of 80 rpm and the rotor with a sinusoidal angular speed with a an amplitude of 80 rpm and a period of 6 s.

It is possible to observe that up to 9 s of simulation time the concentration variance decreases with a similar rate in both systems. However, after 9 s of simulation time the steady angular speed shows a slower decrease in the intensity of segregation with respect to the oscillatory operation, reaching a segregation intensity value of $3.15 \cdot 10^{-5}$ in 110 s, compared to the 29 s of the

oscillatory rotor. This can be attributed to the dynamic nature of the oscillations that induce a disruption in the vortex creating lamellae with smaller thicknesses that decrease the diffusion path and accelerate mixing, with respect to diffusion in a steady vortex. Following this result, it may be possible to decrease the Taylor-vortex space-time using oscillations in the rotor, enhancing the mesomixing while keeping a low overall backmixing.